DROPLET INTERACTIONS WITH MICRO- AND NANOSTRUCTURED SURFACES FOR ADVANCED HEAT TRANSFER APPLICATIONS

BY

PATRICIA BARBARA WEISENSEE

DISSERTATION

Submitted in partial fulfillment of the requirements
for the degree of Doctor of Philosophy in Mechanical Engineering
in the Graduate College of the
University of Illinois at Urbana-Champaign, 2016

Urbana, Illinois

Doctoral Committee:

Professor William P. King, Chair, Director of research
Assistant Professor Nenad Miljkovic, Co-director of research
Professor Anthony Jacobi
Professor David G. Cahill

ABSTRACT

Droplets. Droplets are omnipresent: from rain droplets, over ink-jet printers, to advanced heat exchangers and thermal management systems. But in order to use droplets to our advantage, we need to study and understand how they interact with surfaces. Throughout this dissertation, I use optical photography and high speed imaging to characterize droplet-solid interactions.

When liquid water comes into contact with a hydrophobic surface, such as Teflon, it forms individual droplets. The contact angle that the droplet develops with the surface is well understood in an air environment. However, when placed in a pure water vapor environment, I show that contact angles can decrease by up to 10% as compared to those in air. At the same time, on micro- and nanostructured surfaces, the vapor environment has little effect on the static contact angles. Based on Young's equation and Fowke's concept of the additivity of surface tensions, I propose that the decrease in contact angle on flat hydrophobic Teflon arises from molecular water vapor adsorption to the Teflon surface.

In many engineering applications, the use of metals, as opposed to silicon and polymers, is desired to render surfaces water and oil repellent. I introduce micro electrical discharge machining (mEDM) as a viable tool to fabricate scalable micro-mushrooms (~ 100 μm) on steel blocks (~ 1 cm). I show that narrow micro-mushrooms with wide spacing give the highest contact angles (θ_A/θ_R = 170°/151°) and droplet mobility with water, while microstructures with flat tops, strong re-entrant curvature and smaller gap widths are necessary to support non-wetting droplets with liquids with a low surface tension, such as oils and alcohols (θ_A/θ_R = 148°/74° with isopropanol).

After studying static and quasi-static droplet-surface interactions, I continued characterizing droplet dynamics during impact on micro- and nanostructured surfaces. Contact times during impact on rigid surfaces are constant over a wide range of impact speeds, and are thus difficult to control. I show that contact times of water droplets impacting elastic superhydrophobic surfaces can be reduced by up to 50% when compared to impact on rigid surfaces due to a *springboard effect*, during which droplet lifts off the surface prior to fully recoiling. Upon impact, the droplet excites the substrate to oscillate, while during liquid retraction, the substrate imparts vertical momentum back to the droplet, causing early droplet lift-off with reduced contact time. Through detailed experimental and theoretical analysis, I show that this novel *springboarding* phenomenon is achieved for a specific range of Weber numbers ($We > 40$) and droplet Froude numbers during spreading ($Fr > 1$).

For droplets impacting vibrating superhydrophobic surfaces (60-320 Hz), I show that vibration frequency and phase at impact strongly influence the contact time of the bouncing droplets. I introduce the concept of a frequency-dependent critical impact phase at which contact times transition from a minimum ($t_c \approx 0.5\ t_{c,th}$) to a maximum ($t_c \approx 1.6\ t_{c,th}$). Through semi-empirical modeling I show that average contact times can be actively controlled and varied by controlling the substrate vibration frequency.

Finally, I studied the distribution of droplet sizes during dropwise condensation on liquid infused surfaces (LIS, or SLIPS) with a wide range of lubricant viscosities (12 – 2717 cSt). Through analysis of >1000 individual images I show that the steady-state droplet size distribution is independent of lubricant viscosity. I further developed a numerical model to estimate the effect of sweeping and sweeping frequency on the average heat transfer on a large vertical plate, and conclude that only uncommonly high sweeping rates would affect heat transfer

rates significantly. I estimate average heat transfer rates during dropwise condensation on SLIPS to be 10-15 times greater than during traditional filmwise condensation, and provide a design framework for optimal heat transfer rates based on surface solid fraction and coating thickness.

Overall, this dissertation presents new insights into droplet-solid interactions during traditional wetting, droplet impact, and dropwise condensation, and provides a base line for future research and the development of industrial applications for droplet-based thermal management systems.

To my parents

ACKNOWLEDGMENTS

First, I would like to take the opportunity to thank various people without whom this work would not have turned out the way it did: Foremost my two advisors Bill King and Nenad Miljkovic, and my doctoral committee members Tony Jacobi and David Cahill. Without their knowledge, vast experience and guidance I would not have been able to advance both as a scientist and person. There are many other people at the University of Illinois at Urbana-Champaign – inside and outside of my two research groups (thanks to everyone for being there as mental support!) – who deserve to be mentioned and acknowledged for their support. Nitin Neelakantan and Prof. Kenneth Suslick from the Chemistry department at UIUC for their collaboration on oleophobic surfaces. Prof. John Abelson and Prof. Alfred Hübler for their support and guidance regarding any non-research related issues. And Prof. Andrew Alleyne for referring me to Washington University in St. Louis, where I will be starting a faculty position after the completion of my PhD.

I would also like to thank the following undergraduate and graduate students who assisted me in carrying out some of the research experiments presented here: Yujin Chang (Droplet Impact), Qian Hongliang (Dropsize Distribution), Jingcheng Ma (Droplet Impact), Daniel Schultz (Dropsize Distribution), Young Hwan Shin (Droplet Impact), Junjiao Tian (Droplet Impact), and Yunbo Wang (Dropsize Distribution). I would also like to thank Scott and Cate from the Microscopy Suite at the Beckman Institute for their help using the SEM.

Last but not least, I want to thank my parents for always believing in me and supporting my academic career – especially during my multiple ventures abroad. Thanks!

TABLE OF CONTENTS

LIST OF FIGURES

LIST OF ABBREVIATIONS

AFM	Atomic force microscopy
CA	Contact angle
CAH	Contact angle hysteresis
DI	De-ionized (water)
DSLR	Digital single lens reflex (camera)
EDM	Electrical discharge machining
fps	Frames per second
HTMS	(heptadecafluoro-1,1,2,2-tetrahydrodecyl)trimethoxysilane
IPA	Isopropanol
IR	Infrared
KE	Kinetic energy
LED	Light-emitting diode
LIS	Lubricant-infused surface
mEDM	Micro electrical discharge machining
NCG	Non-condensable gas
PDMS	Polydimethylsiloxane
PFPE	Perfluoropolyether
PHB	Polyhydroxybutyrate
PMMA	Polymethylmethacrylat
PTFE	Polytetrafluorethylen
rpm	Revolutions per minute

SE	Surface energy
SEM	Scanning electron microscopy
SLIPS	Slippery liquid-infused porous surface
TPCL	Three-phase contact line
WEDM	Wire electrical discharge machining

LIST OF SYMBOLS

a	radius of contact area between droplet and solid also: Acceleration also: Fitting parameter for dropsize distribution
A	Surface area (*subscripts* – ***0***: initial, ***spr***: at maximum spreading) also: Maximum diameter (width) of mushroom head
b	fitting parameter for dropsize distribution
B	Minimum base diameter (width) of mushroom stems also: Width of unit cell (slot) during droplet sweeping (*subscripts* – ***exp***: experimental)
Bo	Bond number
D	Droplet diameter (*subscripts* – ***0***: initial, ***max***: maximum diameter during spreading)
d	Particle diameter
E	Young's modulus or Energy (*subscripts* – ***0***: initial, ***spr***: at maximum spreading)
f	Frequency (*subscripts* – ***0***: natural eigenfrequency, ***1,2,…***: higher order eigenfrequencies, ***obs***: observed, ***sweep***: droplet sweeping frequency) also: Heat transfer fraction ($f = \int q/q_{tot}$)
F	Force (*subscripts* – ***0***: initial)
Fr	Froude number
g	Gravity also: geometric parameter
h	Height or thickness (*subscripts* – ***s***: substrate, ***coat:*** coating, ***B***: Boehmite)
h_i	convection coefficient
H	Height
Δh_{fg}	Latent heat of vaporization

I	Area moment of inertia
k	Thermal conductivity (*subscripts* – **coat**: coating, ***l***: liquid = condensate, ***B***: Boehmite, ***o***: oil) also: Stiffness (*subscripts* – ***F***: force gauge)
K	Splashing parameter (*subscripts* – ***c***: critical)
L	Length
m	Mass (*subscripts* – ***s***: substrate, ***″***: area-normalized average mass of the condensed droplets)
N,n	Number density, i.e. drop size distribution
n_s	Number of sweeping events
N_s	Nucleation site density
Oh	Ohnesorg number
p	Pressure also: Probability density function
P	Pitch
q	Heat transfer rate (*subscripts* – ***d***: droplet, ***tot***: total)
q''	Heat flux (*subscripts* – ***0***: at top of plate, ***d***: droplet, ***exp***: experimental, ***film***: filmwise, ***tot***: total)
r	Droplet radius during condensation (*subscripts* – ***e***: effective transition radius (direct condensation -> coalescence), ***min***: minimum droplet radius (nucleation radius), ***max***: maximum droplet radius from force balance, ***max,0***: maximum droplet radius at top of plate, ***max,th***: theoretical maximum droplet radius, ***max,exp***: experimental maximum droplet radius, ***s***: maximum radius of droplet before being swept, ***sw***: radius of sweeping droplet)
$\hat{r}$	Average maximum droplet radius relevant for heat transfer
R	Thermal resistance (*subscripts* –***c***: curvature, ***i***: interfacial, ***s***: structures, ***tot***: total), also: Radius of mushroom head

R_g	Specific gas constant
Re	Reynolds number
s	Distance of droplet impact to mount Also: Distance of droplet to substrate
S	Top deficit ($S = A - 2R$)
t	Time (*subscripts* – ***c***: contact time, ***c,th***: theoretical contact time, ***ch***: characteristic time during condensation, ***cycle***: cycle time (period) between sweeping events, ***min***: minimum contact time, ***max***: maximum contact time, ***p***: predicted, ***spr***: spreading; *superscripts* – *****: non-dimensional)
T	Temperature (*subscripts* – ***s***: substrate, ***sat***: saturation), also: Height of mushroom head
ΔT	Temperature gradient/ difference (*subscripts* – ***c***: curvature, ***cond***: conduction, ***i***: interface, ***s***: structures, ***tot***: total)
u	Speed or Velocity (*subscripts* – ***s***: substrate)
v	Speed or Velocity (*subscripts* – ***c***: critical, ***eff***: effective (net); *superscripts* – *****: normalized)
V	Volume
w	Width
W	Gap width between mushrooms
We	Weber number
y	Vertical coordinate
α	Roll-off angle, or sliding angle
γ	Surface tension (*subscripts* – ***sg** or **s***: solid-gas, ***sl***: solid-liquid, *no subscript or* **lg** *or* ***l***: liquid-gas; *superscripts* – ***d***: dispersive)
Γ	Dimensionless acceleration

δ	Substrate deflection (*subscripts* – ***max***: maximum) also: microscopic thickness (*subscripts* – ***c***: coat)
ζ	Roughness (actual / projected surface area)
η	Fractional droplet coverage
θ	Contact angle (*subscripts* – ***Y***: Young, ***W***: Wenzel, ***C-B***: Cassie-Baxter, ***A***: advancing, ***R***: receding, ***e***: equilibrium; *superscripts* – ***app***: apparent)
$\Delta\theta$	Contact angle hysteresis
μ	Dynamic viscosity
ν	Kinematic viscosity (*subscripts* – ***l***: liquid) also: Poisson's ratio
ξ	Dimensionless spreading parameter (*subscripts* – ***max***: maximum)
ρ	Density (*subscripts* – ***l***: liquid, ***v***: vapor)
τ	Sweeping period Also: Crash time, or non-dimensional time
σ	Condensation accommodation coefficient
φ	Solid-liquid fraction also: Phase (*subscripts* – ***0***: initial, ***1***: integration boundary, ***2***: integration boundary, ***c***: critical, ***d***: departure, ***i***: impact; *superscripts* – ****,*****: normalized)
ψ	Average droplet coverage fraction
ω	Angular frequency

CHAPTER 1

INTRODUCTION AND LITERATURE REVIEW

1.1 Introduction

Water repelling surfaces have been studied for many decades[1,2]. In recent years, extensive research effort has been directed toward modifying surface structures to design water and oil repelling, i.e. (super)hydrophobic and oleophobic, surfaces that can be used in many industrial applications, such as self-cleaning and anti-fouling coatings, anti-icing, heat exchangers and cooling devices for enhanced heat transfer[3–5]. The goal in most of these applications is the formation of individual liquid droplets, as opposed to a liquid film covering the surface. Droplets have a higher mobility and lower overall thermal resistance than films. The shape and performance of a droplet on a solid surface is governed by surface morphology and chemistry of the surface, as well as the surface tension of the liquid and the surrounding medium[5–7].

To render surfaces hydro- or oleophobic, many researchers use polymer coatings, silanes, or similar low surface energy materials to coat Si-based nanofabricated surface structures[8–10]. However, in industrial settings, neither silicon, nor the coatings are widely used because of their high cost, low scalability and degradation. In order to transfer the academic knowledge to industry, we need materials such as metals and self-healing coatings instead of silicon and fluoropolymers, and alternative micro-fabrication techniques that are scalable and compatible with industrial applications.

Droplet wettability and mobility also play an important role in the performance of applications operating under saturation conditions, such as condensers and heat pipes. There has been a long and controversial debate on the influence of the surrounding gas atmosphere on the wetting and mobility of droplets on hydrophobic surfaces[11–13]. Also, while during traditional wetting droplets are brought into contact with a solid, during condensation heat transfer droplets nucleate on the substrate and can thus have vastly different properties and interactions with the solid. The energy and mass transfer during phase change heat transfer occurs near the three-phase contact line (TPCL) between liquid, solid, and gas[14]. However, little is known on the interactions of condensing water droplets when the TPCL consists of a liquid-liquid-gas interface.

It is also unclear whether surface morphology and surface chemistry are the only contributing surface parameters to control wetting, especially during droplet impact[15,16]. Droplet impact is a dynamic process during which the interactions between droplets and substrates can be different from a static scenario. The interplay between droplet kinetic and surface energy, that governs droplet bouncing, provides the possibility of other another energy mechanism to participate in the impact process: substrate potential or kinetic energy. However, little effort has been directed towards understanding the interplay of these three energy modes and how they affect droplet bouncing.

This dissertations aims to answer some of the questions outlined above and to explore fundamentals of droplet-solid interactions with the emphasis on topics relevant to heat transfer applications.

1.2 Surface Wettability

When a small amount of liquid resides on a solid surface, the liquid either spreads or forms discrete droplets. The shape the liquid assumes is governed by the surface tensions γ of the liquid, the surrounding gas and the solid at the contact line. Figure 1.1a shows the equilibrium contact angle (CA) θ, first described by Young, and thus referred to here as Young's contact angle $\theta_Y = \theta$.[17] This contact angle on a flat, homogenous surface can be thought of as a force balance between the solid-gas γ_{sg}, solid-liquid γ_{sl} and liquid-gas γ_{lg} surface tensions:

$$\cos(\theta_Y) = \frac{\gamma_{sg} - \gamma_{sl}}{\gamma_{lg}}. \tag{1-1}$$

Surfaces with $\theta_Y < 90°$ are commonly called hydrophilic for water or oleophilic for liquids with low surface tensions such as oils and alcohols, and hydro- or oleophobic, i.e. non-wetting, for $\theta_Y > 90°$.[18,19] From (1-1) we see that a high liquid surface tension, coupled with a low solid surface energy, is necessary for a non-wetting state. Due to the low surface tensions of oils and alcohols, most surfaces, even when hydrophobic, are oleophilic.

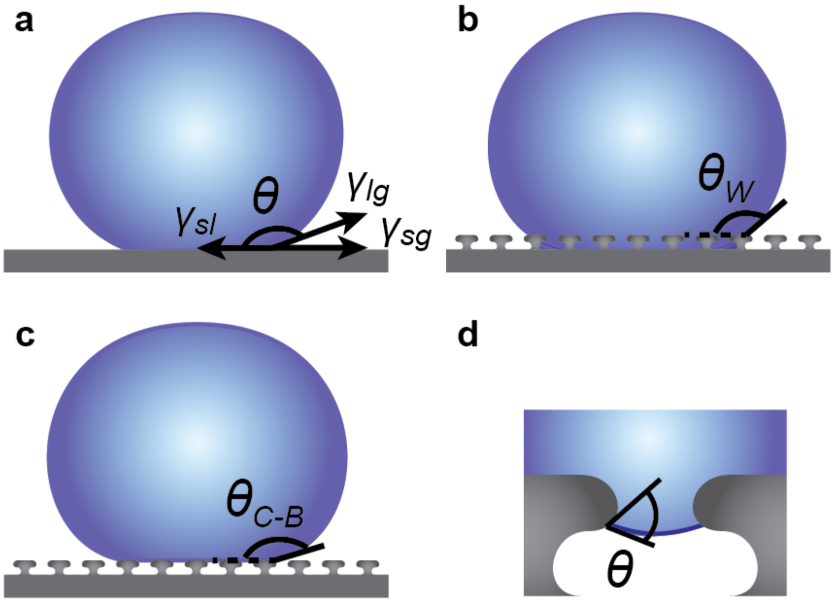

Figure 1.1: Wetting regimes of droplets on flat and microstructured surfaces. (a) Flat and homogeneous (hydro-)phobic surface with the sessile contact angle θ. (b) Wetting Wenzel state with the apparent contact angle θ_W. (c) Non-wetting Cassie-Baxter state with air pockets beneath the droplet and an apparent contact angle $\theta_{C\text{-}B}$. (d) Close-up view of the re-entrant structure in the non-wetting state, showing the sessile contact angle at the three-phase contact line and the convex meniscus, important to maintain liquids with low surface tensions in a partially stable non-wetting state.

Surface roughness enhances the philic or phobic behavior. Wenzel showed that with a roughness factor ζ (actual / projected surface area) the apparent contact angle θ_W, i.e. the angle given for a macroscopic droplet, becomes[20]:

$$cos(\theta_W) = \zeta co\,s(\theta). \tag{1-2}$$

In the Cassie-Baxter, or Cassie, state pockets of air are trapped under the droplet between surface textures and support the liquid droplet like a cushion. The contact area between liquid and solid (solid-liquid fraction φ) is reduced compared to a flat surface. The apparent CA for droplets in the Cassie-state becomes[21]:

$$cos(\theta_{C-B}) = \varphi(cos(\theta) + 1) - 1\,. \tag{1-3}$$

This non-wetting state always increases the apparent CA. Schematics of droplets in the Wenzel and Cassie states are shown in Figure 1.1 b and c, respectively. Surfaces are called superhydrophobic if the apparent contact angle $\theta^{app} \geq 150°$. Figure 1.2 visualizes the different wetting states. Liquids can transition from the Cassie-state to the Wenzel-state (or vice versa) if enough activation energy is provided, for example by drops falling from some height or vibration[6]. Experimentally, the sessile contact angle on a flat surface can take any value between the advancing and receding contact angles. The existence of metastable states allows droplets to manifest contact angles differing from the global equilibrium[22,23].

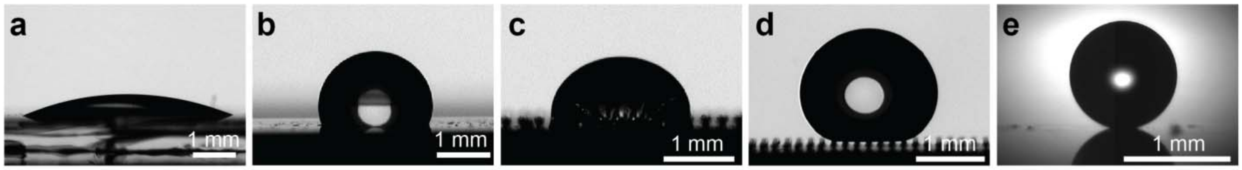

Figure 1.2: Images of droplets in different wetting regimes. (a) Hydrophilic: water on glass, (b) hydrophobic: water on flat Teflon, (c) wetting Wenzel-state: oil on microstructures, (d) non-wetting Cassie-state: water on microstructures, and (e) superhydrophobic: water on hierarchical nanoparticle spray coating.

Liquids with low surface tensions usually penetrate into gaps between micro-structures with vertical or positively tilted edges. The negative slope of re-entrant structures, however, establishes a convex droplet shape that is pinned to the negative slope of the micro-mushroom, as shown in Figure 1.1d. In this case, the intrinsic forces such as gravity are in equilibrium with an upward pointing force due to higher Laplace pressure at the meniscus. A TPCL can form and air can be trapped beneath the droplet, preventing the liquid from fully wetting the solid[8,24–26].

On a real surface, the largest and smallest possible angle for a stationary contact line are the advancing, θ_A, and receding, θ_R, contact angle, respectively. The difference between these angles, the contact angle hysteresis (CAH) $\Delta\theta$, results from energetic barriers to the displacement of the TPCL on non-ideal surfaces[19,23]. Droplets must overcome an activation energy before the contact line moves, which is also known as contact line pinning[22]. For deposited droplets, θ is usually much closer to θ_A than to θ_R.[27] An equilibrium CA $\theta_e = \cos^{-1}(0.5\cos(\theta_A) + 0.5\cos(\theta_R))$ is often defined for surfaces with low CAH to represent θ_A and θ_R.[28] On microstructured surfaces, the energy required for advancing is minimal, as the droplets can simply descend (or fall) onto the next post, whereas receding liquid has to actively unpin or disjoin the surface before moving. Although sessile CAs can vary between measurements on the same surface by up to 20° due to a range of metastable states, advancing and receding CAs are mostly constant and a characteristic of surface chemistry and topography[22]. On superhydrophobic surfaces droplets are very mobile and CAH is small ($\Delta\theta \leq 10°$).

In this dissertation I study the influence of the gas environment on droplet wettability and mobility on flat and micro- and nanostructured hydrophobic surfaces. I also propose a new microfabrication method to achieve oleophobicity on metallic surfaces.

1.3 Dropwise Condensation

As opposed to deposited droplets, those formed via vapor condensation can have vastly different wetting and mobility behaviors on the same surface, as droplets can nucleate between micro- and nanostructures and consequently flood the surface. On industrial condenser applications, which are typically covered with a high surface energy metal oxide (i.e. Al_2O_3, CuO, FeO), condensation initiates in the filmwise mode, typified by the formation of a relatively thick liquid film (~ 100 μm) on the cold surface which acts as a thermal resistance to heat transfer (Figure 1.3a). If the exterior condenser surface is coated with a low surface energy promoter, discrete droplets form, grow, and shed rapidly via gravitational force, allowing for the re-nucleation of small low-thermal-resistance droplets, in what has been termed dropwise condensation (Figure 1.3b).[29,30] Heat transfer rates during dropwise condensation in a pure saturated vapor have been shown to be 6-8X higher than traditional filmwise condensation[29]. After 80 years of research[31], and limited progress due to durability concerns, dropwise condensation has recently gained renewed attention due to its potential in phase-change-based heat transfer applications and significant advances in microfabrication and functional coating techniques[7,18,29–34]. Specifically, researchers have been developing novel methods to further control the condensing surface wettability, which is known to strongly affect the mobility of condensate droplets. Mobile droplets, i.e. those with low contact angle hysteresis, clear nucleation sites more rapidly and thereby allow for high nucleation rates and thus high heat transfer[35].

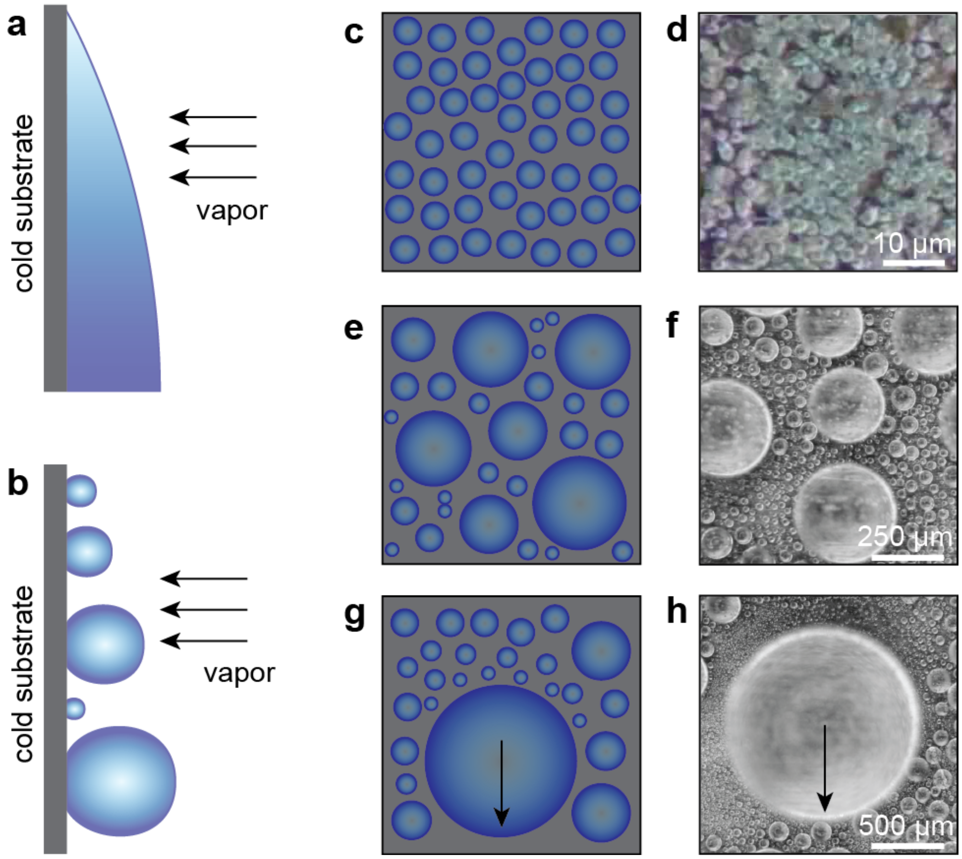

Figure 1.3: Different stages of filmwise and dropwise condensation. (a) Filmwise condensation on a vertical plate. (b) Dropwise condensation on a vertical plate. (c,d) Schematic and photograph of recently nucleated droplets shortly before reaching the effective transition radius r_e. These small droplets grow mainly via direct condensation. (e,f) For $r_e < r < r_{max}$ droplets grow mainly through coalescence with neighboring droplets. (g,h) Once droplets are big enough gravity overcomes surface tension forces and pinning and droplets slide down the surface. Note the different size scales.

Dropwise condensation is a hierarchical and highly transient process[36]. Droplets nucleate with a critical nucleation radius, r_{min} ~ 10-100 nm for water, and a nucleation site density N_{s}. Droplets then grow *via* direct condensation until they come in contact with neighboring droplets at an effective transition radius $r_{\text{e}} = 1/\sqrt{4N_s}$ ~ 0.5 – 10 µm for water, as shown in Figure 1.3c,d. After transition the droplets grow mainly *via* coalescence with other droplets (Figure 1.3e,f). On an inclined surface the droplets will reach a maximum diameter, r_{max} ~ 1 mm for water, at which gravitational forces overcome contact line pinning and the droplet slides down the surface, as shown in Figure 1.3g,h. Droplets can also be removed *via* sweeping or falling droplets prior to reaching $r_{\max}$, in which case nucleation sites are cleared more rapidly and overall heat transfer rates can increase.

To promote dropwise condensation, the solid surface requires a low-energy promoter. Traditionally, low-energy coatings such as fluoropolymers (e.g. Teflon), dioctadecyl disulphide or silanes have been used[11]. However, these coatings experience low durability and short life times under vapor saturation conditions. Chemical and topographical inhomogeneities create defects where droplets can pin and transition to filmwise condensation[18]. Similarly, microstructured surfaces are generally not suited for continuous dropwise condensation, as condensate can nucleate within the microstructures and remain in the wetting Wenzel state even after coalescence and growth[19]. Only once the surface structures are small enough, on the order of 10-100 nm, can droplets form in the favorable non-wetting Cassie-Baxter state[20–22]. However, stable dropwise and jumping-droplet condensation on these nanostructured surfaces can only be achieved for low super-saturation conditions[12,14]. Recently, a new class of surface suitable for dropwise condensation of both water and liquids with lower surface tensions has been introduced: Slippery liquid-infused porous surfaces (SLIPS), also called lubricant-infused surfaces (LIS).[14–16,23–28] If designed correctly, the infused liquid, or lubricant, creates an atomically flat interface for water condensation. Due to the absence of defects on the surface, condensed water droplets have extremely low contact angle hysteresis (~ 2°) and very high mobility, leading to easy shedding and rapid clearing of nucleation sites with increased overall heat transfer[23,24,28]. Figure 1.4 shows a low-energy micro- or nanostructured surface infused with an immiscible liquid such as oil or ionic liquid[45–47].

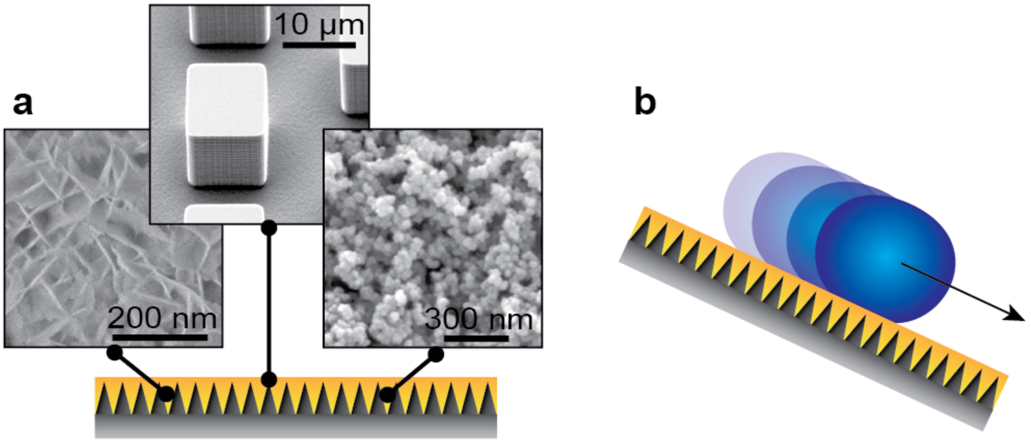

Figure 1.4: Slippery liquid-infused porous surface (SLIPS). (a) Low surface energy micro- or nanostructured surfaces are infused with a secondary, immiscible liquid (lubricant). (b) Condensed water droplet shed easily due to a quasi defect-free interface.

As part of this dissertation I study the distribution of droplet sizes during condensation on SLIPS and create a mathematical model to predict sweeping rates and their influence on heat transfer rates on large vertical plates.

1.4 Droplet Impact

While droplets that are gently deposited on a surface, or condense on it, are in quasi-equilibrium states, non-equilibrium dynamics have to be considered when droplets impact a surface. Dynamics of droplet impact are important in many natural processes[48,49] and industrial applications, including anti-icing[4,50], spray cooling[51,52], pesticide and herbicide delivery[53,54], and ink-jet printing[55]. Droplet impact is governed by the complex flow physics arising within the deforming droplet, manifesting itself in the form of droplet lateral spreading and recoil. As the droplet impacts the surface, its kinetic energy is re-directed in the lateral direction, flattening the droplet and converting the kinetic energy into surface energy. On low-friction surfaces, this kinetic-to-surface energy conversion process is very efficient, resulting in minimal energy dissipation due to viscous effects[15]. Once all of the kinetic energy has been converted to surface energy of the flattened droplet, the reverse surface-to-kinetic energy conversion process initiates, resulting in droplet retraction and lift off in the vertical direction. Figure 1.5 shows the characteristic droplet dynamics for droplet impact at moderate impact speeds on a rigid, superhydrophobic surface. Upon impact, the droplet spreads, reaches a maximum diameter, fully retracts, and vertically lifts off the surface[15,56].

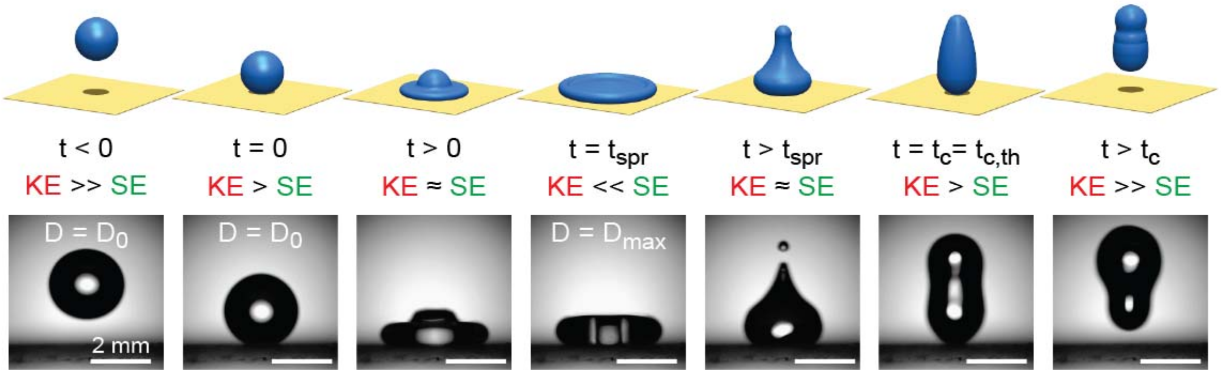

Figure 1.5: Energy conversion mechanisms during droplet impact on a rigid superhydrophobic surface. Droplets impact, spread, reach a maximum diameter, recoil, and lift off.

The total contact time from initial impact to lift-off, t_c, can influence the mass, momentum, and energy exchange between the droplet and the solid. On a plane, rigid superhydrophobic surface the contact time of impacting water droplets is governed by the droplet size. For Weber numbers $We = (\rho v^2 D_0)/\gamma > 1$, where ρ, D_0, v and γ are the droplet density, initial diameter, impact speed, and surface tension, respectively, the droplet undergoes elastic impact. By balancing the droplet impact inertia ($\sim \rho D_0/t_c^2$) with capillarity ($\sim \gamma/D_0^2$), the contact time scales as $t_c \sim (\rho D_0^3/\gamma)^{1/2}$, and is independent of the impact speed[57,58]. Consequently, the only way to adjust the contact time on a plane, rigid, single length scale superhydrophobic surface is by controlling the droplet diameter.

One approach to reduce the contact time is to use a surface with hierarchical super-hydrophobic surface features. Superhydrophobic, sub-millimetric hierarchical posts have shown to reduce the contact time of impacting droplets[59,60]. For $We > 12$, droplets can lift off near their maximum spreading in a pancake-like shape. The contact time is reduced by a factor of 4 compared to impacts at lower Weber numbers. The contact time reduction is governed by capillary-to-inertial energy conversion form liquid penetration in the spaces between microscale posts and increased total surface energy.

By breaking the symmetry of the impacting droplet superhydrophobic, sub-millimetric ridges can decrease contact times of impinging droplets[48,61]. When a millimetric water droplet hits a ridge, the liquid elongates in a butterfly shape perpendicular to the ridge. At moderate impact speeds, globules start forming at the corners of the spreading drop, while the center of the droplet starts de-wetting over the ridge. The droplets then lift off in a bridge-like shape without retracting. Contact times are reduced by $\sqrt{2}$ or $\sqrt{4}$, for 2 or 4 formed finger during spreading, respectively. At high impact speeds, the droplets break up after hitting the ridge, effectively shortening the contact time compared to the theoretical contact time of the impacting droplet. Splashing, i.e. formation of small satellite droplets, can also occur on a flat surface at sufficiently high impact speeds (for water: $v \gtrsim 2$ m/s)[62,63].

In this dissertation I propose two mechanisms – one active and one passive – based on vibrations of the substrate to reduce and control the contact time of impacting droplets without additional modification of the superhydrophobic surface.

1.5 Outline of the Dissertation

This dissertations aims to advance the scientific knowledge on fundamentals of liquid-solid interactions, including wettability, droplet impact and condensation phase change. The dissertation is organized as follows.

In Chapter 2 I will discuss the effect of the gas environment on the wettability of water droplets on various hydrophobic and superhydrophobic surfaces. Droplet wettability and mobility play an important role in dropwise condensation heat transfer. While most literature data for wetting is available for droplets in an air environment, heat exchangers and heat pipes operate at liquid-vapor saturation. We argue that the wetting behavior of liquid water on microstructures surrounded by pure water vapor differs from that for water droplets in air. Our findings show that static advancing contact angles are 9° lower in the water vapor environment than in air on a flat surface. One explanation for this reduction in contact angles is water vapor adsorption to the Teflon. On microstructured surfaces, the vapor environment has little effect on the static contact angles. In all cases, variations in pressure and temperature did not influence the wettability and mobility of the water droplets.

Chapter 3 presents the results on droplet size distribution during condensation heat transfer on SLIPS. Dropwise condensation is an important phase change phenomenon in many industrial applications, including electronics cooling, power generation, and desalination. To accurately predict heat transfer rates the average distribution of droplet sizes has to be know. We show that distribution of droplet sizes on SLIPS is independent of lubricant viscosity, and agrees well with the model developed by Rose for the distribution of droplet sizes on hydrophobic surfaces. Through artificial sweeping experiments and numerical modeling we elucidate the dependence of sweeping periods on the distribution of droplet sizes and on average heat transfer rates, to mimic heat transfer on large vertical plates. The maximum size to which droplets grow before being swept decreases rapidly with only a modest decrease in sweeping period, from 750 to 62 µm. However, heat transfer rates are nearly unaffected by the change in the distribution of droplet sizes, due to a relative insensitivity of heat transfer to droplets with $r > 100$ µm, originating from a large conduction resistance through the droplet. Overall, we provide an experimental and analytical framework to predict heat transfer and sweeping rates for water dropwise condensation on a vertical plate on lubricant infused surfaces.

In Chapter 4 I will elaborate on the dynamics of water droplet impact on elastic, or flexible, superhydrophobic substrates. Dynamics of water droplet impact, and especially the droplet contact time on surfaces, govern heat transfer during spray cooling and ice formation. We study droplet impact on flexible superhydrophobic substrates (stiffness 0.5 - 7630 N/m) and show that the contact time can decrease by a factor of 2 for flexible surfaces, which is due to early droplet lift-off during recoil. Our results show that the oscillation of the substrate can strongly affect the droplet shape and contact time during recoil and lift-off. Upon impact, the droplet excites the elastic substrate to oscillate at the substrate's natural frequency. Spreading on the elastic substrates is similar to that on a rigid surface. During recoil, however, the oscillation of the flexible substrate accelerates the droplet upwards prior to it being able to completely recoil. If the induced upward pointing inertia in the droplet is large enough to overcome the gravitational force, the droplet lifts off in a pancake shape before completely recoiling, reducing the contact time between droplet and substrate by up to a factor of two in a *springboard-like* fashion. Based on these results, we also developed a transient droplet impact heat transfer model to quantify the potential effects of contact time reduction on thermal energy exchange during droplet impact, which I will present at the end of chapter 4.

In Chapter 5 I will focus on droplet impact and droplet dynamics on vibrating rigid and elastic surfaces. Using optical high speed imaging, we investigate the impact dynamics of macroscopic water droplets (~ 1mm) on rigid and elastic superhydrophobic surfaces vibrating at 60 – 300 Hz and amplitudes of 0 – 3 mm and study the influence of the substrate phase at the moment of impact on total contact time. We define a critical impact phase at which contact time is maximum and greater than the theoretical contact time on a rigid, non-vibrating superhydrophobic surface. For impact at higher phases contact times decrease until reaching a minimum of half the theoretical contact time just before the critical phase. The frequency of oscillation determines the homogeneity of droplet contact times at different impact phases: Higher frequencies (> 120 Hz) show less contact time variability and have overall shorter contact times compared to lower frequencies (60 – 120 Hz). The amplitude of vibration has little direct effect on the contact time. Through mathematical modeling we demonstrate, however, that the oscillation amplitude influences the possibility density function of droplet impact at a given phase, and thus indirectly influences the contact time.

Chapter 6 presents the fabrication of metallic micro-mushroom re-entrant structures and the characterization of their hydrophobicity and oleophobicity. Five different microstructure geometries are introduced, with typical feature sizes in the range of 10 - 100 μm. These microstructures are realized in steel, not the commonly used silicon, and are fabricated over the cm-scale using micro electrical discharge machining (mEDM). The liquid repellency of these surfaces is characterized using droplets of either water (surface energy γ_{lg} = 72.4 mN/m), RL-68H oil (γ_{lg} = 28.6 mN/m), or Isopropanol (IPA) (γ_{lg} = 21.7 mN/m). I will show that all studied micro-mushrooms structures are hydrophobic, but that strong re-entrant features and close spacing are necessary to support a fully non-wetting state for use with oil and IPA.

Finally, in Chapter 7 I will summarize my research and provide insights into future research directions relevant to droplet-solid interactions in the field of thermal fluids science and heat transfer applications.

1.6 References

(1) Wenzel, R. N. Resistance of Solid Surfaces to Wetting by Water. *Ind. Eng. Chem.* **1936**, *28*, 988–994.

(2) Öner, D.; McCarthy, T. J. Ultrahydrophobic Surfaces. Effects of Topography Length Scales on Wettability. *Langmuir* **2000**, *16*, 7777–7782.

(3) Banerjee, I.; Pangule, R. C.; Kane, R. S. Antifouling Coatings: Recent Developments in the Design of Surfaces That Prevent Fouling by Proteins, Bacteria, and Marine Organisms. *Adv. Mater.* **2011**, *23*, 690–718.

(4) Mishchenko, L.; Hatton, B.; Bahadur, V.; Taylor, J. A.; Krupenkin, T.; Aizenberg, J. Design of Ice-Free Nanostructured Surfaces Based on Repulsion of Impacting Water Droplets. *ACS Nano* **2010**, *4*, 7699–7707.

(5) Chen, C.-H.; Cai, Q.; Tsai, C.; Chen, C.-L.; Xiong, G.; Yu, Y.; Ren, Z. Dropwise Condensation on Superhydrophobic Surfaces with Two-Tier Roughness. *Appl. Phys. Lett.* **2007**, *90*, 173108.

(6) Tuteja, A.; Choi, W.; McKinley, G. H.; Cohen, R. E.; Rubner, M. F. Design Parameters for Superhydrophobicity and Superoleophobicity. *MRS Bull.* **2008**, *33*, 752–758.

(7) Rykaczewski, K.; Paxson, A. T.; Staymates, M.; Walker, M. L.; Sun, X.; Anand, S.; Srinivasan, S.; McKinley, G. H.; Chinn, J.; Scott, J. H. J.; *et al.* Dropwise Condensation of Low Surface Tension Fluids on Omniphobic Surfaces. *Sci. Rep.* **2014**, *4*.

(8) Tuteja, A.; Choi, W.; Mabry, J. M.; McKinley, G. H.; Cohen, R. E. Robust Omniphobic Surfaces. *Proc. Natl. Acad. Sci.* **2008**.

(9) Li, X.-M.; Reinhoudt, D.; Crego-Calama, M. What Do We Need for a Superhydrophobic Surface? A Review on the Recent Progress in the Preparation of Superhydrophobic Surfaces. *Chem. Soc. Rev.* **2007**, *36*, 1350–1368.

(10) Quéré, D. Wetting and Roughness. *Annu. Rev. Mater. Res.* **2008**, *38*, 71–99.

(11) Hu, P.; Adamson, A. W. Adsorption and Contact Angle Studies: II. Water and Organic Substances on Polished Polytetrafluoroethylene. *J. Colloid Interface Sci.* **1977**, *59*, 605–614.

(12) Fowkes, F. M.; McCarthy, D. C.; Mostafa, M. A. Contact Angles and the Equilibrium Spreading Pressures of Liquids on Hydrophobic Solids. *J. Colloid Interface Sci.* **1980**, *78*, 200–206.

(13) Carey, V. P. *Liquid-Vapor Phase-Change Phenomena: An Introduction To The Thermophysics Of Vaporization and Condensation in Heat Transfer Equipment: An Introduction to the Thermophysics of Vaporization & Condensation in Heat Transfer Equipment*; Taylor & Francis, 1992.

(14) Miljkovic, N.; Enright, R.; Wang, E. N. Effect of Droplet Morphology on Growth Dynamics and Heat Transfer during Condensation on Superhydrophobic Nanostructured Surfaces. *ACS Nano* **2012**, *6*, 1776–1785.

(15) Yarin, A. L. DROP IMPACT DYNAMICS: Splashing, Spreading, Receding, Bouncing…. *Annu. Rev. Fluid Mech.* **2006**, *38*, 159–192.

(16) Pepper, R. E.; Courbin, L.; Stone, H. A. Splashing on Elastic Membranes: The Importance of Early-Time Dynamics. *Phys. Fluids 1994-Present* **2008**, *20*, 82103.

(17) Young, T. An Essay on the Cohesion of Fluids. *Philos. Trans. R. Soc. Lond.* **1805**, *95*, 65–87.

(18) Miljkovic, N.; Wang, E. N. Condensation Heat Transfer on Superhydrophobic Surfaces. *MRS Bull.* **2013**, *38*, 397–406.

(19) Barbieri, L.; Wagner, E.; Hoffmann, P. Water Wetting Transition Parameters of Perfluorinated Substrates with Periodically Distributed Flat-Top Microscale Obstacles. *Langmuir* **2007**, *23*, 1723–1734.

(20) Wenzel, R. N. Surface Roughness and Contact Angle. *J. Phys. Colloid Chem.* **1949**, *53*, 1466–1467.

(21) Cassie, A. B. D.; Baxter, S. Wettability of Porous Surfaces. *Trans. Faraday Soc.* **1944**, *40*, 546–551.

(22) Gao, L.; McCarthy, T. J. Contact Angle Hysteresis Explained. *Langmuir* **2006**, *22*, 6234–6237.

(23) Gao, L.; McCarthy, T. J. "Artificial Lotus Leaf" Prepared Using a 1945 Patent and a Commercial Textile. *Langmuir* **2006**, *22*, 5998–6000.

(24) Choi, H.-J.; Choo, S.; Shin, J.-H.; Kim, K.-I.; Lee, H. Fabrication of Superhydrophobic and Oleophobic Surfaces with Overhang Structure by Reverse Nanoimprint Lithography. *J. Phys. Chem. C* **2013**, *117*, 24354–24359.

(25) Cao, L.; Hu, H.-H.; Gao, D. Design and Fabrication of Micro-Textures for Inducing a Superhydrophobic Behavior on Hydrophilic Materials. *Langmuir* **2007**, *23*, 4310–4314.

(26) Kang, S. M.; Kim, S. M.; Kim, H. N.; Kwak, M. K.; Tahk, D. H.; Suh, K. Y. Robust Superomniphobic Surfaces with Mushroom-like Micropillar Arrays. *Soft Matter* **2012**, *8*, 8563–8568.

(27) Chhatre, S. S.; Choi, W.; Tuteja, A.; Park, K.-C. (Kenneth); Mabry, J. M.; McKinley, G. H.; Cohen, R. E. Scale Dependence of Omniphobic Mesh Surfaces. *Langmuir* **2010**, *26*, 4027–4035.

(28) Miljkovic, N.; Enright, R.; Wang, E. N. Modeling and Optimization of Superhydrophobic Condensation. *J. Heat Transf.* **2013**, *135*, 111004–111004.

(29) Schmidt, E.; Schurig, W.; Sellschopp, W. Versuche über die Kondensation von Wasserdampf in Film- und Tropfenform. *Tech. Mech. Thermodyn.* **1930**, *1*, 53–63.

(30) Attinger, D.; Frankiewicz, C.; Betz, A. R.; Schutzius, T. M.; Ganguly, R.; Das, A.; Kim, C.-J.; Megaridis, C. M. Surface Engineering for Phase Change Heat Transfer: A Review. *ArXiv14095363 Cond-Mat* **2014**.

(31) Rose, J. W. Dropwise Condensation Theory and Experiment: A Review. *Proc. Inst. Mech. Eng. Part J. Power Energy* **2002**, *216*, 115–128.

(32) Ölçeroğlu, E.; Hsieh, C.-Y.; Rahman, M. M.; Lau, K. K. S.; McCarthy, M. Full-Field Dynamic Characterization of Superhydrophobic Condensation on Biotemplated Nanostructured Surfaces. *Langmuir* **2014**, *30*, 7556–7566.

(33) Enright, R.; Miljkovic, N.; Alvarado, J. L.; Kim, K.; Rose, J. W. Dropwise Condensation on Micro- and Nanostructured Surfaces. *Nanoscale Microscale Thermophys. Eng.* **2014**, *18*, 223–250.

(34) Park, K.-C.; Kim, P.; Grinthal, A.; He, N.; Fox, D.; Weaver, J. C.; Aizenberg, J. Condensation on Slippery Asymmetric Bumps. *Nature* **2016**, *531*, 78–82.

(35) Graham, C.; Griffith, P. Drop Size Distributions and Heat Transfer in Dropwise Condensation. *Int. J. Heat Mass Transf.* **1973**, *16*, 337–346.

(36) Khandekar, S.; Muralidhar, K. *Dropwise Condensation on Inclined Textured Surfaces*; SpringerBriefs in Applied Sciences and Technology; Springer New York: New York, NY, 2014.

(37) Enright, R.; Miljkovic, N.; Al-Obeidi, A.; Thompson, C. V.; Wang, E. N. Condensation on Superhydrophobic Surfaces: The Role of Local Energy Barriers and Structure Length Scale. *Langmuir* **2012**, *28*, 14424–14432.

(38) Koishi, T.; Yasuoka, K.; Fujikawa, S.; Ebisuzaki, T.; Zeng, X. C. Coexistence and Transition between Cassie and Wenzel State on Pillared Hydrophobic Surface. *Proc. Natl. Acad. Sci.* **2009**, *106*, 8435–8440.

(39) Liu, T.; Sun, W.; Sun, X.; Ai, H. Thermodynamic Analysis of the Effect of the Hierarchical Architecture of a Superhydrophobic Surface on a Condensed Drop State. *Langmuir* **2010**, *26*, 14835–14841.

(40) Feng, J.; Pang, Y.; Qin, Z.; Ma, R.; Yao, S. Why Condensate Drops Can Spontaneously Move Away on Some Superhydrophobic Surfaces but Not on Others. *ACS Appl. Mater. Interfaces* **2012**, *4*, 6618–6625.

(41) Jo, H.; Hwang, K. W.; Kim, D.; Kiyofumi, M.; Park, H. S.; Kim, M. H.; Ahn, H. S. Loss of Superhydrophobicity of Hydrophobic Micro/nano Structures during Condensation. *Sci. Rep.* **2015**, *5*, 9901.

(42) Anand, S.; Paxson, A. T.; Dhiman, R.; Smith, J. D.; Varanasi, K. K. Enhanced Condensation on Lubricant-Impregnated Nanotextured Surfaces. *ACS Nano* **2012**, *6*, 10122–10129.

(43) Xiao, R.; Miljkovic, N.; Enright, R.; Wang, E. N. Immersion Condensation on Oil-Infused Heterogeneous Surfaces for Enhanced Heat Transfer. *Sci. Rep.* **2013**, *3*.

(44) Kim, H.; Nam, Y. Condensation Behaviors and Resulting Heat Transfer Performance of Nano-Engineered Copper Surfaces. *Int. J. Heat Mass Transf.* **2016**, *93*, 286–292.

(45) Lafuma, A.; Quéré, D. Slippery Pre-Suffused Surfaces. *EPL Europhys. Lett.* **2011**, *96*, 56001.

(46) Daniel, D.; Mankin, M. N.; Belisle, R. A.; Wong, T.-S.; Aizenberg, J. Lubricant-Infused Micro/nano-Structured Surfaces with Tunable Dynamic Omniphobicity at High Temperatures. *Appl. Phys. Lett.* **2013**, *102*, 231603.

(47) Smith, J. D.; Dhiman, R.; Anand, S.; Reza-Garduno, E.; Cohen, R. E.; McKinley, G. H.; Varanasi, K. K. Droplet Mobility on Lubricant-Impregnated Surfaces. *Soft Matter* **2013**, *9*, 1772–1780.

(48) Bird, J. C.; Dhiman, R.; Kwon, H.-M.; Varanasi, K. K. Reducing the Contact Time of a Bouncing Drop. *Nature* **2013**, *503*, 385–388.

(49) Gilet, T.; Bourouiba, L. Fluid Fragmentation Shapes Rain-Induced Foliar Disease Transmission. *J. R. Soc. Interface* **2015**, *12*, 20141092–20141092.

(50) Meuler, A. J.; Chhatre, S. S.; Nieves, A. R.; Mabry, J. M.; Cohen, R. E.; McKinley, G. H. Examination of Wettability and Surface Energy in Fluorodecyl POSS/polymer Blends. *Soft Matter* **2011**, *7*, 10122–10134.

(51) Jia, W.; Qiu, H.-H. Experimental Investigation of Droplet Dynamics and Heat Transfer in Spray Cooling. *Exp. Therm. Fluid Sci.* **2003**, *27*, 829–838.

(52) Hsieh, S.-S.; Luo, S.-Y. Droplet Impact Dynamics and Transient Heat Transfer of a Micro Spray System for Power Electronics Devices. *Int. J. Heat Mass Transf.* **2016**, *92*, 190–205.

(53) Massinon, M.; Lebeau, F. Experimental Method for the Assessment of Agricultural Spray Retention Based on High-Speed Imaging of Drop Impact on a Synthetic Superhydrophobic Surface. *Biosyst. Eng.* **2012**, *112*, 56–64.

(54) Vallet, A.; Tinet, C. Characteristics of Droplets from Single and Twin Jet Air Induction Nozzles: A Preliminary Investigation. *Crop Prot.* **2013**, *48*, 63–68.

(55) van Dam, D. B.; Le Clerc, C. Experimental Study of the Impact of an Ink-Jet Printed Droplet on a Solid Substrate. *Phys. Fluids* **2004**, *16*, 3403–3414.

(56) Clanet, C.; Béguin, C.; Richard, D.; Quéré, D. Maximal Deformation of an Impacting Drop. *J. Fluid Mech.* **2004**, *517*, 199–208.

(57) Richard, D.; Clanet, C.; Quéré, D. Surface Phenomena: Contact Time of a Bouncing Drop. *Nature* **2002**, *417*, 811–811.

(58) Antonini, C.; Amirfazli, A.; Marengo, M. Drop Impact and Wettability: From Hydrophilic to Superhydrophobic Surfaces. *Phys. Fluids* **2012**, *24*, 102104.

(59) Liu, Y.; Moevius, L.; Xu, X.; Qian, T.; Yeomans, J. M.; Wang, Z. Pancake Bouncing on Superhydrophobic Surfaces. *Nat. Phys.* **2014**, *10*, 515–519.

(60) Moevius, L.; Liu, Y.; Wang, Z.; Yeomans, J. M. Pancake Bouncing: Simulations and Theory and Experimental Verification. *Langmuir* **2014**, *30*, 13021–13032.

(61) Gauthier, A.; Symon, S.; Clanet, C.; Quéré, D. Water Impacting on Superhydrophobic Macrotextures. *Nat. Commun.* **2015**, *6*, 8001.

(62) Bussmann, M.; Chandra, S.; Mostaghimi, J. Modeling the Splash of a Droplet Impacting a Solid Surface. *Phys. Fluids* **2000**, *12*, 3121.

(63) Bird, J. C.; Tsai, S. S. H.; Stone, H. A. Inclined to Splash: Triggering and Inhibiting a Splash with Tangential Velocity. *New J. Phys.* **2009**, *11*, 63017.

CHAPTER 2

HYDROPHOBICITY IN DIFFERENT GAS ENVIRONMENTS [1]

2.1 Introduction

As discussed in Chapter 1, heat transfer rates during dropwise condensation can be larger by almost an order of magnitude compared to filmwise condensation[1,2]. The wettability of the surface and the mobility of the droplets after condensation greatly influence the condensation process. Mobile droplets with high contact angles clear nucleation sites rapidly and thereby allow for high nucleation rates and thus high heat transfer across the surface. Most studies on wettability and mobility of water droplets on micro- and nanostructured surfaces have been performed in air with atmospheric relative humidity[3–11]. Heat exchangers, heat pipes and other systems with two-phase flow, however, operate in a pure vapor environment at saturated conditions. It is thus important to have an understanding of how the gas environment influences the droplet wettability and mobility. This part of the dissertation presents the influence of the gas environment on the static and dynamic wetting behavior of water droplets on four different surface morphologies. The effect of pressure and corresponding saturation temperatures are also analyzed.

2.2 Materials and Methods

Figure 2.1 shows scanning electron microscope (SEM) and optical images of water droplets on the four micro- and nanostructured samples, i.e., microfabricated silicon micropillars,

---

[1] Parts of this chapter have been previously published as Weisensee *et al.*, "Impact of Air and Water Vapor Environments on the Hydrophobicity of Surfaces", *J. Colloid Interface Sci.* 543 (2015)

nanoparticles on a flat surface, and a copper mesh with and without a nanoparticle coating. A flat, Teflon-coated Silicon wafer served as a reference sample. Silicon pillars were fabricated using a Bosch etching process. The square pillars have an edge length of 10 μm, a pitch size of 20 μm and a height of approximately 30 μm. The solid-liquid fraction in the Cassie-Baxter state is $\varphi = 0.25$. Nanoparticle samples consist of Zinc Oxide (ZnO) nanoparticles with an equivalent diameter of 40 – 100 nm in a polydimethylsiloxane (Sylgard 182) (PDMS) matrix. For the preparation, ZnO and PDMS were mixed together with hexane in a 1:1 w/w solution. The solution was then sprayed onto a flat Silicon wafer and a 200 mesh (TWP Inc.) to create hierarchical micro- and nanostructures. All samples, except for a bare, as-received copper mesh, were dip coated in liquid Teflon from DuPont in a 5:1 solution of FC-770:Teflon AF with 6% solids. The thickness of the Teflon coating on the flat surface is in the order of 100 nm, as determined by profilometry.

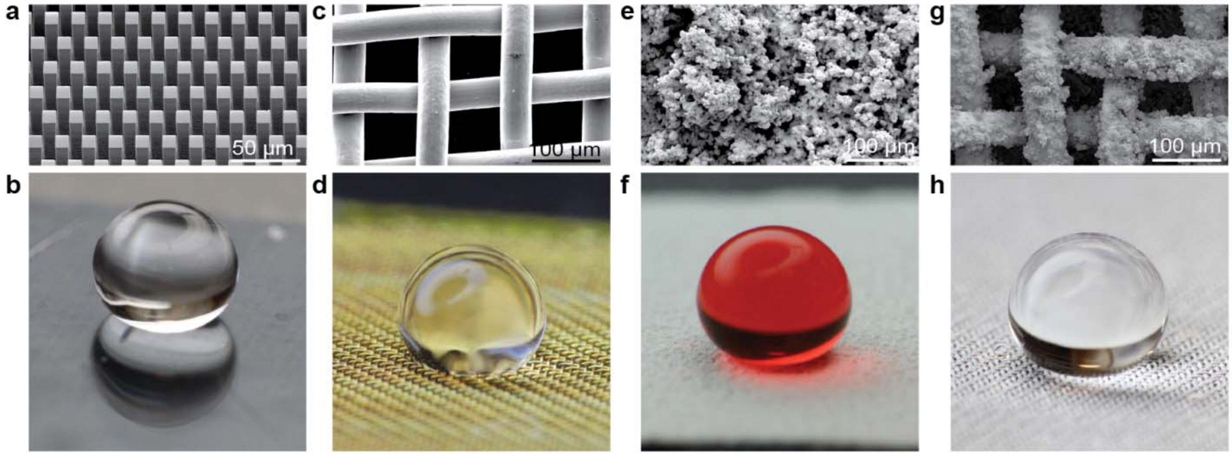

Figure 2.1: Scanning electron microscope (SEM) and optical images of the five samples samples: (a,b) 10x20 μm² (pillar size x pitch) square silicon pillars with a height of 30 μm, (c,d) Teflon-coated 200 mesh with a fiber diameter of 46 μm, (e,f) flat silicon wafer coated with a 1:1 ZnO:PDMS nanoparticle spray, (g,h) 200 mesh coated with nanoparticles. The water droplet on the nanoparticle sample is dyed red for better visualization.

Figure 2.2 shows the experimental setup in which we measured water droplet contact angles in gas environments of either air or pure water vapor. A light source illuminated the sample on the center stage through one of the windows. A Canon T3i camera with a Sigma 70-300 mm lens and a Raynox DCR-150 macro lens monitored the droplets through a second window at 180° from the first. The frame rate of the recorded images was 60 frames per second (fps) at a pixel resolution of 1280×720. The CAs were analyzed using the software DropSnake, which uses active contour B-spline snakes to match the shape of the drop[12]. A 0.2 mL micro-syringe (Gilmont EW-07840-00) with a gauge 33 needle (Hamilton, Metal Hub NDL) positioned the droplets on the surface. A pressure transducer (Omega PX319-100AI; accuracy: ±0.25%) monitored the pressure in the chamber.

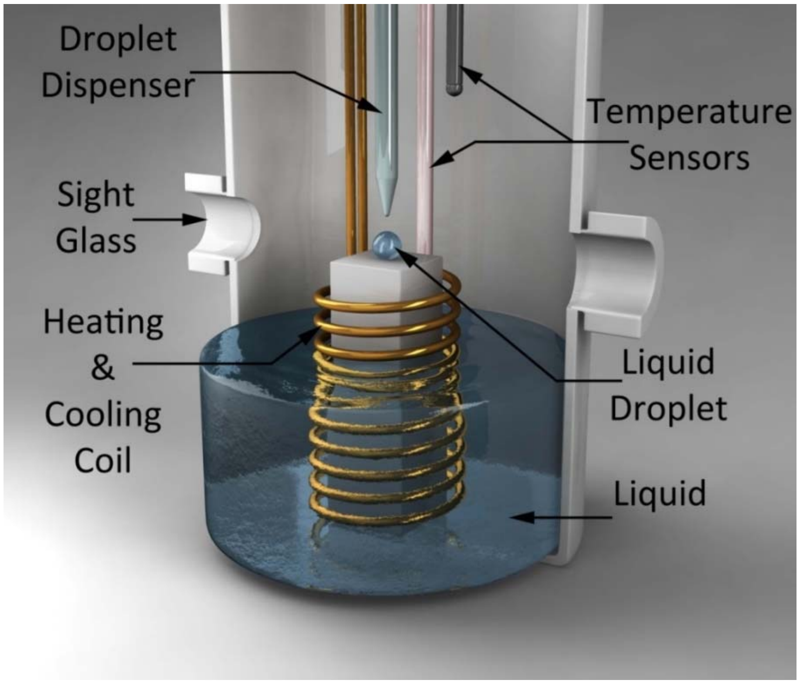

Figure 2.2: Vacuum chamber for the experiments in water vapor environment. Liquid water at the bottom of the chamber is heated by an electrical heater to its saturation temperature while vacuum is pumped continuously at the top of the chamber (not shown). Two thermocouples monitor the temperature in the chamber. A liquid water droplet gets deposited on the sample by a micro-syringe and is captured by a camera through a side glass. The sample is illuminated from the back through a second window.

The simultaneous control of pressure and temperature in the vacuum chamber allowed for measurements at saturated conditions. The pressure in the chamber, ranging from 60 to 1000 mbar, was controlled manually with a needle valve and a vacuum pump. For the measurements in pure water vapor, a custom built electrical heater (OEM Heaters) maintained water in the bottom of the chamber at the respective saturation temperature. A BriskHeat X2 PID Temperature controller, using a J-type thermocouple as input, controlled the temperature of the liquid over the range of 36 – 100 °C (+/- 1°C). A second, T-type thermocouple (Omega TNQSS-125U-6; accuracy: ±0.5°C) recorded the temperature in the chamber. During the experiments, the vacuum pump was operated continuously to counterbalance evaporation. The fraction of water vapor in the chamber, i.e., the temperature-dependent partial pressure of water vapor divided by the measured pressure in the vacuum chamber, was usually above 92%, and always greater than 76%. For measurements in the air environment, the bottom of the vacuum chamber was left empty and the measurements took place at ambient temperatures and moisture, i.e. relative humidity, conditions within the same pressure range.

Static contact angles were measured by depositing a water droplet of volume $V \approx 5$ µl on the horizontal sample. For the advancing CA, the water volume was slowly increased and for the receding CA the drop volume was slowly reduced while the droplet position remained static. The CAs were measured in the frame before the contact line translated to a new position. All of the reported values are averaged over at least four measurements at each pressure level. Their 95% confidence interval, following a t-distribution, is given as a measure of uncertainty.

Dynamic CAs were measured for a droplet sliding or rolling down an inclined sample. The angle of inclination of the sample to the horizontal, the tilt angle α, was 1-2° above the respective critical sliding angle for onset of droplet movement. The needle was placed above the sample such that the droplets of volume $V \approx 5$ µl would gently deposit onto the sample. For the samples with nanoparticles, the droplets were placed onto the horizontal surface. Then the setup was slowly rotated until the droplets started rolling off and the tilt angle was recorded. CAs were measured when the droplets reached a quasi-steady-state velocity. Previous reports point out that velocities for small droplets moving along flat or microgrooved surfaces are approximately constant[13,14]. All of the reported CA values are averaged over at least six measurements at each pressure level to account for inhomogeneities in surface structure and variations in droplet velocity.

2.3 Results and Discussion

2.3.1. Static Contact Angles

Figure 2.3 and Figure 2.4 show the advancing static CAs and CAH, respectively, on all samples in the air (black) and water vapor (gray) environments. The measured CAs are nearly constant over the studied temperature and pressure range. Table 2.1 lists the measured static advancing CAs and CAH for all samples in air and in water vapor, averaged over all pressure and temperature conditions. In air, the flat surface has advancing and receding CAs of θ_A/θ_R = 116°/103°, which agree well with values reported elsewhere[15]. The hysteresis on a flat surface in air is thus $\Delta\theta = 13°$. Both the bare and Teflon-coated meshes have the lowest CAs of all microstructured surfaces. Samples with pillars and nanoparticles achieve CAs between 154° and 159°. As expected, the hysteresis on the pillar sample is relatively large with $\Delta\theta = 25°$ in air and the droplets are not very mobile[3,16]. Interestingly, the mesh + nanoparticle sample with $\Delta\theta = 14°$ in air has a higher CAH than the nanoparticle-only sample with $\Delta\theta = 10°$. Often, dual length scales, i.e. features on both the micro- and nanometer scales, decrease CAH and increase mobility[4,8,17–19]. In the present case, both samples with nanoparticles have features with multiple length scales due to particle agglomeration. The particle density on the mesh, however, is significantly lower than that on the nanoparticle-only sample and the predominant length scale is that of the mesh. The values of the advancing CAs and CAH on the mesh + nanoparticles sample lie thus between those of a mesh without nanoparticles and those of nanoparticles on a flat surface.

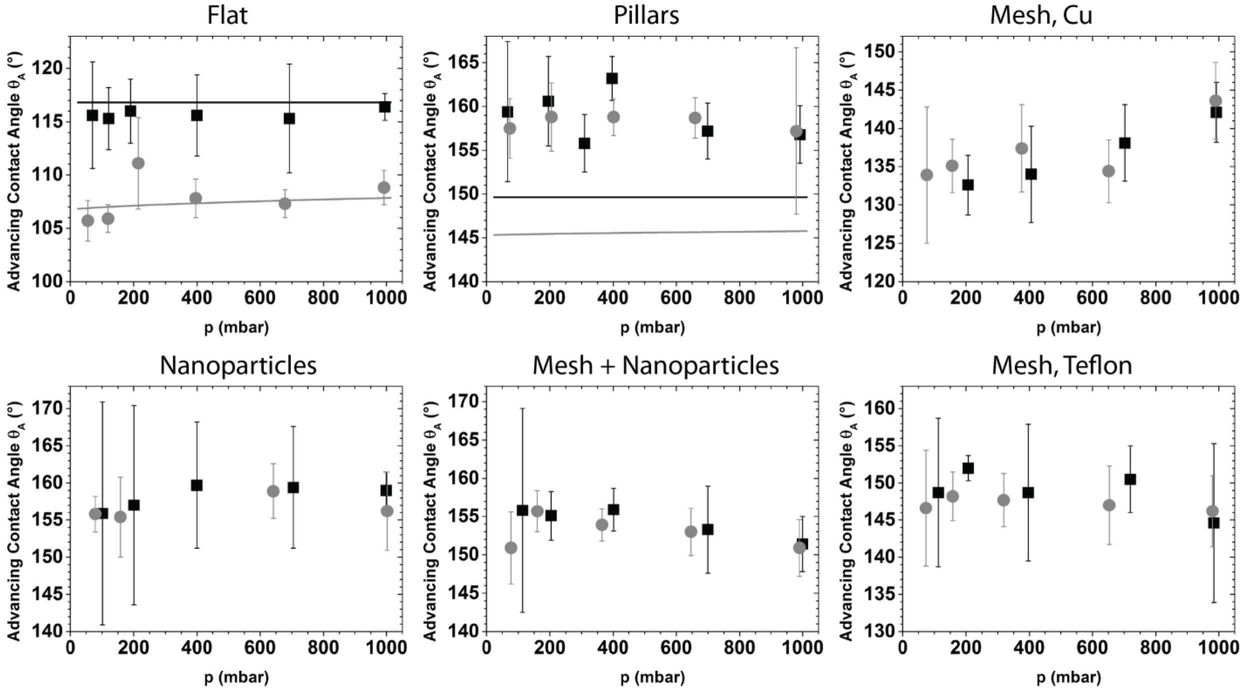

Figure 2.3: Advancing static contact angles of water droplets in air (black) and water vapor (gray) as a function of pressure for the different sample types. In the water vapor environment, the temperature is adjusted to achieve saturation. For the flat, Teflon coated Si wafer, the model predictions for air and water vapor with an adsorption fitting parameter in vapor of $|\pi/\gamma_{lg}| = 0.16$ are included. For the 10x20 μm² (pillar size x pitch) square Teflon coated Si pillars, the model data for the Cassie-Baxter states is shown. The nanoparticles are a 1:1 ZnO:PDMS mixture in weight, and the mesh is a copper 200 mesh. Except for one bare copper mesh all samples are Teflon-coated. The error bars represent the 95% confidence interval as determined with a t-distribution.

In the water vapor environment the advancing CAs on the flat surface are 9° smaller than those in air. We propose that water vapor adsorption to the Teflon causes the apparent surface energy of the solid to rise. When the three-phase contact line moves over the solid with the higher net surface energy, the advancing CA decreases, as can be concluded from Young's equation (Eq. (1-1)). On the microstructured surfaces the gas environment has little to no influence on the wettability of the surface. The advancing CAs in the water vapor environment are at most 2° lower than those in air. Most probably, the active unpinning of the droplets and traversing of a gap during advancing reduces the effect of higher surface energy ahead of the droplet. Also, the contact area between liquid and Teflon is significantly lower than on a flat surface, reducing the influence of the solid's surface energy on the CA. After removal from the vapor environment and subsequent drying, the CAs of all samples returned to their values in air.

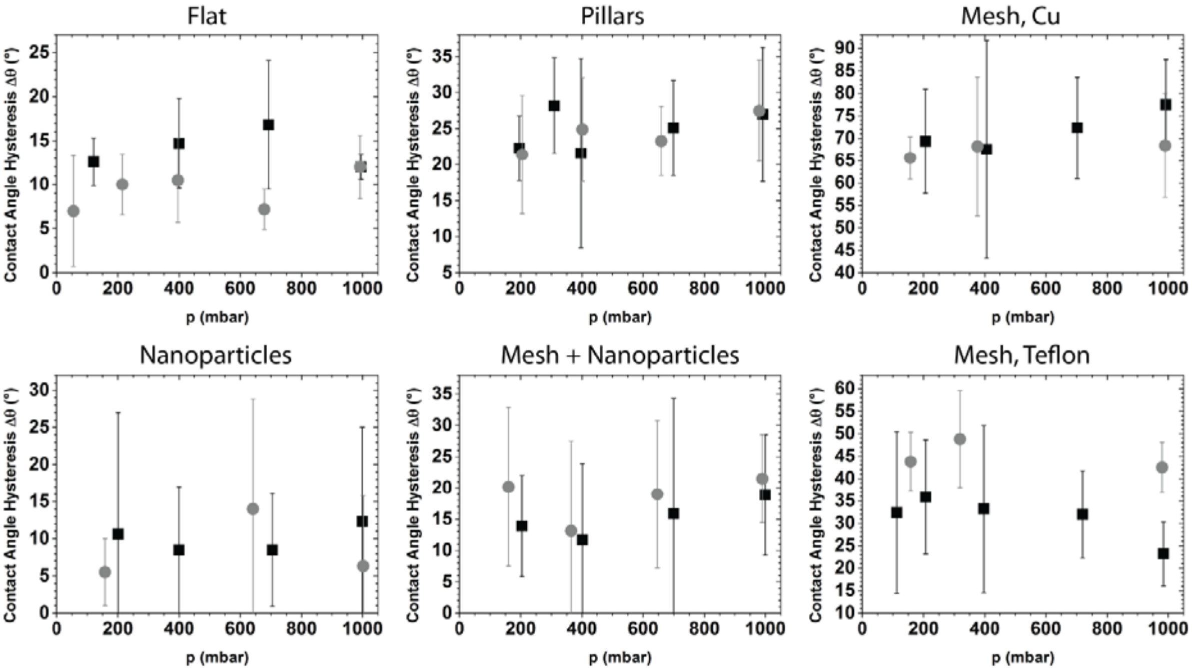

Figure 2.4: Contact angle hysteresis of static water droplets in air (black) and water vapor (gray) as a function of pressure for the different sample types. In the water vapor environment, the temperature is adjusted to achieve saturation. The error bars represent the 95% confidence interval as determined with a t-distribution.

Table 2.1: Summary of static and dynamic advancing contact angles θ_A and hysteresis $\Delta\theta$ in degrees in air and water vapor environments. The values are averaged over all pressures and temperatures. The 95% confidence interval (+/-) of a measurement series is given in parentheses in degrees. Droplets on the meshes, both bare and Teflon-coated, are sticky and therefore have no dynamic contact angles.

Sample	**Static, in Air ($\theta_A - \Delta\theta$)**	**Static, in Water Vapor ($\theta_A - \Delta\theta$)**	**Dynamic, in Air ($\theta_A - \Delta\theta$)**	**Dynamic, in Water Vapor ($\theta_A - \Delta\theta$)**
Flat	116 (0.9) – 13 (1.1)	107 (0.7) – 10 (1.3)	120 (0.6) – 12 (0.6)	112 (1.3) – 17 (1.5)
Pillars	159 (1.2) – 25 (2.3)	158 (1.1) – 24 (2.5)	161 (0.6) – 27 (1.0)	162 (0.7) – 29 (1.3)
Nanoparticles	158 (1.9) – 10 (2.9)	157 (1.7) – 9 (3.2)	160 (1.1) – 5 (1.2)	154 (1.1) – 7 (1.3)
Mesh + Nanoparticles	154 (1.3) – 14 (3.3)	153 (1.1) – 19 (3.7)	157 (1.5) – 11 (2.0)	152 (2.2) – 10 (2.6)
Mesh, Teflon	149 (1.9) – 31 (3.2)	147 (1.5) – 45 (3.3)	-	-
Mesh, Cu	137 (1.9) – 72 (4.0)	137 (2.0) – 67 (3.1)	-	-

2.3.2. Modelling the Static Contact Angles

Figure 2.3a shows the prediction of the static CAs of water droplets on a flat Teflon surface. The predicted values match well with the measured advancing CAs in air. Since Teflon is highly non-polar, the interfacial energy between the liquid and the solid, γ_{sl}, in Young's equation (Eq. (1-1)) can be approximated with Fowkes' relationship for the additivity of intermolecular forces[20]

$$\gamma_{sl} = \gamma_s + \gamma_l - 2\sqrt{\gamma_s{}^d \gamma_l{}^d}\,, \tag{2-1}$$

where γ_s and γ_l are the surface tensions of the solid and liquid, respectively, in vacuum (or air) and the superscript *d* denotes the dispersive components of the surface tension. At room temperature, the surface tension of water is $\gamma_l = \gamma_{lg} = 72.4$ mN/m, and Teflon has a surface energy of $\gamma_s = \gamma_{sg} = 20$ mN/m. The dispersive components for water and Teflon are $\gamma_l{}^d = 21.8$ mN/m and $\gamma_s{}^d = 18.6$ mN/, respectively[21]. The interfacial energy between Teflon and the water droplet is then γ_{sl} = 52.1 mN/m at room temperature. The changes of surface tension with respect to temperature can be approximated with a linear fit. The temperature coefficient for water is $\Delta\gamma_l$ = -0.17 mN/m-K and for Teflon $\Delta\gamma_s$ = -0.06 mN/m-K. The changes in surface tension with pressure are negligible[22].

For droplets in the pure water vapor environment, a spreading pressure π must be introduced that accounts for vapor adsorption to the solid surface[23]. The net solid-gas surface tension becomes

$$\gamma'_{sg} = \gamma_s - \pi \, . \tag{2-2}$$

Normalization with the temperature dependent surface tension of water, γ_{lg}, and combination with Young's equation yields

$$\cos(\theta) = \frac{\gamma_s - \left(-{}^{\pi}/_{\gamma_{lg}}\right)\gamma_{lg} - \gamma_{sl}}{\gamma_{lg}} \, . \tag{2-3}$$

Here, ($-\pi/\gamma_{lg}$) serves as a fitting parameter to match the experimental results. The negative sign indicates that water vapor adsorption increases the net surface energy of the solid. On the flat surface, $|\pi/\gamma_{lg}|$ = 0.16 = 16 %, as shown by the gray solid line in the upper left graph of Figure 2.3. This number can be interpreted as the area percentage of water vapor adsorption onto Teflon. Even though Teflon is hydrophobic, it has some hydrophilic sites that readily adsorb water molecules[24,25]. Since Teflon has a very low surface energy, many researchers have doubted, based on theoretical considerations, that water could adsorb to the surface of the polymer and increase its net surface energy[23,24,26]. However, it has been shown previously that water, in fact, does actively adsorb to Teflon/PTFE surfaces[24,25,27,28]. The present findings are slightly higher than the values reported in literature, which range from $|\pi/\gamma_{lg}|$ = 8 to 12% at room temperature[24,25,27,28].

Combining the model for the flat surface (Eq. (2-3)) with the Cassie-Baxter equation (Eq. (1-3)) gives a prediction of CAs on pillars, as represented by the solid lines in the upper right graph in Figure 2.3. The Cassie model under-predicts the experimental values for advancing CAs on pillars by 6% in air and by 8% in water vapor. A possible reason for the mismatch between model and data are fine ripples at the side walls of the pillars that formed during the Bosch etching process. These small waves act as re-entrant structures and increase the apparent CAs compared to those on smooth walls[29].

2.3.3. Dynamic Contact Angles

Figure 2.5 and Figure 2.6, as well as Table 2.1, present the dynamic advancing CAs and CAH for droplets on the flat sample, pillars and the two samples with nanoparticles. Droplets on the mesh-only samples were sticky and thus do not have dynamic CAs. In air, the advancing CAs are higher for moving droplets than for sessile ones. Except for on the pillars, the dynamic advancing CAs are lower in the water vapor environment than in air. Again, water vapor adsorption to the surface is the most probable explanation for the reduction in CA. At the same time, the dynamic receding CAs on the pillars decrease, which is consistent with previous experiments on flat or microgrooved surfaces where dynamic advancing CAs usually increased but dynamic receding CAs decreased or stayed constant with increasing droplet velocity[10,30–32]. On the flat surface and the nanoparticle samples, however, receding CAs increase in the dynamic regime. The reason for this increase is unknown. A possible explanation lies in the mode of the droplet movement. The study of movies of the displacing droplets at 1/6 of their original speed suggest that the droplets on the flat surface slide, but those on the micro-structured surfaces roll down the sample. We propose that – similar to a solid sliding along another solid – water droplets have two different friction coefficients. Sessile water droplets experience a static friction coefficient, while moving droplets are in the regime of the lower kinetic friction. Sticking of the contact line, i.e. static friction, results from the capillary force ($\pi\, a\, \gamma_{lv}\, (\cos\theta_R - \cos\theta_A)$; where a is the radius of the macroscopic contact area between droplet and solid) being greater than the weight of the droplet ($V \rho\, g \sin\alpha$).[33] For moving droplets on a surface with low CAH, the term ($\cos\theta_R - \cos\theta_A$) is small and pinning of the contact line becomes less important.

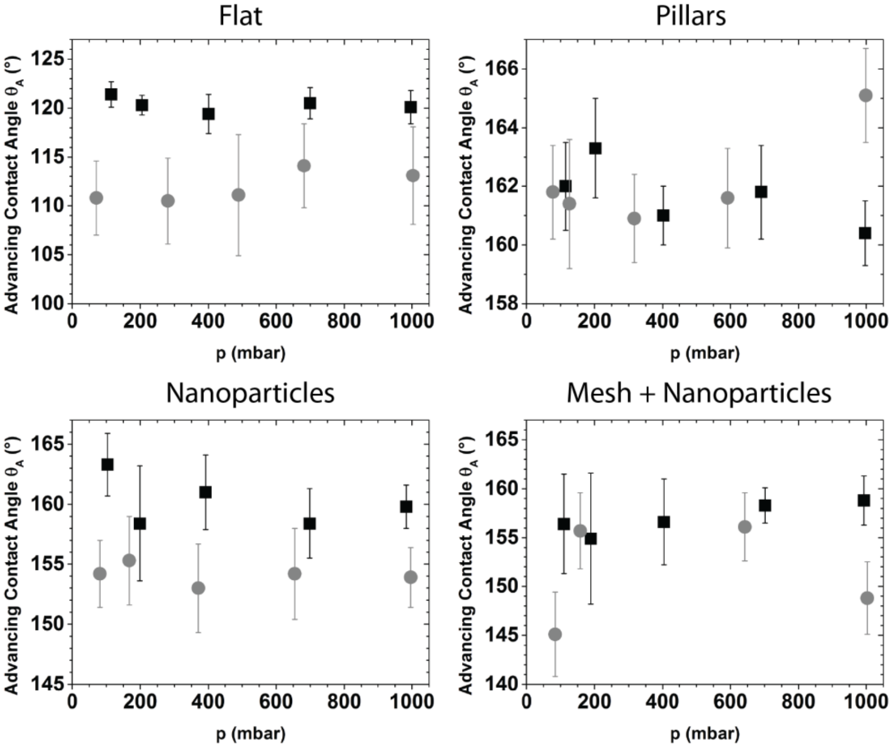

Figure 2.5: Advancing dynamic contact angles of water droplets in air (black) and water vapor (gray) at saturation conditions as a function of pressure for the samples with a sliding angle $\alpha < 45°$. The inclination of the samples was 1-2° above the critical sliding angle. The error bars represent the 95% confidence interval as determined with a t-distribution.

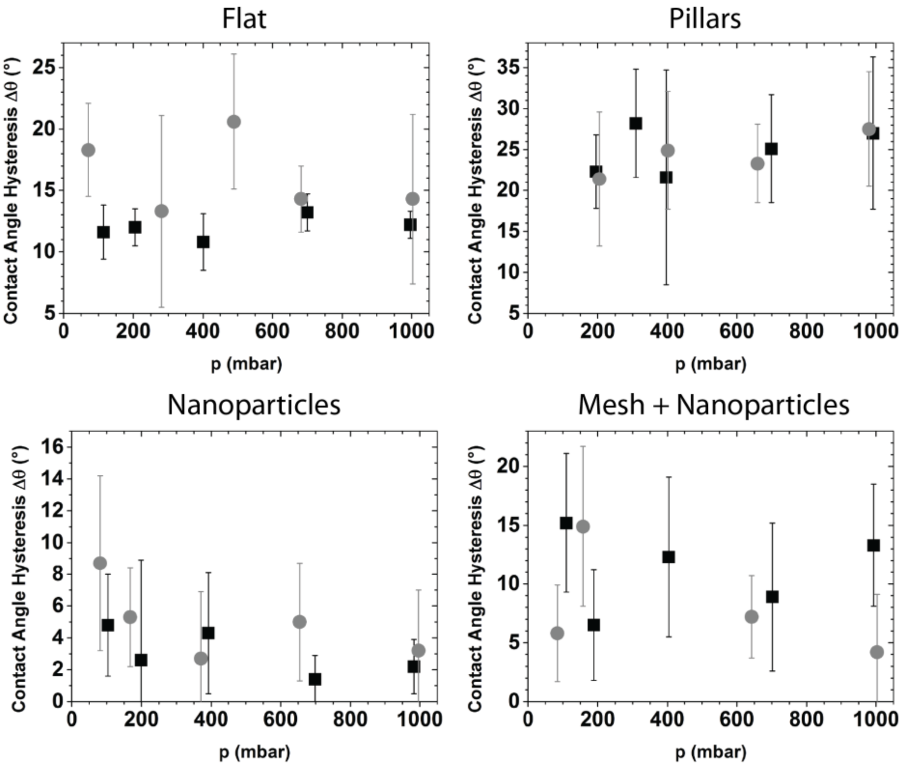

Figure 2.6: Contact angle hysteresis of dynamic water droplets in air (black) and water vapor (gray) at saturation conditions as a function of pressure for the samples with a sliding angle $\alpha < 45°$. The inclination of the samples was 1-2° above the critical sliding angle. The error bars represent the 95% confidence interval as determined with a t-distribution.

Figure 2.7 shows water droplets rolling down an inclined nanoparticle sample at two different velocities. At the lower rolling velocities in the left image the droplet shape is close to that of a sphere, with the dynamic advancing CA being greater than the receding CA. However, at a higher velocity, i.e. higher tilt angle, the droplet distorts and develops a hump at the upper rear flank of the droplet. Interestingly, the apparent dynamic receding CA appears to be higher than the dynamic advancing CA. The seeming reversion of the advancing and receding CA suggests that inertia is dominant over friction.

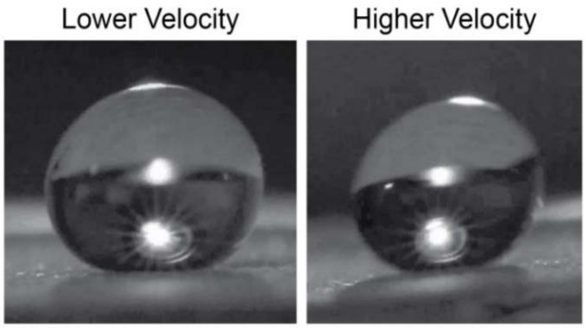

Figure 2.7: Comparison of the shapes and contact angles of water droplets rolling down a 1:1 ZnO:PDMS nanoparticle sample at different velocities. At low velocities, the droplets are almost spherical with the advancing contact angle greater than the receding contact angle. At higher velocities the droplets distort and develop a hump at the rear flank. The dynamic receding contact angle appears greater than the advancing contact angle.

Table 2.2 summarizes tilt angles and average droplet velocities. On all samples, tilt angles were higher in the water vapor environment than in air and decreased slightly with decreasing pressure in both environments. On the flat surface, the average velocity for the sliding droplet is only 3.5 mm/s. Even though CAH is higher for the mesh + nanoparticle sample than for nanoparticles only, the former had the highest droplet velocities of about 148 mm/s. The reason for the faster droplets is the significantly higher tilt angle that was necessary for droplet movement.

Table 2.2: Average tilt angles α and droplet velocities $\bar{u}$ for dynamic contact angle measurements with a droplet volume $V \approx 5$ µl.

Sample	**Tilt Angle *α* [°]**	**Average Droplet Velocity $\bar{u}$ [mm/s]**
Flat	37.5 ± 2.5	3.5 ± 2
Pillars	18 ± 1	11 ± 3
Nanoparticles	4 ± 2	70 ± 6
Mesh + Nanoparticles	9 ± 2	148 ± 16

2.4 Conclusion

We present measurements of static and dynamic contact angles in an air and a pure water vapor environment. For water droplets on flat or micro- and nanostructured hydrophobic surfaces, varying pressure, between 60 and 1000 mbar, and temperature, between 39 and 100°C, have no significant effect on the measured contact angles. On a flat, Teflon-coated surface, static contact angles are lower in the water vapor environment than in air. We propose that vapor adsorption to the Teflon increases the effective surface energy of the solid. While some prior theoretical work concludes that water is not able to adsorb to the low-energy surface of Teflon, our findings match well with adsorption measurements on Teflon or PTFE surfaces reported in literature [24,25,27,28]. On micro- and nanostructured surfaces, static contact angles are similar in air and in water vapor.

In air, dynamic advancing contact angles are slightly higher than the respective static contact angles. In the water vapor environment, the dynamic advancing contact angles on a flat surface and on pillars are higher than in the static case, but lower than for sessile droplets on the samples with nanoparticles. Again, water vapor adsorption to the surface is likely to be the reason for the decrease in advancing contact angles. Interestingly, contact angle hysteresis decreases on the superhydrophobic nanoparticle samples when transitioning from static to dynamic contact angles. Figure 2.8 summarizes the different surfaces with static and dynamic droplets at low droplet velocities. Future work should extend the range of droplet velocities and nanoparticle sizes to gain a better understanding of the influence and mechanism of water vapor adsorption in cavities on the surface.

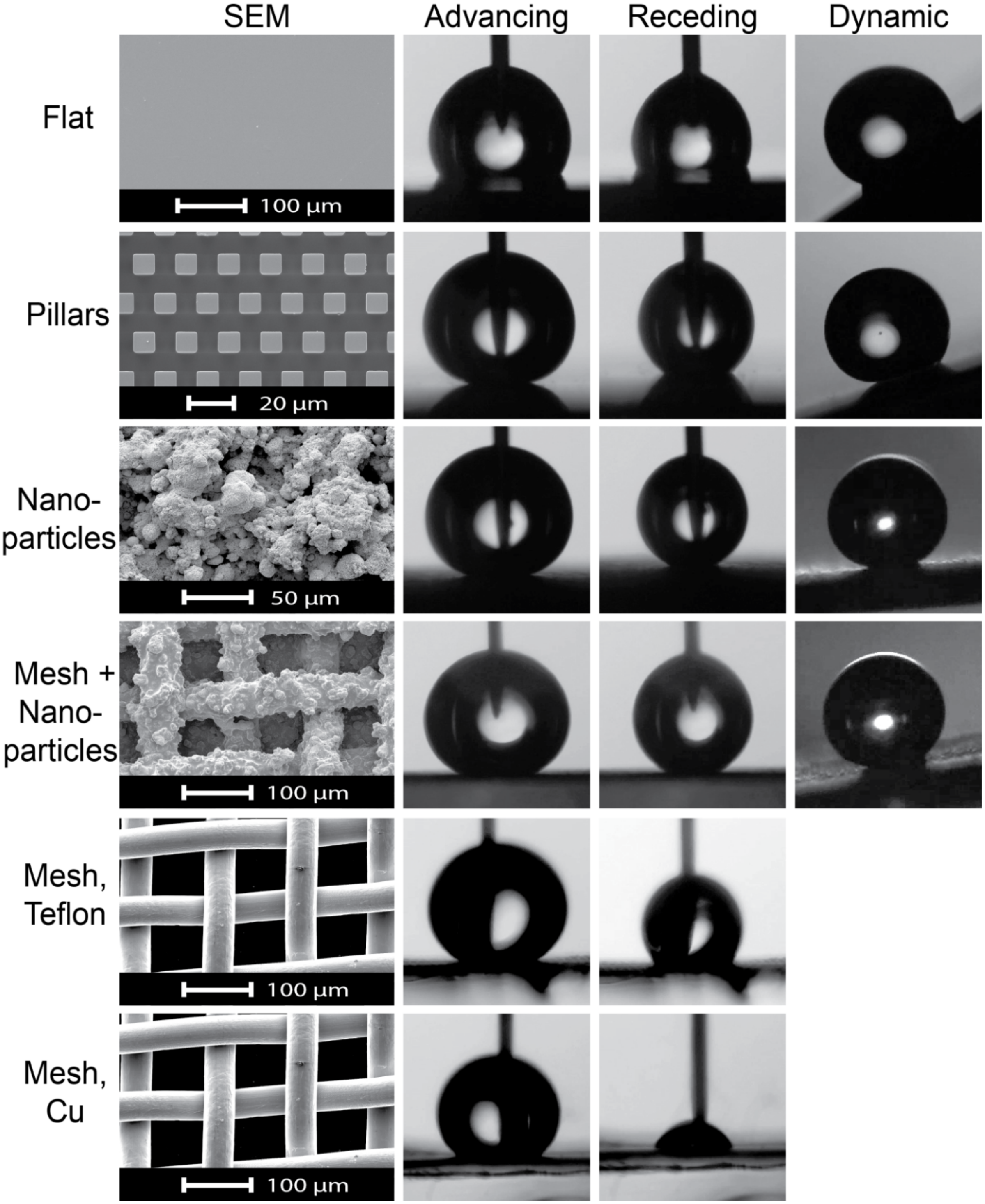

Figure 2.8: Summary of the sample geometries (left) and advancing, static (center left), receding, static (center right) and dynamic (right) water droplets with $V \approx 5$ µl on all samples. Note that the droplets on the meshes were sticky, i.e. non-mobile, and thus do not have dynamic contact angles.

2.5 References

(1) Schmidt, E.; Schurig, W.; Sellschopp, W. Versuche über die Kondensation von Wasserdampf in Film- und Tropfenform. *Tech. Mech. Thermodyn.* **1930**, *1*, 53–63.
(2) Attinger, D.; Frankiewicz, C.; Betz, A. R.; Schutzius, T. M.; Ganguly, R.; Das, A.; Kim, C.-J.; Megaridis, C. M. Surface Engineering for Phase Change Heat Transfer: A Review. *ArXiv14095363 Cond-Mat* **2014**.
(3) Öner, D.; McCarthy, T. J. Ultrahydrophobic Surfaces. Effects of Topography Length Scales on Wettability. *Langmuir* **2000**, *16*, 7777–7782.
(4) Bhushan, B.; Jung, Y. C.; Koch, K. Micro-, Nano- and Hierarchical Structures for Superhydrophobicity, Self-Cleaning and Low Adhesion. *Philos. Trans. R. Soc. Math. Phys. Eng. Sci.* **2009**, *367*, 1631–1672.
(5) Zhu, L.; Xiu, Y.; Xu, J.; Tamirisa, P. A.; Hess, D. W.; Wong, C.-P. Superhydrophobicity on Two-Tier Rough Surfaces Fabricated by Controlled Growth of Aligned Carbon Nanotube Arrays Coated with Fluorocarbon. *Langmuir* **2005**, *21*, 11208–11212.
(6) Gao, L.; McCarthy, T. J. How Wenzel and Cassie Were Wrong. *Langmuir* **2007**, *23*, 3762–3765.
(7) Kondrashov, V.; Rühe, J. Microcones and Nanograss: Toward Mechanically Robust Superhydrophobic Surfaces. *Langmuir* **2014**, *30*, 4342–4350.
(8) Yong, J.; Yang, Q.; Chen, F.; Zhang, D.; Bian, H.; Ou, Y.; Si, J.; Du, G.; Hou, X. Stable Superhydrophobic Surface with Hierarchical Mesh-Porous Structure Fabricated by a Femtosecond Laser. *Appl. Phys. A* **2013**, *111*, 243–249.
(9) Jeong, W.-J.; Ha, M. Y.; Yoon, H. S.; Ambrosia, M. Dynamic Behavior of Water Droplets on Solid Surfaces with Pillar-Type Nanostructures. *Langmuir* **2012**, *28*, 5360–5371.
(10) Wang, X.; Rahman, M. A.; Jacobi, A. M.; Hrnjak, R. S. Dynamic Wetting Behavior and Water Drops on Microgrooved Surfaces. *Heat Transf. Eng.* **2013**, *34*, 1088–1098.
(11) Darmanin, T.; Guittard, F. Homogeneous Growth of Conducting Polymer Nanofibers by Electrodeposition for Superhydrophobic and Superoleophilic Stainless Steel Meshes. *RSC Adv.* **2014**, *4*, 50401–50405.
(12) Stalder, A. F.; Kulik, G.; Sage, D.; Barbieri, L.; Hoffmann, P. A Snake-Based Approach to Accurate Determination of Both Contact Points and Contact Angles. *Colloids Surf. Physicochem. Eng. Asp.* **January 9**, *286*, 92–103.
(13) Song, J.-H.; Sakai, M.; Yoshida, N.; Suzuki, S.; Kameshima, Y.; Nakajima, A. Dynamic Hydrophobicity of Water Droplets on the Line-Patterned Hydrophobic Surfaces. *Surf. Sci.* **2006**, *600*, 2711–2717.
(14) Sakai, M.; Song, J.-H.; Yoshida, N.; Suzuki, S.; Kameshima, Y.; Nakajima, A. Relationship between Sliding Acceleration of Water Droplets and Dynamic Contact Angles on Hydrophobic Surfaces. *Surf. Sci.* **2006**, *600*, L204–L208.
(15) Lee, S.; Park, J.-S.; Lee, T. R. The Wettability of Fluoropolymer Surfaces: Influence of Surface Dipoles. *Langmuir* **2008**, *24*, 4817–4826.
(16) Gao, L.; McCarthy, T. J. Contact Angle Hysteresis Explained. *Langmuir* **2006**, *22*, 6234–6237.
(17) An, T.; Cho, S. J.; Choi, W.; Kim, J. H.; Lim, S. T.; Lim, G. Preparation of Stable Superhydrophobic Mesh with a Biomimetic Hierarchical Structure. *Soft Matter* **2011**, *7*, 9867–9870.

(18) Paxson, A. T.; Varanasi, K. K. Self-Similarity of Contact Line Depinning from Textured Surfaces. *Nat. Commun.* **2013**, *4*, 1492.

(19) Steele, A.; Bayer, I.; Moran, S.; Cannon, A.; King, W. P.; Loth, E. Conformal ZnO Nanocomposite Coatings on Micro-Patterned Surfaces for Superhydrophobicity. *Thin Solid Films* **7**, *518*, 5426–5431.

(20) Fowkes, F. M. Additivity of intermolecular forces at interfaces. I. Determination of the contribution to surface and interfacial tensions of dispersion forces in various liquids. *J. Phys. Chem.* **1963**, *67*, 2538–2541.

(21) Kaelble, D. H. Dispersion-Polar Surface Tension Properties of Organic Solids. *J. Adhes.* **1970**, *2*, 66–81.

(22) Massoudi, R.; King, A. D. Effect of Pressure on the Surface Tension of Water. Adsorption of Low Molecular Weight Gases on Water at 25.deg. *J. Phys. Chem.* **1974**, *78*, 2262–2266.

(23) Carey, V. P. Liquid-Vapor Phase-Change Phenomena: An Introduction To The Thermophysics Of Vaporization and Condensation in Heat Transfer Equipment: An Introduction to the Thermophysics of Vaporization & Condensation in Heat Transfer Equipment; *Taylor & Francis*, 1992.

(24) Fowkes, F. M.; McCarthy, D. C.; Mostafa, M. A. Contact Angles and the Equilibrium Spreading Pressures of Liquids on Hydrophobic Solids. *J. Colloid Interface Sci.* **1980**, *78*, 200–206.

(25) Chessick, J. H.; Healey, F. H.; Zettlemoyer, A. C. Adsorption and Heat of Wetting Studies of Teflon. *J. Phys. Chem.* **1956**, *60*, 1345–1347.

(26) Good, R. J.; Girifalco, L. A. A theory for estimation of surface and interfacial energies. III. Estimation of surfaces energies of solids from contact angle data. *J. Phys. Chem.* **1960**, *64*, 561–565.

(27) Hu, P.; Adamson, A. W. Adsorption and Contact Angle Studies: II. Water and Organic Substances on Polished Polytetrafluoroethylene. *J. Colloid Interface Sci.* **1977**, *59*, 605–614.

(28) Schrader, M. E. Contact Angle and Vapor Adsorption. *Langmuir* **1996**, *12*, 3728–3732.

(29) Zhao, H.; Law, K.-Y.; Sambhy, V. Fabrication, Surface Properties, and Origin of Superoleophobicity for a Model Textured Surface. *Langmuir* **2011**, *27*, 5927–5935.

(30) Johnson Jr., R. E.; Dettre, R. H.; Brandreth, D. A. Dynamic Contact Angles and Contact Angle Hysteresis. *J. Colloid Interface Sci.* **1977**, *62*, 205–212.

(31) Dussan, E. B. On the Spreading of Liquids on Solid Surfaces: Static and Dynamic Contact Lines. *Annu. Rev. Fluid Mech.* **1979**, *11*, 371–400.

(32) Krasovitski, B.; Marmur, A. Drops Down the Hill: Theoretical Study of Limiting Contact Angles and the Hysteresis Range on a Tilted Plate. *Langmuir* **2005**, *21*, 3881–3885.

(33) Richard, D.; Quéré, D. Viscous Drops Rolling on a Tilted Non-Wettable Solid. *EPL Europhys. Lett.* **1999**, *48*, 286.

CHAPTER 3

CONDENSATE DROPLET SIZE DISTRIBUTION ON LUBRICANT-INFUSED SURFACES

3.1 Introduction

Condensation is pervasive both in nature[1,2] and industrial applications, including power generation[3], closed-loop electronics cooling systems[4,5], air conditioning[6], desalination[6,7], and water harvesting[8]. Dropwise condensation has recently gained renewed attention due to its high potential in heat transfer applications and advances in microfabrication and coating techniques[9–16]. Heat transfer rates during dropwise condensation can be 6-8X higher than during traditional filmwise condensation[9].

Despite being a highly transient process, dropwise condensation heat transfer can be modeled using steady-state formulas and time averaged droplet density functions[17–21]. For a single droplet, heat transfer can be thought of as a network of thermal resistances[17,20,22–25]. The network of serial and parallel resistances is illustrated in Figure 1.4 for droplets on a LIS surfaces. The heat transfer q_d through a single droplet is then

$$q_d = \frac{\Delta T_{tot}}{R_{tot}}, \tag{3-1}$$

where ΔT_{tot} is the overall temperature difference between the substrate temperature T_s and the vapor saturation temperature T_{sat}, and R_{tot} is the total thermal resistance through coating and droplet. The overall thermal resistance consists of the interfacial resistance R_i, the curvature resistance of the droplet R_c, conduction resistance R_{cond} and the structure resistance R_s, which includes resistances due to the lubricant (usually oil), the micro- or nanostructures (height h_B) and the low-energy surface coating (thickness δ_{coat}).

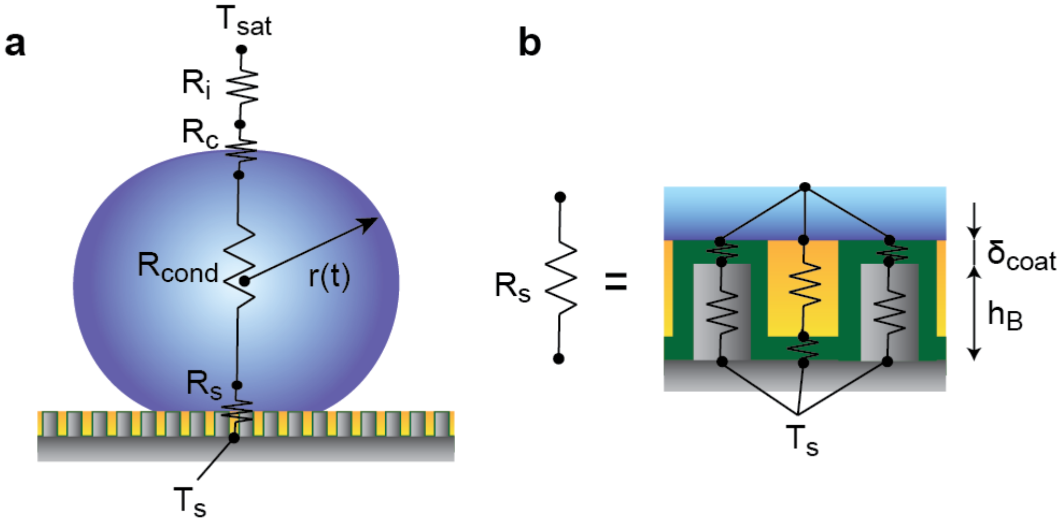

Figure 3.1: Thermal resistor network. (a) Total thermal path through droplet: structural resistance R_s, conduction resistance R_{cond}, curvature resistance R_c, and interfacial resistance R_i. (b) The structural resistance consists of various serial and parallel resistances through the micro- or nanostructures, the low surface energy coating, and the infusion (oil) layer.

The temperature drop ΔT_i at the droplet-vapor interface is caused by convection losses at the interface. The interface resistance can then be written as

$$R_i = \frac{1}{h_i 2\pi r^2 (1 - \cos\theta)}, \tag{3-2}$$

where h_i is the interfacial heat transfer coefficient (note: the interfacial heat transfer coefficient is not the same as the overall heat transfer coefficient resulting from a global energy balance). The interfacial heat transfer coefficient can be derived from kinetic theory and can be described as[23,26]

$$h_i = \frac{2\sigma}{2 - \sigma} \frac{1}{\sqrt{2\pi R_g T_s}} \frac{\rho_v \Delta h_{fg}^2}{T_s}, \tag{3-3}$$

where ρ_v is the vapor density, Δh_{fg} the latent heat of evaporation, R_g the specific gas constant, and σ the condensation accommodation coefficient. The accommodation coefficient represents the fraction of vapor molecules that will be captured by the liquid droplet. It is often assumed that the accommodation coefficient is equal to unity[20,23]. However, experimental data suggest that for droplets the evaporation and condensation coefficients at atmospheric pressure are closer to $\sigma = 0.04$, which will be used throughout this work[26].

Next, a temperature jump ΔT_c due to the droplet's finite curvature, known as Kelvin effect, has to be taken into account[27,28]. For a droplet with radius r the curvature temperature drop can be expressed as

$$\Delta T_c = \frac{2T_{sat}\gamma_l}{\Delta h_{fg} r \rho_l}. \tag{3-4}$$

Equation (3-4) can be re-arranged to

$$\Delta T_c = \frac{r_{min}}{r}\Delta T_{tot}\,, \tag{3-5}$$

where r_{min} is the minimum radius at which nucleation can occur and at which a stable droplet can be formed. This minimum viable droplet radius is determined by the substrate subcooling[29]:

$$r_{min} = \frac{2T_{sat}\gamma_l}{\Delta h_{fg}\rho_l(T_{sat} - T_s)}. \tag{3-6}$$

For water at atmospheric pressure the minimum droplet radius will be on the order of few nanometers ($r_{min} \approx 5$ nm for $\Delta T_{tot} = 5$ K and $T_{sat} = 100$°C).

If the droplet surface temperature is assumed to be uniform, then the temperature drop associated with conduction through the droplet, ΔT_{cond}, can be obtained by integration from the droplet base to the liquid-vapor interphase of the droplet, taking into account the contact angle between the droplet and the solid[25]. The conduction resistance then becomes[20]:

$$R_{cond} = \frac{\theta}{4\pi r k_l \sin\theta}, \tag{3-7}$$

where k_l is the liquid droplet thermal conductivity.

Assuming that the substrate temperature and droplet base temperature are uniform, the temperature gradient through the infusion layer ΔT_{cond} will be uniform as well. The structure resistance beneath the droplet includes conduction resistances through the micro- or nanostructures, the low-energy coating and the lubricant layer. Assuming that the oil infusion and the structures form a level interface with the liquid droplet, and the coating thickness is much smaller than the structural dimensions, the structure resistance can be formulated as[23,25]:

$$R_s = \frac{1}{\pi r^2 k_{coat} sin^2\theta}\left(\frac{k_B\varphi}{\delta_{coat}k_B + h_B k_{coat}} + \frac{k_{oil}(1-\varphi)}{\delta_{coat}k_{oil} + h_B k_{coat}}\right)^{-1}, \tag{3-8}$$

where k_B and k_{oil} are the thermal conductivities of the micro- or nanostructures (here: Boehmite) and the lubricant layer (here: oil), and φ is the solid-liquid fraction as derived from the Cassie-Baxter equation (Eq. (1-3)).

Now, with all the necessary thermal resistances identified, Eq. (1-1) can be written as:

$$q_d = \frac{\Delta T_i + \Delta T_c + \Delta T_{cond} + \Delta T_s}{R_{tot}} = \frac{\Delta T_{tot} - \Delta T_c}{R_i + R_{cond} + R_s}. \tag{3-9}$$

Combining equations (3-2), (3-5), (3-7), and (3-8) with (3-9) the final formula for single droplet heat transfer rate becomes:

$$q_d = \frac{\pi r^2 (T_{sat} - T_s)\left(1 - \frac{r_{min}}{r}\right)}{\frac{1}{2h_i(1-\cos\theta)} + \frac{r\theta}{4k_l \sin\theta} + \frac{1}{k_{coat} sin^2\theta}\left(\frac{k_B\varphi}{\delta_{coat}k_B + h_B k_{coat}} + \frac{k_{oil}(1-\varphi)}{\delta_{coat}k_{oil} + h_B k_{coat}}\right)^{-1}}. \tag{3-10}$$

For very small droplets curvature resistance is dominant while conduction through the droplet becomes more important as droplets grow. Generally, the per droplet heat transfer is smallest for small droplets and grows as the radius increases, as shown in Figure 3.2a.

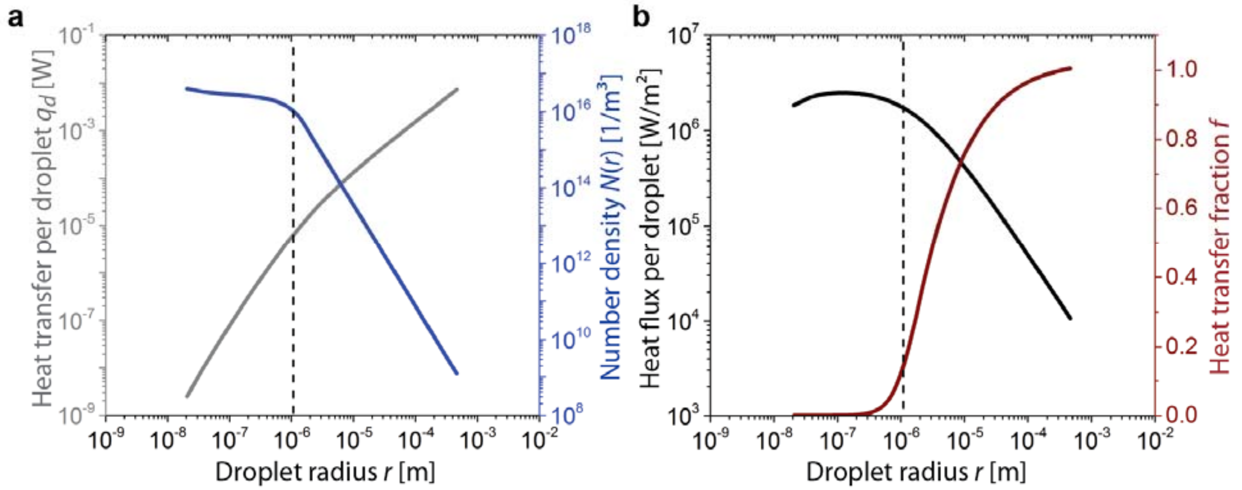

Figure 3.2: Heat transfer predictions for dropwise condensation. (a) Per droplet heat transfer and droplet size distribution as a function of droplet radius. The dashed line represents the transition radius between direct condensation and coalescence, r_e. (b) Per droplet heat transfer normalized by the droplet's base area (πr^2) and the cumulative fraction of heat transfer as a function of droplet radius. 95% of the total heat transfer happens for droplets smaller than 100 μm.

To obtain an overall heat transfer rate, Eq. (3-10) has to be integrated with respect to all existing droplet sizes on a surface. Since the condensation process is highly transient we need to assume a steady state behavior to obtain an average heat flux. Droplet growth can be divided into two regimes: direct condensation and droplet coalescence. The effective transition radius r_e between the two regimes can be approximated as

$$r_e = \frac{1}{\sqrt{4N_s}}, \tag{3-11}$$

where N_s is the nucleation site density. Assuming a number density $n(r)$ for small droplets with $r_{\min} \leq r \leq r_e$ and $N(r)$ for $r > r_e$, the total heat transfer rate is then[20,24]:

$$q''_{tot} = \int_{r_{min}}^{r_e} q_d(r)n(r)dr + \int_{r_e}^{\hat{r}} q_d(r)N(r)dr \ , \tag{3-12}$$

where q_d is given by Eq. (3-10). The upper bound for the integration for larger droplets, $\hat{r}$, is related to the maximum droplet radius before sliding, r_{max}. A force balance on the droplet just as it begins to de-pin and slide on a vertical surface due to the gravitational body force gives[23]:

$$r_{max} = \left(\frac{6(\cos\theta_R - \cos\theta_A)\sin\theta_e \gamma_l}{\pi(2 - 3\cos\theta_e + \cos^3\theta_e)\rho_l g} \right)^{1/2} , \tag{3-13}$$

where θ_A, θ_R, and $\theta_e = \cos^{-1}(0.5\cos(\theta_A) + 0.5\cos(\theta_R))$ are the advancing, receding, and equilibrium contact angles, respectively, γ_l and ρ_l are the droplet surface tension and density, respectively, and g is the gravitational constant. Comparison to experimental data shows that $\hat{r} \approx r_{max}/1.3$.[22] For water droplets on LIS used in this work we obtain $r_{max} \approx 460$ µm.

The most commonly used correlation for the number density of larger droplets ($r > r_e$) was developed by Rose and co-workers for dropwise condensation on flat copper plates treated with promoter layers[17,18,22]:

$$N(r) = \frac{1}{3\pi r^2 \hat{r}} \left(\frac{r}{\hat{r}} \right)^{-2/3} . \tag{3-14}$$

Tanaka *et al.* independently studied the distribution of drop sizes and found similar results[19]. The distribution for small droplet sizes ($r < r_e$) has been derived elsewhere, and can be expressed as[20]:

$$n(r) = \frac{1}{3\pi r_e^3 \hat{r}} \left(\frac{r_e}{\hat{r}} \right)^{-2/3} \frac{r(r_e - r_{min})}{r - r_{min}} \frac{A_2 r + A_3}{A_2 r_e + A_3} exp(B_1 + B_2) , \tag{3-15}$$

where A_i and B_i are parameters that can be solved for by enforcing a continuous boundary condition $n(r_e) = N(r_e)$:[23]

$$A_1 = \frac{\Delta T_{tot}}{\rho_l \Delta h_{fg}(1 - \cos\theta)^2(2 + \cos\theta)} , \tag{3-16}$$

$$A_2 = \frac{\theta}{4k_l \sin\theta} , \tag{3-17}$$

$$A_3 = \pi r^2 (R_i + R_s)\,, \tag{3-18}$$

$$B_1 = \frac{A_2}{\tau A_1}\left[\frac{r_e^2 - r^2}{2} + r_{min}(r_e - r) - r_{min}^2 \ln\left(\frac{r - r_{min}}{r_e - r_{min}}\right)\right], \tag{3-19}$$

$$B_2 = \frac{A_3}{\tau A_1}\left[r_e - r - r_{min} \ln\left(\frac{r - r_{min}}{r_e - r_{min}}\right)\right], \tag{3-20}$$

$$\tau = \frac{3r_e^2 (A_2 r_e + a_3)^2}{A_1 (11 A_2 r_e^2 - 14 A_2 r_e r_{min} + 8 A_3 r_e - 11 A_3 r_{min})}. \tag{3-21}$$

With equations (3-14) and (3-15) through (3-20), the continuous droplet number density function for small and big droplets can now be solved, and is plotted in Figure 3.2a for $r_{\max} = 0.46$ mm.

Figure 3.2b shows the heat flux per droplet, *i.e.* $q_d'' = q_d/(\pi r^2)$, and the cumulative heat transfer fraction $f = \int q(r)/q_{tot}$ as a function of droplet radius. It reveals that bigger droplets are mostly inactive, i.e. more than 80% of the total heat transfer occurs for droplets 1 µm < r < 100 µm. Thus increasing the mobility of droplets and the number of small droplets are necessary increase overall heat transfer rates.

The use of SLIPS, or LIS, for dropwise condensation can significantly increase droplet mobility compared to traditional smooth solid surfaces[30], and hence has the potential to greatly enhance heat transfer. However, more fundamental studies of individual droplet heat transfer and size distributions are needed in order to assess the potential. Given the ultra-smooth liquid interface with the condensing water droplets, the dynamics of condensation may vary from those on smooth copper surfaces for which past droplet size correlations, most notable that of Rose and co-workers (Eq. (3-14)), have been derived[17–19]. Furthermore, SLIPS have been shown to have higher nucleation densities[31] and higher droplet mobility which could potentially shift the droplet number density towards smaller ranges[32]. In addition, the oil lubricant layer has the potential to cloak the condensing droplets, creating a diffusion barrier for water vapor and thus potentially reducing direct condensation and coalescence rates[33]. Hence, to be able to accurately predict dropwise condensation heat transfer rates on LIS or SLIPS surfaces, it is important to experimentally determine an accurate droplet size distribution for this type of surface.

In this work we present experimental measurements of droplet density functions on lubricant-infused surfaces infused with oils of various viscosities (12 – 2717 cSt) and for both cloaking and non-cloaking conditions. We compare our experimental data to the classical Rose correlation for droplet sizes[18]. Finally we integrate our droplet distribution model with the well validated individual droplet heat transfer theory to develop a numerical model of overall surface heat transfer performance. We also discuss the effect of sweeping and droplet mobility on the distribution of droplet sizes on SLIPS and LIS. The work here not only presents the first experimental characterization of condensate droplet distribution on SLIPS and LIS surfaces, it also provides a high fidelity modeling framework for the prediction of condensation heat transfer rates on SLIPS and LIS surfaces that can be extended to other phase change processes such as condensation frosting.

3.2 Materials and Methods

3.2.1. Sample Preparation

Porous surfaces were fabricated using a simple fabrication technique where aluminum is immersed in hot water to create a nano-structured surface (Figure 3.3).[34] First, a polished sheet of aluminum (mirror-like finish, McMaster) of size 1 in x 2 in x 0.05 in was rinsed with acetone, IPA, and deionized (DI) water and blown dry with N_2. Subsequently, the sheet of aluminum was immersed in hot DI-water near its boiling point (≈ 95°C) and was kept there for approximately 15-20 min. The hot water causes a self-limited surface reaction at the aluminum surface to occur, and a thin (≈ 500 nm) boehmite layer is formed, as shown in Figure 3.3c.[16] Once the aluminum sheet cooled down it was treated with air plasma for 1 min to clean the surface from any hydrocarbon contamination and to create free –OH groups at the surface for effective functionalization. To functionalize the surface, Heptadecafluorodecyltrimethoxy-silane (HTMS) was deposited using vapor phase deposition. The cleaned porous surfaces were placed in a container with a vial of 1 mL HTMS toluene solution (5% v/v). A lid was placed on top to seal the container, followed by heating in an atmospheric pressure oven at 80˚C for 3 hours. This process allows for the development of a highly conformal coating as the HTMS molecules evaporate from solution and re-deposit on the porous samples. Contact angle measurements (MCA-3, Kyowa Interface Science Ltd.) of ≈ 300 nL droplets on a HTMS coated smooth silicon wafer showed advancing/receding contact angles of $\theta_A/\theta_R \approx 127 \pm 5.5° / 109 \pm 3.5°$. Once the conformal coating had been applied, the samples were tested for their superhydrophobicity to ensure a high-quality coating was achieved. Contact angle measurements of ≈ 300 nL droplets on a HTMS coated porous aluminum surface showed advancing/receding contact angles of $\theta_A^{app}/\theta_R^{app} \approx 170 \pm 1.5° / 165 \pm 4°$. Finally, the porous boehmite nanostructures were infused with different oils using a spin coating technique at 500-2000 rpm, depending on the viscosity of the oil. Contact angle measurements of ≈ 300 nL droplets on all of the final infused surfaces showed advancing/receding contact angles on of $\theta_A/\theta_R = 122 \pm 2°/118 \pm 2°$.

Table 3.1 lists the lubricant oils with their respective kinematic viscosity, surface tension, and their tendency to cloak. To study the effect of lubricant viscosity on the distribution of droplet sizes, Krytox oils with a wide range of viscosities were used. Due to a positive spreading coefficient with water, the Krytox oils are likely to form a thin oil layer around the individual water droplets, i.e. to cloak them[30,35]. To study the influence of cloaking on the number density of condensing water droplets a non-cloaking Carnation Mineral Oil (Sonneborn LLC) was used.

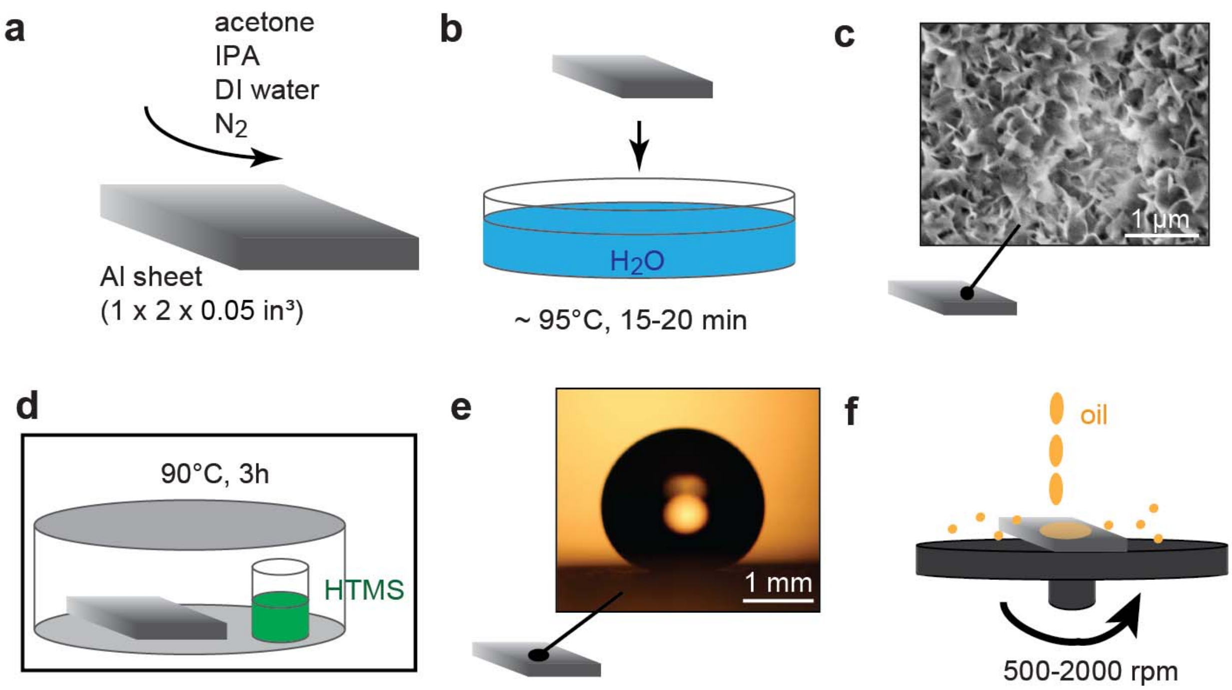

Figure 3.3: Fabrication process of SLIPS. (a) Cleaning of the aluminum sheet, (b) immersion in hot water to form boehmite structures on the surface (c). (d) Vapor phase silane deposition in a furnace to render surface superhydrophobic (e). (f) Oil infusion *via* spin coating at 500-2000 rpm, depending on the viscosity of the oil.

Table 3.1: Lubricant oil properties at room temperature

Name	**Viscosity** ν **[cSt]**	**Surface Tension** γ_{lg} **[mN/m]**	**Cloaking?**
Krytox 16256	2717	19	Yes
Krytox GPL 106	822	18	Yes
Krytox 1514	142	18	Yes [35]
Krytox GPL 100	12	17	Yes
Carnation Mineral Oil	12	28 [16]	No [16]

3.2.2. Experimental Setup and Analysis

Figure 3.4 shows the experimental setup for water condensation on LIS. The sample was attached to a Peltier based thermal plate (TP104SC, Instec), herein called the cold stage, using heat transfer tape (McMaster). The cold stage was connected to a temperature controller (mK2000, Instec) that held the cold plate at 0.05 ± 0.1 °C. A second water bath of DI-water was heated to 73 ± 3 °C using a hot plate. Compressed nitrogen was supplied at the bottom of the second bath water tank at a low flow rate. While rising through the hot water the nitrogen gas saturated with water vapor and was then guided through two thermally insulated 1/4″ pipes to the sample surface. The outlets of the pipes were arranged vertically at a center-center distance of 0.3-0.5 in. The resulting condensation area spanned roughly 1 in horizontally and 0.7 in vertically and represented the top-most area of a vertical pate. All condensation experiments were done in ambient conditions (≈ 23°C, 50% relative humidity). The presence of non-condensable gases (NCGs) was not a concern since steady-state droplet size distribution densities have been shown to be independent of the concentration of NCGs[21]. A Canon T3i camera captured images of the condensing water droplets at 5184 x 3456 pixels, and videos at 60 fps and 1280 x 720 pixels. A telephoto lens (70-300 mm, Sigma) was set to 300mm and infinity focus. To achieve various levels of magnification with a total range of droplet radii from 1 to 1500 μm, a macro lens (DCR-150, Raynox) or a 5x (TU Plan Fluor EPI, Nikon), 10x (TU Plan Fluor EPI, Nikon), 20x (TU Plan Fluor EPI, Nikon), and 50x (TU Plan Fluor EPI ELWD, Nikon) magnification infinity focus microscope lenses with step-down adapters were attached to the regular telephoto lens. Table 3.2 lists the calibration for the different lens combinations for still photographs and videos. For calibration, the outer diameter of a gauge 33 needle or 10 μm Si pillars were measured and compared to the number of pixels within the feature. The sample was illuminated with a LED ring light (LED-144-YK, AmScope). The camera and lens setup were placed on a macro rail and fine linear translation stage (PT1, Thor labs) to allow image focusing. To make focusing easier, the camera was connected to an external monitor. Due to a very shallow depth of focus for high magnification shots, it was crucial to perfectly align the camera to the sample. Any tilt (vertically or horizontally) resulted in droplets that were out of focus and the automated droplet detection software (Matlab) failed.

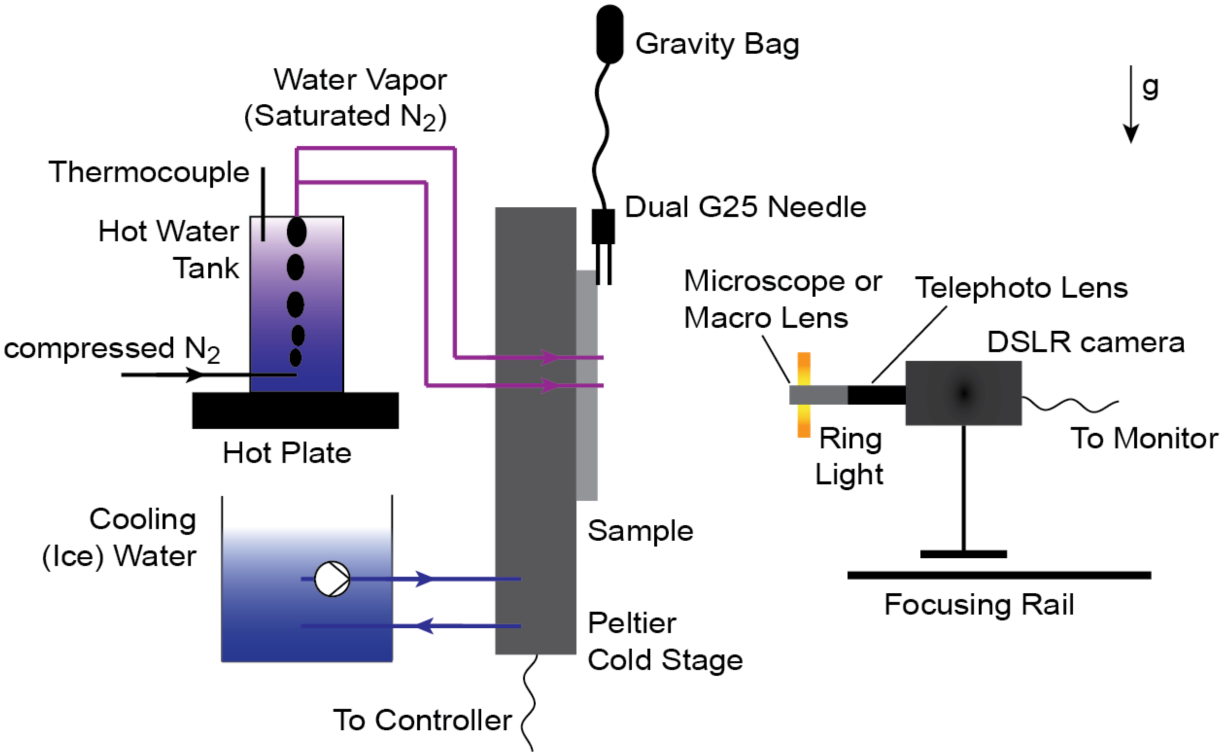

Figure 3.4: Experimental setup. Steam carried by saturated N_2 and supplied to the sample at two vertically stacked locations (diameter tube ¼″, distance between centers 0.3-0.5″) condensed on the sample attached to a Peltier cold stage. A DSLR camera, connected to a monitor to assist focusing, was equipped with a regular 70-300mm telephoto lens and an additional microscope or macro lens. A ring light supplied uniform lighting. A gravity bag and dual needle with gauge 25 simulated high sweeping rates.

Table 3.2: Calibration and resolution of lens setups

lens	resolution photos [µm/pix]	resolution videos [µm/pix]
Raynox macro	3.15	13.07
5x microscope	0.5	2.11
10x microscope	0.26	1.06
20x microscope	0.14	0.616
50x microscope	0.0625	0.255

To simulate higher sweeping rates and to study their effect on the distribution of droplet sizes, additional water droplets were supplied to the sample. A dual twin tip needle with gauge 25 (TS25DSS-1/2, Adhesive Dispensing Ltd) was attached to a gravity bag (Enteral Feeding Gravity Bag, Dynarex) mounted ≈ 1 m above the sample and released individual water droplets ≈ 5 mm above the viewing area. The dispensed droplets would slide down the sample to sweep existing droplets at a rate that was controlled by the flow rate of the water feed. Droplet sweeping rates of 0.3 Hz, 0.6 Hz, and 1.4 Hz were studied.

3.2.3. Uncertainty Analysis

Dropwise condensation is a highly transient and random process. To obtain a steady state representation of the condensation process and distribution of drop sizes a large number of randomly taken photographs can be analyzed and averaged[17,21]. To capture droplets during all stages of a sweeping period and to ensure statistical significance, we captured one image every 10-15 seconds. An exemplary set of randomly timed images for each magnification is shown in Figure 3.5. For the macro lens we analyzed at least 25 images, for the 5x microscope lens at least 50 images and for the 10x and 20x lenses more than 100 images. Videos with a 50x lens were used to determine the nucleation site density of droplets. Droplets were counted in the direct condensation regime after a sweeping event, just before coalescence started, i.e. when droplets in the swept area had a uniform size distribution and were closely packed. The reported values are an average of at least 15 swept areas.

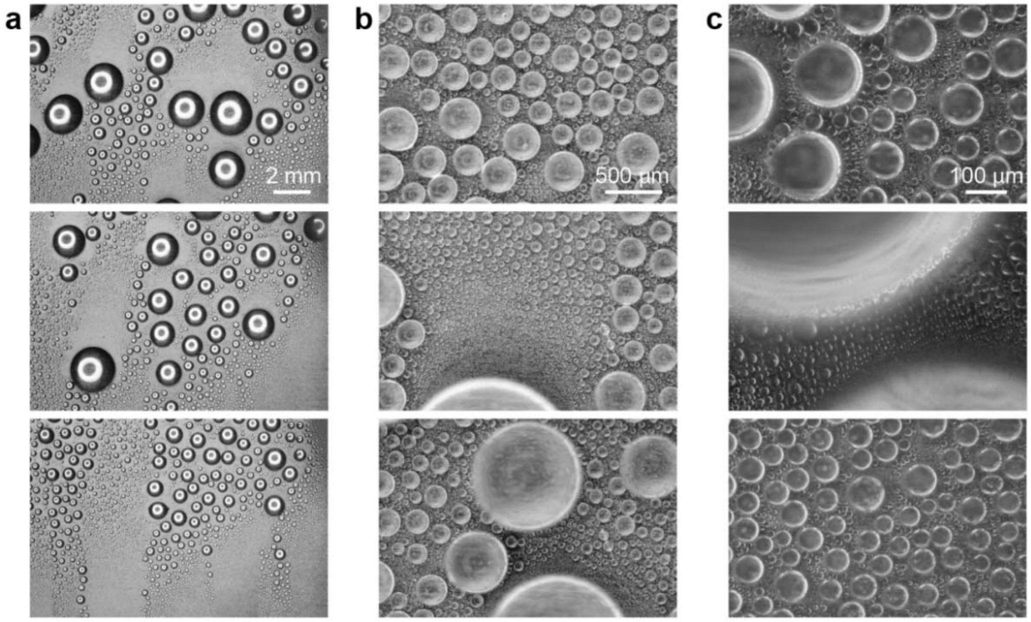

Figure 3.5: Three exemplary transient droplet size distributions with (a) macro lens, (b) 5x, and (c) 20x microscope lens.

Figure 3.6a shows an exemplary set of data with droplet size distributions for 52 measurements with a 5x microscope lens. For small droplets the scatter in data is relatively small. Bigger droplets appear less frequently in randomly taken pictures and scatter is thus larger. Averaging the data from all 52 images gives a uniform steady state droplet size distribution, as shown in Figure 3.6b.

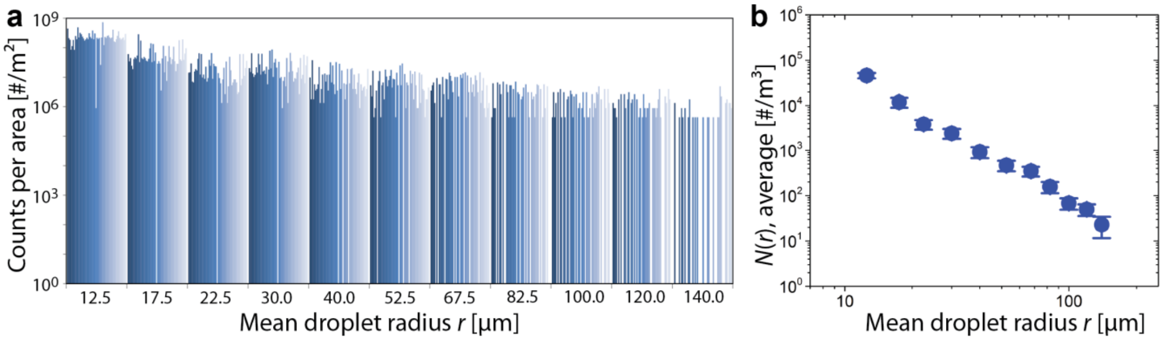

Figure 3.6: Exemplary scattering of droplet size data for a 5x lens measurement on Krytox 16256. (a) Counts per area for 52 individual images for a 5x microscope lens. For small droplets the scatter in data is relatively small. Bigger droplets appear less frequently in randomly taken pictures and scatter is thus bigger. (b) Average droplet size distribution and 95% confidence interval of the 52 measurements shown in (a).

Appendix A lists the Matlab code that was used to detect and analyze the condensing droplets. Briefly, the main body reads all images in a particular folder and then calls a function to detect and analyze all circles, i.e. droplets, in each image. The Matlab function *imfindcircles* is based on a circular Hough transform and detects circles with a radius defined by a given size range in pixels. Here we chose 14 size ranges of increasing size to cover most droplets found in an image. The sensitivity of *imfindcircles* needs to be lower (around 0.94) for smaller circles and higher (around 0.98) for larger circles. It is important to note that the correct sensitivity for each picture set is crucial for accurate determination of droplet sizes. For a too low sensitivity, no droplets are detected. For a sensitivity higher than optimum the function detects false droplets, i.e. over-detects the number of droplets per size range. Through careful analysis of the images and trial runs with individual images the sensitivity of *imfindcircles* could be determined quite accurately and errors were minimized. Since droplets taken with the Raynox macro lens appear black on a lighter background, the object polarity in *imfindcircles* was set to *dark*. Similarly, the droplets taken with the microscope lenses appear bright on a dark background, and a *bright* object polarity was used. Once all droplets have been identified the code checks for overlapping, i.e. over-detected, circles, caused by light- and glare effects on the droplets or a wrong sensitivity. In the case of overlapping or concentric circles the smaller inner circle is deleted. Finally, the number of circles, i.e. droplets, per size range is saved in an excel file.

Figure 3.7 shows three typical images of detected droplets and where the automated detection failed, marked with a red box. The example in Figure 3.7a shows two wrong detections. First, the larger droplet to the left was not detected due to its non-circular shape. The function *imfindcircles* can only detect droplets that perfectly circular, which is true in most cases, especially with the higher magnification microscope lenses. Only few larger droplets taken with the macro lens images appear non-circular. Second, the droplet in the bottom right corner of the red box was detected larger than its actual size, which has been observed infrequently with all lenses. More common errors in droplet detection can be seen in the images b and c of Figure 3.7. As mentioned in section 3.2.2, depth of focus is extremely shallow when using the microscope lenses, and camera and sample have to be perfectly aligned. If the setup is slightly tilted droplets in some area of the image will appear out of focus, i.e. without a clear edge. As a result, *imfindcircles* cannot accurately detect droplets in this area of the image. However, through careful design and realization of the experiments this error can be kept small. The most typical failure mode is shown in Figure 3.7c. When analyzing images taken with the microscope lenses a relatively high sensitivity is required to detect droplets due to poor contrast at the droplet edges. As a result, *imfindcircles* over-detects the smallest droplets where in reality there are none, for example within large droplets (lower box), or many small droplets at the periphery of larger droplets instead of one larger droplet (upper box). However, through manual analysis of randomly chosen images we can conclude that in many cases this over-detection is compensated by a lack of detection of small droplets in areas of poor contrast or focus, or due to shading by larger droplets. Overall, we estimate the error associated with the automated droplet detection to be less than 10%. Lastly, it is worth noting that for the two samples with the very low lubricant viscosity droplet edges were distorted by smaller secondary droplets around the periphery, independent of their tendency to cloaking, as shown in Figure 3.7d. These blurred edges caused the software not to be able to detect droplets, and analysis was performed semi-manually. We did not observe this kind of edge blurring on the other lubricant oils with higher viscosity.

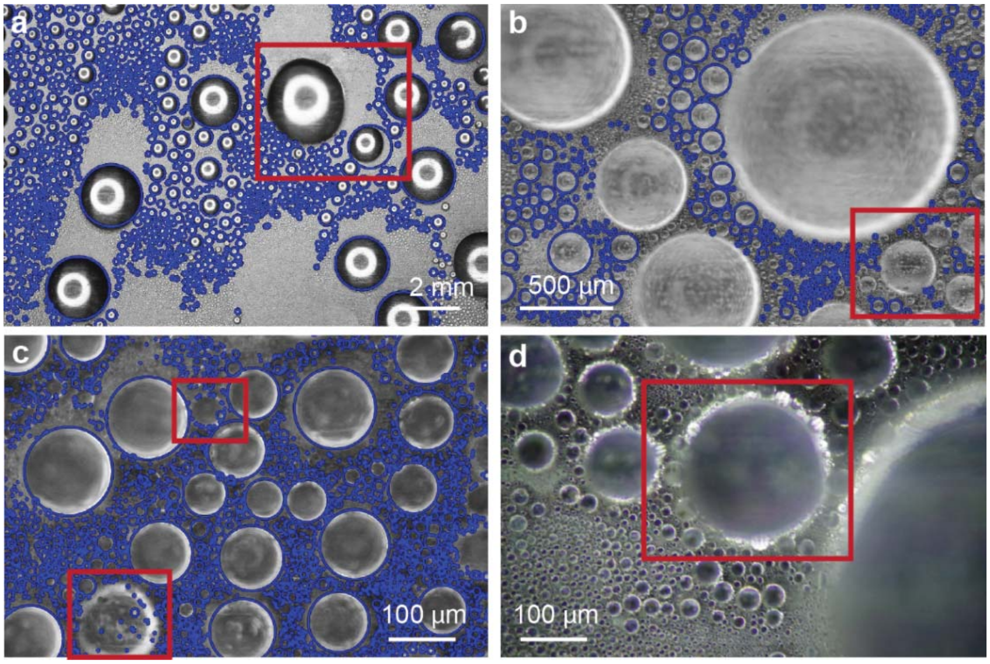

Figure 3.7: Exemplary Matlab droplet detection and failure modes of *imfindcircles* for (a) macro lens, (b) 5x, and (c), (d) 20x microscope lenses. The red squares indicate areas of failed detection.

3.3 Results and Discussion

3.3.1. Natural Droplet Size Distribution

We first measured the average, i.e. steady state, distribution of droplet sizes on all samples (Table 3.1) without artificial sweeping. Figure 3.8 shows the droplet number density $N(r)$ on the five lubricant oils. All data points fall onto the same curve, irrespective of lubricant viscosity or tendency to cloak. It has been shown previously that steady state droplet size distributions are independent of the magnitude of heat transfer[17–19,21]. It can be expected that cloaking influences heat transfer rates, as the oil layer surrounding the water droplet acts as a diffusion barrier to water vapor. However, given the insensitivity of the steady state droplet size distribution on heat transfer rates, the present findings support previous observations of self-similar droplet number densities. The viscosity of the lubricant also does not influence the droplet size distribution of the condensing water droplets. The most predominant effect of lubricant viscosity is the dynamic friction between lubricant and droplet which influences droplet sweeping velocities. However, the droplet size distribution depends mostly on the maximum size that droplets can grow to just before sweeping, and does not depend on the droplet velocity after sweeping. The maximum radius to which a droplet can grow before gravity causes sweeping is independent of the lubricant viscosity. Thus during the direct condensation and coalescence regime, the distribution of droplet sizes is independent of the lubricant viscosity, as well as cloaking. However, we did notice a marked difference in durability when comparing the low and high viscosity lubricants. Low viscosity oils (12 cSt) experienced a relatively fast (~1 hour) depletion from the boehmite structures, irrespective of their tendency to cloak. After two hours of operation, the advancing contact angle of water droplets on the low viscosity oil surfaces increased from ≈ 120° to ≈ 160°, that of non-infused boehmite structures. While the LIS surfaces with lubricants of higher viscosity (> 140 cSt) could be used for many hours (>10 h) without loss of performance, boehmite structures started protruding from the Krytox GPL 100 and Carnation Oil shortly after condensation started. Similar observations of viscosity-dependent oil drainage have been reported previously[36]. Yet, there seems to be little to no effect on the average distribution of drop sizes even after partial depletion.

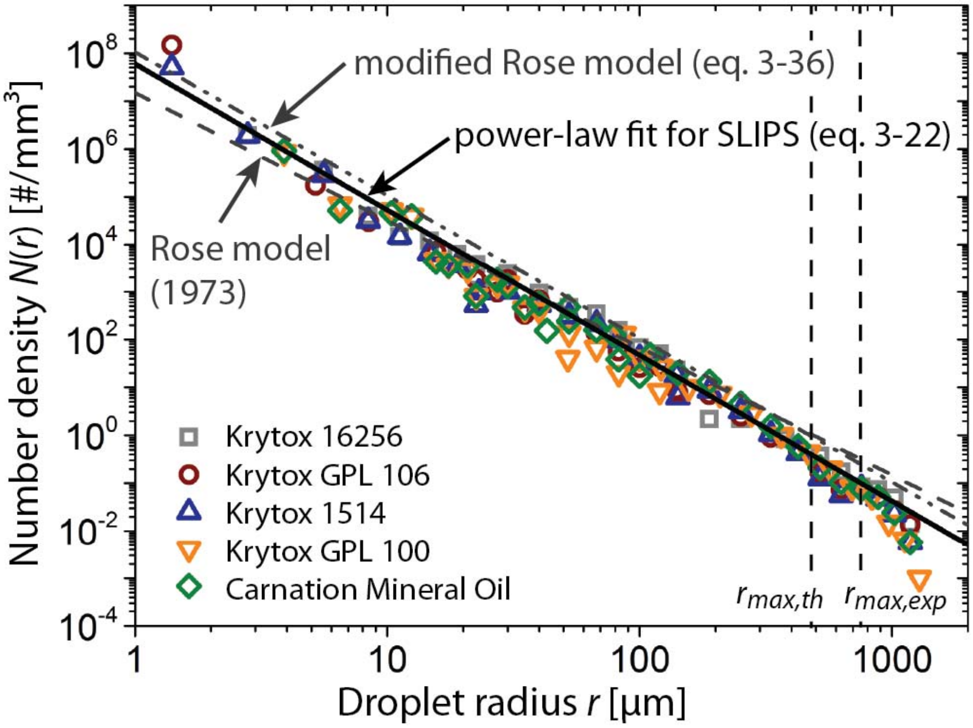

Figure 3.8: Steady state number density, i.e. droplet size distribution, for droplets on all SLIPS surfaces without artificial sweeping. The dotted and dashed lines shows the modified and original number density function by Rose**[18]** with $\hat{r}$ = 0.36 mm, and the solid line shows the fit from Eq. (3-22). The left vertical line shows the theoretical maximum droplet radius, and the right dashed line the experimentally determined radius when droplets begin to slide.

Figure 3.8 also includes Rose's model[18] (Eq. (3-14)) with $\hat{r}$ = 0.36 mm. Our experimental data points agree well with the Rose model, especially in the range $10 < r < 200$ μm, irrespective of the lubricant oil. For $r < 10$ μm, the Rose model slightly underestimates the observed number density of condensing droplets. A possible reason for the discrepancy is the number of nucleation sites. While Rose and co-workers[17,22] used values up to $N_s = 2\times10^{12}$ m^{-2} with $r_e \approx 400$ nm to validate their results, we observe nucleation site densities of approximately $N_s \approx 1\text{-}5\times10^{11}$ m^{-2} with $r_e \approx 0.8\text{-}1.4$ μm. To better account for the higher number of small droplets, we can describe the number density function for droplets on LIS as:

$$N(r) = a\, r^{-b}\ . \tag{3-22}$$

The constants can be determined from a fit to all data points, as shown in Figure 3.8. For $[r]$ = µm, we find that $a = 6\times10^{7}$, and $b = 3.05$, where the unit of a is such that $[N(r)] = 1/\mathrm{mm}^3$. Note that b is slightly higher than most previously found exponents, which are generally between 2.6 and 2.7.[19,21,26] The appearance of larger droplets is slightly overestimated by the Rose model, however, droplets in this size range ($r > 100$ µm) negligibly participate in the overall heat transfer process due to their increased thermal conduction resistance[17]. Thus, for heat transfer modeling purposes, this overestimation is not critical and can be ignored. Figure 3.8 also shows the theoretical and experimental maximum droplet radius at the onset of sliding. While theoretical estimation of the maximum departure radius using Eq. (3-13) yields $r_{\mathrm{max,th}} = 0.46$ mm, we did not observe droplet sliding before droplets reached $r_{\mathrm{max,exp}} = 0.7 - 0.8$ mm. The discrepancy between model and experiment arises from 1) simplifications made in the development of the theoretical model governing Eq. (3-13) (ideal contact line, constant contact angle hysteresis, continuous shape of the contact line – oval, circle), and 2) edge effects at the three-phase contact line of LIS surfaces where the lubricant oil forms a meniscus at the water interface and increases its adhesion force[33,37].

Although not a factor in the droplet distribution results and hence inconsequential to the overall surface heat transfer for the viscosities tested here, the velocity of droplet sliding down the surface was inversely proportional to the viscosity of the lubricant oil used, in agreement to previously reported studies. Figure 3.9 shows the evolution of droplet location for all lubricant oils. While the steady sliding velocity on Krytox 16256 ($\nu = 2712$ cSt) was only $v = 1.30$ mm/s, the droplet speed on Krytox 1514 ($\nu = 142$ cSt) was $v = 1.91$ mm/s and increased to $v = 55.3$ mm/s on Krytox GLP100 ($\nu = 12$ cSt). Note however, although the infused oil viscosities tested here (12 – 2717 cSt) had no effect on the droplet distribution, this may not always be the case. One can imagine if the oil viscosity is so high that the sliding velocity of departing droplets is impeded, that flooding of the surface with large conduction limited droplets might occur.

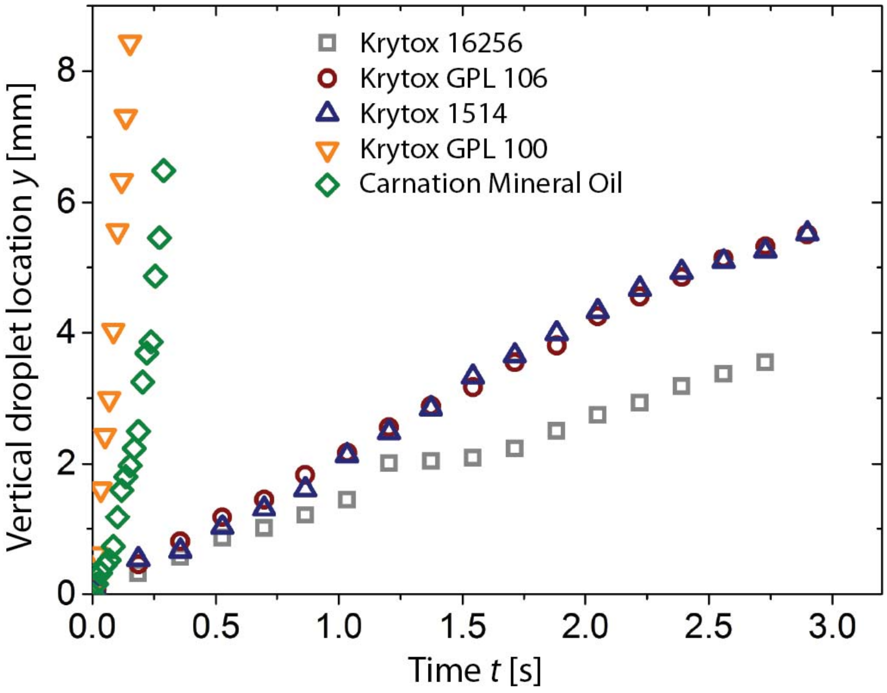

Figure 3.9: Droplet sliding for water droplets on the different lubricants. Initial droplet sizes and resulting sliding velocities were $r_{0,\text{K-16256}}$ = 0.83 mm / $v_{\text{K-16256}}$ = 1.3 mm/s, $r_{0,\text{GPL106}}$ = 0.97 mm / v_{GPL106} = 1.90 mm/s, $r_{0,\text{K-1514}}$ = 0.95 mm / $v_{\text{K-1514}}$ = 1.91 mm/s, $r_{0,\text{GPL100}}$ = 0.77 mm/ v_{GPL100} = 55.3 mm/s, and $r_{0,\text{Carnation}}$ = 1.08 mm / $v_{\text{Carnation}}$ = 22.5 mm/s, respectively.

3.3.2. Heat Transfer and Sweeping Modeling

To quantify the influence of sweeping on average heat transfer rates, and to bring the present results into context, we developed a numerical model. The model determines sweeping rates f_{cycle}, maximum radius of sweeping droplets r_{sw}, maximum radius to which droplets grow before being swept r_{s}, and heat transfer rates q'' as a function of plate height y (maximum height L = 1m). Figure 3.10 shows a schematic of the numerical model. First, we assume that all falling, i.e.

sweeping droplets, originate at the top of the plate[22], and that droplets with $r = r_{\max}$ are distributed evenly within this top region. The average area coverage of these larger droplets is $\eta \approx 82\%$, as derived from the data presented in section 3.3.1. We can then discretize the width of the plate into individual slots of width $B = 2r_{\max}/\eta$ (here: B = 1.12 mm), containing one droplet with $r = r_{\max}$ each. When droplets slide down the vertical plate they absorb smaller droplets ahead of them and grow in size. Assuming that the shape and contact angles of a sliding droplet are constant, the radius at location y becomes

$$r_{sw}(y) = V(y)^{1/3} \cdot g(\theta_e), \tag{3-23}$$

where $g(\theta_e)$ is a geometric factor relating the contact angle to the volume of the droplet. For a spherical cap:

$$g(\theta_e) = \left(\frac{\pi/_3\,(2+\cos(\theta_e))(1-\cos(\theta_e))^2}{sin^3(\theta_e)}\right)^{1/3} . \tag{3-24}$$

We further assume that the droplet size distribution $N(r)$ follows Rose's model with $\hat{r}(y) = r_s(y)/1.3$ everywhere on the plate, and that it has a continuous boundary condition with $n(r)$ at r_e (here: r_e = 1.58 μm), and that no flooding occurs at the bottom of the plate due to accumulation of sweeping droplets.

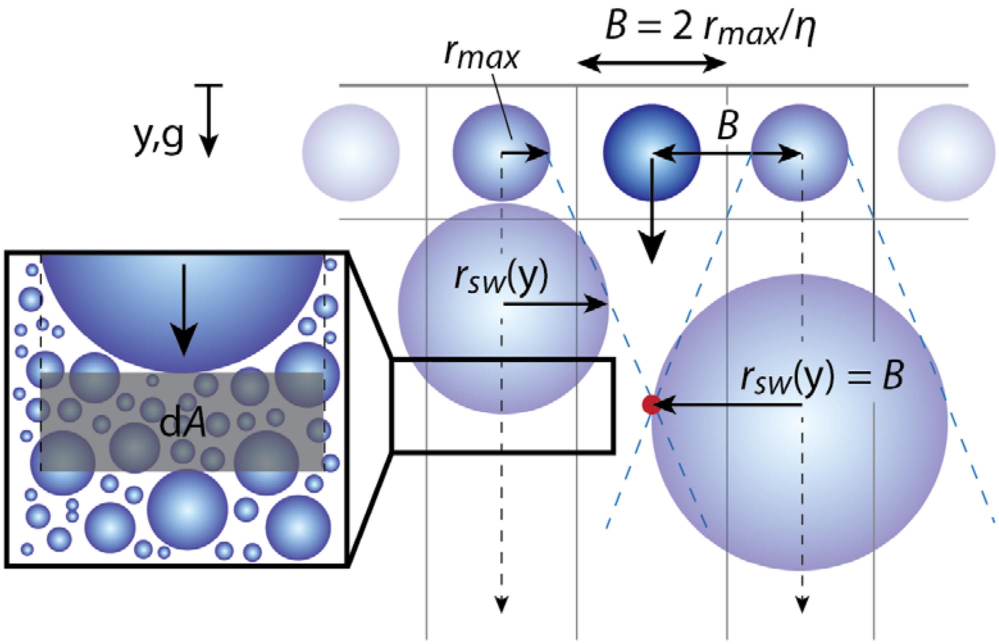

Figure 3.10: Schematic for numerical sweeping model. Droplets grow to $r_{\max}$ in the top-most region of the plate and are equally distributed within slots of width B. When droplets slide down the vertical plate they sweep areas in neighboring slots. Sweeping cones are marked with the blue dotted lines. At some point y down the plate (red dot) where $r_{sw}(y) = B$ the condensing droplets get swept three times as often as at the top of the plate: once from droplet originating within the same slot, and twice from sliding droplets from the two neighboring slots. The same principle applies further down the plate, with droplets from other slots sweep the area. Per integration step droplets sweep an area $dA = dL \cdot 2r_{sw}(y)$ that contains droplets with a droplet size distribution following eqs. (3-14) and (3-15) with $r_{\max}(y) = r_s(y)$.

To model sweeping rates as a function of plate height we first need to determine the steady state, i.e. average heat transfer and mass transfer rates at the top of the plate to define a characteristic time for dropwise condensation, t_{ch}. Using the latent heat of condensation, Δh_{fg}, we can write:

$$q''_{tot} = \frac{m''}{t_{ch}} \Delta h_{fg}\,, \tag{3-25}$$

where q''_{tot} is described by Eq. (3-12), and m'' is the area-normalized average mass of the condensed droplets. The mass of all condensed droplets can be described using the droplet size distribution:

$$m'' = \rho_l\left(\int_{r_{min}}^{r_e} V(r)n(r)dr + \int_{r_e}^{r_{max}} V(r)N(r)dr\right), \tag{3-26}$$

where $V(r) = (r\, g(\theta_e))^3$. Note that the upper bound on the second integral is $r_{\max}$ as opposed to $\hat{r}$, that is typically used for the calculation of the heat flux. For condensation in a pure water vapor environment at T_{sat} = 100°C and ΔT = 5 K, the characteristic time is $t_{ch} = t_{cycle}(y = 0) = 2.05$ s, which is in good agreement with previous experimental results on transient dropwise condensation[21,38].

To determine the sweeping rates and heat transfer along the plate for $y > 0$ we can discretize the plate into rows of height dL (here: dL = 10mm for L = 1 m). A sweeping droplet absorbs all smaller droplets in the area dA = dL $2r_{sw}(y)$ ahead of it. Thus, the volume of the sweeping droplet increases as

$$V(y) = V(y-1) + dV\,, \tag{3-27}$$

where

$$dV = \left(\int_{r_{min}}^{r_e} V(r)n(r)dr + \int_{r_e}^{r_s(y)} V(r)N(r)dr\right)dA\,. \tag{3-28}$$

The new radius of the sweeping droplet can be calculated using Eq. (3-23). Again, note the upper bound in the second integral. To calculate the maximum size to which droplets can grow before being swept, $r_s(y)$, we first need to determine the sweeping cycle time, or sweeping period, t_{cycle}. If $n_s(y)$ is the number of sweeping events within the characteristic time period t_{ch}, then we can write

$$t_{cycle} = \frac{t_{ch}\,\cdot}{n_s} \tag{3-29}$$

From geometric considerations, we can see that for $y > 0$

$$n_s = 1 + 2\frac{r_{sw}(y)}{B}\,. \tag{3-30}$$

The red dot in Figure 3.10 illustrates this relationship. The first term on the right hand side of Eq. (3-30) stems from the sweeping droplet originating at the top of the same slot in which the red dot is located. For an imaginary position at the center of a slot (red dot), the droplets from the neighboring slots will each cause a sweeping event at the red dot when $r_{sw} = B$, and n_s becomes $n_s = 3$. Even further down the plate droplets from the slots next to the neighboring slots will also sweep the center slot, such that when $r_{sw} = 2B$, $n_s = 5$. Since we assume that r_{sw} is only a function of y (i.e. sweeping droplets in all slots behave the same), this progressive series of sweeping events gives rise to the second term on the right hand side of Eq. (3-30).

Last, but not least, we can calculate the radius to which droplets can grow in between sweeping cycles, assuming that sweeping originates at uniform time intervals at the top of the plate. Using a definition similar to Eq. (3-25), we can write:

$$t_{cycle}(y) = \frac{m''(y)}{q''(y)}\Delta h_{fg} = \frac{\rho_l\left(\int_{r_{min}}^{r_e} V(r)n(r)dr + \int_{r_e}^{r_s(y)} V(r)N(r)dr\right)}{\int_{r_{min}}^{r_e} q_d(r)n(r)dr + \int_{r_e}^{r_s(y)/1.3} q_d(r)N(r)dr}. \qquad (3\text{-}31)$$

Numerically, through an iterative method, we can now solve for $r_s(y)$. Finally, we can calculate the heat transfer as a function of plate height using the formula given in the denominator of Eq. (3-31). The Matlab code for above calculations is included in Appendix B.

Figure 3.11 shows the results for the sweeping radius r_{sw}, the maximum droplet radius before sweeping r_s, the cycle period t_{cycle}, and the normalized steady-state heat transfer rate as a function of plate height. As the sweeping droplets slide down the surface they collect and absorb smaller droplets and grow in size. At the same time the cycle period, and thus size to which droplets grow through direct condensation and coalescence before being swept, decrease. It is important to note that this decrease happens quickly over the first 10-20 cm of the plate and then approaches a constant around $t_{cycle} \approx 0.5$ s and $r_s \approx 0.1$ mm, respectively. Similar trends have been reported before where the sweeping period was nearly constant for large distances ($y/(2r_{\mathrm{max},0}) \geq 40$) away from the top of the plate[39]. Despite the strong decrease in maximum droplet size heat transfer rates decrease only minimally. Even at the bottom of the 1m tall plate the heat transfer rate has decreased by only 7.5% compared to the top of the plate. The reason for this small decrease is the relative insensitivity of droplets with $r > 100$ µm on overall heat transfer rates[17,18]. At $L = 1$ m the largest droplets in the condensation distribution, r_{s}, are only slightly smaller than this cut-off, resulting in only a small decrease in heat transfer. Indeed, it has been observed before that heat transfer rates are nearly constant over the length of a vertical plate[18,22]. While nucleation sites get cleared more frequently and we observe many small droplets on those areas, sweeping droplets have a blanketing effect on significant parts of the surface such that the two contributions cancel each other out and average, steady-state heat transfer rates are nearly constant. Similar to the heat transfer rates, the distribution of droplets sizes is hardly influenced by increased sweeping rates at the bottom of the plate. All of the above equations are independent of droplet sliding speed, and we do not expect a variation in average droplet sweeping and heat transfer rates for varying lubricant viscosities. The only difference between the various lubricant oils would be the time a sweeping droplet needs to reach the bottom of the plate, which is irrelevant for a steady-state solution and a discretization in space, not time.

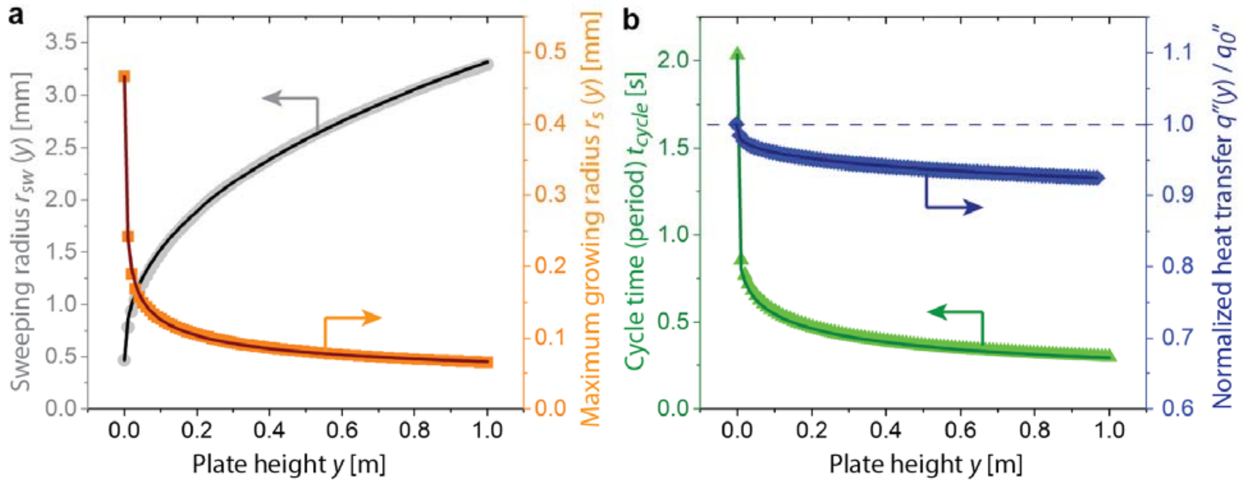

Figure 3.11: Sweeping and heat transfer predictions for a tall vertical plate. (a) Predicted sweeping radius r_{sw} and radius to which droplets grow before being swept r_s as a function of plate height for 100% water vapor environment at T_{sat} = 100°C and ΔT = 5K. (b) Sweeping cycle time, or sweeping period, t_{cycle} and heat transfer rate normalized to the average heat transfer rate at the top of the plate as a function of plate height for the same conditions. For all parameters, results from numerical simulations are depicted as points and analytical fits as lines.

To facilitate estimations of droplet sizes, sweeping periods, and heat transfer rates at vertical plate, Figure 3.11 also includes analytical fits. Fitting to the numerical output, we can write for the radius of the sweeping droplets as a function of plate height:

$$r_{sw} = r_{max,0} + 2.85 \cdot 10^{-3}\, y^{0.43}\,, \tag{3-32}$$

where $y = 0$ is the top of the vertical plate and $r_{max,0}$ is the maximum droplet radius at the top of the plate. The maximum droplet radius to which droplets grow before being swept can be written as:

$$r_s = 6.6 \cdot 10^{-5}\, y^{-0.28}\,. \tag{3-33}$$

The sweeping period can well be estimated using Eqs. (3-29), (3-30), and (3-32). The resulting average heat transfer rates as a function of plate height can be described by:

$$q''(y) = q_0''\left(1 - 0.075\, y^{0.29}\right), \tag{3-34}$$

where $q_0'' = 2.4 \cdot 10^5$ W/m² is the heat transfer rate at the top of the plate for pure water vapor conditions, assuming Rose's model for the distribution of drop sizes.

3.3.3. Experimental Heat Transfer Estimation

Average heat transfer rates for the present condensation experiments with non-condensable gases can be estimated from a time-evolution of the distribution of droplet sizes. Figure 3.12 shows the evolution of condensing and coalescing droplets on a Krytox 1514 oil within one sweeping cycle (here: $t_{\text{cycle}} = 20$ s). Discretizing the cycle period into 63 time steps, we estimate the heat transfer rate averaged over the sweeping period to $q_{exp}'' = 5.22 \cdot 10^4$ W/m². Theoretically, using eqs. (3-25) and (3-26) along with Eq. (3-22) and the experimentally observed cycle time, the average heat transfer would be $q'' = 4.3 \cdot 10^4$ W/m². Despite the fact that the subcooling temperature in the present experiments is unknown, the experimentally determined value is in excellent agreement with the theoretically predicted heat transfer rate, giving us confidence in the validity of the theoretical model presented in section 3.3.2.

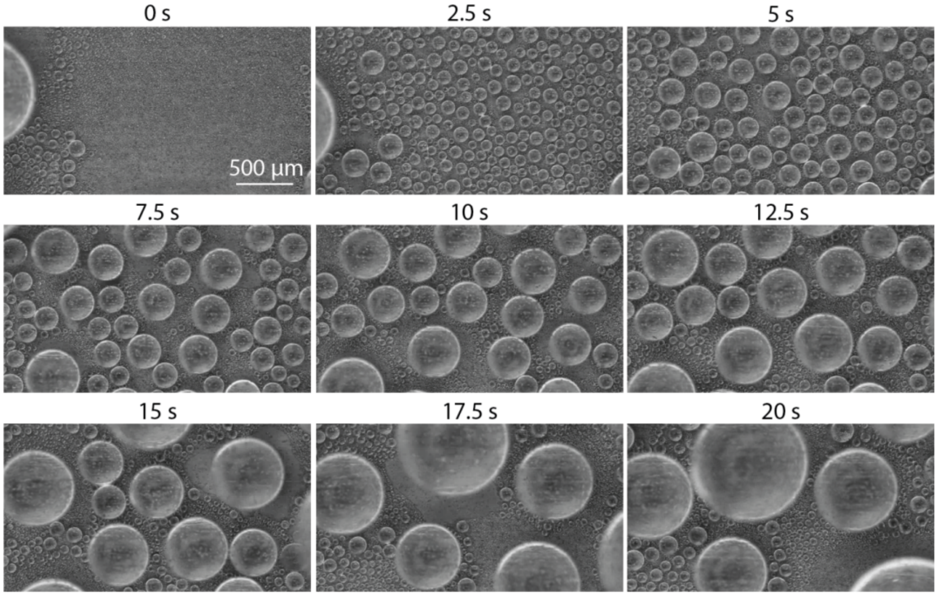

Figure 3.12: Time evolution of droplet condensation for the estimation of heat transfer rates with a time step of 2.5 s each on a Krytox 1514 lubricant oil with the 5x microscope lens.

3.3.4. Droplet Size Distribution with Artificial Sweeping

To experimentally verify the influence of sweeping on the distribution of droplet sizes we performed additional experiments with artificial sweeping where droplets were injected with a needle above the condensation area. Natural average sweeping periods through condensation and coalesces ranged from 9 to 24 s, as defined by the number of droplets sweeping through a specific spot in a 2 minute period, depending on the flow rate of the humid nitrogen gas. Slow, medium, and fast artificial periods were 2.9, 1.8, and 0.7 s, respectively. Figure 3.13 shows the droplet number densities $N(r)$ on the Krytox 1514 oil for the natural, slow, medium, and fast sweeping rates. As expected from numerical modeling presented in section 3.3.2, the time-averaged distribution of droplet sizes is independent of sweeping frequency. At the same time, we observe a strong decrease in the maximum diameter to which droplets grow before being swept. While droplets during natural sweeping at the top of a vertical plate grow to $r_s = r_{max}$ = 0.7-0.8 mm, this value decreases to r_s = 0.5-0.6 mm for the slow and medium sweeping rates and to $r_s \approx 0.25$ mm in the case of fast artificial sweeping, as illustrated in Figure 3.13. Our data suggest that the distribution of droplet sizes on SLIPS is not a function of the maximum droplet size. Indeed, when fitting Rose's model for the distribution of droplet sizes (Eq. (3-14)) to our data (Figure 3.8) by adjusting the exponent, we find the best agreement between data and model for an exponent of negative unity, i.e.

$$N(r) = \frac{1}{3\pi r^2 \hat{r}} \left(\frac{r}{\hat{r}}\right)^{-1}. \qquad (3\text{-}35)$$

We see that the dependence of the maximum droplet size, $\hat{r} \approx r_s / 1.3$, cancels out, and we are left with

$$N(r) = \frac{1}{3\pi r^3}. \qquad (3\text{-}36)$$

Equation (3-36) is independent of the maximum droplet radius. Comparison with the power-law fit from this work reveals strong similarities between the exponent, b = -3.05, from Eq. (3-22), and the droplet size dependence in the modified Rose model (Eq. (3-36)). In fact, Eq. (3-14) was first derived as $N(r) \sim r^{m-3}$, where m was determined experimentally to m = 1/3.[18,19,40,41] In the present study on super-slippery surfaces, we find that $m \approx 0$. The independence of the distribution of droplet sizes on the maximum droplet size before sweeping can also be explained with the self-similarity of droplet sizes on various magnification levels[18]. When small droplets nucleate, condense and coalesce, they are not yet influenced by the size to which they will eventually grow before sweeping. Thus, also conceptually, we do not expect the size distribution of small droplets to differ for various sweeping periods and maximum drop sizes.

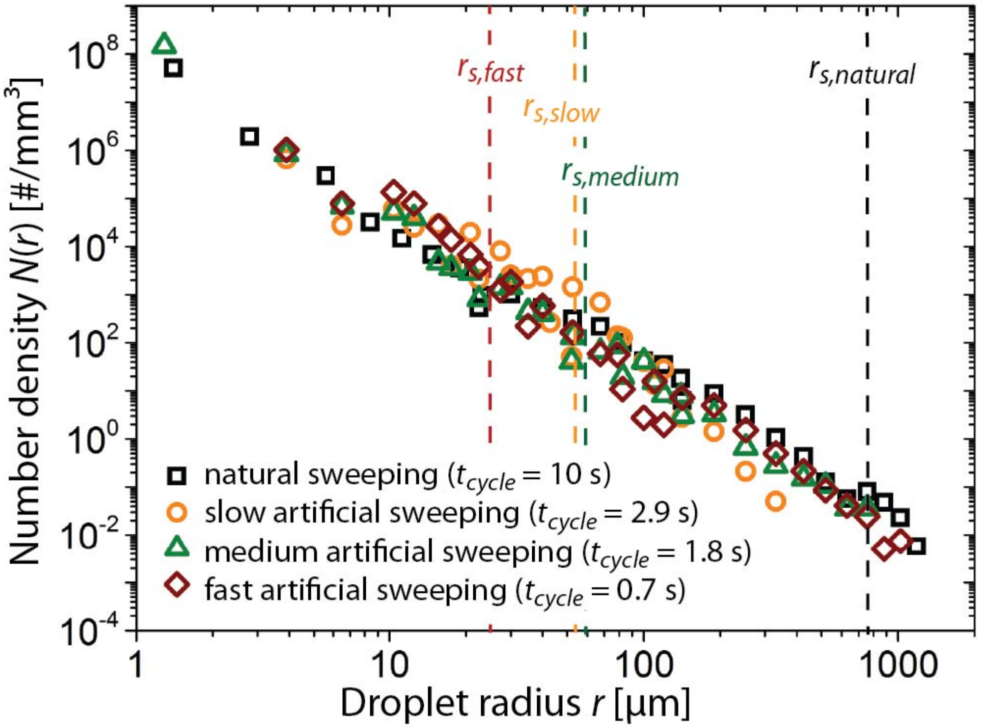

Figure 3.13: Steady state number density, i.e. droplet size distribution, for droplets on the Krytox 1514 oil with artificial sweeping. The time-averaged distribution of droplet sizes is independent of sweeping frequency for small droplets. The dashed lines represent the size to which droplets grow before being swept.

3.3.5. Overall Surface Condensation Heat Transfer

To elucidate the effects of the newly identified droplet distribution results on LIS, or SLIPS, to overall surface heat transfer, we combined the experimental droplet distribution results with individual droplet heat transfer to predict an overall LIS heat transfer performance. Following Eq. (3-12) we can now compare the heat transfer rates following the distribution of droplet sizes for LIS, as derived in the present work (Eq. (3-22)), and with those following the Rose model (Eq. (3-14)). The black curve in Figure 3.14 shows the comparison as a function of coating thickness. Due to the underestimation of small droplet sizes in the Rose model, with the new distribution of droplet sizes on LIS we expect heat transfer rates to almost double compared to previous predictions.

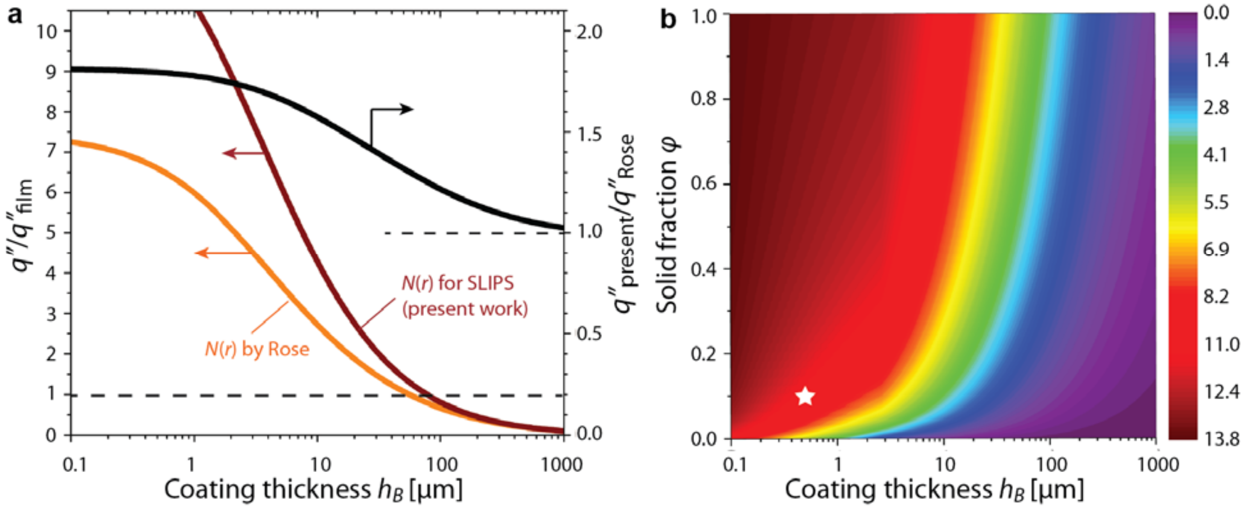

Figure 3.14: Comparison of heat transfer rates for filmwise and dropwise condensation with droplet size distributions following the Rose model (Eq. (3-14)) and the distribution for LIS, as presented here (Eq. (3-22)). (a) Influence of the coating thickness h_B on the relative heat transfer rates for a solid fraction $\varphi = 0.1$. (b) Coupling of coating thickness and solid fraction of the microstructures on dropwise condensation heat transfer rates on LIS (Eq. (3-22)) compared to filmwise condensation on bare substrates at a plate height $y = 10$ cm and $\Delta T_{\text{tot}} = 5$K. The white star marks the parameters of the present study.

In relation to filmwise condensation on bare substrate, the promotion of dropwise condensation on lubricated surfaces adds a thermal resistance between substrate and vapor: the coating. Following Nusselt's theory for laminar filmwise condensation on a bare substrate we can write[42]:

$$q''_{film} = \left(\frac{\Delta h_{fg} g(\rho_l - \rho_v) k_l^3}{4y\Delta T_{tot} \upsilon_l}\right)^{1/4} \Delta T_{tot}\,, \tag{3-37}$$

where ρ_v is the vapor density and υ_l is the liquid kinematic viscosity. To determine the effectiveness of lubricant-infused surfaces on overall heat transfer rates, we compare the heat transfer rates during dropwise condensation with those for filmwise condensation as a function of coating thickness h_B and solid fraction φ (Figure 3.14). For a solid fraction of $\varphi \approx 0.1$, LIS enhance heat transfer rates for coating thicknesses up to $h_B < 80$ µm. Especially for very thin coatings, such as boehmite ($h_B \approx 0.2$-2 µm),[43] we expect heat transfer enhancements on the order of 10-15 compared to traditional filmwise condensation. Within the realm of possible solid fractions ($\varphi \approx 0.1$-0.7) their influence on heat transfer enhancement is minimal. The most important design parameter for the microstructured surface is the coating thickness, as it greatly affects the surface thermal resistance. From a thermal perspective, the thickness of the porous surface structures should be minimized. As a trade-off, such minimization might reduce possible self-healing effects of LIS surfaces[44]. Ultimately, it will be the designers' choice to optimize the surfaces for specific applications. Here we provide an analytical and experimental framework to assist the thermal engineering in designing lubricant-infused surfaces for dropwise condensation heat transfer applications.

3.4 Conclusions

This chapter presented experimental and numerical results on the distribution of droplet sizes and the influence of sweeping on heat transfer rates for water dropwise condensation on lubricant-infused surfaces. Using statistical averaging of droplet densities to determine steady-state droplet size distributions and analytical-numerical modeling, we found that:

1) The average distribution of droplet sizes is independent of lubricant viscosity and follows the Rose model well, but underestimates the number of small droplets ($r < 10$ μm). With Eq. (3-22) we propose an alternative fit that accounts for a larger number of observed droplets at small sizes ($r < 10$ μm): $N(r) = 6\times10^{7}\, r^{-3.05}$ mm^{-3}.
2) Surfaces with the low-viscosity oils ($\nu = 12$ cSt) degraded quickly and the lubricant drained, whereas those surfaces with higher viscosity ($\nu > 140$ cSt) remained stable for > 10 hours of operation. We thus recommend using oils with $\nu > 100$-200 cSt for water condensation on LIS.
3) The experimentally determined droplet sizes for the onset of sliding are almost twice as large as theoretically predicted ($r_{\text{max,ex}} = 750$ μm vs. $r_{\text{max,th}} = 460$ μm). We propose that edge effects at the meniscus of the three-phase contact line between the oil, water, and air increase the droplet sliding resistance.
4) Artificial sweeping through droplet injection can represent increased sweeping rates on large vertical plates. The maximum size to which droplets grow before being swept decreases rapidly with only a modest decrease in sweeping period. While $r_{\text{s}} = r_{\text{max}} \approx 750$ μm with natural sweeping ($t_{\text{cycle}} = 9$-24 s), $r_{\text{s}} \approx 62$ μm for slow and medium artificial sweeping rates ($t_{\text{cycle}} \approx 1$-$2$ s).
5) While the maximum size to which droplets grow *via* condensation and coalescence decreases with increasing sweeping rates and distance from the top of a vertical plate, the distribution of droplet sizes and heat transfer rates remain fairly constant throughout the

height of a vertical plate. Due to a large conduction resistance through the liquid, only droplets with $r < 100$ μm actively participate and influence the heat transfer process.

6) The most important design parameter for LIS is the coating thickness; coating thicknesses of ≈ 0.5-5 μm can increase heat transfer rates up to 10-15 times compared to traditional filmwise condensation.

Overall, this work presents new insights into the characteristics of dropwise condensation on lubricant infused surfaces and provides a framework for analytical modeling and estimation of heat transfer on large vertical plates.

3.5 References

(1) Nørgaard, T.; Dacke, M. Fog-Basking Behaviour and Water Collection Efficiency in Namib Desert Darkling Beetles. *Front. Zool.* **2010**, *7*, 23.

(2) Malik, F. T.; Clement, R. M.; Gethin, D. T.; Beysens, D.; Cohen, R. E.; Krawszik, W.; Parker, A. R. Dew Harvesting Efficiency of Four Species of Cacti. *Bioinspir. Biomim.* **2015**, *10*, 36005.

(3) Paxson, A. T.; Yagüe, J. L.; Gleason, K. K.; Varanasi, K. K. Stable Dropwise Condensation for Enhancing Heat Transfer via the Initiated Chemical Vapor Deposition (iCVD) of Grafted Polymer Films. *Adv. Mater.* **2014**, *26*, 418–423.

(4) Yang, K.-S.; Yang, T.-Y.; Tu, C.-W.; Yeh, C.-T.; Lee, M.-T. A Novel Flat Polymer Heat Pipe with Thermal via for Cooling Electronic Devices. *Energy Convers. Manag.* **2015**, *100*, 37–44.

(5) Rao, Z.; Wang, S.; Wu, M.; Lin, Z.; Li, F. Experimental Investigation on Thermal Management of Electric Vehicle Battery with Heat Pipe. *Energy Convers. Manag.* **2013**, *65*, 92–97.

(6) Nada, S. A.; Elattar, H. F.; Fouda, A. Experimental Study for Hybrid Humidification–dehumidification Water Desalination and Air Conditioning System. *Desalination* **2015**, *363*, 112–125.

(7) Sathyamurthy, R.; El-Agouz, S. A.; Dharmaraj, V. Experimental Analysis of a Portable Solar Still with Evaporation and Condensation Chambers. *Desalination* **2015**, *367*, 180–185.

(8) Seo, D.; Lee, J.; Lee, C.; Nam, Y. The Effects of Surface Wettability on the Fog and Dew Moisture Harvesting Performance on Tubular Surfaces. *Sci. Rep.* **2016**, *6*, 24276.

(9) Schmidt, E.; Schurig, W.; Sellschopp, W. Versuche über die Kondensation von Wasserdampf in Film- und Tropfenform. *Tech. Mech. Thermodyn.* **1930**, *1*, 53–63.

(10) Rose, J. W. Dropwise Condensation Theory and Experiment: A Review. *Proc. Inst. Mech. Eng. Part J. Power Energy* **2002**, *216*, 115–128.

(11) Miljkovic, N.; Wang, E. N. Condensation Heat Transfer on Superhydrophobic Surfaces. *MRS Bull.* **2013**, *38*, 397–406.

(12) Ölçeroğlu, E.; Hsieh, C.-Y.; Rahman, M. M.; Lau, K. K. S.; McCarthy, M. Full-Field Dynamic Characterization of Superhydrophobic Condensation on Biotemplated Nanostructured Surfaces. *Langmuir* **2014**, *30*, 7556–7566.

(13) Attinger, D.; Frankiewicz, C.; Betz, A. R.; Schutzius, T. M.; Ganguly, R.; Das, A.; Kim, C.-J.; Megaridis, C. M. Surface Engineering for Phase Change Heat Transfer: A Review. *ArXiv14095363 Cond-Mat* **2014**.

(14) Enright, R.; Miljkovic, N.; Alvarado, J. L.; Kim, K.; Rose, J. W. Dropwise Condensation on Micro- and Nanostructured Surfaces. *Nanoscale Microscale Thermophys. Eng.* **2014**, *18*, 223–250.

(15) Rykaczewski, K.; Paxson, A. T.; Staymates, M.; Walker, M. L.; Sun, X.; Anand, S.; Srinivasan, S.; McKinley, G. H.; Chinn, J.; Scott, J. H. J.; *et al.* Dropwise Condensation of Low Surface Tension Fluids on Omniphobic Surfaces. *Sci. Rep.* **2014**, *4*.

(16) Park, K.-C.; Kim, P.; Grinthal, A.; He, N.; Fox, D.; Weaver, J. C.; Aizenberg, J. Condensation on Slippery Asymmetric Bumps. *Nature* **2016**, *531*, 78–82.

(17) Graham, C.; Griffith, P. Drop Size Distributions and Heat Transfer in Dropwise Condensation. *Int. J. Heat Mass Transf.* **1973**, *16*, 337–346.

(18) Rose, J. W.; Glicksman, L. R. Dropwise condensation—The Distribution of Drop Sizes. *Int. J. Heat Mass Transf.* **1973**, *16*, 411–425.

(19) Tanaka, H. Measurements of Drop-Size Distributions During Transient Dropwise Condensation. *J. Heat Transf.* **1975**, *97*, 341.

(20) Kim, S.; Kim, K. J. Dropwise Condensation Modeling Suitable for Superhydrophobic Surfaces. *J. Heat Transf.* **2011**, *133*, 081502–081502.

(21) Watanabe, N.; Aritomi, M.; Machida, A. Time-Series Characteristics and Geometric Structures of Drop-Size Distribution Density in Dropwise Condensation. *Int. J. Heat Mass Transf.* **2014**, *76*, 467–483.

(22) Rose, J. W. Further Aspects of Dropwise Condensation Theory. *Int. J. Heat Mass Transf.* **1976**, *19*, 1363–1370.

(23) Miljkovic, N.; Enright, R.; Wang, E. N. Modeling and Optimization of Superhydrophobic Condensation. *J. Heat Transf.* **2013**, *135*, 111004–111004.

(24) Liu, X.; Cheng, P. Dropwise Condensation Theory Revisited Part II. Droplet Nucleation Density and Condensation Heat Flux. *Int. J. Heat Mass Transf.* **2015**, *83*, 842–849.

(25) Kim, H.; Nam, Y. Condensation Behaviors and Resulting Heat Transfer Performance of Nano-Engineered Copper Surfaces. *Int. J. Heat Mass Transf.* **2016**, *93*, 286–292.

(26) Tanasawa, I. Advances in Condensation Heat Transfer. In *Advances in Heat Transfer*; Elsevier, 1991; Vol. 21, pp. 55–139.

(27) Zheng, L.; Wang, Y.-X.; Plawsky, J. L.; Wayner, P. C. Effect of Curvature, Contact Angle, and Interfacial Subcooling on Contact Line Spreading in a Microdrop in Dropwise Condensation. *Langmuir* **2002**, *18*, 5170–5177.

(28) Carey, V. P. *Liquid-Vapor Phase-Change Phenomena: An Introduction To The Thermophysics Of Vaporization and Condensation in Heat Transfer Equipment: An Introduction to the Thermophysics of Vaporization & Condensation in Heat Transfer Equipment*; Taylor & Francis, 1992.

(29) Liu, X.; Cheng, P. Dropwise Condensation Theory Revisited: Part I. Droplet Nucleation Radius. *Int. J. Heat Mass Transf.* **2015**, *83*, 833–841.

(30) Smith, J. D.; Dhiman, R.; Anand, S.; Reza-Garduno, E.; Cohen, R. E.; McKinley, G. H.; Varanasi, K. K. Droplet Mobility on Lubricant-Impregnated Surfaces. *Soft Matter* **2013**, *9*, 1772–1780.

(31) Xiao, R.; Miljkovic, N.; Enright, R.; Wang, E. N. Immersion Condensation on Oil-Infused Heterogeneous Surfaces for Enhanced Heat Transfer. *Sci. Rep.* **2013**, *3*.

(32) Kajiya, T.; Schellenberger, F.; Papadopoulos, P.; Vollmer, D.; Butt, H.-J. 3D Imaging of Water-Drop Condensation on Hydrophobic and Hydrophilic Lubricant-Impregnated Surfaces. *Sci. Rep.* **2016**, *6*, 23687.

(33) Schellenberger, F.; Xie, J.; Encinas, N.; Hardy, A.; Klapper, M.; Papadopoulos, P.; Butt, H.-J.; Vollmer, D. Direct Observation of Drops on Slippery Lubricant-Infused Surfaces. *Soft Matter* **2015**, *11*, 7617–7626.

(34) Yang, Z.; Wu, Y.-Z.; Ye, Y.-F.; Gong, M.-G.; Xu, X.-L. A Simple Way to Fabricate an Aluminum Sheet with Superhydrophobic and Self-Cleaning Properties. *Chin. Phys. B* **2012**, *21*, 126801.

(35) Anand, S.; Paxson, A. T.; Dhiman, R.; Smith, J. D.; Varanasi, K. K. Enhanced Condensation on Lubricant-Impregnated Nanotextured Surfaces. *ACS Nano* **2012**, *6*, 10122–10129.

(36) Wexler, J. S.; Jacobi, I.; Stone, H. A. Shear-Driven Failure of Liquid-Infused Surfaces. *Phys. Rev. Lett.* **2015**, *114*.

(37) Boreyko, J. B.; Polizos, G.; Datskos, P. G.; Sarles, S. A.; Collier, C. P. Air-Stable Droplet Interface Bilayers on Oil-Infused Surfaces. *Proc. Natl. Acad. Sci.* **2014**, *111*, 7588–7593.

(38) Hiroaki, T.; Takaharu, T. A Microscopic Study of Dropwise Condensation. *Int. J. Heat Mass Transf.* **1984**, *27*, 327–335.

(39) Yamali, C.; Merte Jr, H. A Theory of Dropwise Condensation at Large Subcooling Including the Effect of the Sweeping. *Heat Mass Transf.* **2002**, *38*, 191–202.

(40) Le Fevre, E. J.; Rose, J. W. A Theory of Heat Transfer by Dropwise Condensation. *Proc. 3rd Int. Heat Transf. Conf. Chic. 1966* 362–375.

(41) Tanaka, H.; Hatamiya, S. Drop Size Distributions and Heat Transfer in Dropwise Condensation-Condensation Coefficient of Water at Low Pressure. In *Proceedings of the 8th International Heat Transfer Conference*; 1986; Vol. 4, pp. 1671–1676.

(42) Nusselt, W. Die Oberflächenkondensation Des Wasserdampfes. *Z Ver Deut Ing* **1916**, *60*, 541–580.

(43) Altenpohl, D. G. Use of Boehmite Films For Corrosion Protection of Aluminum. *CORROSION* **1962**, *18*, 143t–153t.

(44) Wong, T.-S.; Kang, S. H.; Tang, S. K. Y.; Smythe, E. J.; Hatton, B. D.; Grinthal, A.; Aizenberg, J. Bioinspired Self-Repairing Slippery Surfaces with Pressure-Stable Omniphobicity. *Nature* **2011**, *477*, 443–447.

CHAPTER 4

DROPLET IMPACT ON ELASTIC SUBSTRATES [2]

4.1 Introduction

The importance of droplet impact dynamics in many industrial fields, including anti-icing[1,2], spray cooling[3,4], pesticide and herbicide delivery[5,6], and ink-jet printing[7], has been introduced in Chapter 1. The total contact time from initial impact to lift-off, t_c, influences the mass, momentum, and energy exchange between the droplet and the solid. Hence, achieving control of the contact time through manipulation of the internal flow physics dictates the transport processes occurring at the liquid-solid interface. Taking inspiration from nature (leaves) and human technology (springboards), we study droplet impact dynamics on elastic superhydrophobic substrates as a passive mechanism for controlling and reducing contact time. We hypothesize that droplets impacting elastic surfaces might exhibit distinct dynamics, resulting in energy storage and recovery not just within the droplet but also within the elastic surface. By studying droplet impact on superhydrophobic elastic polymer sheets, we show that droplets can undergo springboarding and reduce contact times by a factor of 2 when compared to rigid superhydrophobic surfaces. Further experimental observation and theoretical analysis elucidates a surface mediated energy storage mechanism arising from the coupling of the substrate elastic response to impact, and the droplet internal flow dynamics. In contrast to previous studies, we show that droplet dynamics can be altered and contact times reduced by introducing a second energy storage mechanism during impact – elastic energy of the substrate – in addition to surface energy of the droplet. We present new fundamental knowledge of droplet

---

[2] Parts of this chapter have been previously published as Weisensee *et al.*, "Water droplet impact on elastic superhydrophobic surfaces", *Sci. Rep.* 6 (2016)

impact physics and provide a starting point for more advanced approaches to enhance the performance of droplet-based applications by using substrate elasticity to achieve enhanced thermal, mass, or momentum transport.

4.2 Materials and Methods

Figure 1.1 a and b show SEM images of the surfaces used in this study. The commercially available superhydrophobic coating NeverWet was sprayed onto different glass and polymer substrates. NeverWet consists of a flat base coat without nanoparticles (water contact angle θ_A/θ_R = 105 ± 3°/66 ± 4°) and a top coat consisting of conformally coated hydrophobic nanoparticles with diameters of ≈ 50 nm. On each sample, 3 base coats and 3-4 top coats were applied, resulting in apparent advancing and receding contact angles of $\theta_A^{app}/\theta_R^{app}$ = 164 ± 4°/159 ± 3°. Polymer sheets (GoodFellow) of various thickness were cut into rectangles with dimensions listed in Table 4.1 and used as substrates. The sheets used in this study were: 500 µm polymethylmethacrylat (PMMA), 250 µm PMMA, 175 µm PMMA, 100 µm polyhydroxybutyrate (PHB), 36 µm PMMA, and 10 µm PMMA. A glass microscope slide coated with NeverWet served as a rigid baseline substrate to ensure that observations on other substrates could be clearly attributed to elasticity, and not the coating itself. The geometric dimensions, including substrate thickness h_s, substrate width w, substrate length L, mass of the substrate m_s (density ρ_{PMMA} = 1180 kg/m³), and distance of impact to the fixture s are listed in Table 4.1. SEM images for surface characterization were obtained using a Quanta 450 FEG ESEM in high vacuum mode. The surface roughness on the macroscale (~µm) was characterized with an Alicona Infinite Focus 3D microscope. The lateral resolution with a 50x lens was 1 µm and the vertical resolution was 40 nm. Multiple scans were combined to measure a larger area.

The roughness was analyzed with the internal software provided by Alicona. It is important to note that the 3D microscope's resolution is much larger than the average nanoparticle size, thus, the roughness determined with the Alicona 3D microscope pertains to differences in microstructure only, for example due to nanoparticle clustering, and does not reflect the underlying nanostructure. The nano-roughness was determined using atomic force microscopy (AFM) (Cypher by Asylum Research) in tapping mode at a scan rate of 0.5 Hz, a scan speed of 5 µm/s, and a step size of 15.6 nm. The roughness was analyzed with the internal software provided by Asylum Research.

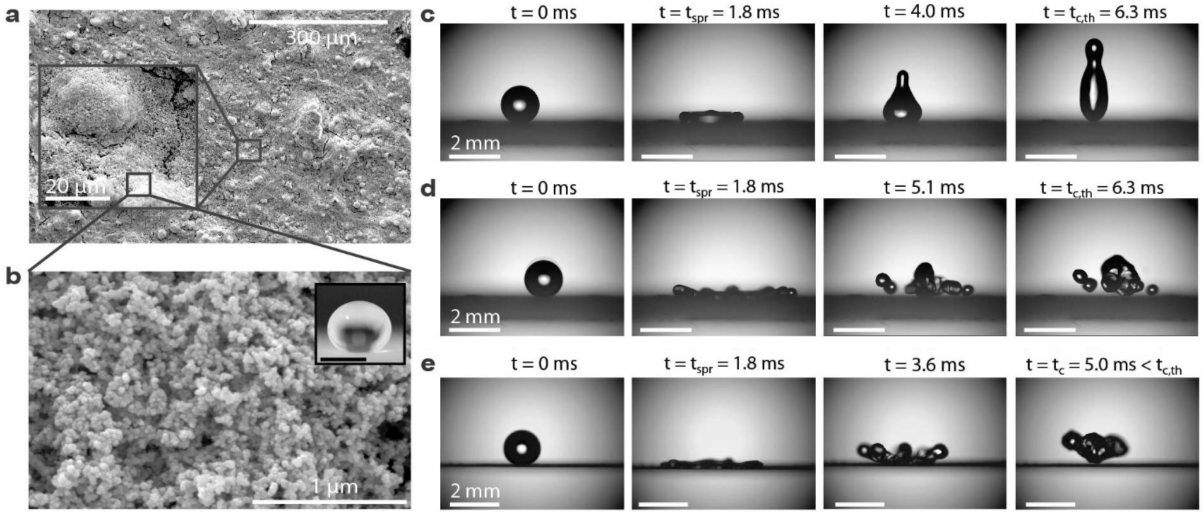

Figure 4.1: Surface characterization and dynamic behavior of water droplet impact on rigid and elastic superhydrophobic surfaces. (a) SEM micrographs showing the macroscale roughness of the NeverWet superhydrophobic coating due to particle clustering. (b) High resolution SEM micrograph showing individual nanoparticles. Inset: water droplet on a NeverWet coated glass slide (scale bar 1 mm). The advancing and receding contact angles were 164 ± 4° and 159 ± 3°, respectively. (c) High speed images showing a low velocity droplet (v = 0.68 m/s) impacting a rigid superhydrophobic surface, and following the classical model of spreading, retraction and lift-off at the theoretical contact time $t_{c,th} = 2.6\ (\rho D_0^3/8\gamma)^{1/2}$. (d) Droplet impact on a rigid superhydrophobic surface at higher impact speeds (v = 1.58 m/s), showing breakup and splashing. (e) Droplet impact on an elastic superhydrophobic surface at higher impact speeds (v = 1.57 m/s), showing substrate oscillation, and early lift-off of the droplet in a pancake shape at reduced contact times ($t_c < t_{c,th}$ = 6.3 ms).

Table 4.1: Substrate and droplet parameters: fixture mode (f-f: fixed-fixed, c: cantilever), substrate geometries, and average droplet sizes for each experimental set.

Fix	h_s (μm)	w (mm)	L (mm)	m_s (kg)	s (mm)	k (N/m)	f_0 (Hz)	$f_{0,obs}$ (Hz)	D_0(G33) (mm)	D_0(G25) (mm)	D_0(G20) (mm)
f-f	1100	25	53	3.69e-3	26.5	7630	247	-	1.49	2.37	2.84
f-f	500	27	64	1.08e-3	32.0	1040	169	-	1.46	2.38	2.89
f-f	250	26	59	5.03e-4	29.5	467	166	244	1.40	2.34	2.89
f-f	175	25	65	3.89e-4	32.5	210	126	147	1.45	2.29	2.72
f-f	100	25	71	2.78e-4	35.5	129	117	96	1.52	2.33	2.75
f-f	36	7.5	63	3.57e-5	31.5	107	298	325	1.51	2.23	2.76
f-f	10	15	53	3.56e-5	26.5	63	229	-	1.38	2.39	2.93
f-f	10	20	110	9.81e-5	55.0	22	81	93	1.47	2.00	2.50
c	175	15	20	1.03e-4	15.0	29.8	122	111	1.44	2.15	2.57
c	175	25	20	6.20e-5	15.0	17.9	122	105	1.55	1.96	2.40
c	175	25	65	3.36e-4	20.0	12.6	11	8	1.50	2.38	2.87
c	175	25	65	3.36e-4	24.0	7.3	11	10	1.44	-	-
c	175	25	65	3.36e-4	35.5	2.2	11	11	1.59	2.36	2.74
c	175	25	65	3.36e-4	46.0	1.0	11	11	1.51	2.36	2.97
c	175	25	65	3.36e-4	59.5	0.5	11	10	1.52	2.35	2.71
c	100	6.5	13	1.07e-5	var.	var.	165	140	-	2.3 - 2.5	-

Figure 4.2 shows three dimensional (3D) shaded surface plots of a glass microscope slide coated with the superhydrophobic NeverWet coating. Figure 4.2 a and b reveal nanoparticle clustering with up to 60 μm tall features, randomly distributed over the surface, leading to a macroscopic roughness of $\zeta_{\text{macro}} = 1.2$, defined as the ratio of the total macroscopic area to the projected area. At the microscale, individual nanoparticles with diameters $d \sim 30$ nm form smaller clusters with re-entrant structures that have a characteristic roughness of $\zeta_{\text{micro}} = 1.5$ (Figure 4.2 c,d). At the nanoscale, *i.e.* the individual nanoparticle level, we can estimate the roughness by modeling the nanoparticles as a monolayer of spheres in contact with each other. With the surface area of an individual nanoparticle, πd^2, and a projected area d^2, the characteristic roughness is $\zeta_{\text{nano}} = (\pi d^2 + d^2)/d^2 = 4.14$. The hierarchical nature of the surface

provides an effective total roughness of $\zeta = \zeta_{\mathrm{macro}} \cdot \zeta_{\mathrm{micro}} \cdot \zeta_{\mathrm{nano}} \approx 7.15$. Using the values of the advancing contact angles on a rough ($\theta_A^{\mathrm{app}} = 164°$) and a smooth ($\theta_A = 105°$) surface, we estimate the effective solid fraction of the superhydrophobic surface to be $\varphi = (\cos \theta_A^{\mathrm{app}} + 1)/(\cos \theta_A + 1) \approx 0.05$.

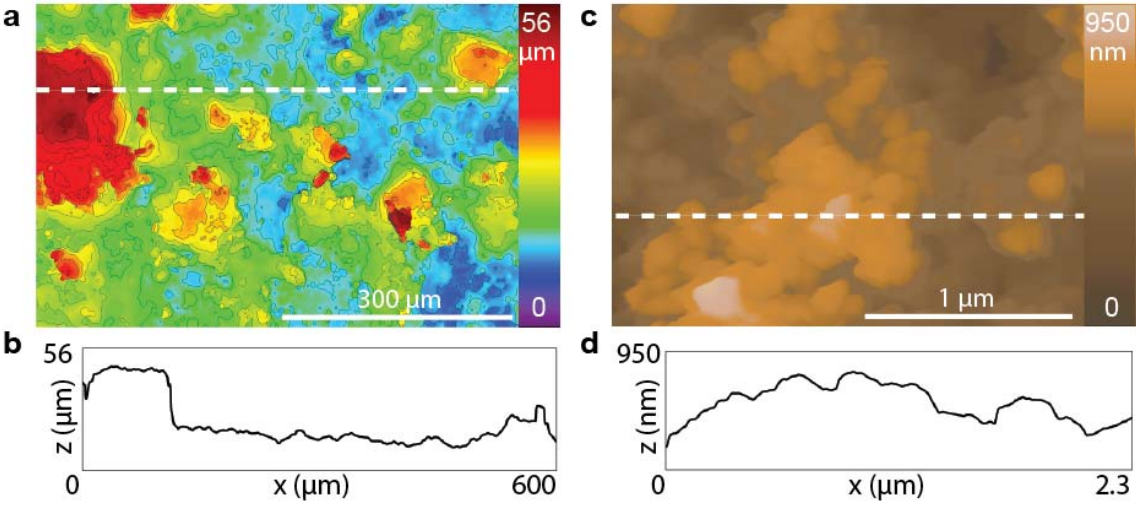

Figure 4.2: Surface characterization of the NeverWet superhydrophobic coating. (a) 3D microscope image showing a typical height distribution and macroscopic roughness. The dashed line indicates the location of the line scan in (b). (c) AFM image showing the microscopic roughness. The dashed line indicates the location of the line scan in (d). Note the different height and length scales in (a) and (c).

Droplet impact was studied with two substrate mountings: fixed-fixed along the short edges of the substrate, and fixed-free along one short edge of the substrate, *i.e.* cantilever-style mounting. The stiffness of the cantilever was determined from geometrical considerations, with the area moment of inertia $I = wh_s^3/12$, where w and h_s are the width and thickness of the substrate. The stiffness was calculated as $k = 3EI/s^3$, where $E_{\mathrm{PMMA}} \approx 3$ GPa is the elastic modulus of the substrate and s is the distance between the centerline of droplet impact and the fixed end. The stiffness of the fixed-fixed substrate depended on the substrate geometry and mounting tension, and was thus experimentally measured. A cylindrical hook with a diameter of 3.3 mm, connected to a force gauge (MG025, Mark-10), contacted the substrate from below, at the location of droplet impact. The hook-gauge-assembly had a stiffness of $k_F \approx 4000$ N/m. The force gauge was mounted on a linear translation stage (Thor Labs) and was slowly moved upwards to a total displacement, Δd_{tot}, at which point the total force F was recorded. The stiffness of the fixed-fixed substrate was determined to be $k = F / (\Delta d_{tot} - F/k_F)$. Table 4.1 lists the calculated and experimentally measured stiffness for each substrate. A schematic of the setup is shown in Figure 4.3.

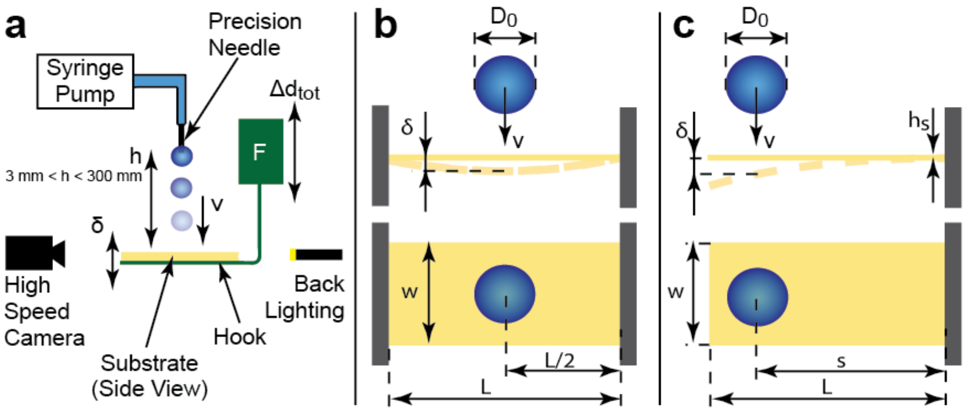

Figure 4.3: Experimental setup and substrate geometries. (a) Droplets, generated with a syringe pump, fall unto the substrate from varying heights (3 mm < h < 300 mm) with the impact speed v (0.05 < v < 2 m/s). A high speed camera records the impact and the deflection of the substrate, δ. To measure the stiffness of a fixed-fixed substrate, a hook is inserted from below and a force gauge (force $\boldsymbol{F}$) is displaced by means of a linear translational stage (Δd_{tot}). (b) and (c) Geometric dimensions of fixed-fixed (membrane) and fixed-free (cantilever) substrates. Substrates are clamped with a uniform pressure distribution over the width of the substrate. The deflection of the substrates is measured at the location of impact.

To conduct the impact experiments, three needles having 33 (G33), 25 (G25) and 20 (G20) gauge with outer diameters of 210 µm, 515 µm and 908 µm, respectively, were connected to a syringe pump at a flow rate of 50 µL/min (Pico Plus, Harvard Apparatus). Individual droplets with diameters ranging from 1.3 to 3 mm (see Table 4.1) were formed at the tip of the needles and detached due to gravitational force. The height of the needle above the surface was varied between 3 and ~300 mm, resulting in impact speeds ranging from 0.05 to 2.1 m/s. Only data for non-splashing droplets was used in this study. The droplets impacted the stationary substrate in the center between the mountings in the fixed-fixed case and at a specified distance s from the single-sided mounting for the cantilever case. A high speed camera (Phantom v711, Vision Research) coupled to a 1-5x tele lens (Canon) recorded the impacting droplets at a frame rate of 9500 fps, resolution of 1024x768 pixels, and exposure time of 30 μs. The images were calibrated for each experiment with respect to the outer diameter of the dispensing needle, obtaining a resolution ranging from 6 to 10 μm/pixel. The images were analyzed with a Matlab code to determine the initial diameter, impact speed, maximum spreading, and substrate deflection, while manual analysis was required to obtain the spreading and contact times.

4.3 Results

4.3.1. Impact Dynamics

We first considered droplet impact on stiff and elastic nanostructured superhydrophobic surfaces. Droplet impact on the elastic surfaces differed greatly from impact on the rigid superhydrophobic surface. Figure 1.1c shows a droplet with D_0 = 1.48 mm impacting the rigid superhydrophobic sample at a speed of v = 0.68 m/s, corresponding to We = 9.6 and Oh = 0.003 << 1 ($Oh = \mu/\sqrt{\rho\gamma D_0}$, where μ is the droplet dynamic viscosity). As expected, impact causes the droplet to spread laterally, undergo kinetic-to-surface energy conversion due to additional surface area creation, and reach a maximum diameter $D_{\max}$ at the spreading time $t = t_{\mathrm{spr}}$. The droplet then undergoes the reverse process and retracts due to surface-to-kinetic energy conversion and finally lifts off the surface at the theoretical contact time $t_c = t_{c,\mathrm{th}} = 2.6\ (\rho D_0^3/8\gamma)^{1/2}$.[8–11] At higher impact speeds, as shown in Figure 1.1d with a droplet with D_0 = 1.49 mm and v = 1.58 m/s (We = 51.7), the droplet splashes, *i.e.* breaks up into a core droplet and several satellite droplets after reaching its maximum spreading diameter. The remaining core of the droplet detaches from the substrate at $t_c = t_{c,th}$. Interestingly, when the droplet impacts the elastic surface, as shown in Figure 1.1e with a droplet with $D_0 = 1.50$ mm and $v = 1.57$ m/s ($We = 51.2$), splashing is eliminated by the droplet edge detachment from the surface. Before the droplet can fully retract, the entire droplet has lifted off the surface in a spread (or pancake) shape at a contact time 21% shorter than the theoretical contact time on a rigid superhydrophobic surface.

4.3.2. Energy Conversion During Impact

Inspired by this unique observation, we hypothesize that substrate elasticity enables a new energy conversion mechanism to come into play during droplet impact. On the elastic surface, two distinct post-impact energy conversion mechanisms exist: kinetic-to-surface within the droplet and kinetic-to-elastic between the droplet and the elastic substrate. If tailored correctly, the elasticity of the substrate can be designed such that the two fundamental energy conversion mechanisms have disparate timescales, allowing for faster vertical momentum transfer from the elastic-to-kinetic energy conversion than from the classical surface-to-kinetic mechanism within the droplet, and thus early droplet lift-off from the surface.

In order to systematically study the effect of substrate elasticity on contact times, we conducted droplet impact experiments on elastic surfaces with varying stiffness ($0.5 < k < 7630$ N/m), fixture mode (fixed-fixed vs. cantilever), as well as varying the droplet size ($1.3 < D_0 < 3.0$ mm) and impact speed ($0.05 < v < 2.1$ m/s), corresponding to $0.05 < We < 115$. For all experiments, the impacting droplet Ohnesorge number $Oh \ll 1$, such that viscous forces were negligible when compared to capillary or inertial forces. Figure 4.4 summarizes the contact times for droplet impact on fixed-fixed substrates (a, b, c) and cantilever-style substrates (d, e, f). For substrate stiffness $20 < k < 150$ N/m and impact speeds greater than a critical impact speed, v_c, contact times were reduced when compared to impact on a rigid superhydrophobic surface (k = 7630 N/m). For small impact speeds ($v < 0.2$ m/s), contact times rapidly decreased with increasing speeds. Droplets in this speed regime behaved similarly to an elastic ball and did not spread. For $0.2 < v < v_c$, substrate mounting and stiffness had no effect on the droplet contact time, which was in excellent agreement with the inertial-capillary scaled contact time, $t_c = t_{c,th}$. For $v > v_c$, splashing occurred for substrates having $k < 20$ N/m and $k > 150$ N/m while on substrates having moderate stiffness ($20 < k < 150$ N/m), splashing was delayed and contact times decreased linearly with increasing impact speeds. The experiments were terminated once splashing occurred. Our data shows that droplet contact times can be halved when compared to droplet impact at lower impact speeds and on rigid superhydrophobic substrates. The reduction in contact time was observed on both fixed-fixed and cantilever-style substrates. Figure 4.5 shows that the contact time depends only weakly on the axial impact location of the droplet due to an increase in substrate stiffness with decreasing distance to the mount. It is important to note that the stiffness of the substrate did not directly influence the slope and magnitude of the decrease in contact times.

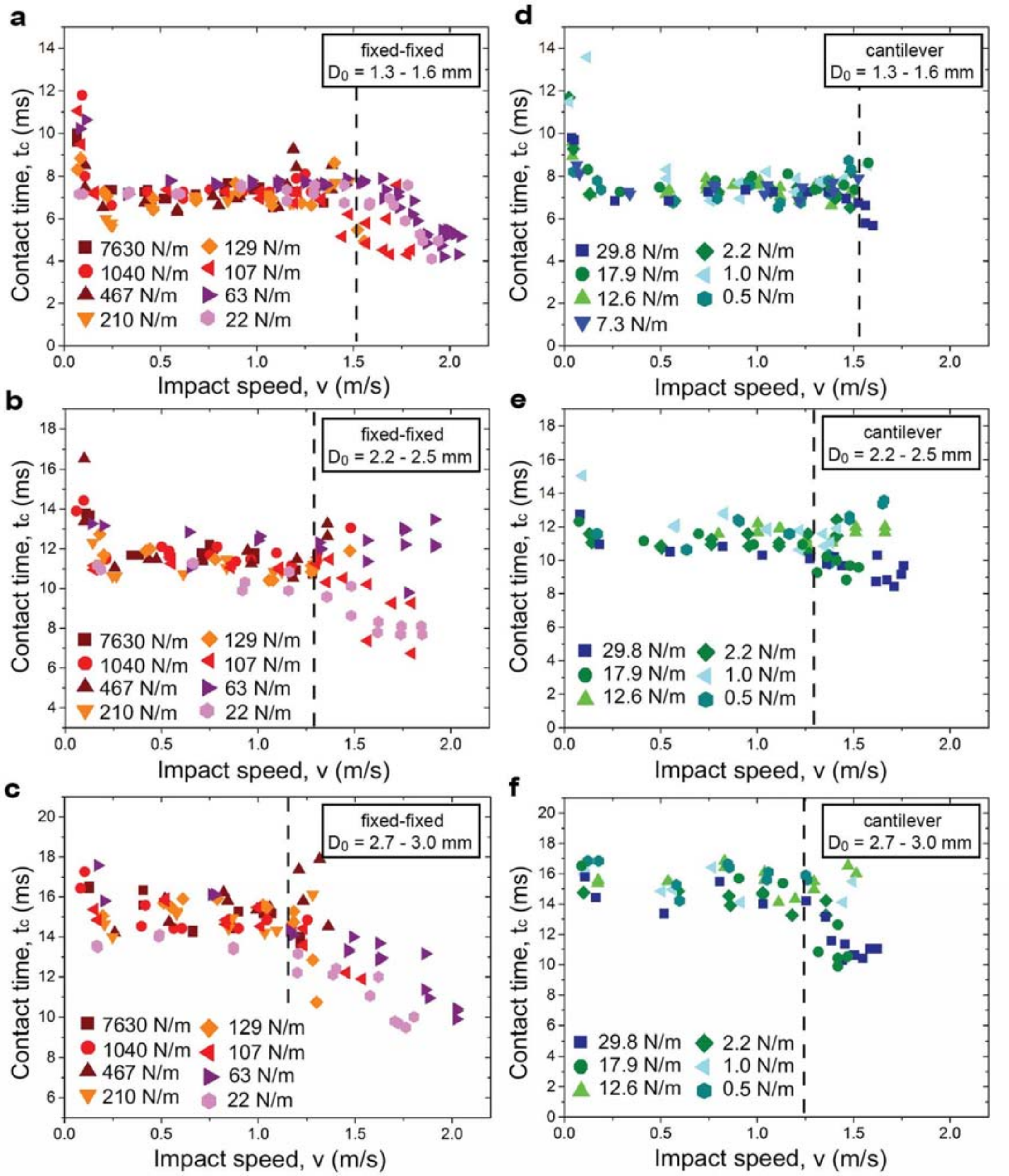

Figure 4.4: Contact times for impacting droplets for fixed-fixed (a-c) and cantilever (d-f) style mounted substrates as a function of impact speed and substrate stiffness for the three droplet diameter ranges. The critical impact speed, v_c, is marked with a dashed line. For impact speeds, $v > v_c$, the contact time decreased as a results of the *springboard* effect where the droplet lifted off the surface prior to fully retracting. Measurements were terminated once splashing occurred. Error bars are smaller than the symbol sizes and are not shown. In (b), droplets impacting the substrate with stiffness k = 63 N/m did so off-center from the axis, inducing a torsion of the substrate rather than an oscillation, and eliminating the possibility for contact time reduction.

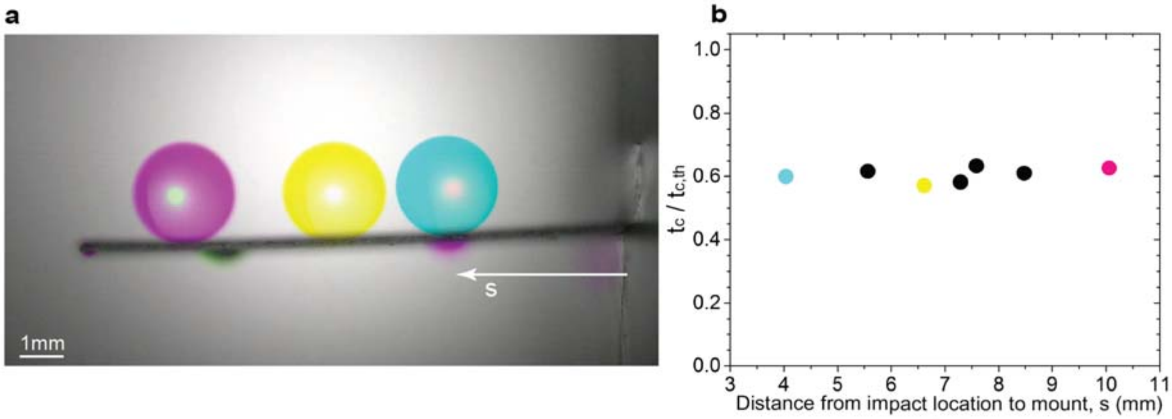

Figure 4.5: Effect of Axial Impact Location on Contact Time. (a) False-color images of three varying droplet impact locations for droplets with $D_0 \approx 2.3$ mm and $v \approx 1.7$ m/s impacting a cantilever-style substrate ($h_s = 100$ µm, $L = 13$ mm, $w = 6.5$ mm, and $f_0 = 140$ Hz) at an impact location ***s*** from the mount. (b) Ratio of contact time over theoretical contact time as a function of the distance between impact location and mount. The range of s was limited by the length of the cantilever and the maximum spreading diameter of the droplets ($D_{max} \approx 6.6$ mm). All droplets were in the springboarding regime with $t_c/t_{c,th} \approx 0.6$.

In addition to contact time reduction, Figure 4.4 shows that splashing, i.e. droplet breakup and creating of satellite droplets, occurs at higher impact speeds on elastic substrates than on rigid substrates, which has been reported previously for ethanol droplets impacting a circular membrane[12]. In the present study, the increase in the splashing threshold speed on fixed-fixed substrates was observed for substrate stiffness up to 130 N/m. The elasticity of the substrate enables kinetic-to-elastic energy conversion between the droplet and the substrate at early stages of impact. Hence, not as much energy is left over for kinetic-to-surface energy conversion, resulting in a decreased spreading inertia and increased critical splashing speed[12]. For all droplet sizes, splashing initiated at higher impact speeds on fixed-fixed when compared to the cantilever-style substrates due to more efficient kinetic-to-elastic energy conversion on the former mounting configuration.

Despite a significant reduction in contact time, droplet spreading times and maximum spreading diameter are not affected by the substrate elasticity and remained constant for all substrate mounting and elasticities, in agreement with previous studies[13,14]. Figure 4.6 shows the spreading time, t_{spr}, defined as the time taken from initial droplet contact with the surface to the time when the droplet reaches its maximum deformed radius, and average spreading speed for droplets of the three needle sizes. Substrate elasticity had no effect on the spreading time and spreading speed of droplets. At low impact speeds ($v < 0.5$ m/s), spreading times quickly decreased with increasing impact speed and remained constant for $v > 0.5$ m/. At high impact speeds (1.5 m/s $< v < v_{\mathrm{splash}}$), spreading times slightly increased due to partial energy transfer from the droplets to the substrate (initiating oscillation) and a reduction in the droplet spreading kinetic energy. The constant spreading time at moderate impact speeds can be understood as a balance of impact inertia and capillary forces during spreading. At low impact speeds ($v < 0.5$ m/s), gravity plays a dominant role over droplet inertia, making inertial-capillary scaling invalid, and increasing the spreading time[15]. Spreading times were independent of the substrate stiffness and increased with increasing droplet size. The data for the average spreading speed of the droplets (Figure 4.6b), defined as the maximum spreading diameter, D_{max}, divided by the spreading time, collapses onto a single curve for all droplet sizes, described by:

$$\frac{D_{max}}{t_{\mathrm{spr}}} = 1.5\, v^{3/4}\,. \tag{4-1}$$

Shortly after impact, instantaneous radial spreading speeds are up to 5 times higher than the impact speed, decrease as the droplet rim expands, and become negligible near the point of maximum spreading[16–18]. The average spreading speed $D_{\mathrm{max}}/t_{\mathrm{spr}} \sim v^{3/4}$ is obtained from droplet geometry, momentum, and mass conservation during the impact process[19], and does not substantially depend on the elasticity of the substrate[20]. However, the interplay between substrate elasticity, substrate oscillation and droplet liftoff may affect the total contact time, which was characterized next.

The maximum spreading of a droplet during impact can be estimated from an energy balance just before impact and at maximum spreading. Just before impact, at time $t = 0$, the energy E_0 consists of kinetic energy and surface energy of the droplet:

$$E_0 = \frac{1}{2} m_d v^2 + A_0 \gamma = \frac{\pi}{12} \rho D_0^3 v^2 + \pi D_0^2 \gamma \,. \tag{4-2}$$

At maximum spreading, the droplet can be approximated as a cylinder with height h. Approximating that $h << D_{\max}$, and neglecting the elastic energy stored in the substrate, the energy at maximum droplet spreading is:

$$E_{spr} = A_{spr} \gamma \approx \frac{\pi}{2} D_{max}^2 \gamma \,. \tag{4-3}$$

By applying the conservation of energy, $E_0 = E_{\mathrm{spr}}$, and dividing by $\pi D_0^2 \gamma$, it follows that:

$$\frac{\rho D_0 v^2}{12\gamma} + 1 = \frac{1}{2} \left(\frac{D_{max}}{D_0} \right)^2 = \frac{1}{2} \xi_{max}^2 \,, \tag{4-4}$$

where $\xi_{\max} = D_{\max}/D_0$ is the dimensionless spreading diameter. Thus,

$$\xi_{max} = \sqrt{\frac{1}{6} \frac{\rho D_0 v^2}{\gamma} + 2} \sim a\, We^{1/2} + b \,. \tag{4-5}$$

Fitting to the data (see Figure 4.6c) yields:

$$\xi_{max} = 0.22\, We^{1/2} + 0.7 \,. \tag{4-6}$$

Figure 4.6c also includes model results from previous studies on droplet spreading on rigid surfaces. The models by Mao[21] and Ukiwe and Kwok[22] include a Reynolds number dependency, whereas Clanet *et al.*[8] argue that $\xi_{\max} \sim We^{1/4}$, stemming from a modified capillary length that depends on the deceleration of the droplet during spreading as opposed to gravity. In the Weber number range of the current experiments ($0.1 < We < 140$), both scaling arguments yield similar spreading parameters. However, we find that the ~ $We^{1/2}$ scaling results in better fits for t_{spr} at low impact speeds. We used Eq. (4-6) to solve Eq. (4-1) and to calculate the spreading time of impacting droplets as:

$$t_{\mathrm{spr}} = 0.67\xi_{\mathrm{max}} D_0 v^{-3/4} \, . \tag{4-7}$$

Model predictions from Eq. (4-7) are included in Figure 4.6a with D_0 = 1.5 mm, D_0 = 2.3 mm and D_0 = 2.8 mm. The predicted values and data match well for all impact speeds. Correlations by other researchers either overestimate the spreading time for small impact speeds and/or underestimate t_{spr} at high impact speeds[8,23].

Figure 4.6d shows the ratio of spreading time to total contact time (t_{spr}/t_c). For $We < 10$, i.e. small impact speeds (region 1), $t_{\mathrm{spr}}/t_c \sim 1/2$, due to the symmetric nature of the spreading and recoil phases during elastic droplet rebound. For $We \geq 60$ (region 3), spreading times remain constant, but contact times decrease, leading to an increase in t_{spr}/t_c with increasing We. The droplets are in a regime that is characterized by the springboard effect and splashing. For $10 \leq We \leq 60$, in the regime of inelastic impact (region 2), the ratio of spreading and contact time are roughly constant. In this region, $t_{\mathrm{spr}}/t_c \sim 1/4$, indicating asymmetry in the impact process and energy dissipative mechanisms that create an imbalance between the inertial-to-capillary energy conversion in the spreading phase, and the capillary-to-inertial energy conversion in the retraction phase.

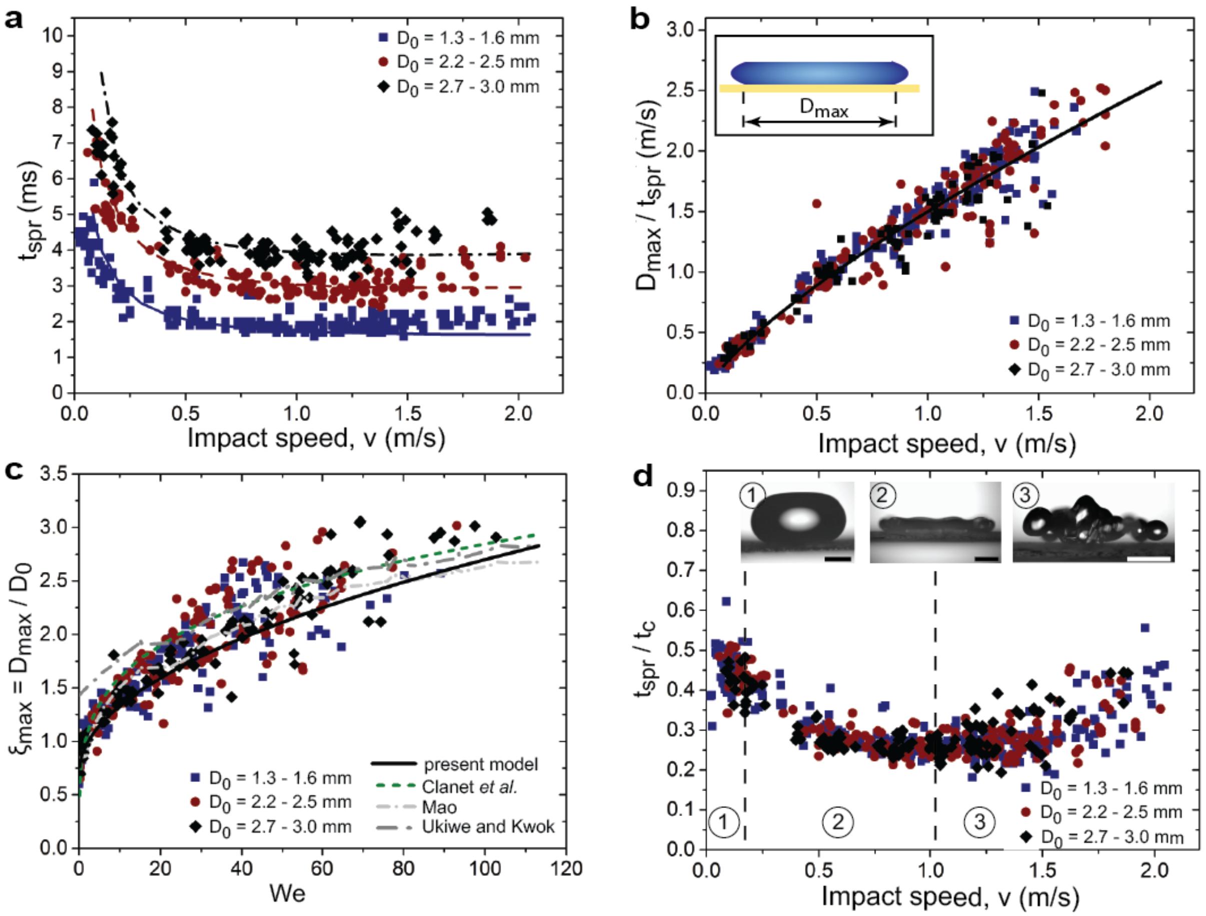

Figure 4.6: Droplet spreading dynamics. (a) Maximum spreading time, t_{spr}, as a function of impact speed for the three droplet diameter regimes. Equation (4-7) is plotted as lines with D_0 = 1.5 mm (blue), D_0 = 2.3 mm (red) and D_0 = 2.8 mm (black). (b) Normalized maximum spreading parameter as a function of impact Weber number, including the model predictions by Clanet *et al.*[8], Mao[21] and Ukiwe and Kwok[22], as well as the present model fit from (4-6). (c) Average droplet spreading speed, D_{max}/t_{spr}, as a function of droplet impact speed. All data collapse onto a single curve described by $D_{max}/t_{spr} \sim v^{3/4}$ (solid line). Insert: Schematic of the maximum spreading diameter, D_{max}, of the droplet. (d) Ratio of the maximum spreading time to total contact time, t_{spr}/t_c, as a function of *We*. Inserted images show the typical shape of droplets for the three regions 1-3. The scale bar is 1 mm. Data points include all experimental runs, *i.e.* fixed-fixed and cantilever for all substrates stiffnesses. Error bars for the impact speed, spreading time, and maximum spreading diameter are smaller than the symbol sizes and are not included.

4.3.3. Mechanism of Elasticity Mediated Contact Time Reduction

In order to better understand the physical mechanism of contact time reduction, we measured the dynamics of the elastic substrate during impact and developed a simple oscillator model of substrate motion. For the fixed-fixed and the cantilever substrates, the eigenfrequencies f_0 can be computed as $f_0 = \frac{1}{2\pi}\sqrt{\frac{k}{m_s(1-\nu^2)}}$ and $f_0 = \frac{3.52}{2\pi}\sqrt{\frac{E\,I}{m_s L^3(1-\nu^2)}}$, respectively, where m_s, L, ν, E, and I are the mass, length, Poisson's ratio ($\nu_{PMMA} = 0.38$), Young's modulus ($E_{PMMA} = 3$ GPa), and area moment of inertia ($I = wh_s^3/12$) of the substrate, where w is the width and h_s the thickness of the substrate. Table 4.1Table 4.1 lists the calculated and observed eigenfrequencies of the substrates, which are in excellent agreement, giving us confidence in the validity of the harmonic oscillator approximation.

Figure 4.7 shows the substrate response for three different substrate and impact conditions. Upon impact, the droplet exerts a force on the substrate, which causes the substrate to oscillate. The upward motion of the substrate during oscillation governs the contact time reduction of an impacting droplet, acting to accelerate the flattened droplet (~ D_{max}) in the vertical direction against gravity. The added upward force from the elastic substrate causes the droplet to detach before fully undergoing surface-to-kinetic energy conversion. During early departure, the droplet remains in a spread, pancake-like shape. We refer to this early lift-off mechanism as the *springboard effect*, or *springboarding*, taking inspiration from a springboard where the vertical acceleration of an elastic membrane or spring (elastic-to-kinetic energy exchange) helps a jumper to rebound. The droplet images in Figure 4.7a illustrate the coupling between the oscillation of an elastic substrate in the fixed-fixed configuration (k = 107 N/m) and droplet lift-off in the pancake-shape. After reaching the maximum spreading diameter (3), the edges of the droplet detach (4) near a minimum substrate position. The subsequent upward motion of the substrate supports the detachment of the center of the droplet and results in early droplet lift-off (5). Figures 3b and c show the cantilever-style substrate responses for k = 29.8 N/m and k = 2.2 N/m, respectively. While for the high stiffness cantilever (k = 29.8 N/m), droplet lift off did not occur in the pancake shape, contact time reduction was observed. However, droplet impact on the low stiffness substrate (k = 2.2 N/m) did not have a reduced contact time. Furthermore, while the stiffer cantilever oscillated at its natural eigenfrequency (f_0 = 112 Hz), the softer substrate showed an additional higher order oscillation (f_0 = 11 and f_1 = 68 Hz). The time scales of droplet spreading and recoil (~ 10 ms) were much shorter than the first order oscillation timescale (~ 100 ms) for the low stiffness substrate, resulting in the inability to accelerate the droplet upwards, and enabling full droplet recoil before lift-off with similar contact times as those on a rigid superhydrophobic surface[24,25]. To enable contact time reduction, our results show that the substrate oscillation and droplet impact timescales must be on the same order of magnitude.

An additional mechanism for contact time reduction can be found by studying the droplet dynamics at high impact speeds. We first determined the critical speed for the onset of contact time reduction, v_c, which was a function of the initial droplet diameter (Figure 4.4). As shown in Figure 4.1e and Figure 4.7a, and explained above, early lift off initiates at the edge of the droplet, analogous to the initial phase of droplet breakup during splashing. When splashing occurs, viscous drag decelerates the rim of the spreading droplet while the edges deform upwards and away from the surface. Although surface tension forces act to minimize the liquid/air surface area, inertia of the spreading droplet coupled with Kelvin-Helmholtz instabilities on the droplet periphery enable the breakup and the formation of satellite droplets, *i.e.* splashing[26–28]. For splashing to occur, the splash parameter, $K = WeRe^{1/2}$, where the droplet Reynolds number is $Re = \rho D_0 v/\mu$, must be greater than a critical parameter K_c. The critical parameter depends on the substrate roughness, and can be approximated as, $K_c \approx 3,600$ for the substrates used in this study[29–31].

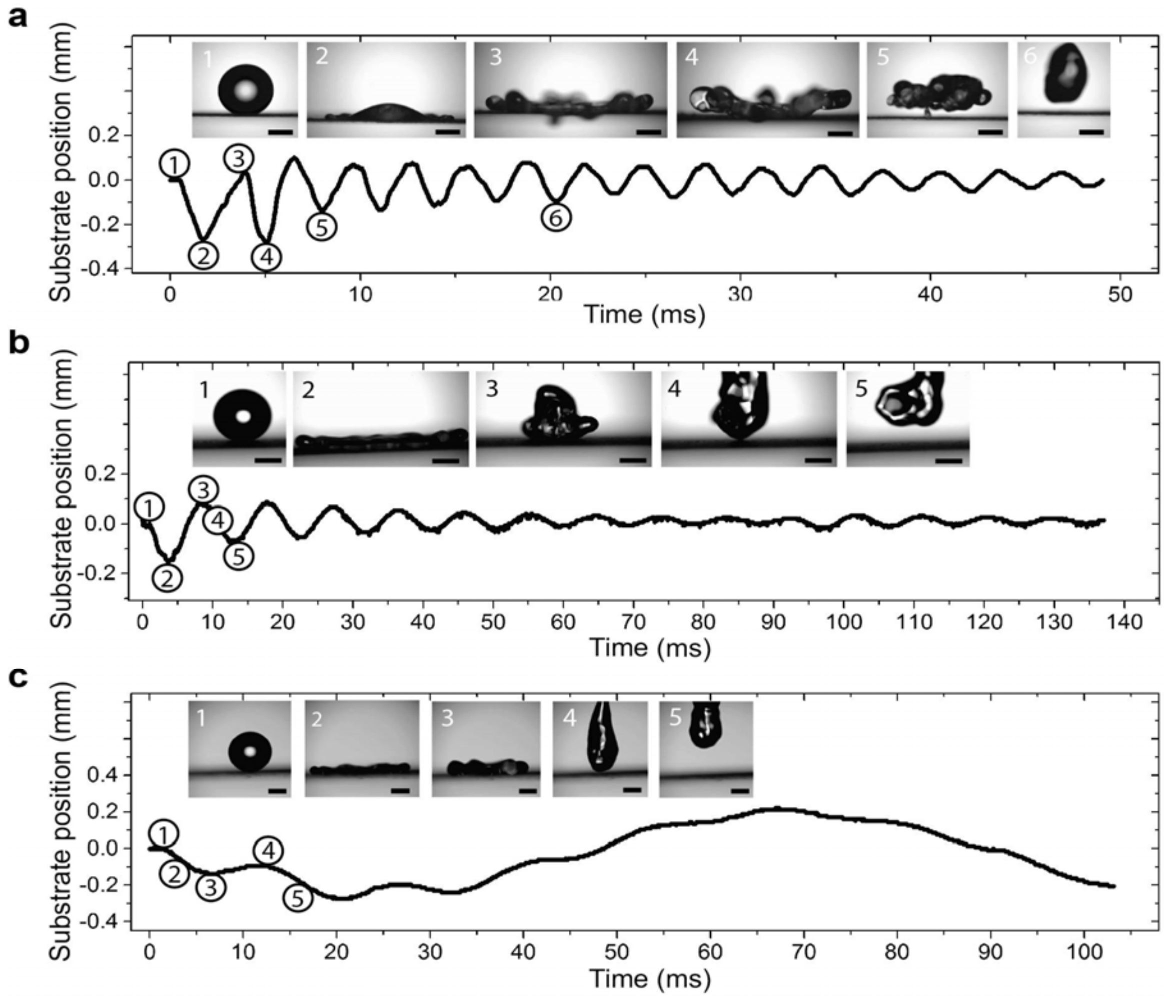

Figure 4.7: Substrate response and droplet shapes after droplet impact (scale bar 1 mm for all inset images). (a) Fixed-fixed substrate with k = 107 N/m, D_0 = 2.2 mm and f_0 = 325 Hz. Inset: Time lapse images of the droplet impact. The substrate starts a harmonic oscillation at its natural frequency shortly after droplet impact. The droplet spreads, and lifts off the surface in a pancake shape (*springboard effect*). (b) Cantilever substrate with k = 29.8 N/m and D_0 = 2.1 mm. The substrate oscillates at its natural frequency, f_0 = 112 Hz. Inset: Time lapse images of the droplet impact showing that droplet lift-off does not occur in a pancake shape, but is distinct from the retraction behavior on a rigid substrate. (c) Cantilever substrate with k = 2.2 N/m and D_0 = 2.4 mm. The substrate is so elastic that the droplet impact activates substrate oscillations with both the natural (f_0 = 11 Hz) and higher order frequencies (f_1 = 68 Hz). Even more elastic substrates exhibit even higher order modes, f_2 = 178 Hz (not shown). Inset: Time lapse images of the droplet impact showing spreading, retraction, and lift-off behavior similar to that on rigid superhydrophobic surfaces.

During droplet bouncing in the present experiments, droplets initiate their lift-off at the edges of the droplet at maximum spreading, as can be seen in Figure 1.1e and Figure 4.7a; a behavior similar to the first step during splashing. During spreading, the leading edge of the radial liquid flows over a small layer of air beneath it which provides lift to the advancing contact line[32]. The lift-force created by the spreading rim acts against gravity and facilitates the subsequent substrate oscillation-driven lift-off of the entire droplet. Recognizing the similarity between early droplet lift-off and initiation of splashing we can write:

$$K_c = \left(\frac{\rho D_0 v_c^2}{\gamma}\right)\left(\frac{\rho D_0 v_c}{\mu}\right)^{1/2} = 3600\,. \tag{4-8}$$

For water, ρ = 1000 kg/m^3, γ = 72 mN/m and μ = 10^{-3} Pa·s, leading to:

$$D_0^{1.25}\, v_c^{2.5} = 2.5 \times 10^{-4}\,. \tag{4-9}$$

Solving for the critical impact speed, we obtain:

$$v_c = \frac{0.036}{D_0^{0.6}}\,, \tag{4-10}$$

Converting the droplet diameter from meters to mm, we can write:

$$v_c = \frac{2.27}{D_0^{0.6}}\,. \tag{4-11}$$

Comparing this to the experimental data reveals that the fit is better for a pre-factor or 2.1 instead of 2.27. Adjusting Eq. (4-11) accordingly, we get:

$$v_c = \frac{2.1}{D_0^{0.6}}\,, \tag{4-12}$$

where D_0 is given in units of millimeters, and v_c is in units of meters per second. Figure 4.8 compares experimental data and model fit for the critical impact speed that is necessary for a reduction in contact times. The scaling $v_c \sim D_0^{-0.6}$ suggests that, for very small droplets, a reduction in contact time might not be possible due to the high critical speed required to overcome the dominant surface tension forces at small length scales. Indeed, it has been observed that micrometric droplets do not splash, even at impact speeds exceeding 10 m/s.[33] Droplet sizes in many applications, including spray cooling, range from 50 to 200 μm with typical impact speeds of 5 to 25 m/s, exceeding the critical impact speed required for contact time reduction[34,35]. Due to scale invariance of droplet impact phenomena for droplets bigger than approximately 50 μm[33], we expect springboarding for droplet size ranges often found in spray cooling. For smaller droplets ($D_0 < 50$ μm), viscous forces begin to dominate droplet inertia and surface tension, resulting in potential elimination of droplet springboarding[36].

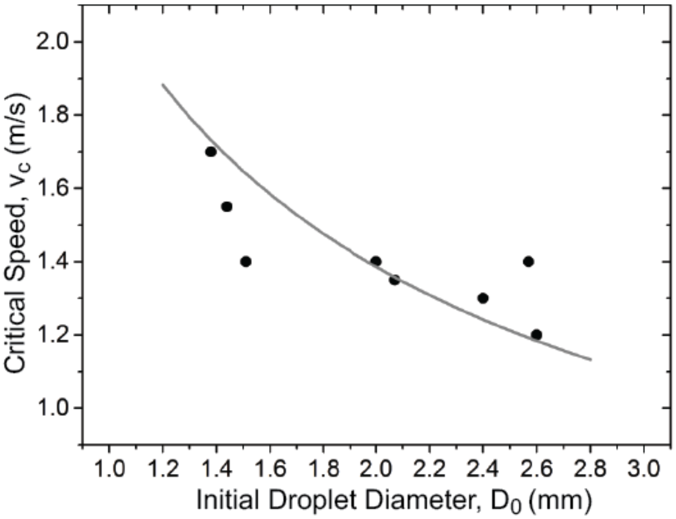

Figure 4.8: Critical impact speed. A comparison of data and Eq. (4-12) for the critical impact speed, v_c, as a function of the initial droplet diameter, D_0. The critical impact speed decreases for increasing droplet diameters as $v_c \sim D_0^{-0.6}$.

4.4 Discussion

In an effort to explain the physics governing the springboard effect on elastic substrates, we identified two fundamental conditions needing fulfilment to enable contact time reduction. The first condition relates the droplet impact speed to the critical impact speed while the second condition relates the droplet and substrate inertia to the gravitational body force. Figure 4.9a shows the experimentally measured contact time as a function of the impact speed normalized by the critical speed. To achieve contact time reduction, the impact speed must exceed the critical speed:

$$\frac{v}{v_c} > 1 \ , \tag{4-13}$$

where $v_c = 2.1/D_0^{0.6}$. For droplets having diameters of $D_0 \approx 1.5$ mm and $D_0 \approx 2.8$mm, Eq. (4-13) can be described by $We > 40$ and $We > 60$, respectively. The need to exceed the critical velocity in order to achieve droplet springboarding does not directly depend on the substrate characteristics, and stems from a balance of kinetic and surface energy required to suppress splashing.

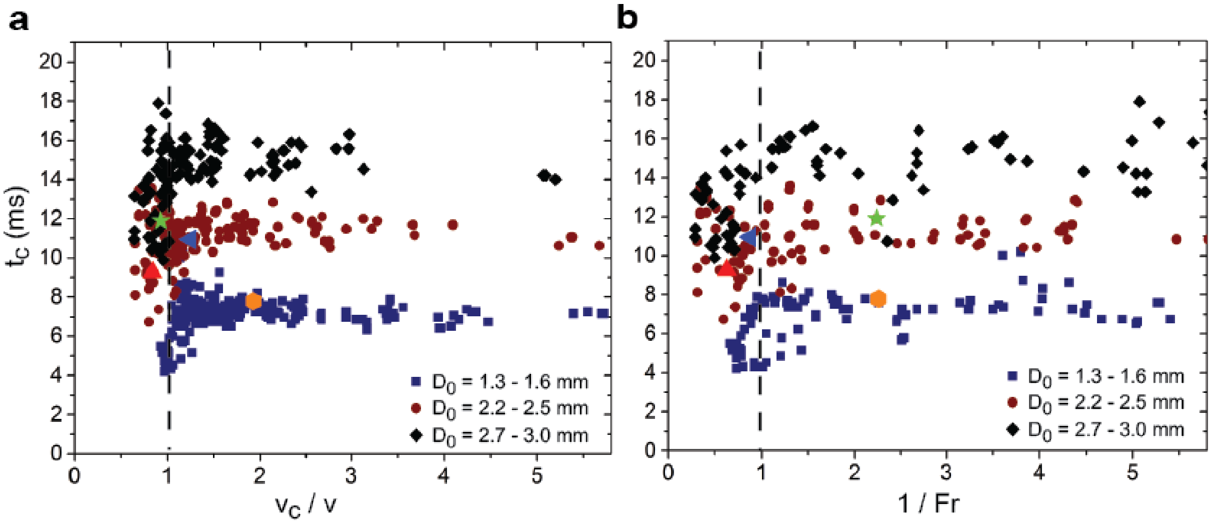

Figure 4.9: Droplet impact conditions for contact time reduction. (a) Contact times for the droplet size regimes as a function of the ratio of critical speed to impact speed, v_c/v. For the springboard effect to occur, the condition $v_c/v \leq 1$ must be met. (b) Contact times for the three droplet size regimes as a function of the inverse Froude number. To reduce contact times, $1/Fr \leq 1$ must be met. (a) and (b) also include four selected points that represent experimental conditions where: both dimensionless parameters (v_c/v and $1/Fr$) were met (▲), only the first (★) or second (◀) condition were met, and where neither of the conditions were met (⬢). The experimental data points include all experimental runs, *i.e.* fixed-fixed and cantilever for all substrate stiffnesses. Error bars in the experimental data points are smaller than the symbol size, and are not shown.

When droplets impact an inclined surface, as shown in Figure 4.10, the first criterion for contact time reduction (Eq. (4-13)) has to be adjusted for substrate-normal impact speeds. While the normal impact speed scales with cos(α) the critical impact speeds is inversely proportional to cos(α), resulting in a corrected critical velocity criterion:

$$\frac{v\cos^2(\alpha)}{v_c} > 1\,, \tag{4-14}$$

where v_c is described by Eq. (4-12). Figure 4.10b compares the ratio of contact time to theoretical contact time for a substrate with two different inclinations (14.9° and 25.5°) using Eq. (4-13) and the inclination-corrected Eq. (4-14), showing that the critical velocity criterion is more accurately fulfilled when using the corrected version. It can also be concluded that, at least for angles $0 < \alpha < 26°$, substrate inclination does not alter the springboarding mechanisms and contact times remain reduced.

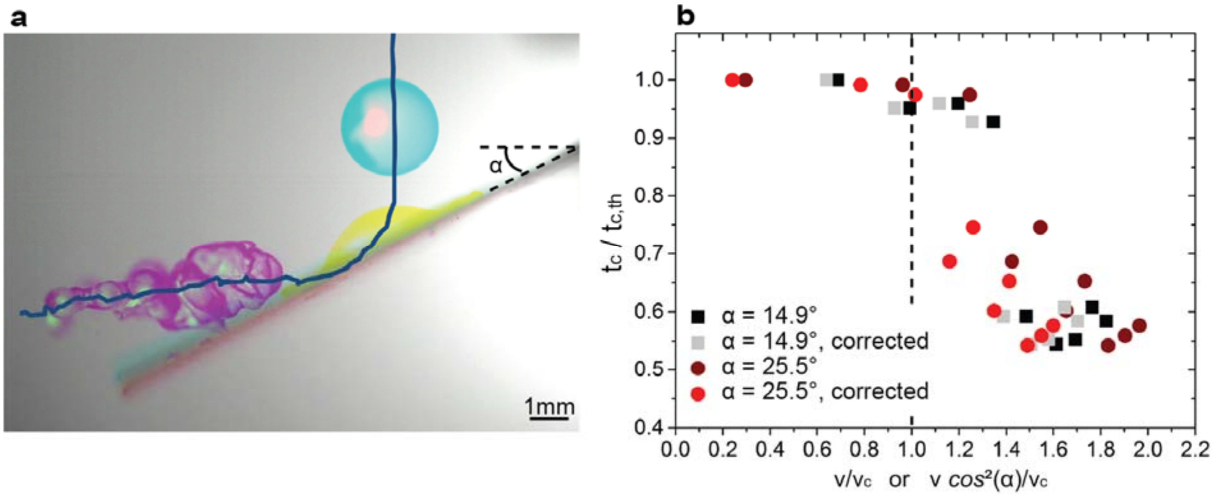

Figure 4.10: Impact on an inclined surface. (a) Center-of-mass trajectory and three exemplary droplet shapes for a droplet with D_0 = 2.52 mm and v = 2.09 m/s impacting a cantilever-style substrate (h_s = 100 µm, L = 13 mm, w = 6.5 mm, and f_0 = 140 Hz) at an angle of α = 25.5° to the horizontal. After impact, the droplet slides along the substrate before lifting off with a spread shape at $t_c/t_{c,th} \approx 0.6$. (b) Ratio of contact time over theoretical contact time as a function of the critical velocity criterion for two substrate inclinations. For impact on an inclined surface, the critical velocity criterion has to be corrected by a factor of cos²(α) to account for substrate-normal impact velocity for both the impact speed as well as the critical impact speed.

The second condition (Figure 4.9b) requiring fulfilment for contact time reduction depends on the substrate stiffness and oscillation frequency after impact. As described earlier, the vertical momentum transfer from the substrate to the droplet causes the droplet to lift-off in the pancake shape, leading to the reduction in contact time. We can quantify the vertical momentum transfer by defining an experimental Froude number (*Fr*) as the ratio of substrate inertia to the gravitational body force acting on the droplet during impact. The substrate inertia is defined as the vertical momentum transfer from the oscillating substrate to the droplet in the upward direction against gravity. For droplets to lift off with lower contact times, i.e. in a pancake shape, the upward substrate inertia must exceed the downward gravitational body force, thus the second condition can be written as:

$$\mathrm{Fr} = \frac{u_s}{(gD_{\max})^{1/2}} > 1\,, \tag{4-15}$$

where $u_s = 2\pi f_0 \delta_{\max}$ is the maximum substrate velocity during oscillation. The maximum impact force of the droplet on the substrate, $F_0 = \pi\rho(D_0/2)^2v^2$, is used to determine the maximum deflection of the substrate, $\delta_{\max} = 2\frac{F_0}{k}\sin(\pi\tau f_0)$, where $\tau = D_0/v$ is the crash time of the droplet[37,38]. A comparison of the experimental and calculated maximum substrate deflection, as shown in Figure 4.11, reveals that the *sin* term can be neglected for fixed-fixed substrate configurations. Correlations found in literature over- or underpredict the actual deflection for most cases[25,38]. Figure 4.11 b and c show the time dependent substrate deflection and spreading diameter of the droplets during impact. The two substrates have similar stiffness, but different eigenfrequencies, and both show springboard effect behavior for $v > v_c$. For the substrate with the higher natural frequency in Figure 4.11b, maximal spreading occurs at the upper peak of the substrate position after the first cycle of oscillation. On the substrate with the lower frequency in Figure 4.11c, droplets reach their maximum diameter at the lower dead point of the substrate, after only one quarter of an oscillation cycle. Interestingly, droplets have early lift-off in both cases. The comparison shows that substrate frequency and the springboard effect are not directly coupled. Whether a reduction in contact time occurs or not strongly depends on other factors, such as maximum membrane deflection and impact speed, as represented by the two conditions shown in and Eqns. (4-13) and (4-15).

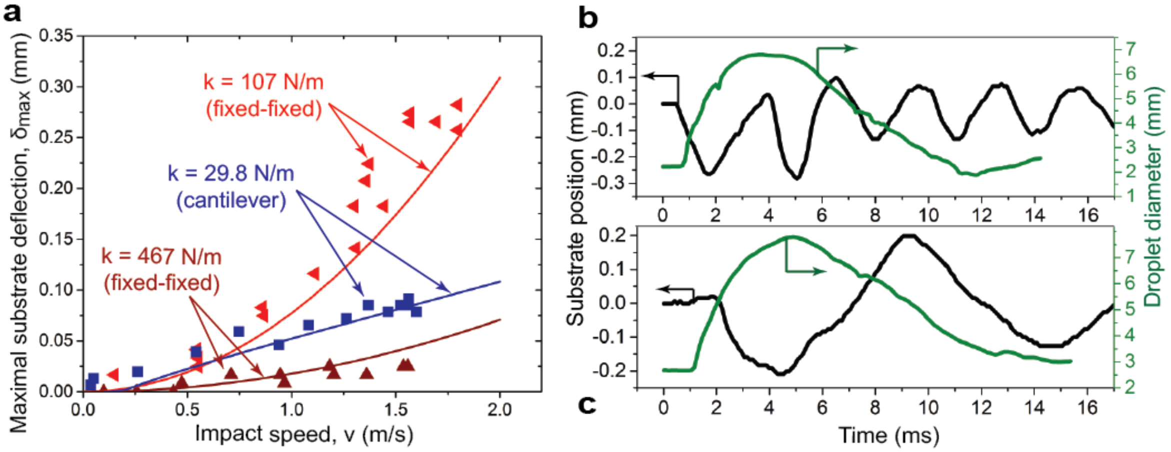

Figure 4.11: Substrate deflection dynamics. (a) Maximum membrane deflection for selected substrates as a function of impact speed with $\delta_{max} \sim v^2$. Shown are the deflection data and models (lines) for the fixed-fixed substrate with $k = 467$ N/m and $D_0 \approx 1.5$ mm, fixed-fixed with $k = 107$ N/m and $D_0 \approx 2.3$ mm and the cantilever style substrate with $k = 29.8$ N/m and a $D_0 \approx 1.5$ mm. Deflections for both fixed-fixed and cantilever style substrates can be well estimated with $\delta_{max} = 2\ F_0/k\ \sin(\pi\tau f_0)$, neglecting the *sin* term for fixed-fixed substrates. (b) and (c) show substrate deflection (black) and droplet diameter (green) profiles as a function of time. In (b), the substrate has a high natural frequency, and the maximum spreading of the droplet occurs near the first high point of the substrate. The substrate in (c) has a lower natural frequency, and the droplet reaches its maximum spreading near the first minimum of the substrate deflection. The maximum spreading and substrate deflection are not directly correlated and their interplay does not have an influence on the occurrence of the springboard effect.

Figure 4.9 a and b also include four select data points where i) both conditions are met (red triangle), ii) only the first condition is met (green star), iii) only the second condition is met (blue triangle), and iv) neither condition is met (orange hexagon). The experimental results show that in order to reduce contact times, both dimensionless conditions have to be satisfied. If designed properly, following the two dimensionless conditions presented above, elastic substrates can lead to a 2-fold reduction in contact time compared to impact on rigid superhydrophobic surfaces.

4.5 Conclusion and Outlook

Equations (4-13) and (4-15) enable us to predict whether impacting droplets will enter the springboard regime and consequently have reduced contact times during impact when impacting elastic substrates at rest. The Froude number criterion represents the coupling of time scales of substrate oscillation and droplet contact time as well as the amplitude of substrate oscillation caused by the impacting force of droplets. When the substrate is oscillating prior to droplet impact, caused, for example, by environmental conductions such as wind or vibrations, these external forces would need to be taken into account when determining the contact time reduction criteria.

We propose that the findings from this work can be used towards engineering new surfaces used in anti-icing and enhanced heat transfer applications. In general, shorter contact times result in smaller heat transfer rates per droplet. On anti-icing surfaces a reduction of the thermal energy transfer between solid and droplet would reduce the risk of droplet freezing[39,40].

We also propose that, when considering at many droplets hitting the surface, as for example in spray cooling, the overall average heat transfer can be increased. If the impact frequency between droplets scales with the contact time of the droplet, then a 50% decrease in contact time could lead to a 2-fold increase in impact frequency. Assuming that the droplets can me modeled as semi-infinite bodies, then the heat transfer q scales as $\sqrt{t}$. For $f_{\text{impact}} \sim 1/t_{\text{c}}$, we get that the overall average heat transfer scales as $\bar{q} \sim 1/\sqrt{t_{\text{c}}}$, i.e. net increasing the overall average heat transfer between many droplets and a surface for reduced contact times.

Thus, we envision that the contact time reduction on elastic surfaces not only extends our fundamental understanding of wetting phenomena, but also offers potential for a wide range of applications including anti-icing[2,39–41], self-cleaning[42], and heat transfer enhancement. Although demonstrated here for membrane and cantilever based systems, future studies on elastic solid substrates such as gels or elastomers is needed to verify the contact time reduction criteria on volumetric based elastic materials that would provide reduced sensitivity to impact location and environmental forces on contact time reduction. Similarly, more work is required on understanding the interaction dynamics between droplets and vibrating surfaces, as would be the case for multi-droplets impact.

4.6 References

(1) Meuler, A. J.; Chhatre, S. S.; Nieves, A. R.; Mabry, J. M.; Cohen, R. E.; McKinley, G. H. Examination of Wettability and Surface Energy in Fluorodecyl POSS/polymer Blends. *Soft Matter* **2011**, *7*, 10122–10134.

(2) Mishchenko, L.; Hatton, B.; Bahadur, V.; Taylor, J. A.; Krupenkin, T.; Aizenberg, J. Design of Ice-Free Nanostructured Surfaces Based on Repulsion of Impacting Water Droplets. *ACS Nano* **2010**, *4*, 7699–7707.

(3) Jia, W.; Qiu, H.-H. Experimental Investigation of Droplet Dynamics and Heat Transfer in Spray Cooling. *Exp. Therm. Fluid Sci.* **2003**, *27*, 829–838.

(4) Hsieh, S.-S.; Luo, S.-Y. Droplet Impact Dynamics and Transient Heat Transfer of a Micro Spray System for Power Electronics Devices. *Int. J. Heat Mass Transf.* **2016**, *92*, 190–205.

(5) Massinon, M.; Lebeau, F. Experimental Method for the Assessment of Agricultural Spray Retention Based on High-Speed Imaging of Drop Impact on a Synthetic Superhydrophobic Surface. *Biosyst. Eng.* **2012**, *112*, 56–64.

(6) Vallet, A.; Tinet, C. Characteristics of Droplets from Single and Twin Jet Air Induction Nozzles: A Preliminary Investigation. *Crop Prot.* **2013**, *48*, 63–68.

(7) van Dam, D. B.; Le Clerc, C. Experimental Study of the Impact of an Ink-Jet Printed Droplet on a Solid Substrate. *Phys. Fluids* **2004**, *16*, 3403–3414.

(8) Clanet, C.; Béguin, C.; Richard, D.; Quéré, D. Maximal Deformation of an Impacting Drop. *J. Fluid Mech.* **2004**, *517*, 199–208.

(9) Richard, D.; Clanet, C.; Quéré, D. Surface Phenomena: Contact Time of a Bouncing Drop. *Nature* **2002**, *417*, 811–811.

(10) Yarin, A. L. DROP IMPACT DYNAMICS: Splashing, Spreading, Receding, Bouncing…. *Annu. Rev. Fluid Mech.* **2006**, *38*, 159–192.

(11) Antonini, C.; Amirfazli, A.; Marengo, M. Drop Impact and Wettability: From Hydrophilic to Superhydrophobic Surfaces. *Phys. Fluids* **2012**, *24*, 102104.

(12) Pepper, R. E.; Courbin, L.; Stone, H. A. Splashing on Elastic Membranes: The Importance of Early-Time Dynamics. *Phys. Fluids 1994-Present* **2008**, *20*, 82103.

(13) Bird, J. C.; Dhiman, R.; Kwon, H.-M.; Varanasi, K. K. Reducing the Contact Time of a Bouncing Drop. *Nature* **2013**, *503*, 385–388.

(14) Liu, Y.; Moevius, L.; Xu, X.; Qian, T.; Yeomans, J. M.; Wang, Z. Pancake Bouncing on Superhydrophobic Surfaces. *Nat. Phys.* **2014**, *10*, 515–519.

(15) Perez, M.; Brechet, Y.; Salvo, L.; Papoular, M.; Suery, M. Oscillation of Liquid Drops under Gravity: Influence of Shape on the Resonance Frequency. *Europhys. Lett. EPL* **1999**, *47*, 189–195.

(16) Pasandideh-Fard, M.; Qiao, Y. M.; Chandra, S.; Mostaghimi, J. Capillary Effects during Droplet Impact on a Solid Surface. *Phys. Fluids* **1996**, *8*, 650.

(17) Roux, D. C. D.; Cooper-White, J. J. Dynamics of Water Spreading on a Glass Surface. *J. Colloid Interface Sci.* **2004**, *277*, 424–436.

(18) Hung, Y.-L.; Wang, M.-J.; Liao, Y.-C.; Lin, S.-Y. Initial Wetting Velocity of Droplet Impact and Spreading: Water on Glass and Parafilm. *Colloids Surf. Physicochem. Eng. Asp.* **2011**, *384*, 172–179.

(19) Lagubeau, G.; Fontelos, M. A.; Josserand, C.; Maurel, A.; Pagneux, V.; Petitjeans, P. Spreading Dynamics of Drop Impacts. *J. Fluid Mech.* **2012**, *713*, 50–60.

(20) Liu, Y.; Andrew, M.; Li, J.; Yeomans, J. M.; Wang, Z. Symmetry Breaking in Drop Bouncing on Curved Surfaces. *Nat. Commun.* **2015**, *6*, 10034.

(21) Mao, T.; Kuhn, D. C. S.; Tran, H. Spread and Rebound of Liquid Droplets upon Impact on Flat Surfaces. *AIChE J.* **1997**, *43*, 2169–2179.

(22) Ukiwe, C.; Kwok, D. Y. On the Maximum Spreading Diameter of Impacting Droplets on Well-Prepared Solid Surfaces. *Langmuir* **2005**, *21*, 666–673.

(23) Roisman, I. V.; Rioboo, R.; Tropea, C. Normal Impact of a Liquid Drop on a Dry Surface: Model for Spreading and Receding. *Proc. R. Soc. Math. Phys. Eng. Sci.* **2002**, *458*, 1411–1430.

(24) Wong, V.-K.; Ho, J.-H.; Yap, E. H. Dynamics of a Piezoelectric Beam Subjected to Water Droplet Impact with Water Layer Formed on the Surface. *J. Intell. Mater. Syst. Struct.* **2015**, *26*, 2170–2180.

(25) Gart, S.; Mates, J. E.; Megaridis, C. M.; Jung, S. Droplet Impacting a Cantilever: A Leaf-Raindrop System. *Phys. Rev. Appl.* **2015**, *3*.

(26) Xu, L.; Zhang, W. W.; Nagel, S. R. Drop Splashing on a Dry Smooth Surface. *Phys. Rev. Lett.* **2005**, *94*.

(27) Mandre, S.; Brenner, M. P. The Mechanism of a Splash on a Dry Solid Surface. *J. Fluid Mech.* **2012**, *690*, 148–172.

(28) Liu, Y.; Tan, P.; Xu, L. Kelvin–Helmholtz Instability in an Ultrathin Air Film Causes Drop Splashing on Smooth Surfaces. *Proc. Natl. Acad. Sci.* **2015**, *112*, 3280–3284.

(29) Bussmann, M.; Chandra, S.; Mostaghimi, J. Modeling the Splash of a Droplet Impacting a Solid Surface. *Phys. Fluids* **2000**, *12*, 3121.

(30) Bird, J. C.; Tsai, S. S. H.; Stone, H. A. Inclined to Splash: Triggering and Inhibiting a Splash with Tangential Velocity. *New J. Phys.* **2009**, *11*, 63017.

(31) Mundo, C.; Sommerfeld, M.; Tropea, C. Droplet-Wall Collisions: Experimental Studies of the Deformation and Breakup Process. *Int. J. Multiph. Flow* **1995**, *21*, 151–173.

(32) Riboux, G.; Gordillo, J. M. Experiments of Drops Impacting a Smooth Solid Surface: A Model of the Critical Impact Speed for Drop Splashing. *Phys. Rev. Lett.* **2014**, *113*.
(33) Visser, C. W.; Frommhold, P. E.; Wildeman, S.; Mettin, R.; Lohse, D.; Sun, C. Dynamics of High-Speed Micro-Drop Impact: Numerical Simulations and Experiments at Frame-to-Frame Times below 100 Ns. *Soft Matter* **2015**, *11*, 1708–1722.
(34) Kim, J. Spray Cooling Heat Transfer: The State of the Art. *Int. J. Heat Fluid Flow* **2007**, *28*, 753–767.
(35) Ortloff, C. R.; Vogel, M. Spray Cooling Heat Transfer — Test and CFD Analysis. In; IEEE, 2011; pp. 245–252.
(36) Visser, C. W.; Tagawa, Y.; Sun, C.; Lohse, D. Microdroplet Impact at Very High Velocity. *Soft Matter* **2012**, *8*, 10732.
(37) Abrate, S. Impact on Laminated Composite Materials. *Appl. Mech. Rev.* **1991**, *44*, 155.
(38) Soto, D.; De Larivière, A. B.; Boutillon, X.; Clanet, C.; Quéré, D. The Force of Impacting Rain. *Soft Matter* **2014**, *10*, 4929.
(39) Shen, Y.; Tao, H.; Chen, S.; Zhu, L.; Wang, T.; Tao, J. Icephobic/anti-Icing Potential of Superhydrophobic Ti6Al4V Surfaces with Hierarchical Textures. *RSC Adv* **2015**, *5*, 1666–1672.
(40) Ramachandran, R.; Kozhukhova, M.; Sobolev, K.; Nosonovsky, M. Anti-Icing Superhydrophobic Surfaces: Controlling Entropic Molecular Interactions to Design Novel Icephobic Concrete. *Entropy* **2016**, *18*, 132.
(41) Maitra, T.; Antonini, C.; Tiwari, M. K.; Mularczyk, A.; Imeri, Z.; Schoch, P.; Poulikakos, D. Supercooled Water Drops Impacting Superhydrophobic Textures. *Langmuir* **2014**, *30*, 10855–10861.
(42) Xu, Q.; Wan, Y.; Hu, T. S.; Liu, T. X.; Tao, D.; Niewiarowski, P. H.; Tian, Y.; Liu, Y.; Dai, L.; Yang, Y.; *et al.* Robust Self-Cleaning and Micromanipulation Capabilities of Gecko Spatulae and Their Bio-Mimics. *Nat. Commun.* **2015**, *6*, 8949.

CHAPTER 5

DROPLET DYNAMICS ON VIBRATING SURFACES

5.1 Introduction

The dynamics of droplets impacting rigid surfaces[1,2], soap films[3,4] and liquids[5–8] have been widely studied due to their high importance in both nature[9,10] and industry[11–13]. In Chapter 4 I presented our work on water droplet impact on elastic superhydrophobic surfaces and showed that contact times, i.e. the time between initial droplet-substrate touch and complete (final) droplet lift-off, could be reduced by a factor of 2 compared to impact on identical rigid surfaces[14]. When a droplet hits a non-wetting surface at moderate impact speeds ($We \lesssim 100$, where $We = (\rho v^2 D_0)/\gamma$ with the initial droplet diameter D_0, the impact speed v, and the droplet density ρ and surface tension γ), it spreads, reaches a maximum spreading diameter, recoils and lifts off due to conversion between kinetic and surface energy. However, on elastic substrates, droplets can lift off at the point of maximum spreading, without recoil, reducing the effective contact time[14]. When designed properly, the upward momentum imposed by the oscillating substrate on the droplet during spreading can counter-act gravity and cause the droplet to lift off in a pancake shape, known as the springboard effect. In our earlier work, the substrate was initially at rest, and the impacting droplet caused the substrate to vibrate at its eigenfrequency. Impact force, i.e. droplet size and speed, and substrate stiffness influence the contact time of the droplets on the elastic superhydrophobic substrates. In the present work, we study the effect of substrate vibration prior to droplet impact on contact times of bouncing droplets. Through high-speed imaging and semi-empirical mathematical modeling, we describe the relationship between contact time and vibration frequency, phase, amplitude, and rigidity of the substrate.

Despite the ubiquitous occurrence of droplet impact on vibrating surfaces in the mid-frequency range of $f = 50 - 500$Hz, such as on turbine blades[15], pumps and compressors[16], insect wings[17], automotive systems[18], and fragmentation and dispersion systems[19], very few studies have characterized the droplet dynamics during such impact conditions. On vibrated liquid baths, droplet dynamics and droplet bouncing have been shown to strongly depend on the relationship of vibration frequency to the droplet eigenfrequency[7], as well as the vertical acceleration of the bath[20]. During droplet impact on heated copper plates, low frequency, high amplitude vibrations at 100 – 250 Hz and accelerations of $a \sim 10^3$ m/s² = 100 g in the direction of the falling droplet have been shown to suppress the Leidenfrost effect[21]. At these high substrate accelerations, the collision force between droplet and substrate increases, allowing droplets to contact the hot plate, resulting in nucleate boiling rather than film boiling (Leidenfrost effect). For temperatures lower than the Leidenfrost temperature (≈ 170°C for water on static plates) spreading dynamics and the maximum spreading diameter are independent of substrate vibration[19]. However, vibrations at $f =$ 80 – 200Hz can enhance secondary fragmentation of fingers near the point of maximum droplet spreading. The resulting satellite droplets have diameters similar to the characteristic size of the fingers during natural impact without vibrations[19]. Non-vibrating, yet motion controlled targets have been shown to influence droplet rebound[22]. Properly timed reversal of vertically moving substrates can suppress or promote droplet rebound on flat hydrophobic polymer surfaces, depending on the direction of substrate motion and speed. When the direction of an originally downward moving target reverses during droplet impact, droplet rebound is enhanced. Similarly, when the substrate movement changes from up to down upon impact, droplet rebound is suppressed[22]. The initial qualitative explanation did not contribute the change in rebound behavior to an effective change in impact speed. Rather, it suggested that a coupling of kinematic and dynamic effects, and consequently a comparison of time scales, influences droplet rebound. Droplet rebound enhancement (sinusoidal and triangular waveforms) and suppression (square waveform) have also been demonstrated for impact on horizontally oscillating surfaces[23]. Rebound suppression was caused by an interference of velocity fields within the droplet during the recoil phase. Due to a non-slip boundary condition at the droplet-substrate interface, the horizontal velocity field of the substrate oscillation superimposes the natural vertical velocity field within the droplet that is responsible for droplet lift-off. Droplets stretch and elongate in one preferential direction, losing their spreading symmetry and the ability to completely rebound[23]. To our knowledge, no study has been published that examines the influence of vertical solid substrate oscillations on droplet impact dynamics.

Here, we study the effect of vertical sinusoidal substrate vibrations at 60 – 320 Hz and amplitudes of 0.3 – 3 mm on the contact times and splashing behavior of droplets impacting superhydrophobic rigid and elastic surfaces. We provide new insights into droplet impact physics on vibrating surfaces and develop guidelines for the rational design of surfaces to achieve controllable droplet wetting in applications utilizing vibration.

5.2 Experimental Setup and Sample Characterization

To represent a wide range of impact scenarios, we used three substrate configurations: (a) vibrating rigid substrate, (b) vibrating elastic substrate with a cantilever mount, and (c) two-droplet impact on a non-vibrating elastic substrate with a cantilever mount. Figure 5.1Figure 4.3 shows the experimental setup and three sample configurations used in this study. In all cases, de-ionized (DI) water was supplied to one or two 25 gauge needles from a gravity bag (Enteral Feeding Gravity Bag, Dynarex) attached to the ceiling of the room (≈ 1.5 m above the sample).

Droplets with a diameter of $D_0 = 2.5 - 2.8$ mm formed at the tip of the needle and impacted the substrate from a height h and with an impact speed $v = 1.2 - 1.75$ m/s, corresponding to Weber, Reynolds, and Capillary numbers of $We = \rho v^2 D_0/\gamma = 50 - 118$, $Re = \rho v D_0/\mu = 3000 - 4900$, and $Ca = \mu v/\gamma \approx 0.02$, respectively, where μ is the dynamic viscosity of water. A high speed camera (Phantom v711, Vision Research), coupled to a 1-5x macro lens (Canon), recorded the impacting droplets at frame rates of 9,500 and 13,000 frames per second (fps) and resolutions of 1024x768 and 800x600 pixels, respectively. A fiber-optic cable connected to a light source (EKE 150W, Kramer Scientific) provided sufficient back-lighting to achieve an exposure time of 10 – 30 µs. The images were calibrated with respect to the outer diameter of the dispensing needle, obtaining a resolution of 17 – 19 µm/pixel, resulting in a droplet size uncertainty of ± 0.2 mm and an impact speed uncertainty of ± 0.05 m/s. The images were analyzed with a Matlab code to determine the initial diameter, impact speed, substrate frequency, amplitude, and phase of impact, while manual analysis was used to obtain contact times (uncertainty: ± 0.2 ms). To render the samples superhydrophobic, the commercially available superhydrophobic coating NeverWet was sprayed onto a microscope slide (rigid substrate) and 100 µm thin polyhydroxybutyrate (PHB) polymer sheets (Goodfellow) (elastic substrates). The inset in Figure 4.3a shows a scanning electron microscopy (SEM) image of the nanoparticle coating. The apparent advancing and receding contact angles were $\theta_A^{app}/\theta_R^{app} = 164 \pm 4°/159 \pm 3°$. A detailed characterization of the coating can be found in Chapter 4, section 4.2[14].

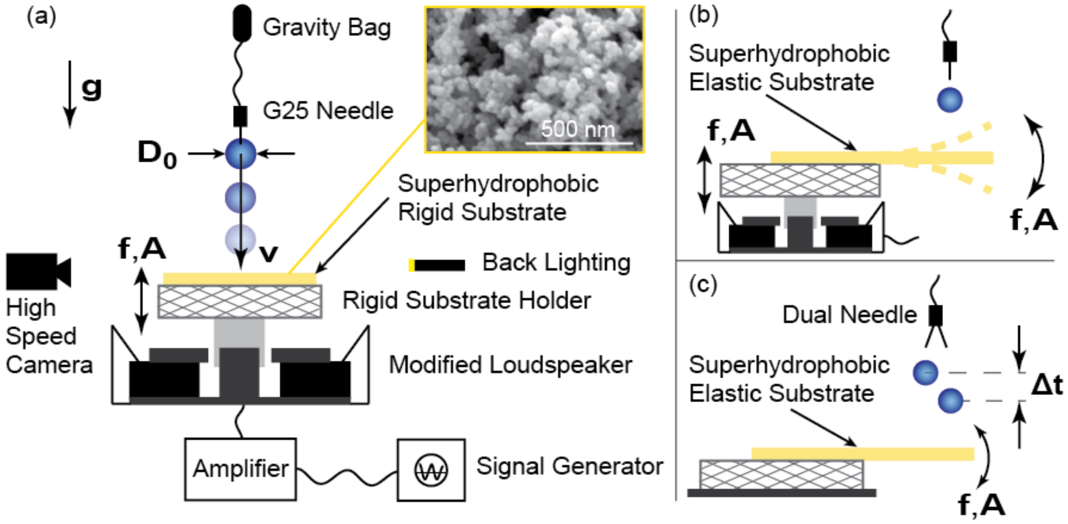

Figure 5.1: Experimental setup and substrate configurations. (a) Droplets formed at the tip of a single needle and fell onto the substrate with a droplet diameter D_0 (2.5 – 2.8 mm) and an impact speed v (1.20 – 1.75 m/s). A high speed camera recorded the impact and the substrate motion (frequency f, amplitude A). The rigid superhydrophobic nano-textured substrate was mounted on a modified loudspeaker, which was connected to a sinusoidal wave form generator and signal amplifier. (b) An elastic superhydrophobic substrate was attached to the same loudspeaker configuration with a cantilever-mount. (c) An elastic superhydrophobic substrate was attached to the stationary plate. Two droplets were generated at a dual needle and impacted the cantilever with a time delay Δt.

In two of the three configurations, the substrate was actively vibrated with a modified loudspeaker setup, while in the third case, substrate vibration was caused solely by droplet impact. For forced vibration scenarios, a laptop generated sinusoidal acoustic waves with frequencies $f = 60 – 320$ Hz that were transferred to a micro stereo amplifier (TDA7297, DROK) using a standard audio cable. The amplified signal was the input to a multimedia speaker (2″, 4Ω 12W Stereo Audi Speaker, DROK), modified by removing the cover and cone to place a rigid substrate holder directly onto the vibrating voice coil. All reported frequencies were experimentally measured using high speed imaging. The measured amplitudes, defined as the half distance between the two vibration extrema, varied between $A = 0.3 – 2.5$ mm. Figure 4.3a shows the setup for the rigid vibrating sample, where a superhydrophobic coated glass slide was placed directly on the rigid substrate holder. Figure 4.3b depicts the setup for the elastic vibrating sample, where a thin superhydrophobic polymer sheet was mounted on the substrate holder, protruding on one side, resulting in a cantilever mount. Individual droplets impacted near the free end of the cantilever substrate (within 6 mm of the edge), where the loudspeaker vibration amplitudes were characterized. The third substrate configuration is shown in Figure 4.3c, where the elastic substrate was mounted as a cantilever on a stationary substrate holder. A dual twin tip needle (TS25DSS-1/2, Adhesive Dispensing Ltd) generated two droplets at a lateral distance Δx (2.5 – 3.0 mm) and with a time delay Δt (10 – 160 ms). The first droplet caused the substrate to vibrate at its natural eigenfrequency, while we monitored the impact dynamics of the second droplet.

The three different configurations allowed us to differentiate between strong and weak amplitudes and accelerations, as well as substrate response to droplet impact. In the following we will present droplet and substrate dynamics for the three configurations individually and then conclude by comparing results from the three scenarios.

5.3 Results and Discussion

5.3.1. Case 1: Forced Vibration of a Rigid Substrate

We first considered droplet impact on rigid superhydrophobic surfaces subject to forced vibration (Figure 5.1a). We find that droplet dynamics and contact times can vary significantly depending on the phase of the substrate vibration at the moment of impact, called impact phase. Substrate frequency and amplitude play only a minor role in altering droplet dynamics. Figure 5.2 shows optical images of rebounding droplets under different impact conditions. The droplet in Figure 5.2a impacted a stationary reference sample and displayed the traditional spreading, recoil and lift-off mechanism governed by the inertial-capillary scaled contact time (in the following called theoretical contact time)[24]:

$$t_{c,th} = 2.6\sqrt{\frac{\rho D_0^3}{8\gamma}}\,. \tag{5-1}$$

For droplet with an initial diameter D_0 = 2.5 mm, the theoretical contact time is $t_{c,th}$ = 13.5 ms. It should be noted that the contact time on stationary rigid hydrophobic surfaces is independent of impact speed[2,24]. Figure 5.2b shows a droplet with the shortest possible contact time with $t_c \approx t_{c,th}/2$. In the example shown, the droplet underwent pancake bouncing, where the droplet lifted off the surface near maximum spreading without recoiling[14]. As we will show later, contact time minimization is associated with impact at a critical phase. Impact at the same phase, but with higher vibration amplitudes, resulted in a superposition of pancake bouncing and crown splashing (Figure 5.2c). The droplet rim detached while the momentum of the center of the droplet was still downward and the droplet thus remained in contact with the substrate. Due to the resemblance of the droplet shape to a calyx, we call this droplet bouncing mechanism *tulip-splashing*. In some cases, when droplets impacted at a phase smaller than the critical phase, we first observed pancake bouncing, with the vibrating substrate catching up with the departing droplet, resulting in droplet re-attachment and another, more chaotic, impact cycle (Figure 5.2d). The combined contact time of first and second impact cycle was longer than the theoretical contact time. Impact at a similar phase, but higher vibration frequency and amplitude led to crown splashing with greatly reduced contact times (Figure 5.2e). Impact slightly after the critical phase also increased contact times. Initial droplet spreading and recoil were similar to those on a stationary substrate; however, the liquid jet remained in contact with the substrate and droplet lift-off was delayed, as shown in Figure 5.2f. In addition to these six droplet behaviors, we observed many hybrid shapes for slightly varying impact conditions, which are not discussed here in detail.

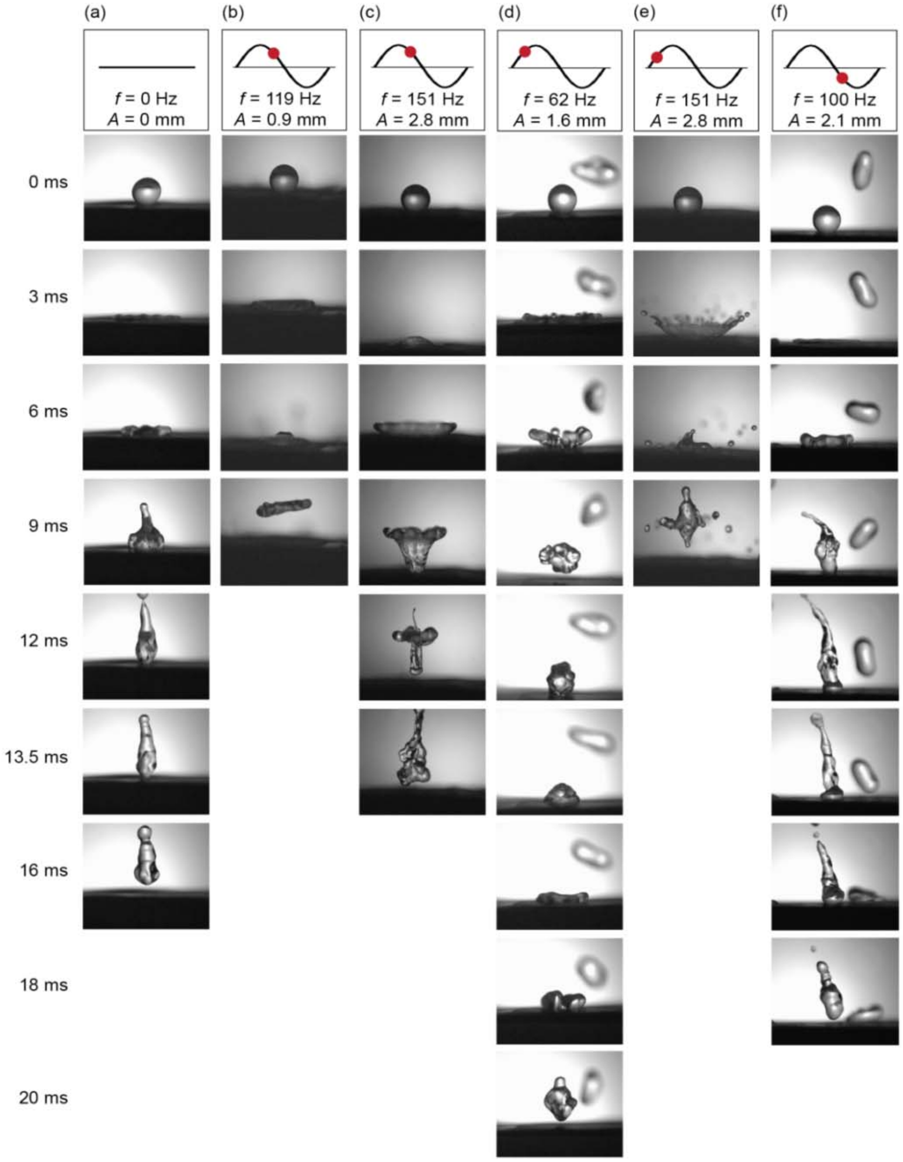

Figure 5.2: Droplet shapes for various impact conditions ($D_0 \approx 2.5$ mm) during impact on rigid superhydrophobic surfaces**.** (a) Impact on a stationary substrate with traditional spreading, recoil and lift-off at the theoretical contact time $t_{c,th}$. (b)-(f) Impact on vibrating substrates. A red dot marks the impact phase. (b) Impact just below the critical impact phase led to pancake bouncing and the shortest contact times $t_c \approx t_{c,th}/2$. (c) At higher amplitudes, a superposition of pancake bouncing and crown splashing occurred, called tulip splashing. (d) At phases smaller than the critical phase, the substrate catched up with the departing droplet after initial pancake bouncing and caused droplet re-attachment. (e) Droplets splashed when the droplet acceleration was greater than a critical value. (f) Impact just above the critical phase led to long jets and the longest contact times $t_c > t_{c,th}$.

As seen from the images in Figure 5.2, contact times and droplet dynamics are very sensitive to impact conditions. Figure 5.3a shows the normalized contact times, i.e. actual contact time over theoretical contact time, $t_c/t_{c,th}$, for all vibration frequencies and amplitudes as a function of impact phase. At first, there seems to be no clear connection between contact time and frequency, amplitude, and phase. However, even from this rather chaotic plot we can identify two important findings: (1) all contact times are well bounded by $0.5t_{c,th} \leq t_c \leq 1.5t_{c,th}$, i.e. contact times can increase or decrease relative to the theoretical contact time on a stationary substrate, and (2) within small frequency ranges, contact times are mostly independent of vibration amplitude (± 7% variation). In light of the amplitude independence, we can combine our data to obtain a clearer depiction of the trends, as shown in Figure 5.3b, for a subset of frequencies including all respective vibration amplitudes. Open symbols represent droplets that splashed during impact. Dotted lines are trend lines of contact times as a function of impact phase. For each frequency, contact times suddenly increase at certain impact phases and decrease monotonically thereafter (recall that 360° = 0° of the next vibration period). For frequencies of 61, 100, 151, and > 200 Hz, the discontinuity occurs at $\varphi \approx 20°$, 175°, 100°, and 100°, respectively. From Figure 5.3b, we can also notice that average contact times decrease for an increase in vibration frequency, and that the jump at the discontinuity becomes smaller for higher frequencies, i.e. contact times become less dependent on the impact phase for increasing vibration frequencies.

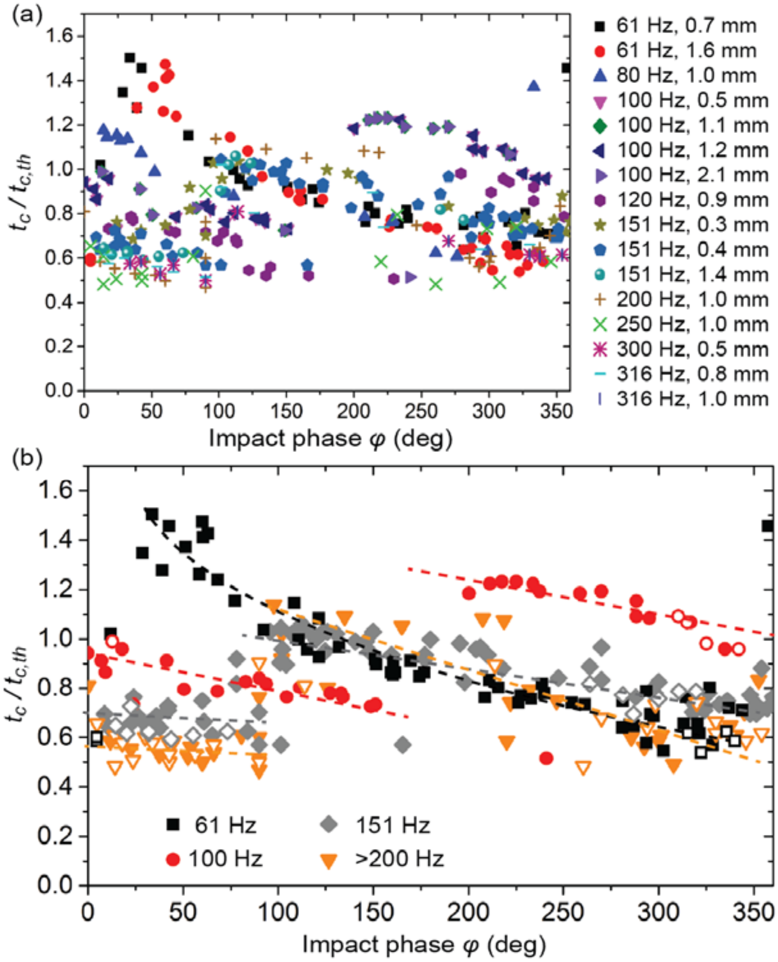

Figure 5.3: Contact time analysis. (a) Normalized contact times as a function of impact phase on vibrating rigid superhydrophobic surfaces for all substrate vibration frequencies and amplitudes. Contact times show a small dependence on vibration amplitude (± 7%). (b) Sub-set of data from (a), where amplitudes for each frequency are combined for a clearer view. Dotted lines represent trend lines. For each frequency, contact times suddenly increase at a certain impact phase and decrease thereafter. Open symbols represent droplets that splashed during impact.

To understand the origin of the discontinuity in contact times, we analyzed the interplay between substrate position and droplet dynamics in more detail. Figure 5.4a shows the distribution of departure phases for bouncing droplets. Intuitively, droplets would lift off when the substrate is at its top dead center, i.e. at 90°, at the point that the substrate starts moving downward. Indeed, most droplets lifted off at phases between 80 and 180°. Experimentally, the average departure phase was $\varphi_d \approx 135°$. Physically, when the substrate moves upwards, it imparts vertical momentum to the spread droplet, and droplet lift-off is initiated. Due to droplet inertia, final droplet departure is delayed beyond $\varphi_d \approx 90°$, until the substrate moves downward, away from the droplet. With the quantification of a mean departure phase, we can now estimate the impact phase that would minimize contact times. From Figure 5.3 the minimum contact time is $t_{min} = t_{c,th}/2$, where $t_{c,th}$ is described by Eq. (5-1). The critical impact phase φ_c when the discontinuity in contact time (Figure 5.3b) occurs can be defined as:

$$\varphi_c = \varphi_d - 2\pi f t_{\text{min}} \,. \tag{5-2}$$

For impact just prior to the critical phase, contact times are minimized, while droplets impacting at a later point cannot detach prior to the next full vibration period. Therefore, for the vibration frequencies (60 – 320 Hz) and amplitudes (0.3 – 2.5 mm) examined in this study, the maximum contact time can be approximated by:

$$t_{\text{max}} = t_{\text{min}} + \frac{1}{f} \,. \tag{5-3}$$

Assuming that contact times vary linearly with impact phase we can then write:

$$t(\varphi - \varphi_c) = t_{\text{max}} - \frac{(\varphi - \varphi_c)}{2\pi f} \,. \tag{5-4}$$

Due to the periodicity of the vibration we introduce a normalized impact phase which includes the modulus of one vibration period, $\varphi^* = [(\varphi - \varphi_c),(\text{mod } 2\pi)]$, and a non-dimensional contact time $t^* = f(t - t_{min})$. Equation (5-5) then becomes:

$$t^* = 1 - \frac{\varphi^*}{2\pi} \,. \tag{5-5}$$

Figure 5.4b compares the experimental data along with Eq. (5-5). The excellent agreement between model and data supports our hypothesis of a critical impact phase at which contact times transition from a minimum to a maximum. The scatter in data in the upper right and lower left corners in Figure 5.4b arises from deviations of the actual departure phase from φ_d = 135°.

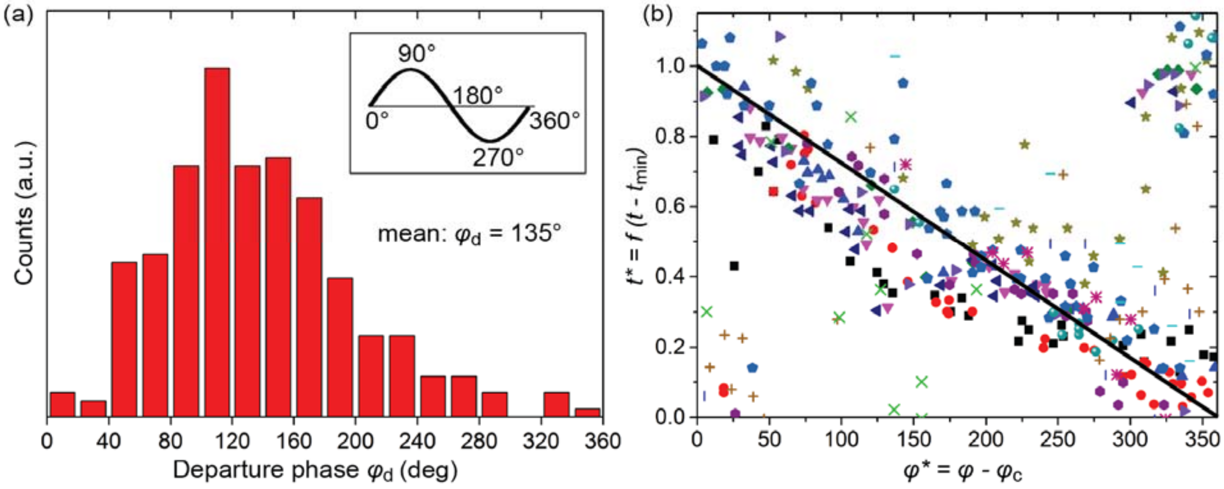

Figure 5.4: Departure phase and non-dimensional contact times for droplet impact on vibrating rigid superhydrophobic surfaces. (a) Distribution of droplet departure phase. (b) Non-dimensional contact times as a function of normalized impact phase with φ_d = 135°. Data points used were the same plotted in Figure 5.3a. The solid line shows Eq. (5-5).

In an effort to explain the origin of the minimum contact time, we considered the free oscillation of a droplet and identified the point of maximal vertical droplet momentum. When droplets impact a rigid stationary solid, they are compressed and loose a degree of freedom during spreading. For modeling purposes, we assume that during impact on vibrating surfaces, droplets can re-gain the vertical degree of freedom when the substrate retreats downwards during a vibration cycle. During spreading and recoil, droplets then undergo a quasi-free oscillation with an oscillation period $\omega = 2\pi/t_\mathrm{c,th}$. The time evolution of the droplet diameter during oscillation can then be written as:

$$D(t) = D_0 \xi^{\frac{1}{4}(3+\sin(\omega t))\sin(\omega t)}, \tag{5-6}$$

where $\xi = 0.22\ We^{0.5} + 0.7$ is the dimensionless maximum spreading parameter, as outlined in Chapter 4, Eq. (4-6). For the impact conditions in this study, $We \approx 65$, and thus $\xi \approx 2.45$. Assuming an elliptical shape of the droplet, the height evolution becomes:

$$H(t) = \frac{D_0^3}{D(t)^2}. \tag{5-7}$$

Figure 5.5 compares the analytical model with the experimental time evolution of the droplet diameter and height. The agreement between model good enough to provide an estimate of the minimal contact time. We propose that the minimum contact time occurs when the droplet internal vertical momentum is maximum:

$$\left.\frac{d^2H}{dt^2}\right|_{t=t_{min}} = 0. \tag{5-8}$$

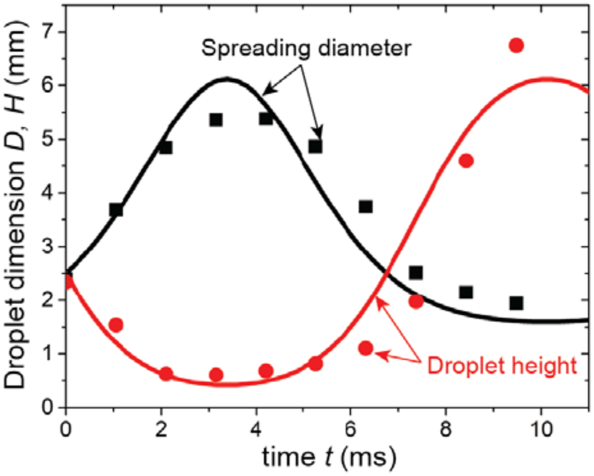

Figure 5.5: Spreading droplet diameter and height as a function of time for droplet impact on vibrating rigid superhydrophobic surfaces.

Solving Eq. (5-8) with (5-7) yields $t_{\mathrm{min}} = 0.54t_{\mathrm{c,th}}$; the characteristic time we would expect for a freely oscillating droplet. This is in good agreement with the lowest contact times observed in our experiments, $t_{\mathrm{c,exp}} \approx 0.5t_{\mathrm{c,th}}$. The presence of the substrate partially restrains such free oscillation, and real contact times are a superposition of the theoretical minimum contact time based on the droplet internal maximum vertical momentum and momentum imposed by the substrate.

As discussed earlier in this section, and as can be seen in Figure 5.3, vibration amplitudes in the range A = 0.3 – 2.1 mm have little effect on contact times. However, when the amplitude approaches zero, i.e. no vibration, contact times should be constant at $t_c = t_{c,th}$. Additionally, average contact times decrease with increasing vibration frequency and become more homogeneous with impact phase. To better understand the interplay between vibration frequency, amplitude, impact phase, and contact time, we numerically modeled the average contact times, taking into account the probability density function for droplet impact at a certain phase given vibration amplitude and frequency. It is easy to imagine that for high vibration frequencies and amplitudes the probability of the droplet hitting the substrate at a certain phase is not equally distributed. Assuming that the droplet makes contact with the substrate at phase φ, then the vertical distance s between droplet and substrate prior to impact can be described using:

$$s = A - vt - A\sin(2\pi f t + \varphi_0)\,, \tag{5-9}$$

where the position of an initial impact phase φ_0 is shown in Figure 5.6a. At impact (s = 0) the position of φ_0 becomes:

$$\varphi_0 = v^*(\sin\varphi - 1) + \varphi\,, \tag{5-10}$$

where $v^* = A\omega/v$ is the normalized substrate velocity. Equation (5-10) represents the impact probability as a function of substrate phase. Figure 5.6b plots the initial phases as a function of impact phase for various normalized substrate velocities. For $v^* \to 0$, i.e. for very small vibration amplitudes, as expected, the probability for droplet impact is the same for all phases. However, for increasing amplitudes, the probability for impact at $\varphi \approx 115 - 270°$ becomes increasingly smaller. For an impact speed of v = 1.35 m/s, as used in the current experiments, the critical normalized substrate velocity $v^* = 1$ is reached for amplitudes A = 3.5 mm, 1.4 mm, and 0.7 mm for vibration frequencies of f = 61 Hz, 151 Hz, and 300 Hz, respectively. For $v^* > 1$ it is physically impossible for droplets to impact the substrate at $\varphi_1 \leq \varphi \leq \varphi_2$, as marked with the dashed line in Figure 5.6b.

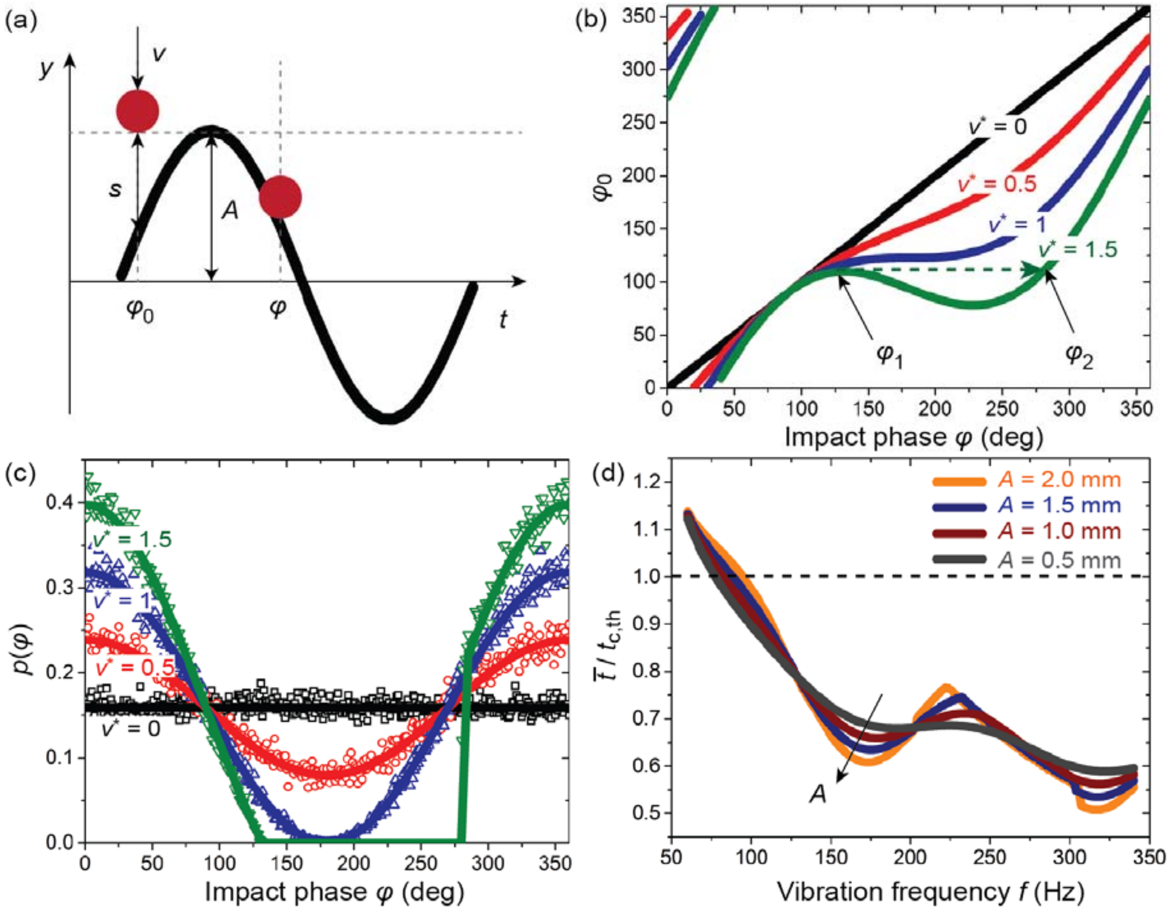

Figure 5.6: Effect of vibration frequency, amplitude, and phase on contact times for droplet impact on vibrating rigid superhydrophobic surfaces. (a) Schematic showing the initial and impact phases. (b) Initial phase as a function of the impact phase as defined by Eq. (5-10). (c) Probability density function for droplet impact at a certain phase following Eq. (5-11). Symbols show results from a Monte-Carlo simulation with 100,000 runs. For $v^* > 1$, impact becomes physically impossible at $\varphi_1 \leq \varphi \leq \varphi_2$ (discontinuity in green curve). (d) Predicted average normalized contact time as a function of frequency and amplitude following Eq. (5-14).

The probability density function for droplet impact at the phase φ then is:

$$p(\varphi) = \begin{cases} 0, & \varphi_1 \le \varphi \le \varphi_2 \\ \dfrac{1}{2\pi}(v^* \cos\varphi + 1), & \text{else} \end{cases}, \tag{5-11}$$

where the phase angles φ_1 and φ_2 are defined as:

$$\varphi_1 = \cos^{-1}\left({-1}/{v^*}\right), \tag{5-12}$$

$$\varphi_2 + v^* \sin\varphi_2 = \sqrt{v^{*2} - 1} + \cos^{-1}\left({-1}/{v^*}\right). \tag{5-13}$$

Figure 5.6c shows Eq. (5-11) along with the results from a Monte-Carlo simulation with 100,000 runs. The match between the simulation and the analytical model is excellent. For $v^* > 1$, impact becomes physically impossible at $\varphi_1 \le \varphi \le \varphi_2$, as illustrated by the discontinuity in the green curve. Comparison to Figure 5.3a shows good agreement between observed data and predicted gaps in the impact phase. The phase-averaged contact time of an impacting droplet can then be calculated using:

$$\bar{t}(f, A) = \int_{\varphi_2}^{\varphi_1} t(\varphi) p(\varphi) d\varphi\,. \tag{5-14}$$

The contact time $t(\varphi)$ is described by Eq. (5-4), using the modulus of ($\varphi - \varphi_c$). Note that the validity of this model is restricted to the amplitudes (0.3 – 2.5 mm) and frequencies (60 – 320 Hz) used in the present experiments, due to the definition of $t_{\max}$ (Eq. (5-3)). Equation (5-14) was solved numerically (Appendix C) and is plotted in Figure 5.6d. Qualitatively, the numerical model matches our experimental observations well. Figure 5.6d confirms that contact times depend only weakly on the vibration amplitude. The discontinuity in the average contact time for higher amplitudes arises from the impossibility of droplets to impact the substrate at certain vibrational phases. Overall, contact times decrease with increasing vibration frequency, and show local minima at $f \approx 170$ Hz and 320 Hz. Average contact times for small vibration frequencies $f < 80$ Hz are higher than the theoretical contact time on a stationary rigid superhydrophobic substrate. For $f > 80$ Hz, contact times are reduced.

5.3.2. Case 2: Forced Vibration of an Elastic Substrate

After understanding the effect of frequency, amplitude and phase on the contact times on vibrating rigid surfaces, we were interested in studying the effect of the same parameters on vibrating elastic or flexible, surfaces. In this section we focus on elastic superhydrophobic substrates subject to forced vibrations at $f = 60$ and 120 Hz and effective amplitudes of $A = 0.8 – 2.7$ mm at the location of droplet impact. The next section (5.3.3) presents results on freely vibrating elastic surfaces.

Droplet dynamics and contact times during impact on elastic surfaces subject to forced vibration are similar to those on vibrating rigid surfaces. Figure 5.7 shows graphs of the substrate deflection δ along with optical images to illustrate droplet dynamics for three different impact conditions. Figure 5.7a shows a droplet impacting the vibrating substrate at $\varphi = 295°$, near the bottom dead center of substrate vibration, such that the impact has little influence on the vibration of the substrate. With a substrate vibration at $f = 60$ Hz and $A = 2.7$ mm, the droplet hit the substrate just prior to the critical phase $\varphi \lesssim \varphi_c = 316°$. The droplet spread and lifted off in a pancake shape with a contact time shorter than the theoretical contact time, $t_c < t_{c,th}$. When the droplet impacted the substrate at $\varphi > \varphi_c$, as shown in Figure 5.7b for $f = 60$ Hz and $A = 1.4$ mm, it first spread and then elongated vertically, forming a jet-like shape. When the substrate moved upwards, the droplet compressed. Finally, near the substrate top dead center, the droplet lifted off at $t_c > t_{c,th}$.

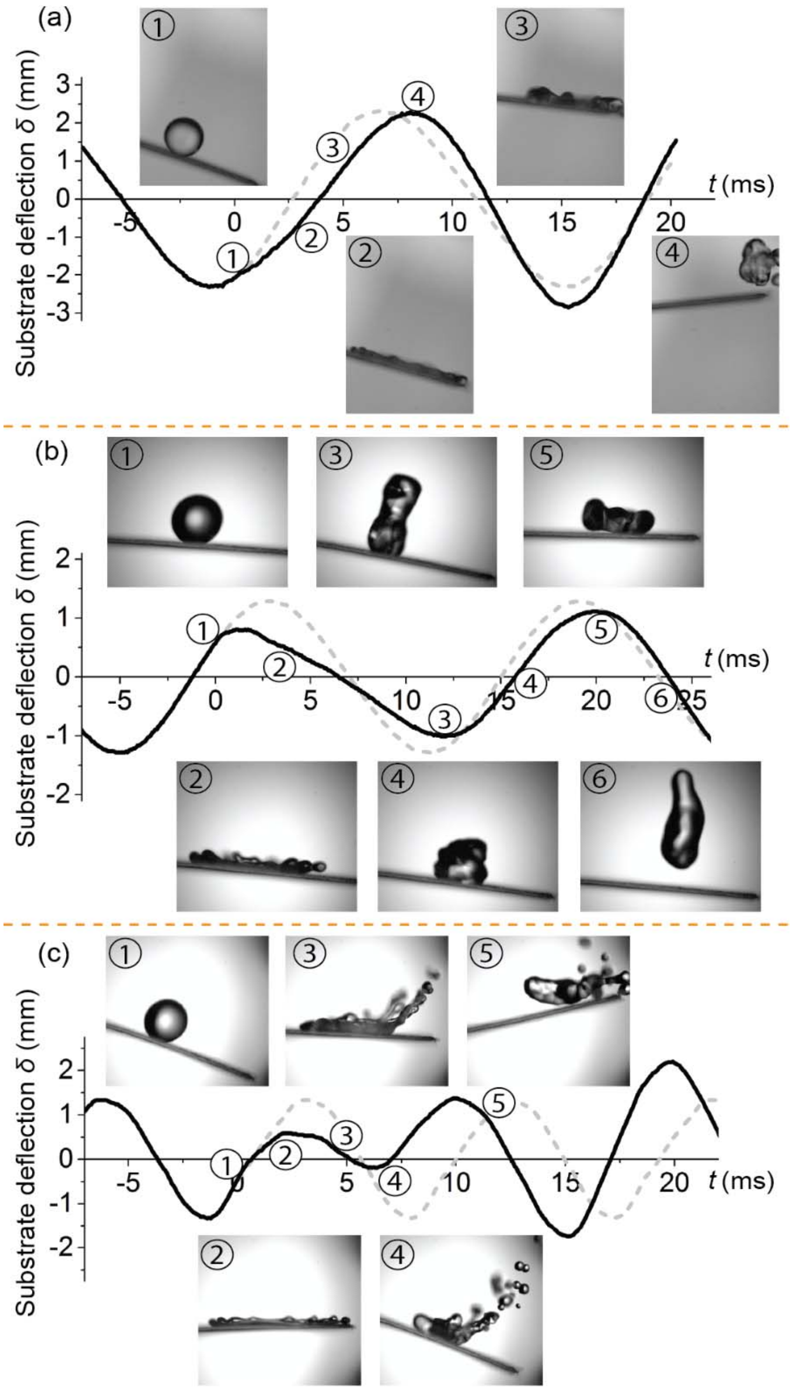

Figure 5.7: Substrate deflection and droplet shapes for various impact conditions ($D_0 \approx 2.5$ mm) on elastic superhydrophobic surfaces under forced vibration. The droplet impact influences the substrate movement on the elastic vibrating substrates. Solid black curves represent the actual substrate deflection, while the gray dotted lines represent the natural substrate vibration without impact. (a) Impact at $\varphi = 295°$ ($\varphi_c = 316°$) resulted in a reduced contact time ($t_c < t_{c,th}$) ($f = 60$ Hz, $A = 2.7$ mm). (b) Impact at $\varphi = 26°$ ($\varphi_c = 322°$) resulted in an elongated contact time ($t_c > t_{c,th}$) ($f = 60$ Hz, $A = 1.4$ mm). (c) The droplet splashed at $\varphi = 326°$ ($f = 120$ Hz, $A = 2.0$ mm).

Figure 5.7c shows the dynamics of a splashing droplet impacting at $\varphi = 326°$ on a substrate with $f = 120$ Hz and $A = 2.0$ mm. The substrate vibrated as a cantilever, i.e. the droplet impacted an inclined surface for $\varphi \neq 0, 180°$. Due to a faster vertical acceleration away from the substrate mount, the droplet splashing symmetry was broken and satellite droplets ejected preferentially at the side facing the substrate free end where acceleration was maximum and the slope of inclination highest. The remaining droplet core lifted off in a pancake-like shape. A similar non-symmetric splashing has been observed for oblique droplet impact[25,26].

When droplets impacted the substrate away from the top and bottom dead ends of vibration, as seen in Figure 5.7 b and c, they manipulated the substrate vibration. The vibration amplitude decreased in the cycle after the droplet impact and the local vibration frequency shifted. After a few vibration periods, however, the original vibration frequency and amplitude were re-established. The detailed substrate response was extremely complex, and dependent on the axial impact location, phase, frequency, amplitude, and is out of the scope of this work. Droplet dynamics for other impact conditions were similar to those presented above and mainly depended on the impact phase and its relation to the critical impact phase. Vibration frequency and amplitude affected the likelihood of splashing, but had little influence on the dynamics of non-splashing droplets.

Figure 5.8 shows the contact times for droplets impacting elastic substrates subject to forced vibration. Qualitatively, the contact times are identical to those on vibrating rigid surfaces. Figure 5.8a shows the normalized contact time as a function of impact phase for two vibration frequencies and two amplitudes. Contact times are well bounded by $0.5\mathrm{t}_{\mathrm{c,th}} < t_c < 1.6\mathrm{t}_{\mathrm{c,th}}$. Similar to the observations made in section 5.3.1, contact times jumped from a minimum to a maximum at a critical frequency-dependent impact phase, and were independent of the vibration amplitude.

Open symbols in Figure 5.8a represent droplets that splashed during impact. We can conclude that splashing did not influence the contact time of impacting droplets. Figure 5.8b shows that all data collapses onto a single line according to Eq. (5-5).

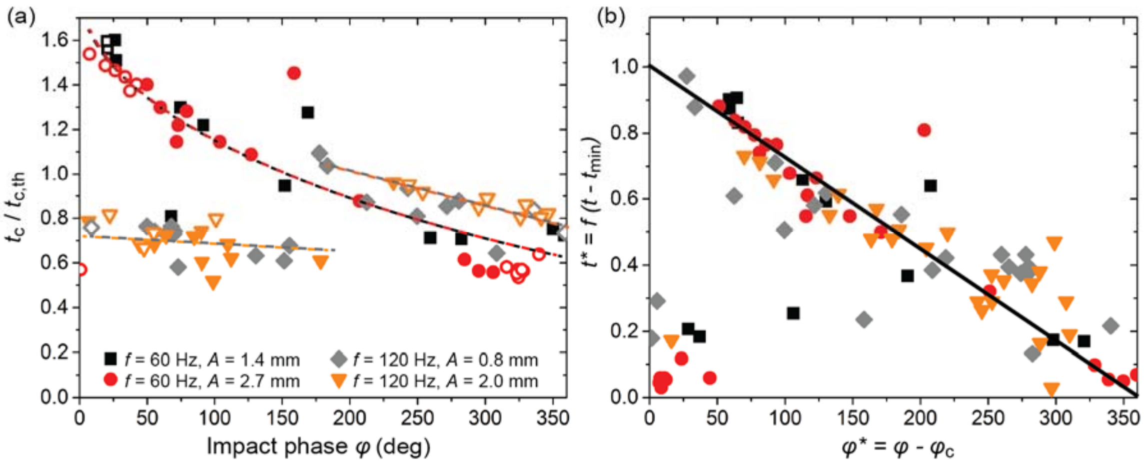

Figure 5.8: Normalized and non-dimensional contact times for impacting droplets on vibrating elastic superhydrophobic surfaces as a function of impact phase**.** (a) All experimental data as a function of substrate vibration frequency and amplitude. Open symbols represent droplets that splashed during impact. Dotted lines represent trend lines. Contact times are similar to those on vibrating rigid surfaces shown in Figure 5.3. (b) Non-dimensional contact times as a function of normalized impact phase with $\varphi_d = 135°$. The solid line represents Eq. (5-5).

5.3.3. Case 3: Free Vibration of an Elastic Substrate

After ascertaining that droplet dynamics and contact times on rigid and elastic substrates subject to forced vibration are identical, we next turned to freely vibrating elastic substrates. Here, two droplets impacted an elastic substrate initially at rest (Figure 4.3c). While the first droplet caused the substrate to undergo a free, damped vibration, we were interested in the droplet dynamics and contact times of the second droplet. The frequency and amplitude of the vibration were set by the eigenfrequency and stiffness of the substrate, the impact force of the first droplet[14], and the time delay Δt between first and second droplets. The substrate was designed such that it obeyed both conditions for contact time reduction, as outlined in Chapter 4, section 4.4,[14] for the given impact speeds ($v \approx 1.2$ m/s). We tested vibration frequencies of $f \approx 60$ and 140 Hz. The maximum amplitude after impact ranged from $A = 0.25$ to 2.0 mm. Amplitudes just prior to impact were smaller, and in the range $A = 0.04 – 0.9$ mm.

Figure 5.9 shows graphs of the substrate deflection δ along with droplet images to illustrate droplet dynamics for short and long time delays between first and second droplet impact. For a short delay time between the two droplets ($\Delta t = 20$ ms), the peak amplitude before the second impact was greatest (Figure 5.9a). At longer time delay ($\Delta t = 75$ ms), the vibration amplitude decreased (Figure 5.9b). However, we did not observe a difference in droplet dynamics and contact times based on the time delay between both droplets. Irrespective of the vibration amplitude prior to impact, the impact force of the second droplet caused the substrate to instantly deflect downward to a maximum amplitude corresponding to the droplet impact force. Thus, droplet dynamics were almost identical to those during impact on stationary elastic substrates, which have been presented in Chapter 4,[14] and are also illustrated in Figure 5.9.

The insensitivity of droplet dynamics on substrate vibration is reflected in contact times, which are similar to those on stationary elastic substrates. Figure 5.10a shows the normalized contact times of droplets impacting freely vibrating elastic substrates. In contrast to contact times presented in the previous sections on substrates undergoing forced vibration, contact times for the present case were always equal to, or smaller than the theoretical contact time ($t_c \leq t_{c,th}$). Contact times decreased for increasing vibration frequency, but were independent of vibration amplitude. Contact times also appeared to be independent of impact phase.

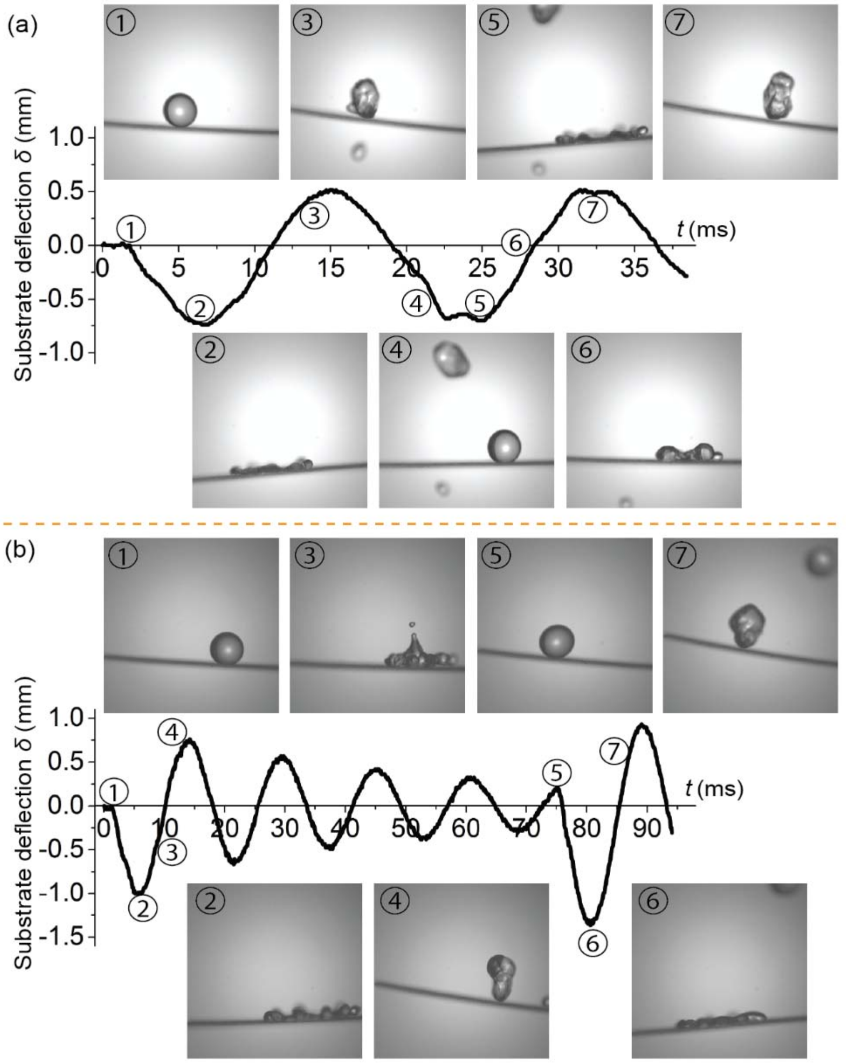

Figure 5.9: Substrate deflection and droplet shapes for short and long time delays during two-droplet impact on elastic superhydrophobic surfaces ($D_0 \approx 2.5$ mm). (a) Short time delay (Δt = 20 ms) between both droplets. (b) Long time delay (Δt = 75 ms) between both droplets.

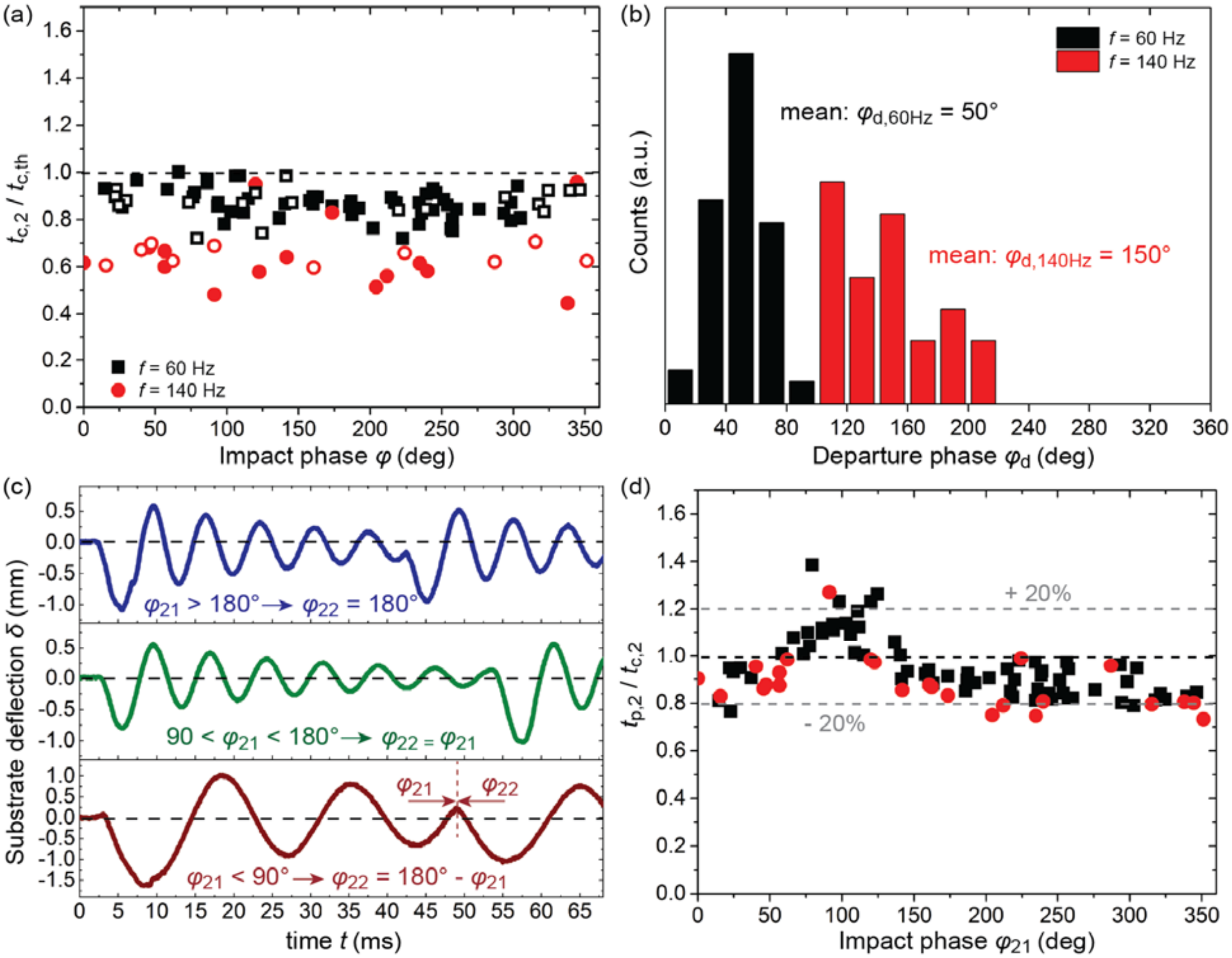

Figure 5.10: Contact times and phase dependence for two-droplet impact on elastic superhydrophobic surfaces. (a) Normalized contact times as a function of impact phase. Contact times decrease for increasing substrate eigenfrequencies. In all cases, contact times are independent of impact phase, and $t_c \leq t_{c,th}$. Open symbols represent droplets that splashed during impact. (b) Distribution of droplet departure phase as a function of vibration frequency. Droplets lifted off earlier for the lower vibration frequencies (f = 60 Hz) than during the faster substrate oscillations. (c) Substrate deflection curves for three impact conditions: $\varphi_{21} > 180°$, $90° < \varphi_{21} < 180°$, and $\varphi_{21} < 90°$. (d) Ratio of predicted to observed contact times of the second droplet as a function of impact phase φ_{21}.

To understand the connection between the substrate vibration eigenfrequency and contact time, we analyzed the droplet departure phases for f = 60 Hz and 140 Hz (Figure 5.10b). Droplets on the substrate vibrating at 60 Hz lifted off the substrate at phases ranging from 0 to 100°, while those on the f = 140 Hz substrate departed at phases between 100 and 220°. There was no overlap in departure phase for the two frequencies. The mean departure phases are thus $\varphi_{\mathrm{d,60Hz}}$ = 50° and $\varphi_{\mathrm{d,140Hz}}$ = 150°, which deviate from the departure phase on substrates subject to forced vibration. Most probably, droplet inertia and the related time scale caused the difference in departure phases for the two vibration frequencies.

Next, we turned to examining the effect of impact on the substrate vibration. Figure 5.10c illustrates three impact scenarios. As mentioned above, immediately after impact ($\mathrm{d}t \rightarrow 0$), the substrate moves down, irrespective of its momentum prior to impact, and the phase jumps to a different value. We thus define the phase just prior to impact as φ_{21}, i.e. $\lim_{\varphi \to -\varphi_i} \varphi = \varphi_{21}$, and the phase right after impact as φ_{22}, i.e. $\lim_{\varphi \to +\varphi_i} \varphi = \varphi_{22}$, as illustrated in the bottom chart of Figure 5.10c. In the first case (top curve), the second droplet impacted the substrate at $180° < \varphi_{12} < 360°$. At the moment of impact the substrate commenced a new vibration cycle with full amplitude, allowing us to write $\varphi_{22} = 180°$. For an impact at $90° < \varphi_{12} < 180°$, as shown in the middle curve, the substrate started the new vibration at a phase that is equivalent to the instantaneous amplitude at φ_{12}, thus allowing us to write $\varphi_{22} = \varphi_{12}$. In the third case, the droplet impacted at $0° < \varphi_{12} < 90°$ (bottom curve). The substrate completely reversed its momentum and – similar to the second case – initiated a new vibration cycle with an amplitude superposition caused by the impact force and the residual amplitude of the previous vibration cycle. The new impact phase thus becomes $\varphi_{22} = 180° - \varphi_{12}$. To summarize:

$$\varphi_{22} = \begin{cases} 180°\ , & 180° < \varphi_{22} < 360° \\ \varphi_{21}\ , & 90° < \varphi_{22} < 180° \\ 180° - \varphi_{21}\ , & 0° < \varphi_{22} < 90° \end{cases} . \tag{5-15}$$

It should be noted that Eq. (5-15) is a simplification of the actual substrate and droplet dynamics, and captures the physics of many, but not all, experimental cases (an exception can be seen, for example, in Figure 5.9a).

Combining the information of impact and departure phases we can estimate the contact time of droplets impacting freely vibrating substrates. Observing that the droplets lift off in the period directly following impact, the predicted contact time becomes:

$$t_p(\varphi) = t_p(\varphi_{21}) = \frac{\varphi^{**}}{2\pi f}, \tag{5-16}$$

where $\varphi^{**} = (360° - \varphi_{22}) + \varphi_{\mathrm{d}}$ is the net normalized impact phase. Equation (5-16) shows good agreement with experimental data (± 20%), as depicted in Figure 5.10d.

Overall, droplet dynamics and contact times are very different on freely vibrating elastic substrates from those on forced vibrating substrates. Specifically, contact times were determined to be consistently smaller than the theoretical contact time. However, the vibration frequency has a stronger influence on the contact times for freely vibrating elastic substrates when compared to forced vibration. Freely vibrating elastic superhydrophobic surfaces thus have the potential to passively reduce contact times of impacting droplets. Successive droplet impacts (Δt = 10 – 160 ms) do not influence the potential of contact time reduction on elastic superhydrophobic surfaces.

5.3.4. Comparison of Droplet Dynamics

Having investigated droplet dynamics and contact times for the forced rigid, forced elastic, and free elastic scenarios separately, we now directly compare data for the three cases. Figure 5.11 shows droplet images acquired during similar impact conditions on the three substrates. Impact frequency and phase were approximately the same ($f \approx$ 120 Hz, $\varphi \approx$ 60 and 280°), while the vibration amplitude differed slightly (A = 0.2 – 0.9 mm). However, as pointed out in the previous sections, the amplitude had little effect on droplet dynamics, and thus a direct comparison, even with different amplitudes, is justified. Figure 5.11a and b compare droplet shapes at $f \approx 120$ Hz and $\varphi \approx 60°$, i.e. close to the top dead center, and $f \approx 120$ Hz and $\varphi \approx 280°$, i.e. near the bottom dead center, respectively. From section 5.3.1 we estimate the critical phase at which contact time jumps from a minimum to a maximum to be $\varphi_c \approx 200°$ for $f = 120$ Hz. Thus Figure 5.11a compares droplet dynamics for $\varphi < \varphi_c$, while Figure 5.11b represents impact conditions with $\varphi > \varphi_c$. Droplet dynamics and contact times were similar for all three scenarios at $\varphi \approx 60°$. On the substrates undergoing forced vibration, the edges of the droplet, or the lamella, lifted off at early stages of the spreading process (2-4 ms), while the substrate moved downwards. As the substrate moved upwards, the lamella re-attached, and the entire droplet lifted off near the top dead center of the substrate vibration. Due to the inclination of the elastic substrate during vibration, the droplet slid along the substrate, resulting in a loss of symmetry. However, this sliding did not influence the contact time of the bouncing droplet[14,27]. On the freely vibrating substrate, we observed the traditional droplet spreading, followed by a superposition of traditional recoil and pancake bouncing.

Droplet dynamics and contact times at $\varphi \approx 280° > \varphi_c$ differed greatly for the three impact scenarios. On the rigid vibrating substrate the droplet showed strong fingering and underwent splashing with $t_c \approx t_{c,th}$. Droplet dynamics on the elastic substrate subject to forced vibration were similar to those for $\varphi \approx 60°$, however the contact time was slightly longer, yet still $t_c < t_{c,th}$. On the freely vibrating substrate, the droplet spread and formed small satellite droplets during recoil. The contact time was strongly reduced to $t_c << t_{c,th}$. Summarizing Figure 5.11, we can conclude that droplet dynamics, including droplet shape, splashing, and contact times, are extremely complex, and vary strongly with various impact conditions (substrate mount and flexibility, impact phase, vibration frequency, etc.).

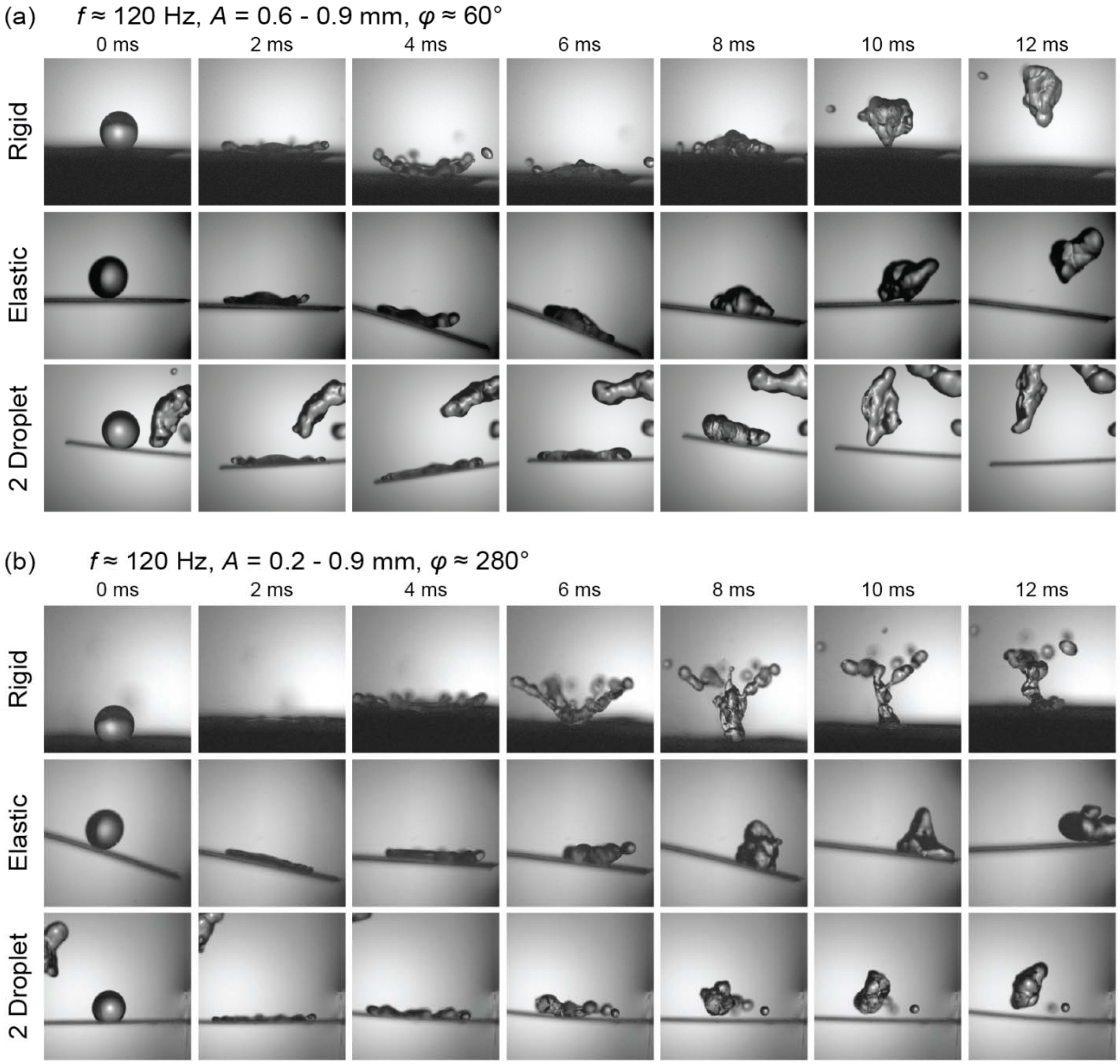

Figure 5.11: Comparison of droplet dynamics for impact on rigid vibrating, elastic vibrating and freely vibrating elastic surfaces (D_0 = 2.5 – 2.8) under similar impact and vibration conditions. (a) Vibrations with $f \approx 120$ Hz, A = 0.6 – 0.9 mm, and $\varphi \approx 60°$. Contact times on the rigid, forced vibration elastic and free vibration elastic surfaces are t_c = 9.8 ms, t_c = 10.0 ms, and t_c = 9.1 ms, respectively. (b) Vibrations with $f \approx 120$ Hz, A = 0.2 – 0.9 mm, and $\varphi \approx 280°$. Contact times on the rigid, forced vibration elastic and free vibration elastic surfaces are t_c = 13.2 ms, t_c = 11.9 ms, and t_c = 7.0 ms, respectively.

After comparing droplet dynamics, we now turn to a direct comparison of contact times for the three vibration scenarios. Figure 5.12 displays the contact times for all experimental data as a function of the effective impact speed, v_{eff}. The effective impact speed, or net impact speed, is a superposition of droplet speed and substrate velocity at the moment of impact:

$$v_{eff} = v + 2\pi f A \cos\varphi \,. \tag{5-17}$$

For impact on forced vibrating substrates (both rigid and elastic), the effective impact speeds were $0 < v_{\mathrm{eff}} < 3.5$ m/s. Due to low vibration frequencies and amplitudes of the freely vibrating substrates, effective impact speeds were limited to a small range of $v_{\mathrm{eff}} = 1.5 - 2.0$ m/s. As expected[22], the effective impact speed did not influence contact time. As derived in the three previous sections, contact times are influenced by the vibration frequency and impact phase (forced vibration). Contact times on the freely vibrating substrate are independent of the impact phase and limited to $t_c \leq t_{c,\mathrm{th}}$, while contact times of droplets impacting substrates subject to forced vibration can be up to 1.6 times higher than the theoretical contact time.

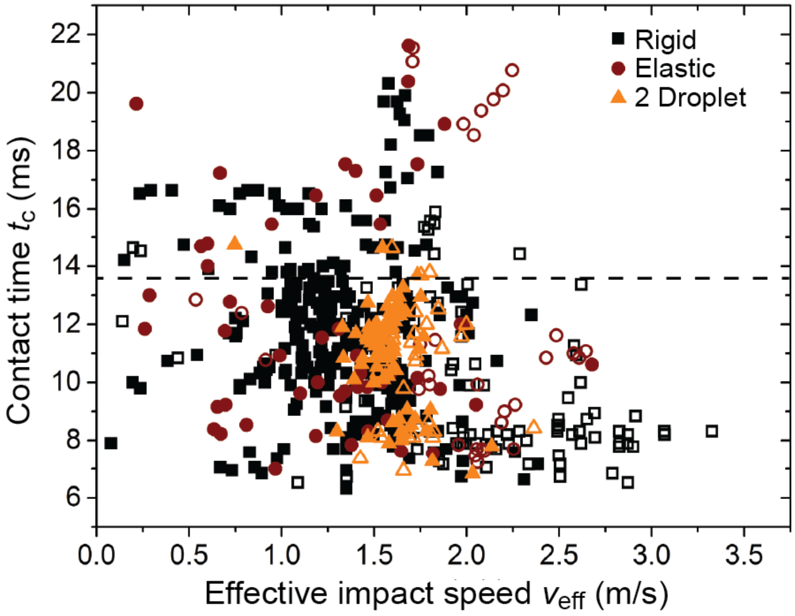

Figure 5.12: Droplet contact times as a function of effective impact speed on rigid vibrating, elastic vibrating and freely vibrating elastic surfaces (D_0 = 2.5 – 2.8 mm). Open symbols represent droplets that splashed during impact. Contact times are not uniquely described by the effective impact speed. The likelihood of splashing, however, increases strongly with increasing effective impact speed ($v_{\mathrm{eff}} \gtrsim 1.75$ m/s). The dashed horizontal line shows the theoretical contact time for $D_0 = 2.5$ mm.

While the effective impact speed did not affect contact times, it influenced the likelihood of droplet splashing (open symbols in Figure 5.12). For $v_{\mathrm{eff}} \gtrsim 1.75$ m/s ($We \gtrsim 106$) most droplets splashed, while below this threshold only few droplets splashed. Droplet splashing occurred mainly during the process of spreading (crown splash – compare to Figure 5.2e) for the highest v_{eff}, or near the point of maximum spreading (Figure 5.11a - rigid) for moderate v_{eff}. The splashing threshold we observed compares well to previous studies on droplet splashing on superhydrophobic surfaces[28,29]. Note, however, that even for very small effective impact speeds ($v_{\mathrm{eff}} < 0.5$ m/s), droplets can still splash. At these low impact speeds, substrate vibration amplitude and frequency are high, and we observed secondary droplet splashing during the recoil and lift-off phases. The substrate motion compressed the droplets and the high vertical acceleration caused droplet break-up during jetting (similar to Figure 5.11b - rigid). Overall, contact times of the core droplets were not influenced by splashing.

5.4 Conclusions

Using high speed imaging we studied droplet dynamics and contact times during droplet impact on vibrating superhydrophobic surfaces with frequencies between 60 and 320 Hz and amplitudes from 0.3 to 2.5 mm, and compared the results for three impact scenarios: forced vibration of a rigid substrate, forced vibration of an elastic substrate, and free vibration of an elastic substrate. We demonstrated that contact times can increase by 160% and decrease by up to 50% when compared to impact on stationary rigid superhydrophobic surfaces. Detailed analysis revealed that during forced vibration, the contact time is most sensitive to changes in the impact phase. On freely vibrating substrates, however, the vibration frequency was the main contributor to a variation in contact time. In all cases, the amplitude of vibration had little direct effect on the contact time. For droplet impact on forced vibrating substrates, we introduced the concept of a frequency-dependent critical impact phase at which contact times transitioned rapidly from a minimum ($t_c \approx 0.5t_{c,th}$) to a maximum ($t_c \approx 1.6t_{c,th}$). Using analytical models, we provided a formula to predict the contact times of impacting droplets on superhydrophobic surfaces subject to forced vibration (Eq. (5-5)). On freely vibrating substrates contact times ranged from $0.5t_{c,th} < t_c < t_{c,th}$, and could be estimated to within ± 20% using Eq. (5-16). Lastly, we elucidated the effect of net impact speed on splashing, and showed that for many droplets, $v_{eff} \gtrsim 1.75$ m/s is an accurate threshold for splashing. High substrate vibrating frequencies and amplitudes, i.e. high vibration accelerations, caused secondary droplet break-up during the recoil stage of droplet bouncing, even for $v_{eff} \rightarrow 0$.

This study not only provides new insights into droplet impact physics on vibrating surfaces, but develops guidelines for the rational design of surfaces to achieve controllable droplet wetting in applications utilizing vibration. The present findings can have a substantial impact on industrial applications where the contact time influences the transfer of momentum, energy (heat), and species. During spray cooling, for example, the per droplet heat transfer rates increase (decrease) for longer (shorter) contact times. Thus, by tailoring the vibration frequency of the substrate, the average contact time, and consequently the average heat transfer, can be actively controlled.

5.5 References

(1) Josserand, C.; Thoroddsen, S. T. Drop Impact on a Solid Surface. *Annu. Rev. Fluid Mech.* **2016**, *48*, 365–391.
(2) Antonini, C.; Amirfazli, A.; Marengo, M. Drop Impact and Wettability: From Hydrophilic to Superhydrophobic Surfaces. *Phys. Fluids 1994-Present* **2012**, *24*, 102104.
(3) Gilet, T.; Bush, J. W. M. The Fluid Trampoline: Droplets Bouncing on a Soap Film. *J. Fluid Mech.* **2009**, *625*, 167.

(4) Fell, D.; Sokuler, M.; Lembach, A.; Eibach, T. F.; Liu, C.; Bonaccurso, E.; Auernhammer, G. K.; Butt, H.-J. Drop Impact on Surfactant Films and Solutions. *Colloid Polym. Sci.* **2013**, *291*, 1963–1976.

(5) Yarin, A. L. DROP IMPACT DYNAMICS: Splashing, Spreading, Receding, Bouncing…. *Annu. Rev. Fluid Mech.* **2006**, *38*, 159–192.

(6) Gilet, T.; Bush, J. W. M. Droplets Bouncing on a Wet, Inclined Surface. *Phys. Fluids* **2012**, *24*, 122103.

(7) Moláček, J.; Bush, J. W. M. Drops Bouncing on a Vibrating Bath. *J. Fluid Mech.* **2013**, *727*, 582–611.

(8) Manzello, S. L.; Yang, J. C. An Experimental Study of a Water Droplet Impinging on a Liquid Surface. *Exp. Fluids* **2002**, *32*, 580–589.

(9) Gilet, T.; Bourouiba, L. Fluid Fragmentation Shapes Rain-Induced Foliar Disease Transmission. *J. R. Soc. Interface* **2015**, *12*, 20141092–20141092.

(10) Massinon, M.; Lebeau, F. Experimental Method for the Assessment of Agricultural Spray Retention Based on High-Speed Imaging of Drop Impact on a Synthetic Superhydrophobic Surface. *Biosyst. Eng.* **2012**, *112*, 56–64.

(11) Mishchenko, L.; Hatton, B.; Bahadur, V.; Taylor, J. A.; Krupenkin, T.; Aizenberg, J. Design of Ice-Free Nanostructured Surfaces Based on Repulsion of Impacting Water Droplets. *ACS Nano* **2010**, *4*, 7699–7707.

(12) Jia, W.; Qiu, H.-H. Experimental Investigation of Droplet Dynamics and Heat Transfer in Spray Cooling. *Exp. Therm. Fluid Sci.* **2003**, *27*, 829–838.

(13) Hsieh, S.-S.; Luo, S.-Y. Droplet Impact Dynamics and Transient Heat Transfer of a Micro Spray System for Power Electronics Devices. *Int. J. Heat Mass Transf.* **2016**, *92*, 190–205.

(14) Weisensee, P. B.; Tian, J.; Miljkovic, N.; King, W. P. Water Droplet Impact on Elastic Superhydrophobic Surfaces. *Sci. Rep.* **2016**, *6*, 30328.

(15) Subrahmanyam, K. B.; Kaza, K. R. V. Vibration Analysis of Rotating Turbomachinery Blades by an Improved Finite Difference Method. *Int. J. Numer. Methods Eng.* **1985**, *21*, 1871–1886.

(16) Schaffer, M. E. *A Practical Guide to Noise and Vibration Control for HVAC Systems*; 2nd ed.; American Society of Heating, Refrigerating, and Air-Conditioning Engineers: Atlanta, GA, 2011.

(17) Ha, N. S.; Truong, Q. T.; Goo, N. S.; Park, H. C. Relationship between Wingbeat Frequency and Resonant Frequency of the Wing in Insects. *Bioinspir. Biomim.* **2013**, *8*, 46008.

(18) Griffin, M. J. Discomfort from Feeling Vehicle Vibration. *Veh. Syst. Dyn.* **2007**, *45*, 679–698.

(19) Brothier, M.; Moulinier, D.; Bertaux, C. Drop Impact on a Vibrated, Heated Surface: Towards a Potential New Way of Elaborating Nuclear Fuel from Gel Microspheres. *World Acad. Sci. Eng. Technol. Int. J. Chem. Mol. Nucl. Mater. Metall. Eng.* **2012**, *6*, 238–246.

(20) Terwagne, D.; Ludewig, F.; Vandewalle, N.; Dorbolo, S. The Role of the Droplet Deformations in the Bouncing Droplet Dynamics. *Phys. Fluids* **2013**, *25*, 122101.

(21) Ng, B. T.; Hung, Y. M.; Tan, M. K. Suppression of the Leidenfrost Effect via Low Frequency Vibrations. *Soft Matter* **2015**, *11*, 775–784.

(22) Lee, H. J.; Kim, H.-Y. Control of Drop Rebound with Solid Target Motion. *Phys. Fluids* **2004**, *16*, 3715.

(23) Raman, K. A.; Jaiman, R. K.; Sui, Y.; Lee, T.-S.; Low, H.-T. Rebound Suppression of a Droplet Impacting on an Oscillating Horizontal Surface. *Phys. Rev. E* **2016**, *94*.

(24) Richard, D.; Clanet, C.; Quéré, D. Surface Phenomena: Contact Time of a Bouncing Drop. *Nature* **2002**, *417*, 811–811.

(25) Bird, J. C.; Tsai, S. S. H.; Stone, H. A. Inclined to Splash: Triggering and Inhibiting a Splash with Tangential Velocity. *New J. Phys.* **2009**, *11*, 63017.

(26) Aboud, D. G. K.; Kietzig, A.-M. Splashing Threshold of Oblique Droplet Impacts on Surfaces of Various Wettability. *Langmuir* **2015**, *31*, 10100–10111.

(27) Antonini, C.; Villa, F.; Marengo, M. Oblique Impacts of Water Drops onto Hydrophobic and Superhydrophobic Surfaces: Outcomes, Timing, and Rebound Maps. *Exp. Fluids* **2014**, *55*.

(28) Pearson, J. T.; Maynes, D.; Webb, B. W. Droplet Impact Dynamics for Two Liquids Impinging on Anisotropic Superhydrophobic Surfaces. *Exp. Fluids* **2012**, *53*, 603–618.

(29) Hu, H.; Chen, L.; Huang, S.; Song, B. Rebound Behaviors of Droplets Impacting on a Superhydrophobic Surface. *Sci. China Phys. Mech. Astron.* **2013**, *56*, 960–965.

CHAPTER 6

OMNIPHOBIC STEEL MICRO-MUSHROOMS [3]

6.1 Introduction

Water repelling surfaces have been studied for many decades[1–5]. In recent years, extensive research effort has been directed toward modifying surface structures to design oleophobic, i.e. oil repelling, surfaces[6–8]. Hydro- and oleophobicity are key factors for many industrial applications, such as self-cleaning fabrics, anti-fouling coatings, desalination equipment, and heat exchangers[9–15]. Fouling, i.e. unwanted deposition of oil on surfaces, negatively influences the performance of many applications, including refrigeration systems, gas turbines and crude oil heat exchangers and refinery distillation and causes financial losses of several billions of US dollars each year[16–19]. Fouling could potentially be reduced by making the surfaces repelling. However, for liquids with very low surface tensions, physical limitations prevent oleophobicity on flat surfaces. Non-polar liquids, such as oils, with a surface tension less than about 22 mN/m are not able form contact angles greater than 90° on a flat surface due to intermolecular forces and a lowest possible surface tension of approx. 6 mN/m for solids[20–22]. In order to overcome these limitations, this research examines the surface structure of metallic surfaces to achieve non-wetting for liquids with high and low surface tensions.

The goal for topographically modified surfaces is to promote nearly spherical droplet shapes (Figure 6.1a-c). Re-entrant structures like reverse micro-cones or micro-mushrooms have shown promising non-wetting behavior with oils[23–28]. The three most common types of re-entrant

---

[3] Parts of this chapter have been previously published as Weisensee *et al.,* "Hydrophobic and Oleophobic Re-Entrant Steel Microstructures Fabricated Using Micro Electrical Discharge Machining", *J. Micromech. Microeng.* 24 (2014) © IOP Publishing. Reproduced with permission. All rights reserved

structures that have been shown to produce oleophobicity are meshes or fibers[27,29], nanoparticle coatings[25,30], and micro-cones or micro-mushrooms, sometimes called micro-hoodoos[23,25–28]. Most fabrication methods included photo or imprint lithography, etching processes and subsequent micromolding. The materials used in the cases of micro-mushrooms were either silicon wafers[23–25,27,28] or polymers such as PDMS (polydimethyl siloxane) and PFPE (perfluoropolyether)[26]. None of these materials are commonly used for heat exchangers in industrial applications such as refrigeration, heat pumping, air conditioning, or crude oil refining. In those applications, steel, aluminum and copper are routinely used. These metals are very economical, widely available and can be easily machined to be integrated into other applications. Recently, a process using laser ablation of a steel plate and subsequent copper electrodeposition was presented as a method to fabricate super-hydrophobic metallic re-entrant structures[31]. However, the process uses multiple steps and may not be as scalable as other fabrication techniques. Another study used wire electrical discharge machining (WEDM) to fabricated super-hydrophobic surfaces from a block of aluminum alloy[32]. Small craters, caused by the fabrication process, added a second length scale to the general sinusoidal pattern. However, the authors did not present a way to fabricate re-entrant structures by WEMD.

Here we present a technique to fabricate metallic hydro- and oleophobic micro-mushrooms. Micro electric discharge machining (mEDM) is demonstrated to be a suitable method of fabricating re-entrant structures. The micro-mushrooms are scalable (Figure 6.1d), and also durable, corrosion and solvent resistant, electrically and thermally conductive and easily implemented in classical fabrication processes. The sessile-drop contact angle along with advancing and receding contact angles is reported for water, RL-68H, often used as lubricant oil in combination with common refrigerants[33], and the low surface tension liquid Isopropanol (IPA) on various micro-mushroom geometries and a comparison between different shapes and performances is made.

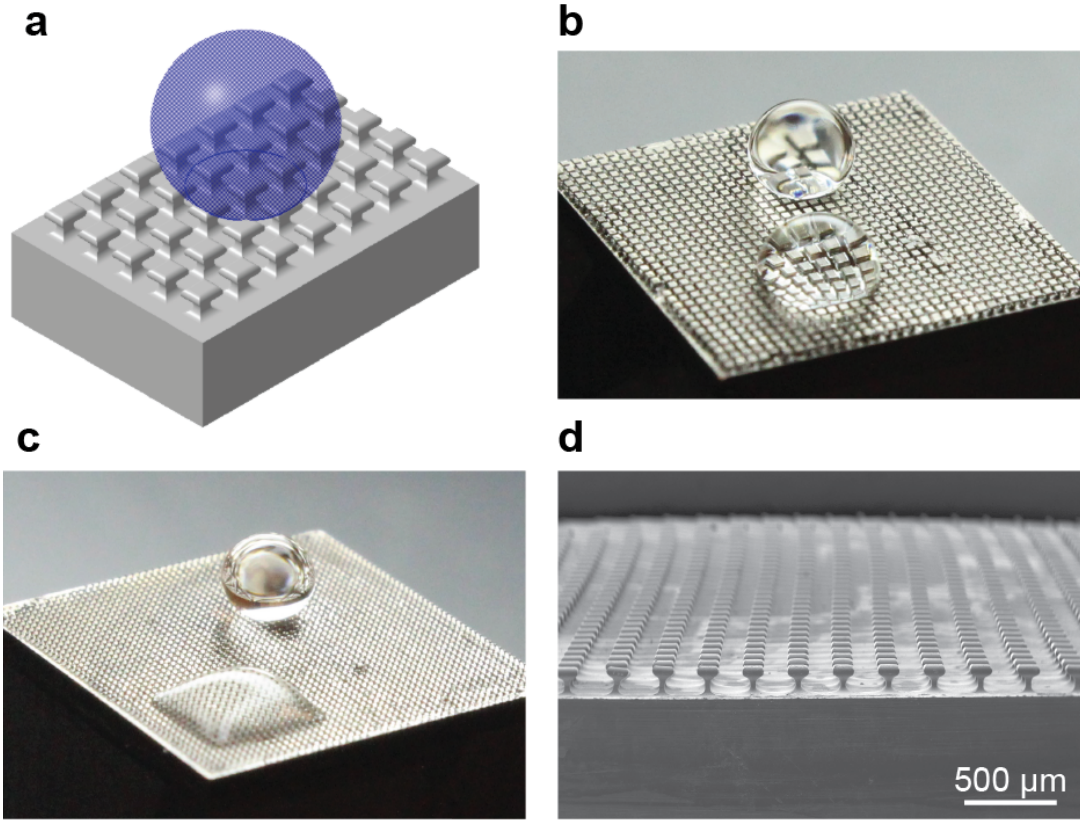

Figure 6.1: Concept and scalability of micro-mushrooms. (a) Model of a droplet on a micro-mushroom-surface. (b) Photograph of water (back) and IPA (front) droplets on a hydro- and oleophobic surface. (c) Photograph of droplets on a surface with strong non-wetting characteristics with water (back) and partial wetting with IPA (front). (d) SEM image of a "micro-mushroom-forest".

6.2 Materials and Methods

6.2.1. Micro-Mushroom Design and Fabrication

The microfabrication process, by which the microstructures were fabricated using micro electrical discharge machining (mEDM), is illustrated in Figure 6.2. Fabrications started with blocks of low carbon steel of size 1 cm x 1 cm x 2 cm, mounted in a Makino UPJ wire EDM machine. The pure tungsten EDM wire of 20 μm diameters was aligned with and then brought into contact with the steel block. The wire and the steel block were immersed in dielectric cooling oil. The wire was run continuously at a speed of 0.18 m/s and was held at a voltage of 23 - 38 V. The lower voltage allows for finer surface conditions and smaller craters compared to other EMD fabrication techniques[32]. Successive cuts through the steel were made as shown in Figure 6.2, and then the steel block was rotated, followed by additional cuts. The steel block was translated during cutting in order to achieve the undercut features required for oleophobicity. Each cut took approximately one minute. The process time could be reduced by improving the wire speed and voltage.

Figure 6.3f shows the dimensions of the micro-mushroom structures where A is the maximum width of the top, in the following called diameter, W the minimal width of the gap between the micro-mushrooms, P the size of a repeating unit, i.e. the pitch, B the minimal width of the base of the micro-mushroom, T the height of the mushroom heads and H the total height of the micro-mushrooms, R the radius of the top and S – where applicable – the difference (deficit) between the flat top of the micro-mushroom and the diameter.

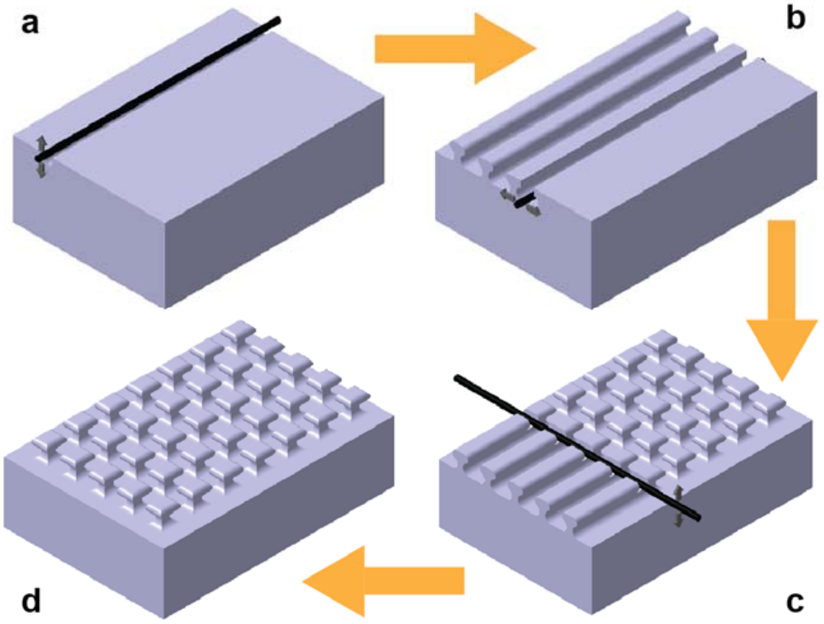

Figure 6.2: Fabrication process of mushrooms using mEDM. (a) A wire cuts channels by vertical motion into a steel block and undercuts by lateral displacement in (b). Then the sample is rotated by 90° (c) and the procedure repeated until completion (d).

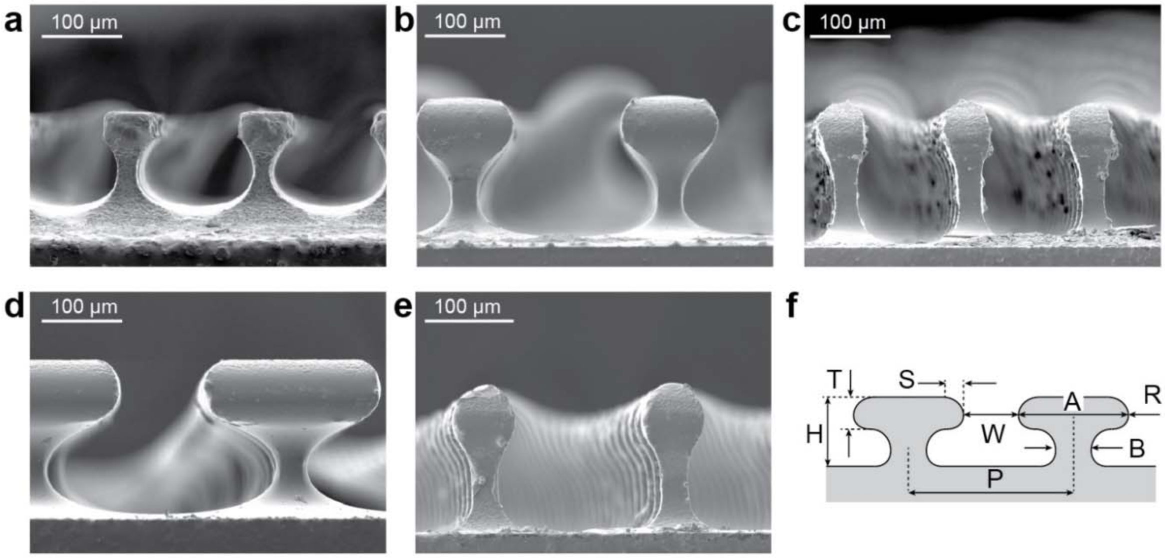

Figure 6.3: **Scanning electron microscope images of the micro-mushrooms** of samples A-E (a-e), respectively, and (f) geometric dimensions of micro-mushrooms. Important are mostly the diameter A of the mushroom heads, the gap width W, the radius R and the deficit S between the diameter and the flat top (not applicable to all micro-mushroom geometries).

The fabricated microstructures are shown in Figure 6.3, and Table 6.1 provides the actual dimensions of the five micro-mushroom samples as determined by SEM. The uncertainty, arising from fabrication tolerances and curvature approximations, is given in brackets. The Cassie-Baxter factor φ and the Wenzel roughness factor ζ are also given in Table 6.1. For samples A, B and D we assumed that in the Cassie-Baxter state the droplets sit on the flat top only ($A - 2S$). Samples C and E are modeled with the diameter ($S = 0$). The fraction of solid-liquid contact area is then

$$\varphi = \frac{(A - 2S)^2}{P^2}. \tag{6-1}$$

For the Wenzel roughness factor ζ the micro-mushrooms are approximated as two concentrical quadratic boxes on top of each other. It can be calculated as:

$$\zeta = \frac{A^2 + 4\,T\,A + (A^2 - B^2) + 4\,(H - T)B + (P^2 - B^2)}{P^2}. \tag{6-2}$$

Table 6.1: Dimensions and Cassie-Baxter and Wenzel roughness factors for the micro-mushroom samples A-E in µm with uncertainties in brackets

	Mushroom A	**Mushroom B**	**Mushroom C**	**Mushroom D**	**Mushroom E**
Pitch *P* (±2)	163	247	149	280	191
Base Width *B* (±2)	20	33	27	33	30
Diameter *A* (±2)	65	117	56	190	64
Top Height *T* (±2)	28	52	66	64	66
Total Height *H* (±2)	118	157	163	160	130
Top Deficit *S* (±1)	-	15	-	22	-
Gap Width *W* (±2)	98	130	95	90	129
Top Radius *R* (±5)	-	17	38	21	39
Cassie Roughness φ	0.12	0.12	0.14	0.27	0.11
Wenzel Roughness ζ	1.65	2.04	2.33	1.84	1.84

The samples were dip coated in liquid Teflon from DuPont in a 5:1 solution of FC-770:Teflon AF with 6% solids to functionalize their surfaces. The samples were submerged in the solution for 10 – 20 s to ensure the surface was entirely covered with Teflon and then held at 330°C for 15 minutes to fully cure the coating. Visual inspection of the coating with an optical microscope confirmed that the coating was evenly applied and had a negligible impact on the dimensions of the micro-mushrooms. A flat silicon wafer was also Teflon dip coated, and its contact angles were measured as a baseline. The thickness of the Teflon coating on the flat surface is in the order of 100 nm, as determined by profilometry with a Sloan Dektak(3) ST.

6.2.2. Contact Angle Measurements

Liquid droplet contact angles were measured on a KSV Instruments CAM 200 goniometer and Fisherbrand Redi-Tip General Purpose 1-200µL pipettes in a class 1000 cleanroom. The images were recorded using a planar CCD camera. For advancing and receding contact angle measurements the frame rate was 10 - 30 frames per second, and the sessile drops were recorded 10 s after their deposition to ensure that the droplet was in local equilibrium. The CAs were analyzed using the software DropSnake, which uses active contour B-spline snakes to match the shape of the drop[34].

Advancing and receding CA measurements were conducted in two different manners. In the first method, the liquid drop volume was increased at 1 µl/s to measure the advancing CA and decreased at 0.1 µl/s to obtain the receding CA. For the second method, the pipette tip was immersed into the liquid drop and the sample stage was moved laterally such that the advancing and receding CAs developed on either side of the drop. The CAs were measured in the frame before the corresponding contact line translated to a new position. The advancing and receding CAs from both methods were within 6% of each other. The liquid was either deionized water, RL-68H oil from Emkarate or Isopropanol (IPA). Sessile drops had a volume V of 5 - 15 µl for the water and 4 - 10 µl for the oil and IPA. The droplets were large compared to the surface structures. We found that the measured CAs were consistent across this range of droplet volumes. Due to strong hydrophobicity and the high surface tension of water, water droplets with $V < 8$ µl would not detach from the pipette. They were thus deposited manually with a micro syringe and a gauge 33 needle. The samples were rinsed with IPA and/ or blown dry with nitrogen gas after each measurement to avoid the effects of potential previous wetting.

The Bond number as a comparison of gravitational to surface tension forces can be used as a measure for the distortion of the drop from a perfect spherical shape and can be expressed as

$$Bo = \frac{\rho\, g\, a^2}{\gamma_{lg}}, \tag{6-3}$$

where ρ is the liquid's density, g the gravitational constant, a the radius of contact area between droplet and solid, and the γ_{lg} the liquid-gas surface tension. In the present experiments, for the sessile droplets, $Bo < 0.3$ with the surface tensions $\gamma_{\mathrm{H2O}} = 72.4$ mN/m for water, $\gamma_{\mathrm{RL\text{-}68H}} = 28.6$ mN/m for RL-68H and $\gamma_{\mathrm{IPA}} = 21.7$ mN/m for IPA[33,35–37]. Even for these low Bond numbers, sagging of droplets with very high CAs leads to non-negligible uncertainties[38,39]. Where the CA is greater than 160° or lower than 70° the measured CAs are expected to have an uncertainty up to ±13°,[39] otherwise the uncertainty is ±6° as determined from the standard deviation of the measurements at each sample and condition. The reported values are averaged over a minimum number of five measurements at different locations of each sample to minimize errors due to chemical and topographical inhomogeneities.

6.3 Results and Discussion

6.3.1. Characterization with Water

All studied micro-mushroom structures are hydrophobic. The flat reference surface has a sessile water CA of $\theta_Y = 111°$. This value is used in the calculation of Cassie-Baxter and Wenzel CA predictions. The advancing and receding CAs are $\theta_A/\theta_R = 119°/94°$, agreeing well with values reported by Gao and McCarthy[40]. Table 6.2 lists the measured apparent CAs for the Teflon-coated micro-mushroom structures, roll-off angles and the predicted Cassie-Baxter $\theta_{C\text{-}B}$ and Wenzel θ_W CAs. All samples have sessile CAs near or greater than 150° and advancing CAs between 165 and 170°. CAH is between 19 and 35°, and roll-off angles are as low as 8° on sample E and > 30° for the sample with the highest diameter-to-gap-width ratio (i.e. largest solid contact area). All CAs match well with the predicted Cassie-Baxter angles, consistent with the non-wetting Cassie-Baxter state across all of the samples. Samples with higher CAH also have higher roll-off angles, which is attributed to contact line pinning especially at the receding end of the droplet[25,41,42].

Table 6.2: Measured and predicted CAs, CAH and roll-off angles α for samples A-E with water (γ_{lg} = 72.4 mN/m)

	Mushroom A	Mushroom B	Mushroom C	Mushroom D	Mushroom E
Sessile θ	156	159	157	146	162
Cassie-Baxter $\theta_{C\text{-}B}$	157	157	156	149	159
Wenzel θ_W	127	138	148	-	132
Advancing θ_A	167	168	169	165	170
Receding θ_R	143	139	147	130	151
Hysteresis $\Delta\theta$	24	29	22	35	19
Roll-off angle α	14 ± 1	14 ± 1	14 ± 1	> 30	8 ± 1

By comparing the micro-mushroom parameters to the achieved CAs, favorable dimensions for high hydrophobicity can be identified. The advancing CA is nearly unaffected by the variation of any parameter (compare to Figure 6.4). When moving, the droplet falls onto the next micro-mushroom, independent of the dimensions. The receding CAs, however, are influenced by the diameter D (Figure 6.4a) and the ratio of diameter to the gap-width A/W (Figure 6.4b). Figure 6.4b also includes the Cassie-Baxter predictions for $S = 0$ (no flat top on micro-mushrooms) and $S = 15$ and 22 μm, respectively. Recalling that $A + W$ is the size of the repeating unit, P, the Cassie-Baxter factor φ in (**6-1**) can easily be written as a function of A/W. Sessile and receding CAs decrease as A and A/W increase. CAH is thus decreased with larger relative spacings between the micro-mushrooms. Decreasing CAH has been observed before for square posts and was attributed to the decrease in length of the contact line, thus reducing the overall energy barrier[4]. The radius of the micro-mushrooms has only little influence on the CAs and CAH (see Figure 6.4c). The height of the microstructures does not influence the CAs since the droplets sit on top of the micro-mushrooms (not shown).

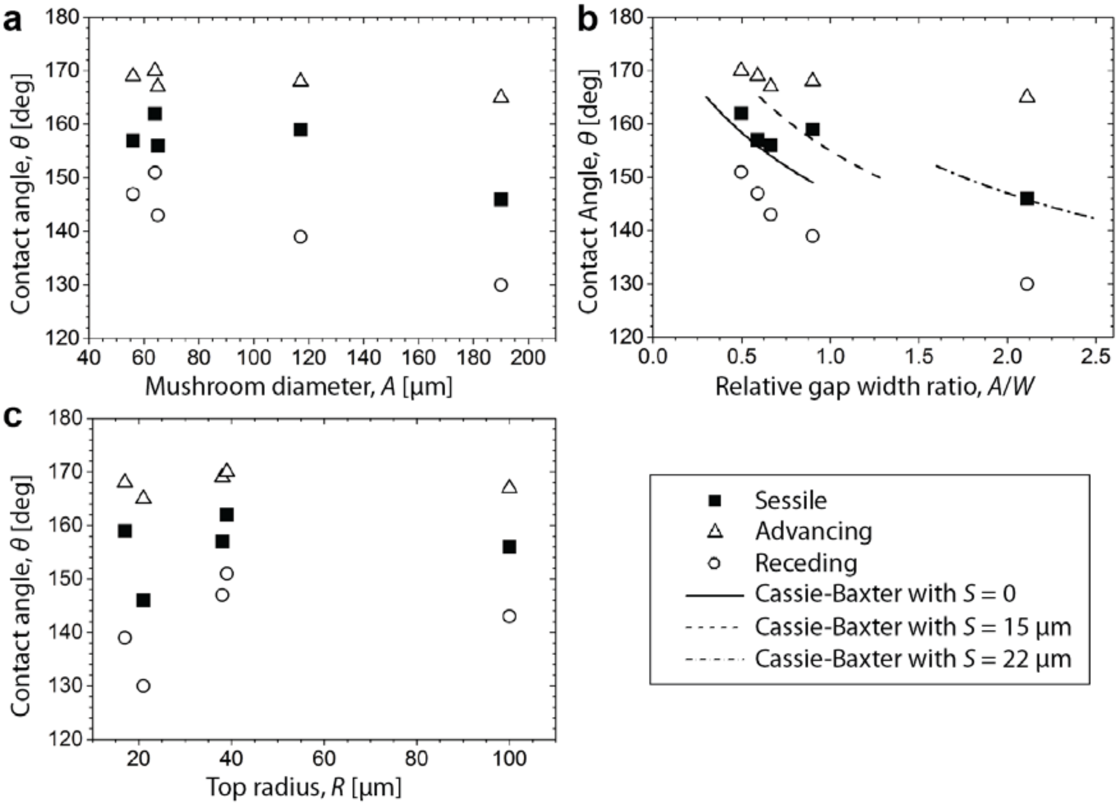

Figure 6.4: **Measured apparent contact angles** for sessile (filled squares), advancing (open triangles) and receding (open circles) contact angles with water. Shown are the influences of (a) the diameter *A*, (b) the ratio of the diameter to the gap-width *A*/*W* including Cassie-Baxter predictions for different values of *S* and (c) the radius *R*. Sample A is plotted with a radius of 100 μm.

6.3.2. Characterization with Oil

The micro-mushroom geometries also promote oleophobic behavior. While water is phobic even on a flat Teflon-coated surface, the oil has a sessile CA of only $\theta_Y = 75°$ on the flat reference surface. The values for the sessile, advancing and receding CAs on the micro-mushrooms as well as the Cassie-Baxter predictions are listed in Table 6.3. All samples have CAs $\theta > 90°$ and CAH between 55 and 100°. Some samples have sessile CAs lying between the predicted Cassie-Baxter and Wenzel states. Two samples, however, have CAs higher than the Cassie-Baxter CA approximation, which has been previously observed for octane on micro-hoodoos[43]. A possible reason for the discrepancy between the predictions and the data lies in the modelling of the solid-liquid fraction φ, which is only an approximation of the surface geometry and does not, for example, take into account the re-entrant feature of the micro-mushrooms. Also, the convex shape of the droplet between the microstructures increases the effective contact area between the liquid and the air. The Cassie-Baxter prediction assumes a flat interface. It also has to be taken into account that droplets on structured surfaces are in local equilibrium, whereas the Cassie-Baxter prediction assumes a droplet in global equilibrium[41].

Table 6.3: Measured and predicted CAs and CAH for samples A-E with RL-68H (γ_{lg} = 28.6 mN/m)

	Mushroom A	**Mushroom B**	**Mushroom C**	**Mushroom D**	**Mushroom E**
Sessile θ	106	152	122	149	111
Cassie-Baxter $\theta_{C\text{-}B}$	147	147	146	131	149
Advancing θ_A	121	164	133	159	118
Receding θ_R	63	94	37	71	18
Hysteresis $\Delta\theta$	58	70	96	88	100

Oil droplets on the micro-mushrooms do not show a unique trend in CAs and CAH with respect to geometric parameters. Small diameters and low diameter-to-gap-width ratios (i.e. big relative spacing) lead to CAs below the Cassie-Baxter limit (Figure 6.5a,b). Increasing A and A/W leads to non-wetting. The lowest CAH is achieved at a diameter-to-gap-width ratio around unity. The radius of the micro-mushroom heads has a more pronounced influence on the CAs (Figure 6.5c). The smallest radius shows the highest (advancing) CA, which decreases as the micro-mushroom's radius increases, while CAH is almost unaffected by the variation in radius. Sample A with an almost vertical wall is plotted as R = 100 μm.

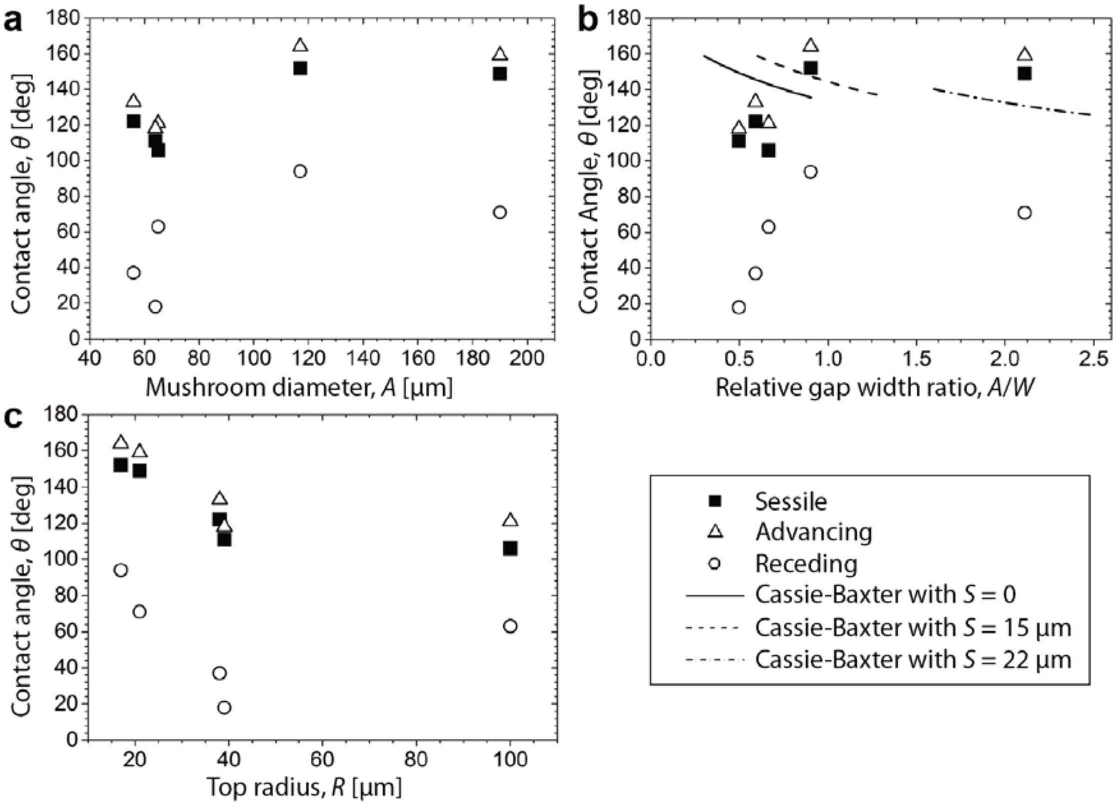

Figure 6.5: **Measured apparent contact angles** for sessile (filled squares), advancing (open triangles) and receding (open circles) contact angles with oil. Shown are the influences of (a) the diameter *A*, (b) the ratio of the diameter to the gap-width *A*/*W* including Cassie-Baxter predictions for different values of *S* and (c) the radius *R*. Sample A is plotted with a radius of 100 µm.

Differences in droplet volumes in the studied ranges usually do not affect the CAs. The micro-mushroom of type A has the reported values $\theta \approx 106°$ for most volumes. The droplets with V = 8 and 9 µl, however, show a sessile apparent CA of 157°. Kang *et al.* observed a similar transition for Ethanol on PFPE mushroom-like micro-pillar arrays, where the different states were a function of the spacing ratio: medium spacings lead to a non-wetting behavior while small and large spacings fully wetted the surface[26]. The reason for the jump in CA is not yet understood. However, it is noteworthy that the micro-mushrooms of sample A are the only ones with a sharp edge and vertical slope at the head of the micro-mushrooms (compare to Figure 6.3). Without external forces such as due to vibration or drops falling from some height, the droplets might be intrinsically metastable in the non-wetting regime. Slight perturbations can lead to the collapse of the weak Cassie-State and the oil glides down the vertical wall until a stable contact line can be re-established at the overhang.

6.3.3. Characterization with IPA

The contact angles of IPA on the micro-mushrooms continue the trend observed when decreasing the surface tension from water to RL-68H. On the flat reference surface the sessile contact angle is 55° and $\theta_A/\theta_R = 58°/50°$. Table 6.4 lists the measured and predicted contact angles for the structured surfaces. For sample D the sessile contact angle and the predicted Cassie-Baxter angle match well. This is the only geometry that supports the fully non-wetting regime, resulting also in the lowest hysteresis. All other samples have droplets in a partially wetting state, as can be seen not only from the relatively low contact angles, but also from residue that is left over in between the micro-mushrooms when the liquid recedes. The receding contact angles become very small and go to zero for these cases. On sample D, the IPA droplets transition from the Cassie-Baxter state to the partially wetting state with a droplet volume of $V \approx 17$ µl when the gravitational force exceeds the force due to the Laplace pressure in between the re-entrant geometries.

Table 6.4: Measured and predicted CAs and CAH for samples A-E with IPA (γ_{lg} = 21.7 mN/m)

	Mushroom A	Mushroom B	Mushroom C	Mushroom D	Mushroom E
Sessile θ	75	79	93	123	78
Cassie-Baxter $\theta_{C\text{-}B}$	143	143	142	125	146
Advancing θ_A	98	104	116	148	101
Receding θ_R	12	15	19	74	19
Hysteresis $\Delta\,\theta$	86	88	97	74	82

A comparison between the micro-mushroom geometries (SEM images on left) and droplet shapes and states for water (center, left), oil (center, right) and IPA (right) is shown in Figure 6.6. All samples are hydrophobic. The water droplets sit on top of the micro-mushrooms and air gets trapped beneath them, preventing the liquid from wetting the sides of the microstructures. The droplets have an almost spherical shape with negligible distortion due to gravity. The oil droplets either sit on top of the micro-mushrooms or penetrate some distance into the gaps, depending on the geometry of the micro-mushroom. For water, the samples with flat and wide tops yield lower CAs than the elongated micro-mushrooms with a curved head, especially sample D. As discussed earlier, wider spacing and thus a decrease in contact line length between the droplet and the solid increases the CA for water. It is also obvious why the radius of the micro-mushroom geometry does not influence the CA: the droplets merely sit on top of the microstructures, independent of the shape of the micro-mushroom below them. Straight pillars would have most probably given the same result[44]. On the other hand, oil forms a higher CA on geometries with a flat top part and narrower spacing. Only samples B and D are non-wetting. The gaps between the micro-mushrooms of these samples are smaller and the oil does not penetrate through them. With IPA only sample D with a diameter-to-gap-width ratio greater than unity supports the Cassie-Baxter state. Narrow micro-mushrooms that have a less pronounced curvature cause smaller CAs. In general, the geometries supporting high CAs for liquids with high and low surface tensions are opposed to each other.

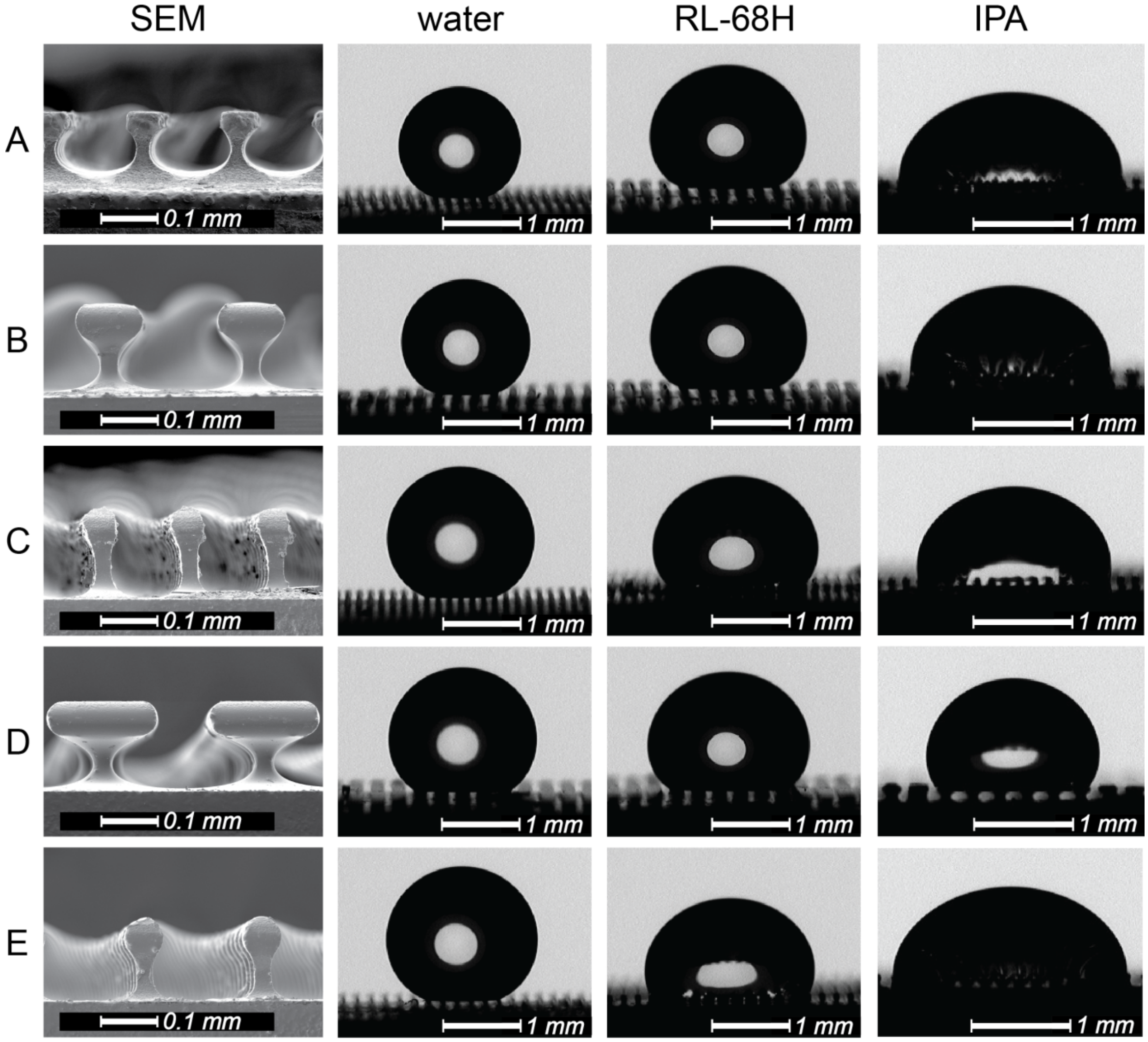

Figure 6.6: **SEM of the micro-mushroom geometries (left) and images** of sessile droplets of water (center left), RL-68H (center right) and IPA (right) with $V \approx 5$ µl on samples A-E. Narrow and widely spaced micro-mushrooms yield higher CAs for water while micro-mushrooms with flat tops, strong re-entrant features and narrow spacings are preferable for the use with liquids with low surface tensions.

6.4 Conclusions

This chapter presented re-entrant structures in the shape of micro-mushroom geometries that are hydro- and oleophobic with apparent contact angles $\theta > 90°$ for most cases. While those micro-mushrooms with narrow structures and wide spacing are preferable for use with water, which has a high surface tension, microstructures with flat tops, strong curvature and re-entrant features and smaller gap widths yield higher contact angles when used with liquids with a low surface tension. Only latter mentioned geometries support a fully non-wetting Cassie-Baxter state for RL-68H with a surface tension of 28.6 mN/m. IPA exists in the Cassie-Baxter state only for the sample with a diameter-to-gap-width ratio greater than unity. Despite the high achievable sessile contact angles up to 148° with IPA, 152° for the oil and 162° for the water, the Teflon-coated micro-mushroom structures exhibit a contact angle hysteresis between 58 and 100° for the oil and IPA and between 19 and 35° for water. It is shown that micro electrical discharge machining is a good and scalable method to fabricate hydro- and oleophobic re-entrant structures. Micro EDM allows the use of metallic materials that are not only durable and corrosion resistant, but are also very economical and allow the integration into other applications or machine structures.

6.5 References

(1) Wenzel, R. N. Resistance of Solid Surfaces to Wetting by Water. *Ind. Eng. Chem.* **1936**, *28*, 988–994.

(2) Wolf, E. WATER-REPELLENT TEXTILES. **1942**.

(3) Humenik, M.; Kingery, W. D. Metal-Ceramic Interactions: III, Surface Tension and Wettability of Metal-Ceramic Systems. *J. Am. Ceram. Soc.* **1954**, *37*, 18–23.

(4) Öner, D.; McCarthy, T. J. Ultrahydrophobic Surfaces. Effects of Topography Length Scales on Wettability. *Langmuir* **2000**, *16*, 7777–7782.

(5) Park, K.-C.; Choi, H. J.; Chang, C.-H.; Cohen, R. E.; McKinley, G. H.; Barbastathis, G. Nanotextured Silica Surfaces with Robust Superhydrophobicity and Omnidirectional Broadband Supertransmissivity. *ACS Nano* **2012**, *6*, 3789–3799.

(6) Kota, A. K.; Choi, W.; Tuteja, A. Superomniphobic Surfaces: Design and Durability. *MRS Bull.* **2013**, *38*, 383–390.

(7) Liu, Y.; Xiu, Y.; Hess, D. W.; Wong, C. P. Silicon Surface Structure-Controlled Oleophobicity. *Langmuir* **2010**, *26*, 8908–8913.

(8) Campos, R.; Guenthner, A. J.; Meuler, A. J.; Tuteja, A.; Cohen, R. E.; McKinley, G. H.; Haddad, T. S.; Mabry, J. M. Superoleophobic Surfaces through Control of Sprayed-on Stochastic Topography. *Langmuir* **2012**, *28*, 9834–9841.

(9) Liu, Y.; Tang, J.; Wang, R.; Lu, H.; Li, L.; Kong, Y.; Qi, K.; Xin, J. H. Artificial Lotus Leaf Structures from Assembling Carbon Nanotubes and Their Applications in Hydrophobic Textiles. *J. Mater. Chem.* **2007**, *17*, 1071–1078.

(10) Nakata, N.; Kakimoto, M.; Nishita, T. Animation of Water Droplets on a Hydrophobic Windshield. *WSCG2012* **2012**.

(11) Banerjee, I.; Pangule, R. C.; Kane, R. S. Antifouling Coatings: Recent Developments in the Design of Surfaces That Prevent Fouling by Proteins, Bacteria, and Marine Organisms. *Adv. Mater.* **2011**, *23*, 690–718.

(12) Larbot, A.; Gazagnes, L.; Krajewski, S.; Bukowska, M.; Wojciech, K. Water Desalination Using Ceramic Membrane Distillation. *Desalination* **8**, *168*, 367–372.

(13) Chen, F.; Julie, E. S.; Fu-Min, W.; Kenneth, E. G. Impact of Wall Hydrophobicity on Condensation Flow and Heat Transfer in Silicon Microchannels. *J. Micromechanics Microengineering* **2010**, *20*, 45018.

(14) Miljkovic, N.; Enright, R.; Wang, E. N. Effect of Droplet Morphology on Growth Dynamics and Heat Transfer during Condensation on Superhydrophobic Nanostructured Surfaces. *ACS Nano* **2012**, *6*, 1776–1785.

(15) Sommers, A. D.; Jacobi, A. M. Creating Micro-Scale Surface Topology to Achieve Anisotropic Wettability on an Aluminum Surface. *J. Micromechanics Microengineering* **2006**, *16*, 1571.

(16) Diakunchak, I. S. Performance Deterioration in Industrial Gas Turbines. *J. Eng. Gas Turbines Power* **1992**, *114*, 161–168.

(17) Jafari Nasr, M. R.; Majidi Givi, M. Modeling of Crude Oil Fouling in Preheat Exchangers of Refinery Distillation Units. *Appl. Therm. Eng.* **2006**, *26*, 1572–1577.

(18) Polley, G. T.; Wilson, D. I.; Yeap, B. L.; Pugh, S. J. Use of Crude Oil Fouling Threshold Data in Heat Exchanger Design. *Appl. Therm. Eng.* **2002**, *22*, 763–776.

(19) Radhakrishnan, V. R.; Ramasamy, M.; Zabiri, H.; Do Thanh, V.; Tahir, N. M.; Mukhtar, H.; Hamdi, M. R.; Ramli, N. Heat Exchanger Fouling Model and Preventive Maintenance Scheduling Tool. *Appl. Therm. Eng.* **2007**, *27*, 2791–2802.

(20) Fowkes, F. M. ADDITIVITY OF INTERMOLECULAR FORCES AT INTERFACES. I. DETERMINATION OF THE CONTRIBUTION TO SURFACE AND INTERFACIAL TENSIONS OF DISPERSION FORCES IN VARIOUS LIQUIDS1. *J. Phys. Chem.* **1963**, *67*, 2538–2541.

(21) Nishino, T.; Meguro, M.; Nakamae, K.; Matsushita, M.; Ueda, Y. The Lowest Surface Free Energy Based on −CF3 Alignment. *Langmuir* **1999**, *15*, 4321–4323.

(22) Jarvis, N. L.; Zisman, W. A. *Surface Chemistry of Fluorochemicals*; DTIC Document, 1965.

(23) Choi, H.-J.; Choo, S.; Shin, J.-H.; Kim, K.-I.; Lee, H. Fabrication of Superhydrophobic and Oleophobic Surfaces with Overhang Structure by Reverse Nanoimprint Lithography. *J. Phys. Chem. C* **2013**, *117*, 24354–24359.

(24) Cao, L.; Hu, H.-H.; Gao, D. Design and Fabrication of Micro-Textures for Inducing a Superhydrophobic Behavior on Hydrophilic Materials. *Langmuir* **2007**, *23*, 4310–4314.

(25) Dufour, R.; Perry, G.; Harnois, M.; Coffinier, Y.; Thomy, V.; Senez, V.; Boukherroub, R. From Micro to Nano Reentrant Structures: Hysteresis on Superomniphobic Surfaces. *Colloid Polym. Sci.* **2013**, *291*, 409–415.

(26) Kang, S. M.; Kim, S. M.; Kim, H. N.; Kwak, M. K.; Tahk, D. H.; Suh, K. Y. Robust Superomniphobic Surfaces with Mushroom-like Micropillar Arrays. *Soft Matter* **2012**, *8*, 8563–8568.

(27) Tuteja, A.; Choi, W.; Mabry, J. M.; McKinley, G. H.; Cohen, R. E. Robust Omniphobic Surfaces. *Proc. Natl. Acad. Sci.* **2008**.

(28) Zhao, H.; Law, K.-Y.; Sambhy, V. Fabrication, Surface Properties, and Origin of Superoleophobicity for a Model Textured Surface. *Langmuir* **2011**, *27*, 5927–5935.

(29) Chhatre, S. S.; Choi, W.; Tuteja, A.; Park, K.-C. (Kenneth); Mabry, J. M.; McKinley, G. H.; Cohen, R. E. Scale Dependence of Omniphobic Mesh Surfaces. *Langmuir* **2010**, *26*, 4027–4035.

(30) Lakshmi, R. V.; Bharathidasan, T.; Bera, P.; Basu, B. J. Fabrication of Superhydrophobic and Oleophobic Sol–gel Nanocomposite Coating. *Surf. Coat. Technol.* **5**, *206*, 3888–3894.

(31) Kwon, M. H.; Shin, H. S.; Chu, C. N. Fabrication of a Super-Hydrophobic Surface on Metal Using Laser Ablation and Electrodeposition. *Appl. Surf. Sci.* **2014**, *288*, 222–228.

(32) Bae, W. G.; Song, K. Y.; Rahmawan, Y.; Chu, C. N.; Kim, D.; Chung, D. K.; Suh, K. Y. One-Step Process for Superhydrophobic Metallic Surfaces by Wire Electrical Discharge Machining. *ACS Appl. Mater. Interfaces* **2012**, *4*, 3685–3691.

(33) Goswami, D. Y.; Shah, D. O.; Jotshi, C. K.; Bhagwat, S.; Leung, M.; Gregory, A. *Foaming Characteristics of Refigerant/lubricant Mixtures*; 1997.

(34) Stalder, A. F.; Kulik, G.; Sage, D.; Barbieri, L.; Hoffmann, P. A Snake-Based Approach to Accurate Determination of Both Contact Points and Contact Angles. *Colloids Surf. Physicochem. Eng. Asp.* **2006**, *286*, 92–103.

(35) Vazquez, G.; Alvarez, E.; Navaza, J. M. Surface Tension of Alcohol Water + Water from 20 to 50 .degree.C. *J. Chem. Eng. Data* **1995**, *40*, 611–614.

(36) Jasper, J. J. The Surface Tension of Pure Liquid Compounds. *J. Phys. Chem. Ref. Data* **2009**, *1*, 841–1010.

(37) Cini, R.; Loglio, G.; Ficalbi, A. Temperature Dependence of the Surface Tension of Water by the Equilibrium Ring Method. *J. Colloid Interface Sci.* **1972**, *41*, 287–297.

(38) Srinivasan, S.; McKinley, G. H.; Cohen, R. E. Assessing the Accuracy of Contact Angle Measurements for Sessile Drops on Liquid-Repellent Surfaces. *Langmuir* **2011**, *27*, 13582–13589.

(39) Extrand, C. W.; Moon, S. I. Contact Angles of Liquid Drops on Super Hydrophobic Surfaces: Understanding the Role of Flattening of Drops by Gravity. *Langmuir* **2010**, *26*, 17090–17099.

(40) Gao, L.; McCarthy, T. J. Teflon Is Hydrophilic. Comments on Definitions of Hydrophobic, Shear versus Tensile Hydrophobicity, and Wettability Characterization. *Langmuir* **2008**, *24*, 9183–9188.

(41) Gao, L.; McCarthy, T. J. Contact Angle Hysteresis Explained. *Langmuir* **2006**, *22*, 6234–6237.

(42) Sommers, A. D.; Jacobi, A. M. Wetting Phenomena on Micro-Grooved Aluminum Surfaces and Modeling of the Critical Droplet Size. *J. Colloid Interface Sci.* **2008**, *328*, 402–411.
(43) Tuteja, A.; Choi, W.; McKinley, G. H.; Cohen, R. E.; Rubner, M. F. Design Parameters for Superhydrophobicity and Superoleophobicity. *MRS Bull.* **2008**, *33*, 752–758.
(44) Wier, K. A.; McCarthy, T. J. Condensation on Ultrahydrophobic Surfaces and Its Effect on Droplet Mobility: Ultrahydrophobic Surfaces Are Not Always Water Repellant. *Langmuir* **2006**, *22*, 2433–2436.

CHAPTER 7

CONCLUSIONS AND OUTLOOK

7.1 Conclusion

Having a deep understanding of the interaction between a liquid and a solid is critical for many industrial applications, including thermal management systems, desalination, anti-icing coatings, self-cleaning surfaces, pesticide delivery, etc. In this thesis I have studied and analyzed various fundamental aspects of droplet-solid interactions with an emphasis on those found in heat transfer applications.

Based on the theories of wetting, developed by Young, and Fowke's interaction of molecules at interfaces, I have studied the influence of the gas environment (air *vs*. pure water vapor) on the wetting behavior of (super)hydrophobic surfaces. The findings showed that in the presence of pure water vapor static and dynamic advancing CAs can decrease by almost 10% as compared to an air environment. I proposed that this decrease is due to molecular water vapor adsorption to the Teflon surface. On micro- and nanostructured surfaces the reduction in CA was less dominant than on a flat surface due to a decreased solid-liquid fraction and consequently a reduction of the relative importance of the solid surface energy.

While the functionalization of a surface towards (super)hydrophobicity is relatively easy and can be achieved in many different ways, the use of complex re-entrant microstructures is necessary for oil repellency, or oleophobicity. Furthermore, it is desirable to fabricate such structures from materials commonly found in engineering applications, such as metals, as opposed to silicon. I presented mEDM as a viable tool to fabricate scalable oleophobic micro-mushrooms on steel blocks. Contact angle measurements with water, oil, and alcohol revealed necessary design parameters to achieve reliable omniphobicity. While narrow micro-mushrooms with wide spacing gave the highest CAs and lowest CAH with water, microstructures with flat tops, strong re-entrant curvature and smaller gap widths were necessary to support non-wetting droplets with liquids with a low surface tension.

I also studied the interaction of droplets with a solid during dropwise condensation of water on liquid infused surfaces (LIS, or SLIPS), to develop a heat transfer model valid for these ultra-slippery surfaces. I presented steady-state droplet size distributions for lubricants of various viscosity and concluded that Rose's model for the distribution of droplet sizes can be used for condensation on LIS, regardless of lubricant viscosity. I further developed a numerical model and performed experiments to estimate the effect of sweeping and sweeping frequency on the average heat transfer on a large vertical plate. Both model and experimental data suggest that only uncommonly high sweeping rates would have a significant effect on heat transfer rates.

Besides droplet deposition on a surface and condensation, droplet impact is a third kind of droplet-solid interaction that I presented as part of this thesis. I showed that contact times of water droplets impacting elastic superhydrophobic surfaces can be reduced by up to 50% when compared to impact on rigid surfaces. Furthermore, I showed that the critical impact speed for splashing increases on flexible substrates. Through high speed imaging, I studied the complex droplet dynamics during impact, spreading, and lift-off, and found that the *springboard effect*, where the droplet lifts off the surface prior to fully recoiling, is responsible for the reduction in contact time. Furthermore, I developed two non-dimensional criteria based on the interplay of droplet and substrate momenta that can accurately predict the conditions for the springboard effect and thus a reduction in contact time to occur.

As a continuation of my work on droplet impact on initially stationary elastic substrates I studied the effect of a priori substrate vibration on droplet dynamics. Experiments on rigid and elastic vibrating superhydrophobic surfaces revealed that vibration frequency and phase at impact greatly influence the contact time of bouncing droplets. I introduced a critical impact phase for which contact times quickly transitioned from a minimum (smaller than theoretical contact time) to a maximum (larger than theoretical contact time). To enhance our understanding of the physical basics underlying droplet impact on vibrating surfaces, I presented a semi-empirical model to describe the relationship between contact time and vibration frequency, phase, and amplitude of the substrate.

7.2 Outlook and Future Work

While the results and findings from this dissertation are a first step towards a better understanding of the complex interactions between droplets and solids, much is yet to be done to unveil the secrets of mother nature. With my work I have paved the way for more exciting fundamental and applied research in the areas of surface omniphobicity, dropwise condensation heat transfer, and droplet impact.

As already hinted to in Chapter 4, the effect of volumetric elasticity, for example gels, on contact times would be an interesting question to answer; both from a physical standpoint as well as from an application point of view. In power electronics, for example, gel-like elastomers are often used to insulate the electronic components from contact with water, as well as for vibration confinement. I propose that, if properly designed, these gels might additionally be used for spray cooling of the electronic components by taking advantage of the *springboard effect* and the resulting increase in impact frequency.

To better understand the physics of spray cooling and anti-icing systems, thermal responses should be studied in addition to droplet fluid dynamics. The small length scales (µm – mm), coupled with short time scales (ms) pose a challenge on traditional thermal measurement techniques. Using high speed infrared (IR) thermometry and other imaging and thermal techniques, I want to study the fundamentals of temperature distributions in droplets during impact and phase change, and use the obtained experimental results to validate computational efforts. I am interested in studying single droplet thermal behaviors as well as the effect of the interplay of multiple droplets, i.e. time-averaged temperature profiles. A deeper understanding of thermal gradients in droplet-based systems will allow us to improve heat transfer models and to optimize heat transfer systems.

Dropwise condensation has been shown to have many advantages over condensation on traditional flat and structured surfaces, including high droplet mobility and the ability for dropwise condensation of low surface tension fluids. Many open questions remain, however, regarding durability and the effect of oil depletion in lubricant-infused surfaces. The main reason for the high droplet mobility is the absence of defects and roughness on the lubricant surface. What if we could design and fabricate a surface that is equally flat and defect-free, but bonded to the substrate, so that drainage losses are avoided? Not only would it increase the long-term durability of the surfaces, but it could also be used as friction reduction in high shear environments, such as duct flows or naval applications.

Answers must also be found to a controversial discussion currently taking place in the scientific community concerning the nucleation of droplets on SLIPS. One option that is being discussed is droplet nucleation and growth directly on the solid surface, i.e. beneath the lubricant layer, where micro- and nanostructures and surface defects can assist the nucleation process and lower the minimum nucleation radius. At the same time water vapor would first need to diffuse through the lubricant layer to reach the solid. This poses an additional constraint on the nucleation, as less water molecules are present to form a droplet. Following this argument, nucleation and droplet growth on top of the lubricant layer seem more likely. Detailed experiments with good spatial and temporal resolution will be necessary to find an answer to this important aspect of condensation.

Last, but not least, I think it is important to realize that with the growing complexity of technical systems, be it electronics, power generation, or agriculture, interdisciplinary collaborations and approaches will be necessary to solve some of the biggest challenges of our time. For example, the electrical engineer and the thermal engineer will need to work hand in hand to provide more energy efficient and compact electronic systems. Phase change heat transfer allows for the highest heat fluxes we know of due to latent heat effects. However, a challenge remains in directing and routing heat flows in electronics systems. Certainly a deeper understanding of liquid-solid, vapor-liquid, and vapor-solid interactions will enable us to create new avenues for thermal management, not only in in confined spaces, but also on the larger scale in, for example, power generation, desalination, and other thermal systems.

APPENDIX A

CODE: Droplet Detection and Analysis

Main Script

```
clear all;

scriptfolder = 'C:\Users\...\Matlab code\image_read_code\';
filefolder='C:\Users\...\input\';
filefolderout = 'C:\Users\...\output\'';
cd(filefolder);
allnames=struct2cell(dir('*.jpg'));
[k,len]=size(allnames); %get the number of pictures in folder
len
 for filecount=1:len,
   filename=allnames{1,filecount}
   filecount
   rgb=imread(filename); %read image
   cd(scriptfolder);
   droplet_detection;  %function call
   clear imfindcircle
   cd(filefolder);
 end
```

Function (droplet_detection)

```
%recognizing standard:
%smaller circles need more sensitive recognition and larger one need less
%higher 'Sensitivity'->more sensitive;lower 'EdgeThreshold'->can read
%smaller gradient value; both make it easier to recognize
%(more detail: http://www.mathworks.com/help/images/examples/detect-and-measure-circular-objects-in-an-
image.html)

%ratio between pixel and picture:
%20x:
% calib=0.14; % um/pix
%10x:
% calib=0.26;   % um/pix
%5x:
% calib=0.50; % um/pix
%macro:
calib=3.15; % um/pix

% size brackets [pix]
range=[20, 30, 40, 50, 70, 90, 120, 150, 180, 220, 260, 300, 350, 400];
n=size(range,2)-1;
sens = 0.94; %need to adjust
edg = 0.05;
```

```
A=size(rgb,1).*size(rgb,2)*calib^2*1e-12; %area of the picture, unit: m2


% % DARK (macro)
[centers1, radii1] = imfindcircles(rgb,[range(1,1)
range(1,2)],'ObjectPolarity','dark','Sensitivity',sens,'EdgeThreshold',edg);
[centers2, radii2] = imfindcircles(rgb,[range(1,2)
range(1,3)],'ObjectPolarity','dark','Sensitivity',sens,'EdgeThreshold',edg);
[centers3, radii3] = imfindcircles(rgb,[range(1,3)
range(1,4)],'ObjectPolarity','dark','Sensitivity',sens+0.01,'EdgeThreshold',edg);
[centers4, radii4] = imfindcircles(rgb,[range(1,4)
range(1,5)],'ObjectPolarity','dark','Sensitivity',sens+0.01,'EdgeThreshold',edg);
[centers5, radii5] = imfindcircles(rgb,[range(1,5)
range(1,6)],'ObjectPolarity','dark','Sensitivity',sens+0.02,'EdgeThreshold',edg);
[centers6, radii6] = imfindcircles(rgb,[range(1,6)
range(1,7)],'ObjectPolarity','dark','Sensitivity',sens+0.02,'EdgeThreshold',edg);
[centers7, radii7] = imfindcircles(rgb,[range(1,7)
range(1,8)],'ObjectPolarity','dark','Sensitivity',sens+0.03,'EdgeThreshold',edg);
[centers8, radii8] = imfindcircles(rgb,[range(1,8)
range(1,9)],'ObjectPolarity','dark','Sensitivity',sens+0.03,'EdgeThreshold',edg);
[centers9, radii9] = imfindcircles(rgb,[range(1,9)
range(1,10)],'ObjectPolarity','dark','Sensitivity',sens+0.03,'EdgeThreshold',edg);
[centers10, radii10] = imfindcircles(rgb,[range(1,10)
range(1,11)],'ObjectPolarity','dark','Sensitivity',sens+0.04,'EdgeThreshold',edg);
[centers11, radii11] = imfindcircles(rgb,[range(1,11)
range(1,12)],'ObjectPolarity','dark','Sensitivity',sens+0.04,'EdgeThreshold',edg);
[centers12, radii12] = imfindcircles(rgb,[range(1,12)
range(1,13)],'ObjectPolarity','dark','Sensitivity',sens+0.04,'EdgeThreshold',edg);
[centers13, radii13] = imfindcircles(rgb,[range(1,13)
range(1,14)],'ObjectPolarity','dark','Sensitivity',sens+0.04,'EdgeThreshold',edg);

% %%%%%BRIGHT (5x, 10x, 20x) – sometimes need to adjust sensitivity!!
% [centers1, radii1] = imfindcircles(rgb,[range(1,1)
range(1,2)],'ObjectPolarity','bright','Sensitivity',sens,'EdgeThreshold',edg);
% [centers2, radii2] = imfindcircles(rgb,[range(1,2)
range(1,3)],'ObjectPolarity','bright','Sensitivity',sens,'EdgeThreshold',edg);
% [centers3, radii3] = imfindcircles(rgb,[range(1,3)
range(1,4)],'ObjectPolarity','bright','Sensitivity',sens+0.01,'EdgeThreshold',edg);
% [centers4, radii4] = imfindcircles(rgb,[range(1,4)
range(1,5)],'ObjectPolarity','bright','Sensitivity',sens+0.01,'EdgeThreshold',edg);
% [centers5, radii5] = imfindcircles(rgb,[range(1,5)
range(1,6)],'ObjectPolarity','bright','Sensitivity',sens+0.02,'EdgeThreshold',edg);
% [centers6, radii6] = imfindcircles(rgb,[range(1,6)
range(1,7)],'ObjectPolarity','bright','Sensitivity',sens+0.02,'EdgeThreshold',edg);
% [centers7, radii7] = imfindcircles(rgb,[range(1,7)
range(1,8)],'ObjectPolarity','bright','Sensitivity',sens+0.03,'EdgeThreshold',edg);
% [centers8, radii8] = imfindcircles(rgb,[range(1,8)
range(1,9)],'ObjectPolarity','bright','Sensitivity',sens+0.03,'EdgeThreshold',edg);
% [centers9, radii9] = imfindcircles(rgb,[range(1,9)
range(1,10)],'ObjectPolarity','bright','Sensitivity',sens+0.03,'EdgeThreshold',edg);
```

```
% [centers10, radii10] = imfindcircles(rgb,[range(1,10)
range(1,11)],'ObjectPolarity','bright','Sensitivity',sens+0.04,'EdgeThreshold',edg);
% [centers11, radii11] = imfindcircles(rgb,[range(1,11)
range(1,12)],'ObjectPolarity','bright','Sensitivity',sens+0.04,'EdgeThreshold',edg);
% [centers12, radii12] = imfindcircles(rgb,[range(1,12)
range(1,13)],'ObjectPolarity','bright','Sensitivity',sens+0.04,'EdgeThreshold',edg);
% [centers13, radii13] = imfindcircles(rgb,[range(1,13)
range(1,14)],'ObjectPolarity','bright','Sensitivity',sens+0.04,'EdgeThreshold',edg);


   %*******************************
   %start inner-droplet deletion
   %*******************************

   deletion_count = 0; %counts droplet cancellations
      for h = 1:(n-1) %refers to smaller centers and radii
         centerSmall = eval(sprintf('centers%0.f', (h)));
         heightSmall = size(centerSmall);
         for i = (h+1):n %refers to larger centers and radii
            centerLarge = eval(sprintf('centers%0.f', (i)));
            heightLarge = size(centerLarge);
            radiiLarge = eval(sprintf('radii%0.f', (i)));
            for d=1:heightLarge(1) % start zero assigning process
               for j=1:heightSmall(1)
                  if sqrt(((centerLarge(d,1)) - centerSmall(j,1))^2 + ((centerLarge(d,2)) - centerSmall(j,2))^2) <
1*(radiiLarge(d))
                     centerSmall(j,1) = 0;
                     centerSmall(j,2) = 0;
                     deletion_count = 1 + deletion_count;
                  end
               end
            end %end zero assigning process
         end
            %start zero deletion process
         if eval(sprintf('isempty(centers%0.f) ~= 1', h)) %checks if centers h is not empty
            for i=heightSmall(1):-1:1
               if centerSmall(i,1) == 0
                  eval(sprintf('centers%0.f(%0.f,:) = [];', h, i)) %deletes [0,0] cells in centers h
                  eval(sprintf('radii%0.f(%0.f,:) = [];', h, i)) %deletes [0,0] cells in radii h
               end
            end
         end
            %end zero deletion process
      end

   %*******************************
   %end inner-droplet deletion
   %*******************************

allcenters = [centers1; centers2; centers3; centers4; centers5; centers6; centers7; centers8; centers9; centers10;
centers11; centers12; centers13];
```

```
allradii = [radii1; radii2; radii3; radii4; radii5; radii6; radii7; radii8; radii9; radii10; radii11; radii12; radii13];

alldata = [allcenters allradii allradii*calib];

cd(filefolderout);

%%%%%%%%%%%%% output an excel file %%%%%%%%%%%
inputdata={filename '' '' '' '' '';
        'range (min_um)' 'range (max_um)' 'mean radius (um)'  'count(#)' 'area(m2)' 'count/area(#/m2)';
        range(1,1)*calib, range(1,2)*calib, (range(1,2)+range(1,1))/2*calib, size(centers1,1),A,size(centers1,1)/A;
        range(1,2)*calib, range(1,3)*calib, (range(1,3)+range(1,2))/2*calib, size(centers2,1),A,size(centers2,1)/A
        range(1,3)*calib, range(1,4)*calib, (range(1,4)+range(1,3))/2*calib, size(centers3,1),A,size(centers3,1)/A;
        range(1,4)*calib, range(1,5)*calib, (range(1,5)+range(1,4))/2*calib, size(centers4,1),A,size(centers4,1)/A;
        range(1,5)*calib, range(1,6)*calib, (range(1,6)+range(1,5))/2*calib, size(centers5,1),A,size(centers5,1)/A;
        range(1,6)*calib, range(1,7)*calib, (range(1,7)+range(1,6))/2*calib, size(centers6,1),A,size(centers6,1)/A;
        range(1,7)*calib, range(1,8)*calib, (range(1,8)+range(1,7))/2*calib, size(centers7,1),A,size(centers7,1)/A;
        range(1,8)*calib, range(1,9)*calib, (range(1,9)+range(1,8))/2*calib, size(centers8,1),A,size(centers8,1)/A;
        range(1,9)*calib, range(1,10)*calib, (range(1,10)+range(1,9))/2*calib, size(centers9,1),A,size(centers9,1)/A;
        range(1,10)*calib, range(1,11)*calib, (range(1,11)+range(1,10))/2*calib,
size(centers10,1),A,size(centers10,1)/A;
        range(1,11)*calib, range(1,12)*calib, (range(1,12)+range(1,11))/2*calib,
size(centers11,1),A,size(centers11,1)/A;
        range(1,12)*calib, range(1,13)*calib, (range(1,13)+range(1,12))/2*calib,
size(centers12,1),A,size(centers12,1)/A;
        range(1,13)*calib, range(1,14)*calib, (range(1,14)+range(1,13))/2*calib,
size(centers13,1),A,size(centers13,1)/A;};
   xlswrite('07-26 5x data.xls',inputdata,filename,'A1');
%
  %%%%% show images and save them%%%%%
figure
imshow(rgb);impixelinfo
hbright=viscircles(eval(sprintf('allcenters')), eval(sprintf('allradii')),'EdgeColor','b');

saveas(gcf,[filename,'_processed','.jpg'])

savefig([filename,'_fig','.fig'])

dlmwrite([filename,'_data','.txt'],alldata,'delimiter','\t')
```

APPENDIX B

CODE: Heat Transfer and Sweeping

```
clear all;

Ts = 95+273; %surface temperature [K]
Tsat = 100+273; %saturation temperature
dT = Tsat-Ts; %subcooling temp [K]
thetaA = 122;   %advancing contact angle [deg]
thetaR = 118;   %receding contact angle [deg]
theta = acosd(0.5*cosd(thetaA)+0.5*cosd(thetaR));   %contact angle [deg]
kl = 0.6;   %thermal conductivity liquid [W/m.K]
alpha = 0.04; %condensation coefficient
rho_v = 1/1.679;  %density vapor/air [kg/m³]
rho_w = 1000;   %density liquid water [kg/m³]
mu_o = 140*10^-6*1900; %dynamic viscosity Krytox oils @20°C [Pa.s]
gamma = 72e-3;  %surface tension [J/m²]
Hfg = 2257e3; %latent heat water [J/kg]
Rg = 461.5; %specific gas constant water vapor [J/kg.K]
dcoat = 1e-9;   %coating thickness (silane) [m]
hB = 500e-9; %height of Boehmite [m]
kcoat = 0.1;    %thermal conductivity (silane) coating [W/m.K]
kB = 10;    %thermal conductivity Boehmite [W/m.K]
koil = 0.08;    %thermal conductivity oil (lubricant) [W/m.K]
f =  0.1 ;  %solid liquid fraction Bohemite
f_g = (pi/3*(2-3*cosd(theta)+cosd(theta)^3)/sind(theta)^3)^(1/3); %contact angle function
g = 9.81;   %gravitational constant [m/s²]

Ns = 1e11;  %nucleation site density [1/m²]

rmin = 2*Tsat*gamma/(rho_w*Hfg*dT);   %minimum nucleation radius [m]
re = 1/2/sqrt(Ns);   %transition radius nulceation -> coalescence [m]
rmax=sqrt((6*(cosd(thetaR)-cosd(thetaA))*sind(theta)*gamma)/(pi*(2-
3*cosd(theta)+cosd(theta)^3)*rho_w*9.81*1));  %maximum radius [m]

Lmax = 1;  %height of plate [m]
L = linspace(0,Lmax,100);
dL = abs(L(1,2)-L(1,1)); %step size [m]
q_tot=zeros(1,size(L,2));
q_L=zeros(1,size(L,2));
q_tot_Ns=zeros(1,size(L,2));
Rz=zeros(1,size(L,2));
rs=zeros(1,size(L,2));
r_sw=zeros(1,size(L,2));
V_0=zeros(1,size(L,2));
fz=zeros(1,size(L,2));
t_cycle=zeros(1,size(L,2));

R1 = linspace(rmin,re,100);
R2 = linspace(1.1*re,rmax,1000);
```

```
R = [R1 R2];   %radius variable [m]

Nz=zeros(size(R,2),size(L,2));
fr=zeros(size(R,2),size(L,2));
fr_Ns=zeros(size(R,2),size(L,2));

q_tot = 1e-5;
q_0 = 0;

%loop until find q_0 to use in V_0 for constants
while abs(q_tot(1,1)-q_0)/q_tot(1,1) > 0.01,
   q_0 = q_tot(1,1);
   r_z = @(r,z) (rmax(1,1)/1.3);

   %resistances for qd
   AdT = @(r,z) (dT*pi.*r.^2.*(1-rmin./r));
   hi = @(r,z) (2*alpha/(2-alpha)*1/sqrt(2*pi*Rg*Ts)*rho_v*Hfg^2/Ts*(1-rmin./r));  %HTC of droplet at interface
   Rhi = @(r,z) (1./(2.*hi(r,z)*(1-cosd(theta))));    %condensation resistance
   Rc = @(r,z)  ((theta/180*pi).*r/(4*kl*sind(theta)));   %curvature resistance
   Rcoat = @(r,z) (1/(kcoat*sind(theta)^2)*(kB*f/(dcoat*kB+hB*kcoat)+koil*(1-f)/(dcoat*koil+hB*kcoat))^(-1)); %coating and lubricant resistance

   %for n(r)
   A1 = @(r,z) (dT/(Hfg*rho_w*(1-cosd(theta))^2*(2+cosd(theta)))); %constant for n(r)
   A2 = @(r,z) ((theta/180*pi)/(4*kl*sind(theta))); %constant for n(r)
   A3 = @(r,z) (Rhi(r,z)+Rcoat(r,z)); %constant for n(r)
   tau = @(r,z) ((3*re^2.*(A2(r,z)*re+A3(r,z)).^2)./(A1(r,z).*(11.*A2(r,z)*re^2-14.*A2(r,z)*re*rmin+8.*A3(r,z)*re-11.*A3(r,z)*rmin)));    %sweeping constant
   B1 = @(r,z) (A2(r,z)./(tau(r,z).*A1(r,z)).*((re^2-r.^2)/2+rmin.*(re-r)-rmin^2.*log((r-rmin)/(re-rmin)))); %constant for n(r)
   B2 = @(r,z) (A3(r,z)./(tau(r,z).*A1(r,z)).*(re-r-rmin.*log((r-rmin)/(re-rmin)))); %constant for n(r)

   V = @(r,z) (pi/3.*r.^3*(2-3*cosd(theta)+cosd(theta)^3)/sind(theta)^3);    %volume of a spherical cap

   N_r_z = @(r,z) (1./(3*pi.*r.^2.*r_z(r,z)).*r.^(-2/3)./r_z(r,z).^(-2/3)); %dropsize distribution large droplets [1/m³]
   n_r_z = @(r,z) ((1./(3*pi*re^3.*r_z(r,z)).*(re./r_z(r,z)).^(-2/3)).*r*(re-rmin)./(r-rmin).*(A2(r,z).*r+A3(r,z))./(A2(r,z)*re+A3(r,z)).*exp(B1(r,z)+B2(r,z)));   %dropsize distribution small droplets [1/m³]

   qd_small = @(r,z) (AdT(r,z)./(Rhi(r,z)+Rc(r,z)+Rcoat(r,z)).*n_r_z(r,z));  %q*n for small droplets
   qd_big = @(r,z) (AdT(r,z)./(Rhi(r,z)+Rc(r,z)+Rcoat(r,z)).*N_r_z(r,z));    %q*N for large droplets

   Vd_small = @(r,z) (V(r,z).*n_r_z(r,z)); %V*n for small droplets
   Vd_big = @(r,z) (V(r,z).*N_r_z(r,z)); %V*N for big droplets

   q_tot(1,1) = integral2(qd_small,rmin,re,0,Lmax)/Lmax + integral2(qd_big,re,rmax(1,1)/1.3,0,Lmax)/Lmax;
   m = rho_w*(integral2(Vd_small,rmin,re,0,Lmax)/Lmax + integral2(Vd_big,re,rmax(1,1),0,Lmax)/Lmax);
end

t_ch = m/q_tot(1,1)*Hfg;
a=1/125;
b=1/2;
r_sw(1,1) = rmax(1,1);
```

```
V_0(1,1) = f_g^3*rmax(1,1)^3;
B = 2*rmax(1,1)/0.82;    %slot size
t(1,1)=0;
rs(1,1)=rmax(1,1);  %radius to which droplets grow before being swept
r_sw(1,1)=rmax(1,1);    %radius of sweeping drops
q_L(1,1)=q_tot(1,1);
t_cycle(1,1)=t_ch;

%discretizing plate height
for i=2:size(L,2),

  N_r_z = @(r,z) (1./(3*pi.*r.^2*rs(1,i-1)/1.3).*r.^(-2/3)/(rs(1,i-1)/1.3)^(-2/3)); %dropsize distribution large
droplets [1/m³]
  n_r_z = @(r,z) ((1./(3*pi*re^3*rs(1,i-1)/1.3).*(re./(rs(1,i-1))*1.3).^(-2/3)).*r*(re-rmin)./(r-
rmin).*(A2(r,z).*r+A3(r,z))./(A2(r,z)*re+A3(r,z)).*exp(B1(r,z)+B2(r,z)));   %dropsize distribution small droplets [1/m³]

  Vd_small = @(r,z) (V(r,z).*n_r_z(r,z)); %V*n for small droplets
  Vd_big = @(r,z) (V(r,z).*N_r_z(r,z)); %V*N for big droplets

  %volume increase
  As = dL*2*r_sw(1,i-1);   %swept area
  dV = (integral2(Vd_small,rmin,re,L(1,i-1),L(1,i))/dL + integral2(Vd_big,re,rs(1,i-1),L(1,i-1),L(1,i))/dL)*As;
  V_0(1,i) = V_0(1,i-1)+dV; %new volume
  r_sw(1,i) = V_0(1,i)^(1/3)/f_g;

  t_cycle(1,i) = t_ch/(2*r_sw(1,i)/B);
  if t_cycle(1,i) > t_ch,
    t_cycle(1,i)=t_ch;
    qc=q_tot(1,1);
  end

  %find rmax(y) = rs
  %i.e. find droplet size to which droplets grow through D.C. and coalescence
  %in time t = t_cycle, i.e. in between sweeping cycles
  rcoal = rmax(1,1)+1e-4;
  t=t_ch+1;

  while t-t_cycle(1,i) > 0.01,
    rcoal=rcoal-1e-6;
    N_r_z = @(r,z) (1./(3*pi.*r.^2*(rcoal/1.3)).*r.^(-2/3)/(rcoal/1.3)^(-2/3)); %dropsize distribution large droplets
[1/m³]
    n_r_z = @(r,z) ((1./(3*pi*re^3*(rcoal/1.3)).*(re./(rcoal/1.3)).^(-2/3)).*r*(re-rmin)./(r-
rmin).*(A2(r,z).*r+A3(r,z))./(A2(r,z)*re+A3(r,z)).*exp(B1(r,z)+B2(r,z)));   %dropsize distribution small droplets [1/m³]
    qc = integral2(qd_small,rmin,re,0,L(1,i))/L(1,i) + integral2(qd_big,re,rcoal/1.3,0,L(1,i))/L(1,i);
    mc = rho_w*(integral2(Vd_small,rmin,re,L(1,i-1),L(1,i))/dL + integral2(Vd_big,re,rcoal,L(1,i-1),L(1,i))/dL);
    t = mc/qc*Hfg;
  end

  rs(1,i)=rcoal;
  q_tot(1,i) = qc;
```

```
%heat flux as a function of vertical position on plate
   q_L(1,i) = integral2(qd_small,rmin,re,L(1,i-1),L(1,i))/dL+integral2(qd_big,re,rs(1,i)/1.3,L(1,i-1),L(1,i))/dL;

   %dropsize distribution
   for j=1:size(R,2),
      if R(1,j)<1.01*re,
         Nz(i,j) = n_r_z(R(1,j),L(1,i));
      else
         Nz(i,j) = N_r_z(R(1,j),L(1,i));
      end
   end

end
```

APPENDIX C

CODE: Average Contact Time Integration

```
% average contact time vibrating rigid surface

clear all;
clc;

tc = 13.5/1000;    %theoretical contact time s
u = 1.35;   %falling velocity
% A =1*0.001; %amplitude m
f=[60:1:350];    %frequency range Hz
A = [0.1:0.2:3]/1000; %amplitude m

pi = 3.141592654;

t_average=zeros(size(f,2),size(A,2));

phi_d = 135/180*pi;    %departure phase

for j = 1:size(A,2),
   for i=1:size(f,2),
      u_star=A(1,j)*2*pi*f(1,i)/u;  %dimensionless susbtrate velocity
      tmax = tc/2+1/f(1,i);
      phi_c = phi_d - 2*pi*f(1,i)*tc/2;

      % find integration boundaries
      % phi1: where re-entrant of possibility curve starts
      % phi2: where re-entrant of possibility curve ends
      % phi3: modulus of critical phase
      if u_star<=1, %w/o re-entrant assume phi1=phi2=180°
         phi1 = pi;
         phi2 = pi;
      else
         phi1 = acos(-1/u_star);
         phi1 = real(phi1);

         %find phi0(phi1)
         syms phi
         phi0(phi) = u_star*(sin(phi)-1)+phi;
         phi0_1 = phi0(phi1);
         %find phi0(phi) == phi0(phi1) -> phi = phi2
         phi2=phi1+1/180*pi;
         while phi0(phi2)<phi0_1,
            phi2=phi2+1/180*pi;
         end
      end
```

```
      phi3 = mod(phi_c,2*pi);
      n = floor(abs(phi_c)/(2*pi));

      % contact times as a function of impact phase
      % instead of modulus can divide integral into 3 regions;
      % need to subtract n*360deg instead of modulus
      % t1(phi) for phi < mod(phi_c,360deg)
      % t2(phi) for phi > mod(phi_c,360deg)
      t1 = @(phi) (tmax - 1/(2*pi*f(1,i)).*(phi-phi_c-n*2*pi));
      t2 = @(phi) (tmax - 1/(2*pi*f(1,i)).*(phi-phi_c-(n+1)*2*pi));
      % possibility density function for impact at phase phi
      p = @(phi) (1/(2*pi).*(u_star.*cos(phi)+1));

      tp1 = @(phi) (t1(phi).*p(phi));
      tp2 = @(phi) (t2(phi).*p(phi));

      % integration
      if phi3>phi1,
         if phi3<phi2,
            time = integral(tp1,0,phi1)+integral(tp2,phi2,2*pi);
         elseif phi3>=phi2,
            time = integral(tp1,0,phi1)+integral(tp1,phi2,phi3)+integral(tp2,phi3,2*pi);
         end
      else
         time = integral(tp1,0,phi3)+integral(tp2,phi3,phi2)+integral(tp2,phi2,2*pi);
      end

      %normalized contact time
      t_average(i,j) = real(time)/tc;

   end
end



dlmwrite('C:\...\Vibrating Rigid Surface\tav_A.txt',t_average,'delimiter','\t')
```